STUDYING APTAMER-LIGAND INTERACTIONS AND DYNAMICS IN THE COCAINE-BINDING APTAMER THROUGH NMR SPECTROSCOPY

ZACHARY R. CHURCHER

A DISSERTATION SUBMITTED TO
THE FACULTY OF GRADUATE STUIDES
IN PARTIAL FULFILLMENT OF THE REQUIREMENTS
FOR THE DEGREE OF
DOCTOR OF PHILOSOPHY

GRADUATE PROGRAM IN CHEMISTRY
YORK UNIVERSITY
TORONTO, ONTARIO

April 2022

Abstract

Aptamers are oligonucleotide molecules with applications in biosensors, analytical chemistry, and therapeutics. They are often to 10 to 100 nucleotides in length and can be selected to bind a wide range of targets from ions to cells. The cocaine-binding aptamer was selected in 2000 by Milan Stojanovic to bind cocaine but not benzoylecgonine and ecgonine methyl ester, two common cocaine metabolites. Since its development the cocaine-binding aptamer has been found to bind to quinine with an affinity ~50 times stronger than to cocaine. The cocaine-binding aptamer has been used to help test and develop new biosensing systems.

This research hopes to further the understanding of how the cocaine-binding aptamer interacts with its ligands in the hope that these interactions could be used to help understand other aptamer-ligand systems. Using nuclear magnetic resonance (NMR) spectroscopy the base pair dynamics of the cocaine-binding aptamer was investigated as a function of ligand binding. This study was later expanded to include the effects of temperature and buffer composition to determine thermodynamic parameters of base pair dissociation. The results showed a general reduction in dynamics with ligand binding in the aptamer at the ligand-binding site, but little change elsewhere in the aptamer.

The binding of additional ligands to the cocaine-binding aptamer was characterized by NMR spectroscopy. Levamisole is an anti-parasitic worm medication and one of the most common adulterants found in cocaine. Levamisole was found to bind the cocaine-binding aptamer with a weak affinity at the same site as cocaine. The binding of the cocaine-binding aptamer to a set of three-way junction-binding dyes was also investigated. These dyes share a common structure but bind to the aptamer with a range of affinities. These dyes also bound at the same site as cocaine

and quinine, with the dyes being able to be displaced by cocaine or quinine depending on their affinity.

Finally, the binding of ochratoxin A to the ochratoxin A-binding aptamer was investigated using NMR. This aptamer had not been previously studied using NMR, was found to fold tightly in response to its ligand, and NMR proton assignments were obtained.

Acknowledgements

I would like to thank my parents and sister for their love and support during this period in my life. Without the supportive environment you all helped create I do not think I could have done this. I would also like to thank my parents again for keeping a roof over my head so I could focus on my research. Without all your support this would not have been possible.

I would like to sincerely thank my supervisor Professor Philip Johnson for allowing me to work in his lab and trusting me with the valuable compounds our lab works with. You taught me so much I don't think there's ever a way I could fully repay you. You created a wonderful environment for me to learn in and were always there when I needed assistance. Thank you so much for allowing me to be part of your research group for all these years.

To my friends that I've met throughout the years, thank you for being there for me. Thank you for your kind words of support and for listening when I talked about my research. It all helped support me and get to the finish line.

I want to thank my committee members Logan Donaldson and Gerald Audette for all of the advice, guidance and feedback thy provided to me about my work. I would also like to thank Howard Hunter for keeping the NMR spectrometer functioning so I could run all my experiments.

I want to extend a warm thanks to all the member of the Johnson lab past and present for all their help over the years. A special thanks to Aron Shoara and Sladjana Slavkovic for all the work they did. Thank you for your day-to-day support and help, I am truly honored to have worked alongside the both of you. I hope our paths stay close together and we can work alongside each other again.

Table of contents

List of Tables

List of Figures

List of Abbreviations

1D	One dimensional
2D	Two dimensional
CD	Circular dichroism
ΔG	Change in free energy
ΔH	Change in enthalpy
ΔS	Change in entropy
DANTE	Delayed alternating with nutation for tailored excitation
DCA	Deoxycholic acid
ddH_2O	Double distilled water
DMSO	Dimethyl sulfoxide
DNA	Deoxyribonucleic acid
DSC	Differential scanning calorimetry
HSQC	Heteronuclear single quantum coherence
ITC	Isothermal titration calorimetry
k_{ex}	Exchange rate constant
K_d	Dissociation constant
MN#	Cocaine-binding aptamer variants
mRNA	Messenger ribonucleic acid
NMR	Nuclear magnetic resonance
NOESY	Nuclear Overhauser effect spectroscopy
OTA-1	Ochratoxin A-binding aptamer
PHASA	Photochrome aptamer switch assay

R_{1a}	Relaxation constant of a proton
R_{1w}	Relaxation constant of water
RE-BURP	Band-selective Uniform-Response Pure-phase (RE refers to the fact that this BURP sequence creates a 180° pulse)
RNA	Ribonucleic acid
SELEX	Systematic evolution of ligands by exponential enrichment
τ_m	Mixing time
TOCSY	Total correlation spectroscopy
TWJ	Three-way Junction
UV-Vis	Ultraviolet-Visible

Chapter 1 An Introduction to Aptamers

1.1 Background

When most people think of nucleic acids, they imagine the typical double stranded DNA helix found in eukaryotic cells. Nucleic acids can take other forms both in nature and in the lab with uses besides information storage. These can include RNA Riboswitches found within cells acting as regulatory elements, to nanostructures built using DNA origami, to ligand targeting aptamers. Aptamers are short nucleic acid strands that are generally on the order of 10 to 100 nucleotides long. They were first developed independently in 1990 by Tuerk and Gold who were trying to find an RNA sequence that would bind to T4 DNA polymerase [1], and Ellington and Szostak who used the process to select RNA sequences to bind organic dyes [2]. This led to the development of a process called Systemic Evolution of Ligands by Exponential Enrichment (SELEX), which is used to generate ligand binding aptamers from a library of randomized sequences. Both groups first developed aptamers from RNA libraries, with DNA aptamers being developed a few years later [3], and peptide aptamers being developed a few years after that when Colas *et al.* developed peptide aptamers that interact with cyclin-dependent kinase 2 [4].

DNA and RNA aptamers feature some small differences between the two groups even though both are based on similar nucleic acid structures. RNA aptamers can fold into a more diverse range of 3D structures, which can allow them to bind more ligands when compared with DNA aptamers [5]. DNA aptamers however are easier to produce, cheaper, and more biologically stable than their RNA counterparts which can make them a more promising target for certain applications.

Aptamers can bind a wide array of ligands, from small molecules to cell surface proteins which they can do with high binding affinity and specificity. Because of this, aptamers are often

compared to antibodies [6]. Aptamers have several advantages over antibodies. Firstly, nucleic acid aptamers can be repeatedly unfolded with heat and still fold back into their original structures, whereas spoilage due to denaturation is a concern with antibodies. Secondly, after initial selection using SELEX, regenerating a known aptamer sequence is a straightforward and reproducible process. In addition, the bases in an aptamer can be modified with a number of different chemical groups to give them added functionality such as linkers for attaching them to surfaces, fluorophores and quenchers for detecting folding/unfolding, and groups designed to increase the unfolding temperature of the aptamer. Finally, nucleic acids do not cause a large response from the immune system allowing them to be used in medical applications.

1.2 SELEX

Aptamers are selected using a process known as Systematic Evolution of Ligands by Exponential Enrichment, or commonly referred to as SELEX [1], [2]. Generally, in SELEX, a ligand of choice is exposed to a large pool of ~10^{13} - 10^{16} sequences, usually between 20 and 100 nucleotides in length. These sequences start and end with the conserved primer sites required for PCR amplification, and a central region of randomized bases. The pool of potential sequences is exposed to the target ligand, then the sequences which do not interact with the ligand are removed, and those that do interact are collected. These collected sequences are amplified using PCR methods, and the process is repeated 10 to 20 times, until a set of sequences are generated which interact with the target ligand with specific characteristics. An overview of this process can be seen in Figure 1.1. This process can be lengthy taking ~3-7 weeks and there is no guarantee that an aptamer will be generated with the desired binding characteristics [7].

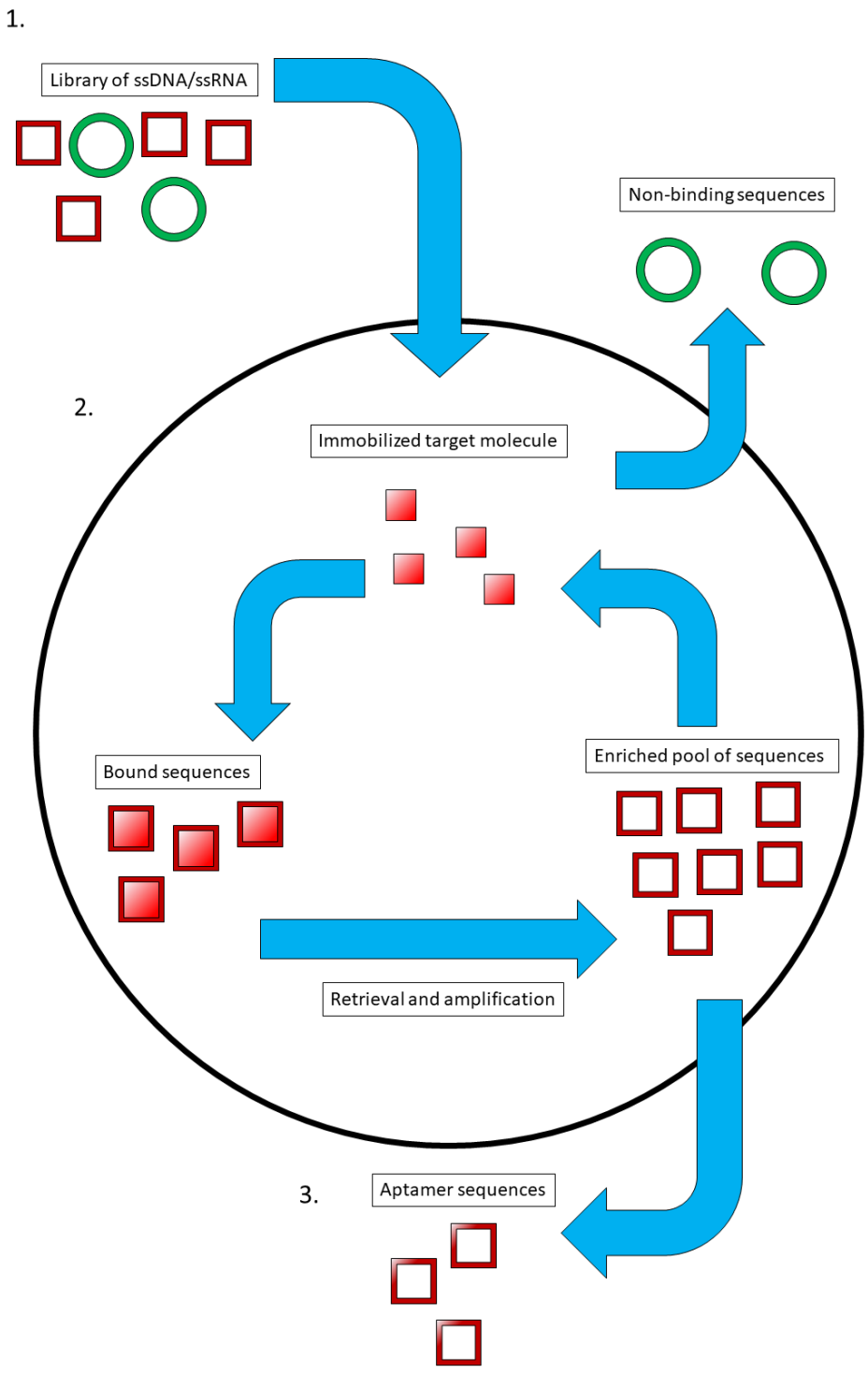

Figure 1.1. Basic diagram of SELEX. **1.** Initial library is exposed to the ligand of interest. **2.** Non-binding sequences are discarded while bound sequences are retrieved, amplified, and re-exposed to the ligand of interest. This cycle is repeated several times. **3.** Once the cycles are finished a set of aptamer sequences with the desired characteristics are collected and sequenced.

The SELEX method can be integrated with other methods to improve its accuracy. One of these methods is called Negative SELEX [3], [7]. False positives may occur during the SELEX process from sequences interacting with the chemical supports which immobilize the ligand. After 3 rounds of selection, the pool of potential aptamers is exposed to the ligand support, which is usually agarose gel, without any immobilized ligand. In this case the sequence which do not bind the support are collected, and the sequences which do bind the supports are removed from the potential pool. This method can increase the affinity of generated aptamer by ~10 times. This method is generally incorporated into most modern SELEX experiments. Counter SELEX is another technique [8] which can be integrated with SELEX and works similarly to negative SELEX. The difference with Counter SELEX is that the pool of potential aptamers is exposed to a molecular target for which the experimenter does not want the potential aptamers to interact with. This usually includes structural similar molecules to the target ligand such as metabolites, related proteins, etc.

Other more specialized SELEX methods also exist for generating aptamers in living systems. In cell SELEX sequences are exposed to whole cells in solution, allowing to select for targets found on the surface of cells [9]. In this technique the ligand of interest doesn't need to be identified beforehand, only the cell of interest. This technique was first used in 2003 by Daniels *et al.* [9], allowing them to develop an aptamer to a glioblastoma cell line. *In Vivo* SELEX is also possible, allowing for selection of aptamers that would function properly under biological conditions. This would be useful for aptamers generated for use in therapeutics and biosensors. This was first performed in 2010 by Mi *et al.* [10], who selected aptamers against liver tumors in tumor affected mice. This processed involved injecting the pool of sequences into the tumor, allowing the sequences to incubate, then harvesting them and injecting them into other mice

carrying the same tumors. Toggle SELEX is a method used in the development of aptamers for pharmaceutical products that allows the aptamer in question to be studied better during pre-clinical and clinical trials. Toggle SELEX involves exposing the potential aptamer pool to the human version of the target protein during one round of SELEX [11], but in the next round exposing it to an animal version of the same protein. The animal chosen matches with the animal model being used to study the aptamer in the lab during the preclinical trial phase of development. This prevents the aptamer from solely binding to the human form of the protein, which would make it difficult to study in animal models and gather enough efficacy data to start human trials in the future.

The SELEX method can also be performed using specialized systems in order to reduce the time required to perform the selection or reduce the quantity of reagents required. CE-SELEX uses capillary electrophoresis to separate sequences which bind the target ligand from non-binding sequences [12], [13]. This greatly reduces the number of selection rounds required to 1-4 rounds and removes the need to immobilize the ligand of interest. Though, this technique is unsuited for small ligands as the mobility between the bound and unbound sequences will not be large enough to detected. Capture-SELEX instead immobilizes the pool of aptamer and collects the sequences which interact with free floating ligand [14]. This method is useful for finding aptamers which bind small molecules but can run into issues since some sequences may not detach from the support when binding the target ligand. M-SELEX takes place in a microfluidic system which allows for a very efficient selection which uses a small amount of reagents and is very quick [15]. This method is also automatable. This method still suffers from traditional problems related to immobilizing the target ligand.

1.3 Aptamer Structure

1.3.1. Base Pairs. A single strand of DNA will generally fold up on itself so that the largest number of bases are bound together through hydrogen bonds, unless something prevents the DNA bases from interacting, like high a concentration of urea. In most cases guanines and cytosines will bind together, and adenines and thymines will bind together. These interactions are known as the Waston-Crick base pairs. In these interactions the two bases are interacting with the Watson-Crick edges of their DNA bases (Figure 1.2a-b). Several non-Watson-Crick base pairs exist such as guanine-adenine and guanine-thymine to name a few. These non-canonical base pairs can interact through their Watson-Crick and/or Hoogstein edges (Figure 1.2c-f). While most base pairs are Watson-Crick style interactions, non-canonical base pairs are not an uncommon site in an aptamer. When multiple base pairs are found side by side, they will form a helix. Helices can vary in shape but are grouped into A-form, B-form, and Z-form with B-form being the most common in DNA. Helices are usually joined at a junction with the ends of other helices. The ends of these helices can also end in nucleotide loops usually consisting of 3 to 6 nucleotides but can be larger. Many aptamers have structures that include these types of elements such as the cocaine-binding aptamer [16], [17] and the ATP-binding aptamer [18].

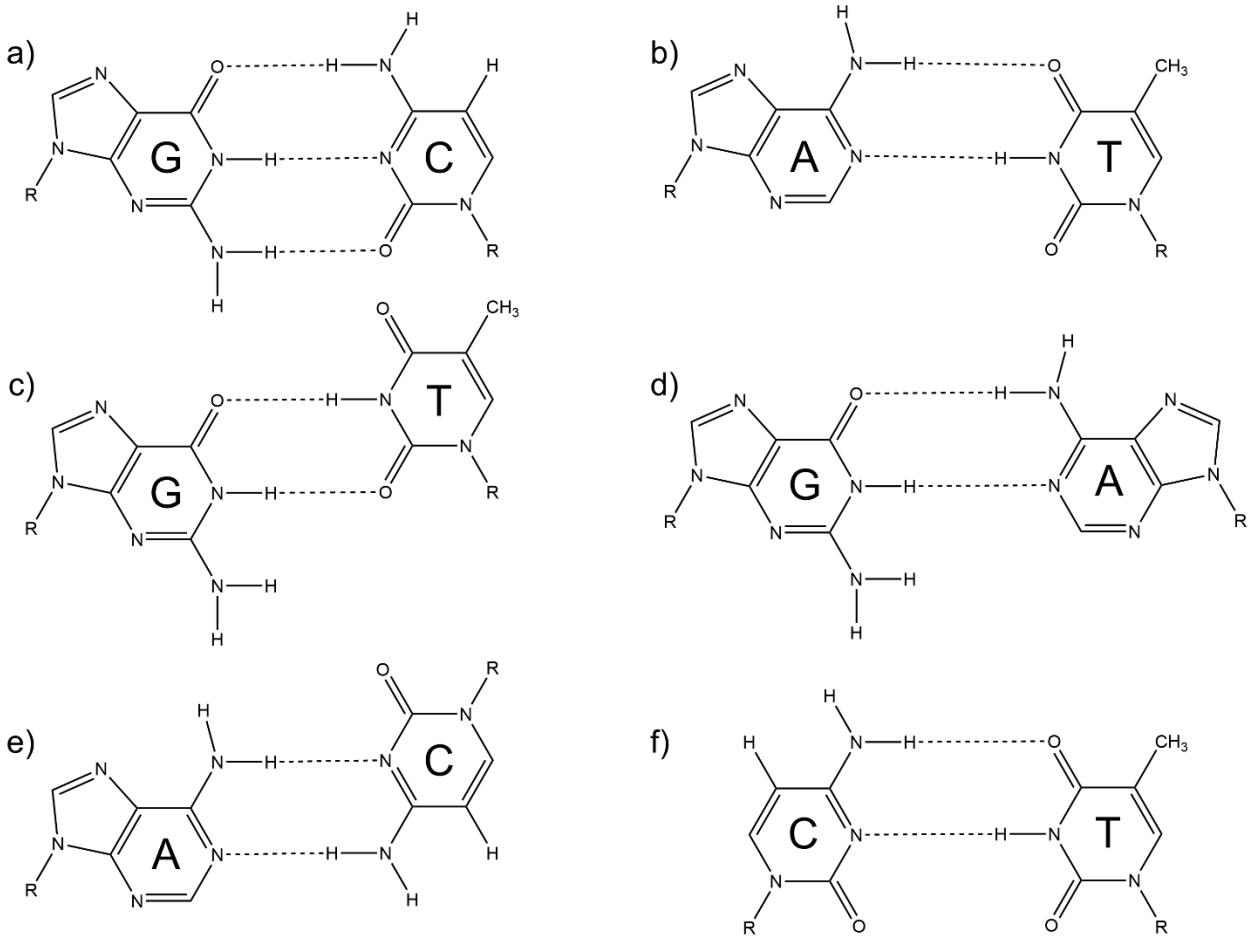

Figure 1.2. A non-exhaustive list of two nucleotide base pairs. Watson-Crick base pairs: a): Guanine-Cytosine; b): Adenine-Thymine. Non-Watson-Crick base pairs: c): Guanine-Thymine; d) Guanine-Adenine, e): Adenine-Cytosine, f): Cytosine-Thymine. Bases marked with a G are Guanine; A are Adenine; C are Cytosine; T are Thymine. Dashed lines represent hydrogen bonds between the various bases.

1.3.2. Base Triples. More than two nucleotides can interact at a time. When three bases come together a base triple is formed, with many base triples stacking on top of each other forming a triplex. Base triples are usually structured with two base pairs interacting with each other, with a third nucleotide coming in and interacting with its Watson-crick edge to one of the other nucleotides Hoogstein edges [19]. The central base in a base triple is a purine, as pyrimidines do not have as many hydrogen bond donors/acceptors to allow for multiple nucleotides to hydrogen bond with them. Examples of base triples can be seen in Figure 1.3

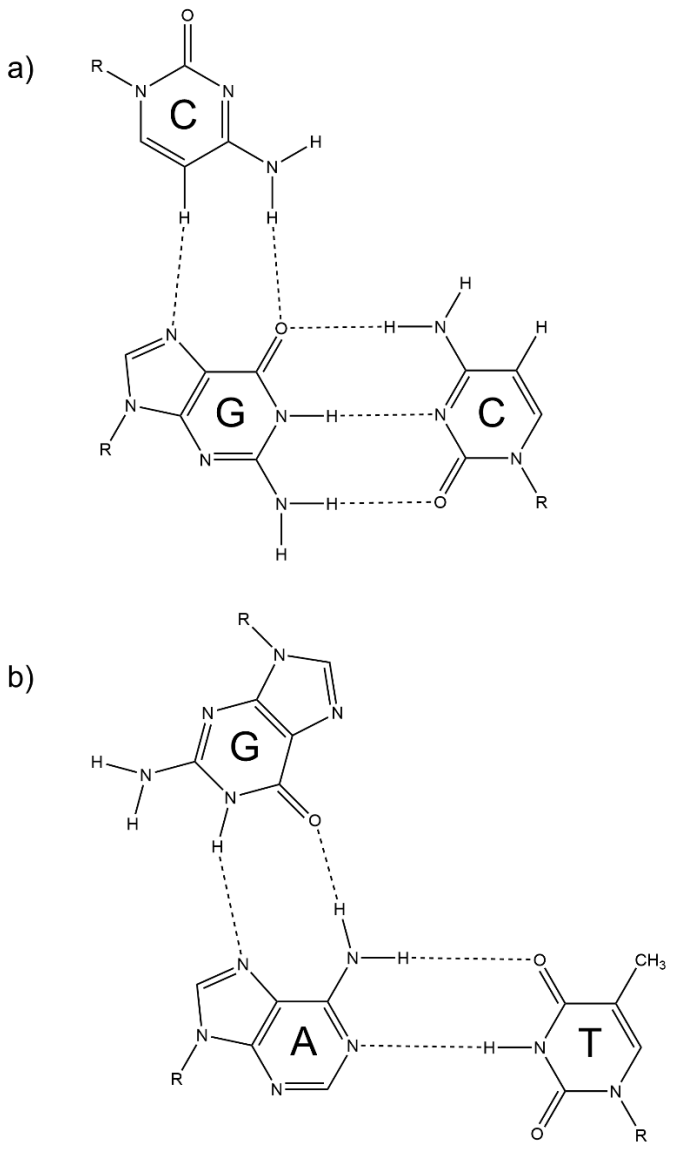

Figure 1.3. A non-exhaustive list of example base triples. a) a C-G-C base pair, and b) a G-A-T base pair. Bases marked with a G are Guanine; A are Adenine; C are Cytosine; T are Thymine. Dashed lines represent hydrogen bonds between the various bases.

Several aptamers found in the literature contain a triplex structure. One of these is the codeine-binding aptamer characterized by Bing *et al.* [20] This aptamer contains a triplex of six base triples stacked on each other, and a quadruplex structure below that (see section 1.3.3 for more information on quadruplexes) with the codeine binding site being at the interface of these two structural elements. Patel and colleagues used a triplex based aptamer structure to create an

adenosine biosensing platform [21]. Their work produced a biosensor with a limit of detection of 50 nM, and a working range of 50 nM to 2 μM.

1.3.3. G-Quadruplexes and i-motifs. Quadruplexes are a common structural motif formed from guanine rich nucleic acid strands and are found in aptamers as well as in living cells. In living cells, quadruplexes are often found in telomeres and as regulatory elements in the genome [22]. A quadruplex is made up of a series of G-quartets stacked one on top of the other [23]. A G-quartet is made up of 4 guanines interacting with each other using their Watson-Crick and Hoogstein edges (Figure 1.4). In between these G-quartets sits a cation, usually a potassium or sodium ion to help balance the charges on the inside of the quartet. This is important to know when designing SELEX buffers, as these ions are required for quadruplex formation and quadruplexes tend to bind to specific ligands.

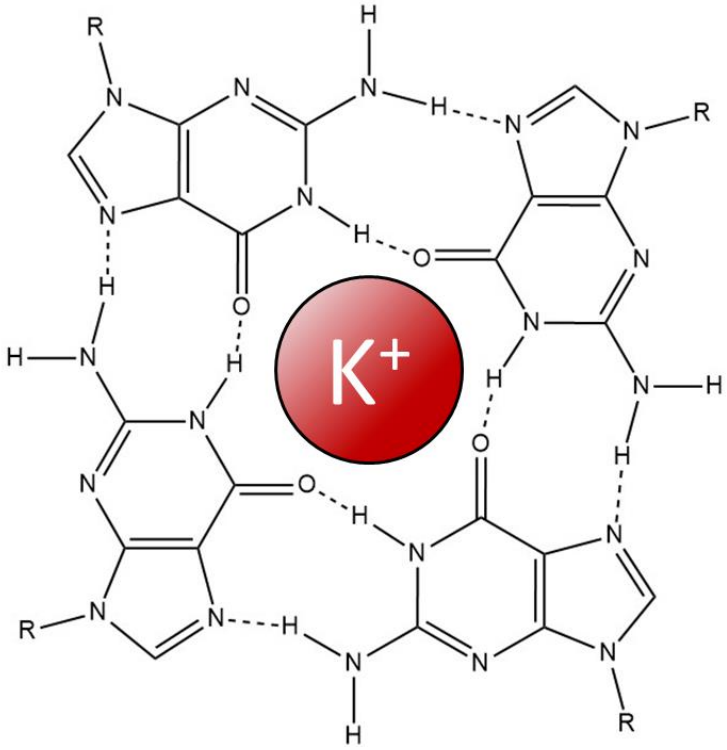

Figure 1.4. Hydrogen bonding pattern amongst the 4 guanines present in a single G-quartet, surrounding a potassium ion. Dashed lines represent hydrogen bonds between the various guanine bases.

Quadruplexes can be monomolecular, bimolecular, or tetramolecular in their composition, and a small number of tri-molecular quadruplex structures have also been identified. The backbones of the quartets can have a parallel, anti-parallel, or mixed/hybrid topology [23]. A parallel quadruplex has all 4 of the backbone strands of the quartets running in the same 3' to 5' direction (Figure 1.5a). An anti-parallel quadruplex differs in that, 2 strands of the quadruplex run 1 direction (3' to 5) while the other 2 strands run in the opposite direction (Figure 1.5b & c). A mixed or hybrid topology occurs when 3 strands run in one direction and the last strands runs in the opposite direction (Figure 1.5d), but this structure is uncommon compared with the other two. Outside of the G-quartet core of these structures can be nucleotides linking the backbone of the G-quartets, these linkers fall can be diagonal, lateral, or propeller loops. Propeller loops run along the sides of a quadruplex resembling a propeller when looking down the center of the quadruplex. Lateral loops link two strands along the top or bottom most quartet, while diagonal loops are similar but link the two non-adjacent strands of the quartets.

These G-quadruplex structures are not limited to aptamers found in solution but have also been found *in vivo*. G-quadruplexes have been found to form in telomere regions at the end of a cell's DNA. Paeschke *et al*. used nuclear electroelution to find G-quadruplexes in *Stylonychia* nuclei and found that their formation was mediated by the presence of two proteins, TEBPα and TEBPβ [24]. Summers and co-workers have more recently used fluorescence lifetime imaging microscopy to track the formation of G-quadruplexes in Human Bone Osteosarcoma Epithelial Cells [25]. In addition, Yang *et al*. found RNA G-quadruplex structures are able to form within plants and demonstrated that these structures can affect plant growth in both *Arabidopsis* and rice plants [26].

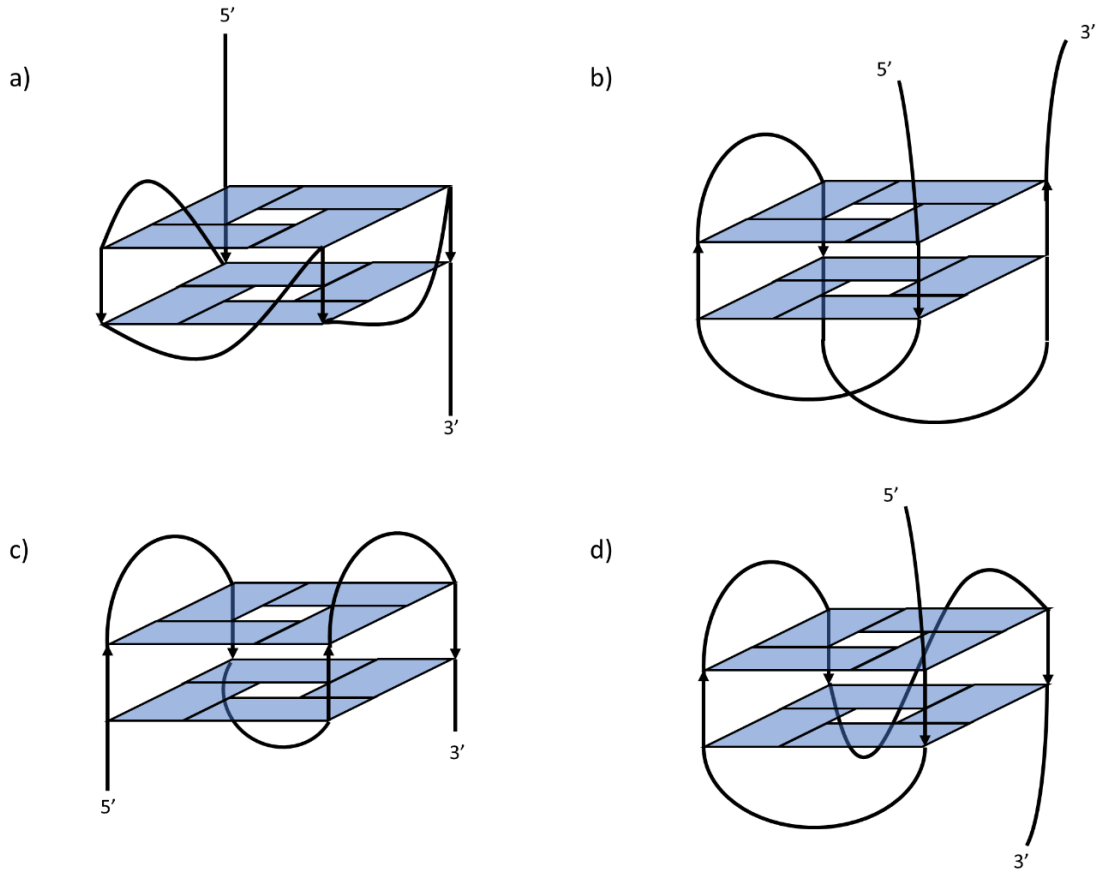

Figure 1.5. Structural diagrams of various G-quadruplex backbone topologies a) parallel, b) & c) anti-parallel, and d) 3+1.

I-motifs are another set of four stranded oligonucleotide structures. Unlike G-Quadruplexes, i-motifs are often formed from cytosine rich strands. In an i-motif, two sets oligonucleotide strands each form a helix, with these two helices being intercalated with one another [27] (Figure 1.6). The base pairs in an i-motif are mostly C-C^+ base pairs where the central nitrogen on one of the cytosines has been protonated allowing it to hydrogen bond with the nitrogen on the opposing cytosine. T-T and C-T base pairs can also be found in i-motifs but these great destabilize the structure. I-motifs can and do form under physiological conditions, but are most likely to form between pH 4.2 and 5.2, and at colder temperatures of 4 °C [27].

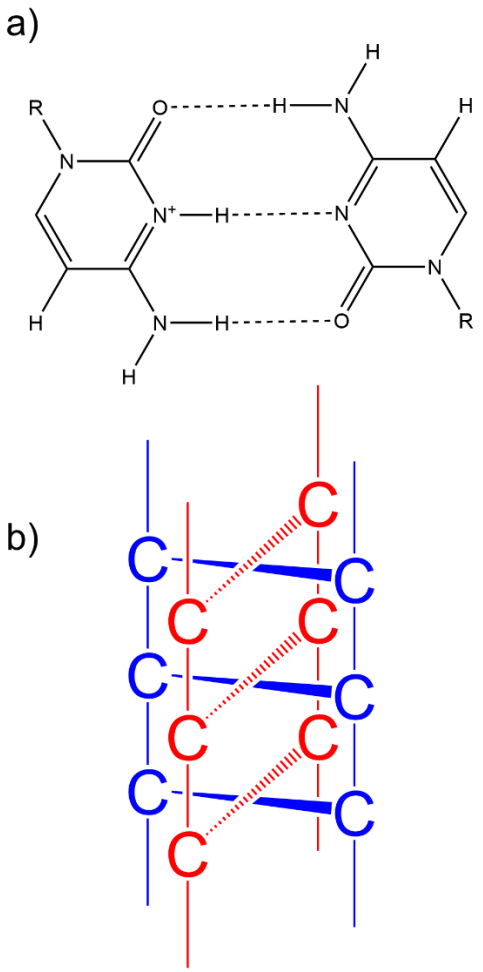

Figure 1.6. a) An example of a cytosine-cytosine base pair often found in an i-motif. The central nitrogen on the left cytosine has been protonated allowing it to hydrogen to the adjacent cytosine. b) An example of the interlaced helical structure that makes up an i-motif.

Much like G-quadruplexes, i-motifs have also been found to form *in vivo,* though their presence has only been discovered much more recently [28]. Dzatko *et al*. used NMR spectroscopy and CD spectroscopy to investigate if these structures are forming within HeLa cells [29]. Zeraati *et al*. selected a set on antibodies against i-motifs and used those to find i-motifs in HeLa cells [30]. They determined that the formation of these structures is dependent on pH of the environment and its place in the cell cycle.

1.4 Aptamer Ligands

Aptamers can be selected against a number of different types of ligands ranging in size from single ions up to entire cells. By far the largest categories of ligands for aptamers are proteins and small molecules. As mentioned previously, aptamers can have a high degree of specificity for their ligand which allows them to discriminate between molecules that are structurally similar. Generally, aptamers and their ligand interact through hydrogen bonding, which can help stabilize the folded structure of the aptamer. Other ligands interact with their aptamer by intercalating between the base pairs themselves and being stabilized by π- π stacking interactions. Sometimes an aptamer's overall structure can influence the types of ligands it may bind to. Proteins often interact with aptamers at loop regions [31], and G-quadruplex ligands are often large planar molecules which stack against the G-Tetrad and take advantage of the π-π stacking interactions [32]. A chart representing the relative amount of aptamer ligand from aptamer selected from 1990 to 2021 has been summarized below in Figure 1.7. This data was generated from aptagen.com/aptamer-index and accessed on November 23rd 2021.

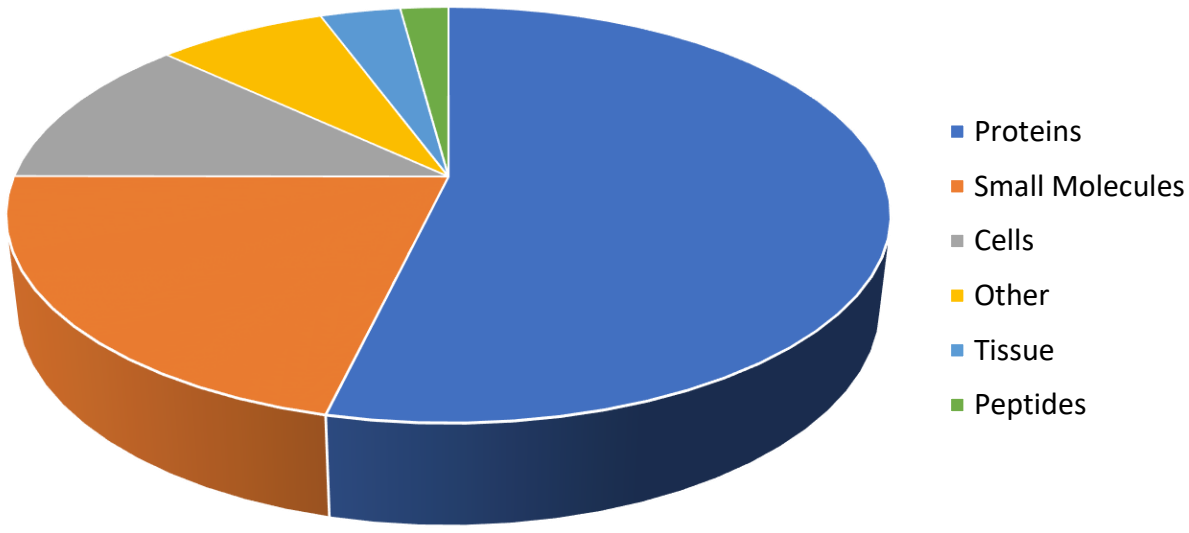

Figure 1.7. Relative amounts of aptamer ligands for aptamers selected from 1990 to 2021.

1.5 Aptamer Applications

Due to their potential high affinity and specificity, aptamers can have a number of different applications, often in the fields of therapeutics/medicine and as biosensors. In addition, aptamer like structures do exist in nature in the form of riboswitches.

Riboswitches are regulatory mRNA sequences often found in bacteria, which bind to small molecules causing a structural change in the mRNA [33], [34]. This structural change in the mRNA can have a number of different effects on how the mRNA is treated in the cell. This change in structure can prevent the mRNA from being read leading to the gene being silenced. It can lead to alternate splicing pathways, leading to a different product being produced. Riboswitches can also interact with other genes in the cell, causing them to be silenced.

Aptamers can act as therapeutics in different ways, either interacting directly with a target, by being conjugated to another drug and having the aptamer act as a sensor for the drug target, or in a diagnostic role. The first aptamer to be used as a therapeutic is Macugen which was developed in 1998 [35]. Macugen is an aptamer that treats age related macular degeneration. The aptamer itself binds to the vascular endothelial growth factor (VEGF), which is responsible for creating new blood vessels in the eye and is responsible for leakages from these vessels. This leakage leads to swelling in the eye and macular degeneration. Macugen is an anti-VEGF aptamer, which binds to its target and prevents its function, reducing one of the main causes of age-related macular degeneration.

Aptamers can be used in the delivery of drugs to a specific cellular target. Nucleolin is cellular protein often over expressed in the cytoplasm of cancerous cells, and a nucleolin aptamer was used as a delivery system to deliver anti-cancer drugs to cancerous mice [36]– [40]. The aptamer was conjugated to doxorubicin and internalized into the cell upon interacting with

nucleolin. This showed an inhibition in tumour growth in mouse models. This type of aptamer-drug conjugated system has also been tested with aptamers targeting the prostate-specific membrane antigen [41]– [43], the MUC1 glycoprotein [44], protein tyrosine kinase 7 [45], [46], and the T cell receptors OX40 and 4-1BB [47], [48].

Aptamers work as great detection molecules for sensor systems as well. These sensors often fall under the broad categories of electrochemical sensors, optical sensors, or mass sensitive sensors, and sensors can fall into multiple categories simultaneously. For electrochemical sensors, the aptamer is generally immobilized on the surface on some form of electrode, and the binding of the target ligand stimulates a detectable electrochemical change in the system. For example, the aptamer could be conjugated to a redox moiety which sits away from the surface of the electrode when not interacting with the ligand. When interacting with the ligand however the redox moiety would be brought closer to the electrode surface allowing for an electron transfer between the moiety and the surface to take place. This would require that the aptamer undergoes a shift from being non-structured or loosely structured in its free state to being structure in its bound state. Zhang *et al.* [49] used the electrochemical approach to design an aptasensor to detect prostate specific antigen. This sensor used aptamers attached to palladium nanoparticles on the surface of a carbon electrode.

Optical sensors generally illicit some form of colour change in the sensor when the aptamer meets its ligand. This could be done using fluorescence methods or by using a dye. Many dyes will interact with an aptamer with a lower affinity than their target ligand. Upon binding with the target ligand, the dye would become displaced, and the free-floating dye would induce a visible colour change in the solution. For fluorescence methods the aptamer could be conjugated to a fluorescent group on one end of the strand, while a fluorescent quencher could be conjugated to

the opposite end of the strand. In the free state the aptamer would fluoresce as the quencher would be separated from the fluorescent group, but upon binding the two groups would be brought closer together and quench the fluorescence. Lee *et al.* used a bisphenol A aptamer to create an optical sensor for the determination of bisphenol A in food samples [50]. Their sensor used aptamers conjugated to gold nanoparticles to create a colour change upon binding to bisphenol A that can be seen with the eye in solution. The presence of bisphenol A causes the nanoparticles to aggregate changing the colour of the solution from red to blue.

Mass sensitive sensors require that there be a large change in the mass of the system upon the binding of the ligand to the aptamer. These systems usually work better for aptamers which interact with proteins than those which bind to small molecules. For these sensors the aptamer is attached to a piezoelectric crystal, which oscillates at a specific frequency. The binding of the target ligand causes a shift in the mass on the surface of the crystal, causing a change in frequency. Goda and Miyahara used an anti-histone aptamer attached to a quartz crystal microbalance to create a system to detect acetylation in histone molecules [51].

1.6 The cocaine-binding aptamer

The cocaine-binding aptamer was originally selected in 2000 by Stojanovic *et al.*, with their efforts focused on selecting a cocaine-binding aptamer that did not bind to benzoylecgonine and ecgonine methyl ester which are two common cocaine metabolites [52]. The original aptamer was referred to as MNS 4.1 with a structure of three stems attached together via a three-way junction. This three-stem/three-way junction structure is conserved in all the cocaine-binding aptamer variants derived from this original sequence. This original MNS 4.1 sequence was 39 nucleotides long and bound to cocaine with an affinity of 5 μM. It was proposed that the binding of cocaine caused stem 3 of the aptamer to form into a helix (Figure 1.8).

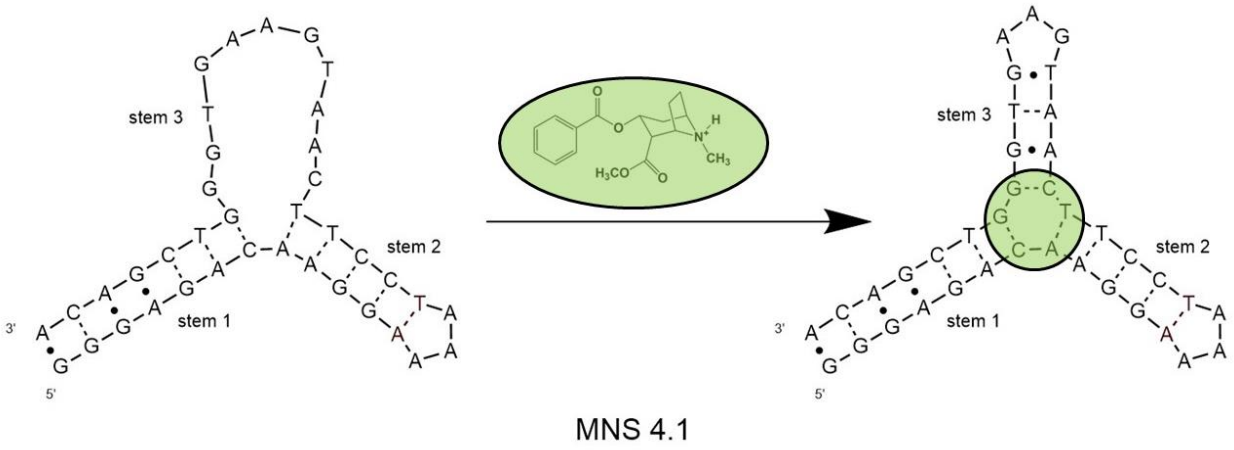

Figure 1.8. Secondary structure of the MNS 4.1. The structure of the free aptamer is shown on the left, and the structure of the ligand-bound aptamer is shown on the right, with the ligand shaded in green. This Figure is adapted from reference 52.

In 2010 Neves *et al*. [16] through a mutation study using NMR and ITC found that the original proposed structure of the aptamer was incorrect, and that the three way junction of the aptamer was centered around a tandem A*G mismatch (Figure 1.9). The structure studied was also changed slightly, stem 1 was shortened by one base pair by removing the terminal G*A base pair, and the T*G base pair in stem 3 was changed to a C-G base pair. This paper also investigated the binding mechanism of the aptamer and found the binding mechanism was tied to the length of stem 1. If stem 1 is four or more base pairs long, then the free aptamer is folded, and very little structural change occurs upon binding. If stem 1 is three base pairs or shorter, the free aptamer is not fully folded and the aptamer becomes more structured upon binding.

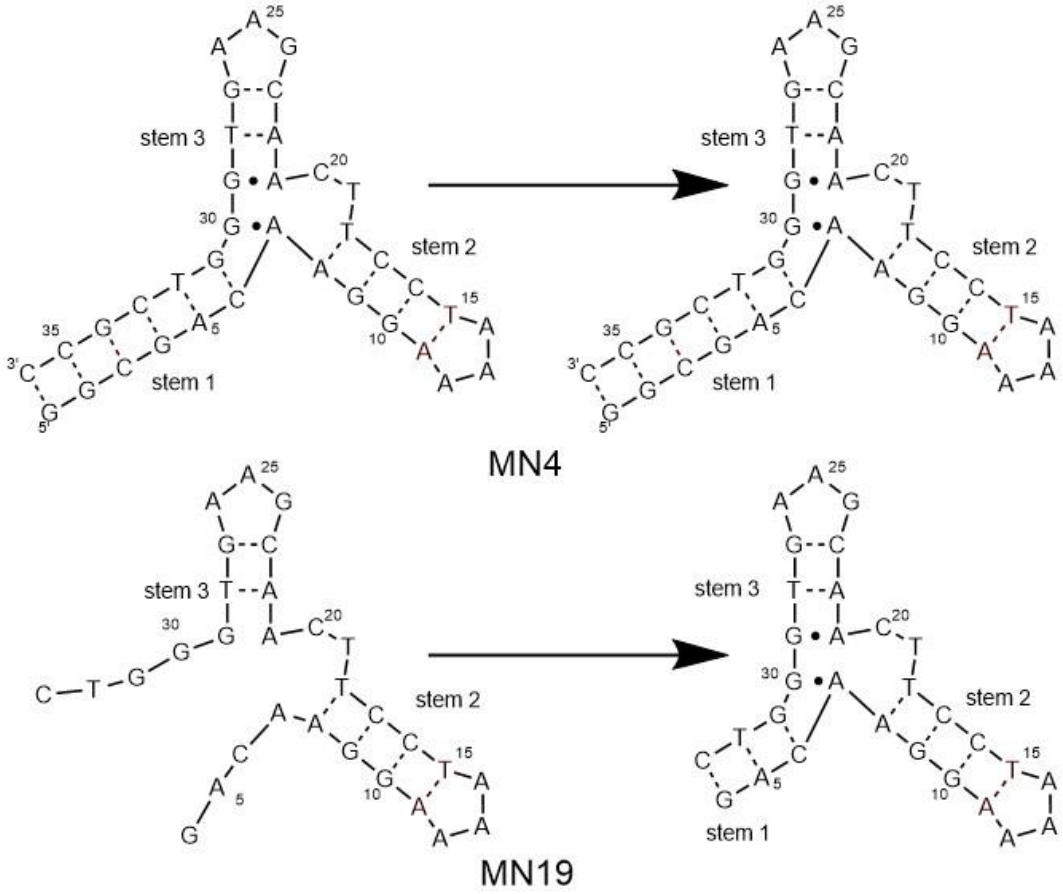

Figure 1.9. Secondary structures of the MN4 and MN19 aptamer constructs. The structure of the free aptamers is shown on the left, and the structure of the ligand-bound aptamers is shown on the right.

Though selected to bind to cocaine and not cocaine metabolites, it was found that the cocaine-binding aptamer does show some off-target ligand binding. In 2003, Stojanovic *et al.*, found that a variant of their cocaine-binding aptamer could bind to deoxycholic acid (DCA) but there was very weak binding to cocaine [53], and in 2009 showed that the aptamer could also bind to quinine, an anti-malaria drug [54]. Later, Reinstein *et al.* quantified the binding of the cocaine-binding aptamer to DCA [55]. In addition, it was also found that quinine also bound to the cocaine-binding aptamer ~50 times tighter than cocaine, for which it was originally selected. In 2015 Slavkovic *et al.* investigated the ability of the cocaine-binding aptamer to bind a number of quinine

derivatives [56], and in 2018 investigated the binding of non-quinine based anti-malarial compounds [57].

The cocaine-binding aptamer has been well studied, and several sensors using it as a detector have been made. In 2001, Stojanovic *et al.* used the aptamer to make a fluorescent biosensor for cocaine [58]. By attaching a fluorophore to the 5' end and a quencher to the 3' end, the aptamer will fluoresce in the free state but folds when bound to cocaine and the fluorescence is quenched. This was done using a variant of their MNS 4.1 aptamer with a shortened stem 1 named MNS-7.9. More recently, Xiao *et al.* used an MNS 4.1 based variant referred to as 38-GC to create a different fluorescence-based sensor for detecting cocaine in biofluids [59]. This system has the aptamer bind to a fluorescent dye at the three-way junction where cocaine binds. When the fluorescent dye is bound to the aptamer it is quenched and doesn't fluoresce, but when cocaine binds to the aptamer the dye is displaced, and fluorescence is seen in solution. This sensor was shown to be able to detect cocaine in both urine and saliva-based solutions. Being able to use these types of sensors in complex matrices is important as detecting analytes in samples from outside the laboratory is not often straight forward. In 2009 Plaxco *et al.* worked on using the cocaine-binding aptamer to create a microfluidic system to detect cocaine levels in undiluted blood [60]. This system involved using a 5' thiolated cocaine-binding aptamer bound to a gold surface. The aptamer also contained a methylene blue group at the 3' end. When not bound to ligand the methylene blue group remained away from the gold surface, but interaction with the ligand folds the aptamer bringing the methylene blue group close to the gold surface. This causes a transfer of electrons between the methylene blue and the gold surface, which can be detected.

1.7 Studying Aptamers

Probing aptamer-ligand interactions can be done in a variety of ways. For determining the strength of an aptamer-ligand interaction, isothermal titration calorimetry (ITC) is considered the gold standard [61]. In ITC, the ligand is titrated into an aptamer sample at a constant temperature, and the heat that is either produced or consumed by the interaction is measured. This creates a binding isotherm curve which can be used to determine several thermodynamic parameters of interaction such as K_d, ΔH and ΔS of ligand binding. Differential scanning calorimetry (DSC) is another heat measuring method that can be used [62]. DSC involves measuring the energy difference required to heat a sample compared with a reference cell. Usually this allows for the unfolding temperature of the aptamer to be detected, and how that temperature can change as a result of different sample conditions or aptamer changes. As nucleic acids absorb UV light, similar melting experiments can also be done using UV-Vis spectroscopy and tracking the absorbance at 260 nm [63], in addition G-quadruplexes also absorb at 280 nm [64]. As the aptamer unfolds the absorbance of the sample changes, allowing for the melting point to be determined. Aptamers themselves do not have as strong ability to fluoresce, so fluorescence experiments on aptamer systems either require the fluoresce of the ligand to be tracked, or a fluorescent tag must be added to the aptamer [65]. Aptamers have also been known to enhance the fluorescence of other weakly fluorescent small molecules [66]. The above methods can provide information of the properties of the aptamer, but do not provide information about the overall structure of the aptamer. The methods that are often used to determine the 3D structure of aptamers themselves are x-ray crystallography and NMR spectroscopy, the latter of which will be discussed in the following section in detail. In addition, for G-quadruplexes CD spectroscopy can be used to determine information about the backbone orientation of the aptamer [67]. In x-ray crystallography the

aptamer sample is first crystallized, though this can often be difficult and could require the aid of other biomolecules to aid in the formation usable crystals [68], [69]. The crystallized aptamer is then exposed to x-rays of a specific wavelength which the sample crystals cause to diffract. The crystal will be observed from many different angles and tens thousands of reflections will be collected. The diffraction pattern of the x-rays is used to create an electron density map of the sample and create an atomic model of the system in question, referred to as a crystal structure. The structure of the thrombin aptamer was discovered in this way [70].

1.8. NMR Spectroscopy

In solution NMR spectroscopy, the sample studied is placed in a strong magnetic field that enables the spin ½ nuclei present in nucleic acids (^{1}H, ^{13}C, ^{15}N and ^{31}P) to be studied. The nuclei will resonate at a characteristic frequency depending on chemical identity and local environment. NMR is a non-destructive technique allowing for multiple experiments to be performed on the same sample under different conditions such as temperature, the amount of ligand present in the sample, and/or different buffer compositions.

In NMR studies of aptamers, the resonances belong to the imino protons are often the first to be studied. The imino protons are so useful because their signals are located downfield (at higher ppm values), well separated from the signals of the rest of the protons found in nucleic acids (Figure 1.10). Imino proton signals generally only show up when hydrogen bonded, such as in a base pair. The position of an imino proton signal in an NMR spectrum is dictated by its chemical identity and environment. Imino protons in Watson-Crick base pairs are the most downfield, showing up around 12-14ppm with guanine iminos around 12-13ppm and iminos from thymine or uracil around 13-14ppm. Non-Watson-Crick base pairs are generally found upfield of the Watson-Crick base pairs in the 10-12ppm range. To provide the most useful information the identity of the

imino resonances should be determined. This can be done by analysis of a 2D NOESY experiment acquired in H_2O [71].

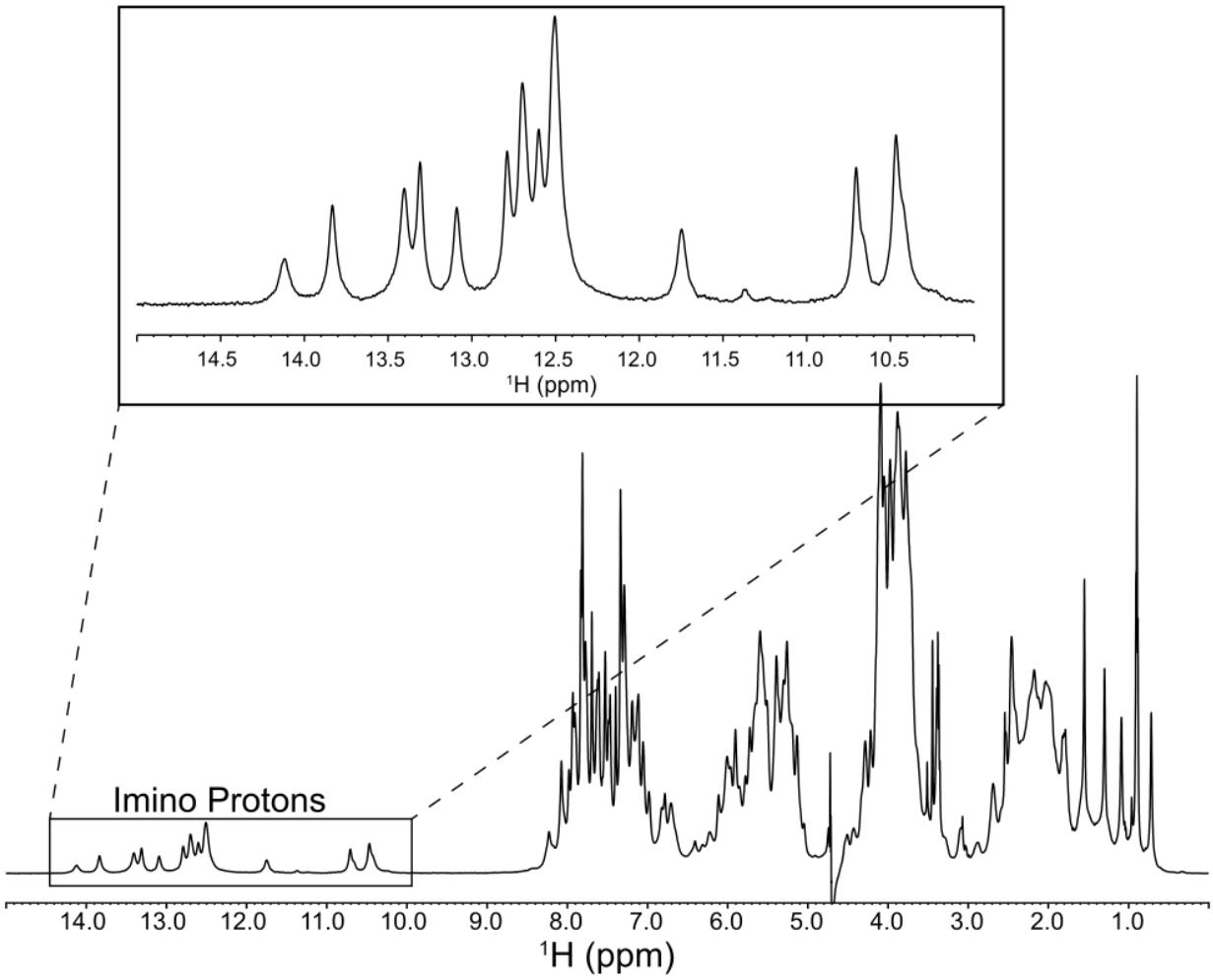

Figure 1.10. 1D ^{1}H NMR spectrum of a DNA cocaine-binding aptamer bound to cocaine with an inset focused on the imino region.

1.8.1 Sample Preparation. The first step in NMR experiments is to prepare the aptamer sample. NMR samples generally require 500-600 μL of liquid placed in a standard 5 mm Pyrex NMR tube. For DNA aptamers, sample is typically not limiting due to the ease of purchasing material and the high solubility of DNA. For typical 1D NMR experiments the aptamer concentration should be ~500 μM, but can go down to 200 μM, if required. For 2D experiments, a 0.8 mM sample is typically needed, though higher is preferable. If sample material is limited and a choice between

volume and concentration must be made, concentration should be the variable favored, as the signal intensity is directly proportional to the concentration of the sample. For NMR experiments, typically 2 to 4 samples of 1 μmole scale DNA syntheses are required.

DNA samples typically need only be buffer exchanged after purchase to remove any salts and reagents left over from the synthesis. Other forms of purification, such as preparative gel electrophoresis, are not needed when nucleic acid samples are purchased. Upon arrival, samples are dissolved in purified filtered water from a system such as a Milli-Q unit and placed in an Amicon type centrifugal filter. For aptamers in the 30-40 nucleotide range a 5 mL tube with a molecular weight cut-off of 3,000 MW is ideal. First, the sample should be exchanged four times against a 2 M NaCl solution. This helps removes any leftover salts and reagents from synthesis. The sample can then be exchanged into the desired buffer.

1.8.2 Sample Considerations. There are three main considerations that should be taken into account when choosing a buffer for an NMR sample. Firstly, the amount of salt should be kept to a minimum. A high concentration of salt in the sample (greater than 75-100 mM) can lower the signal to noise ratio of the sample, especially when using a cryogenic probe. An example of this can be seen in Figure 1.11. A good amount of salt in an NMR buffer is 20-50 mM, this amount should not cause too much of a problem with the signal to noise ratio. More salt can be present in an NMR buffer if it is required for the aptamer to fold, be stable or to function.

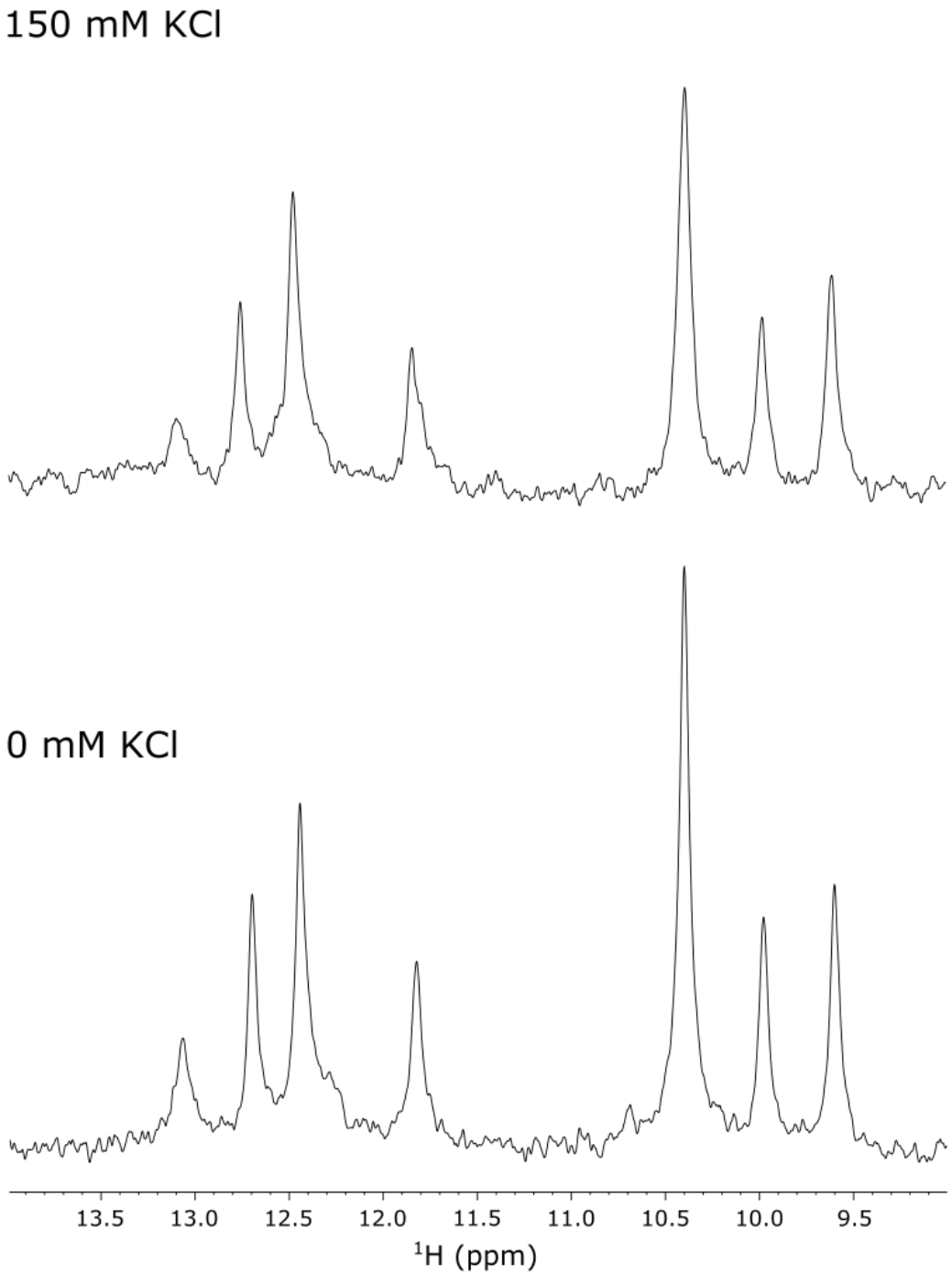

Figure 1.11. NMR spectra of a cocaine-binding aptamer bound to quinine, with either 0 mM or 150 mM KCl, illustrating the effect of salt on the NMR spectra. Samples are in 10 mM NaH_2PO_4 /Na_2HPO_4 (pH 7.4) 10% ^2H_2O, with an aptamer concentration of 360 µM. The quinine:aptamer molar ratio is 1:1.

The next consideration should be that many buffers used in molecular biology such as TRIS and HEPES contain protons. These protons will show up in your NMR sample and generally

drown out the signals from the aptamer. If the buffer does contain proton-rich reagents, deuterated versions of these reagents should be used. These deuterated versions are usually ~99% deuterated, meaning that there will be a small signal from the non-deuterated protons, but this is unavoidable. A 10-20 mM phosphate buffer is recommended for a working pH range of 6.2-8.2.

NMR buffers require 5-10% v/v ^2H_2O to allow for the NMR probe to lock onto the sample. This means when preparing the sample buffer an appropriate amount of ^2H_2O needs to be incorporated into the buffer. This should also be incorporated into your ligand solution, if applicable, to keep the NMR environment constant. In addition, some experiments will require the aptamer to be in a 100% ^2H_2O buffer, so that the signal from exchangeable protons will not be observed. Typically, experiments in H_2O are acquired first then the sample is lyophilized and taken up in ^2H_2O for experiment to be run in ^2H_2O.

Finally, it should be noted that NMR spectra where imino protons are to be detected are typically acquired at 5 °C. Generally, the higher the temperature the data is acquired at, the lower the signal to noise ratio the iminos will have as they exchange with the bulk water faster at higher temperature. Temperatures lower than 5 °C should be used with caution as the freezing point of 100% ^2H_2O is 3.8 °C.

1.8.3 Ligand preparation. As with selecting a proper NMR buffer, there are considerations that should be made when preparing the ligand sample. The smallest practical volume of ligand should be added in order to not dilute the sample too much and reduce the NMR signal. Adding 25-50 μL of ligand to the 500-600 μL NMR sample is fine and will not reduce the signal to noise appreciably.

Some ligands are not soluble or only sparingly soluble in water, which means they may need to be dissolved in an organic co-solvent, such as DMSO. If this is needed, a deuterated form should be used, as that amount of protonated organic solvent will drown out the NMR signal from

the aptamer. As with deuterated buffer reagents, there will be small NMR signals from residual protons in the deuterated organic solvent, but this is unavoidable. Small amounts of organic solvent (>5% v/v) should not cause much of a disruption of the aptamer sample [72]. Figure 1.12 shows a titration of DMSO into an aptamer resulting in only small changes in the NMR spectrum. Even for a ligand needing a solution of 100% organic solvent like DMSO, adding 30 μL to a 600 μL NMR sample will only result in a ~5% final solution. Before performing a titration of the aptamer and ligand in organic solvent, it may be worthwhile to do a titration of the aptamer with only the organic solvent, to see how the organic solvent affects the NMR signals.

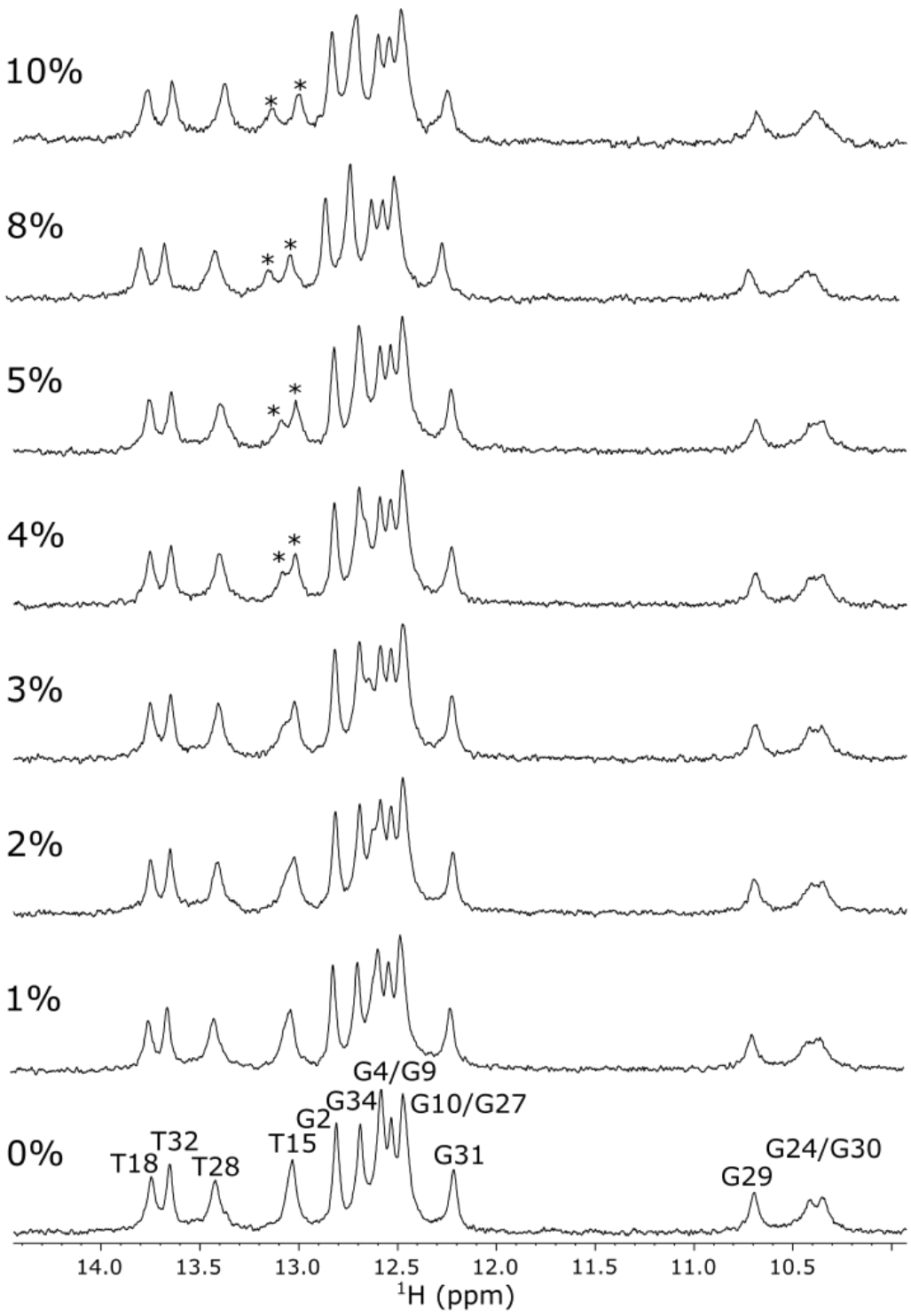

Figure 1.12. NMR spectra of an unbound cocaine-binding aptamer being titrated with DMSO. The percentage DMSO (v/v) is indicated. The DMSO does not have a large effect on the spectra until approximately 4% v/v. The asterisk denotes T15 splitting into 2 peaks possibly indicating that DMSO binds near this nucleotide. Titration takes place in 10 mM NaH_2PO_4/Na_2HPO_4 (pH 7.4) 10% ^2H_2O, with an aptamer concentration of 200µM.

1.8.4 Imino ^{1}H assignments. The 2D NOESY experiment allows for the imino proton resonances to be assigned so that in further experiments it is known which resonances correspond to which base pairs. A NOESY experiment detects which protons are close in space, typically within 5 Å. In a standard B-form or A-form helix the imino proton in a base pair will show an NOE signal to the imino protons of the adjacent base pairs in the helix. Depending on the structure of the aptamer, this should allow for most of the imino protons in the spectrum to be assigned. An example of this can be seen in Figure 1.13.

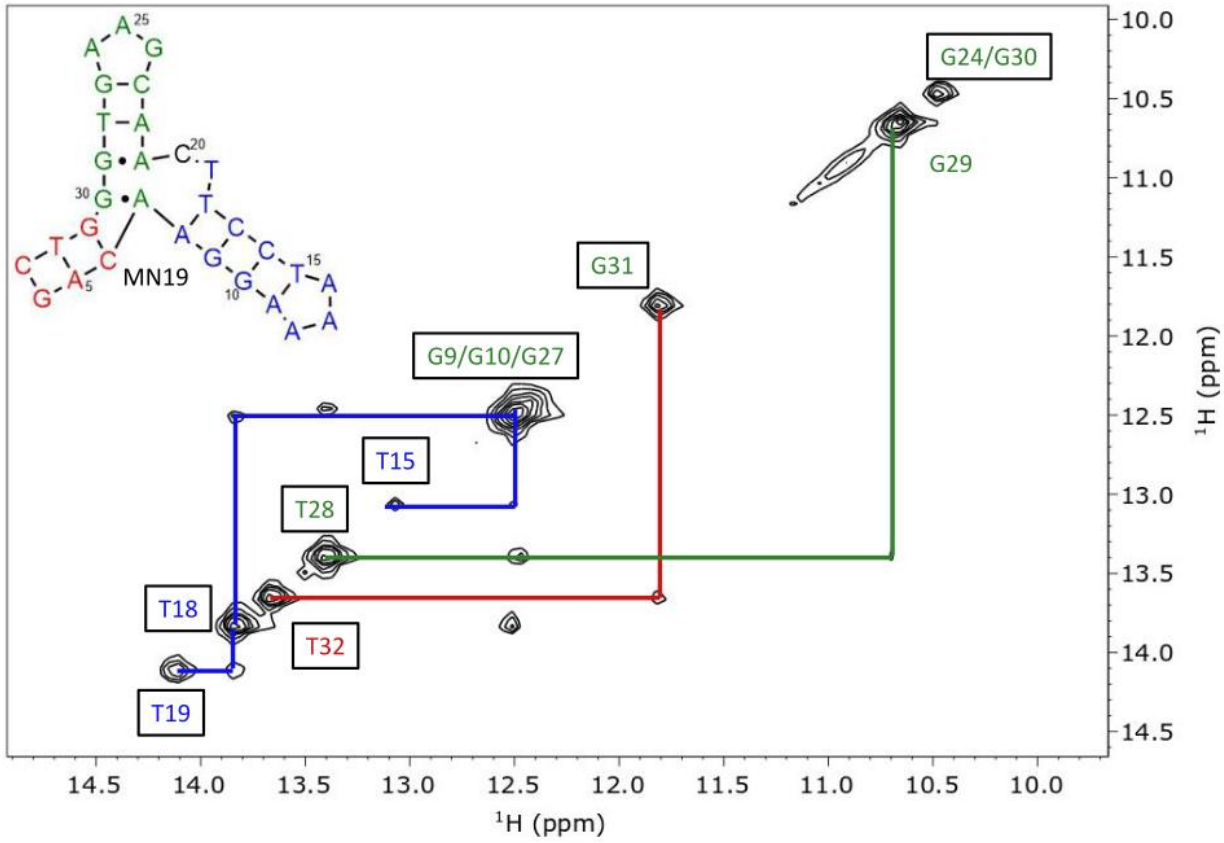

Figure 1.13 NOESY of a cocaine-binding aptamer (MN19) bound to cocaine. The secondary structure of the aptamer is shown in the top left, with the three stems being highlight in red (stem 1), blue (stem 2), and green (stem 3). The NOE steps are coloured to show which stem they represent in the aptamer. This experiment was conducted in 245 mM KCl, 5 mM KH_2PO_4/K_2HPO_4 (pH 6.8) 10% $^{2}H_2O$, with an aptamer concentration of 1.5 mM. The ligand:aptamer molar ratio is 1:1.

1.8.5 Ligand binding titrations. A titration of the aptamer with ligand monitored by a series of 1D ^{1}H spectra can yield very useful information about the location of the binding site as well as if, and how, the structure of the free aptamer changes as ligand binds. Resonances can change chemical shift with ligand addition due to: (1) being close to the binding site and having their magnetic environment affected by presence of the ligand; or (2) due to structural change occurring with ligand binding, even if the structural change is away from the binding site. A key consideration when analyzing a titration is if there is a change in the number of imino protons observed in the free and bound spectra. If there is an increase or decrease in the number of imino protons observed, that can indicate that new base pairs are being formed or broken during binding and this is often an indication of structure being formed or lost. If the number of imino peaks observed is the same free and bound, there can still be structural changes taking place, just without changing the number of base pairs present.

An example of a titration of an aptamer with a ligand is shown in Figure 1.14 where the MN4 cocaine-binding aptamer is titrated with amodiaquine [57]. In this titration, imino resonances change their position with ligand binding but the total number of resonances changes very little, if at all. Here, the resonances that change chemical shift are most likely close to the ligand-binding site of the aptamer.

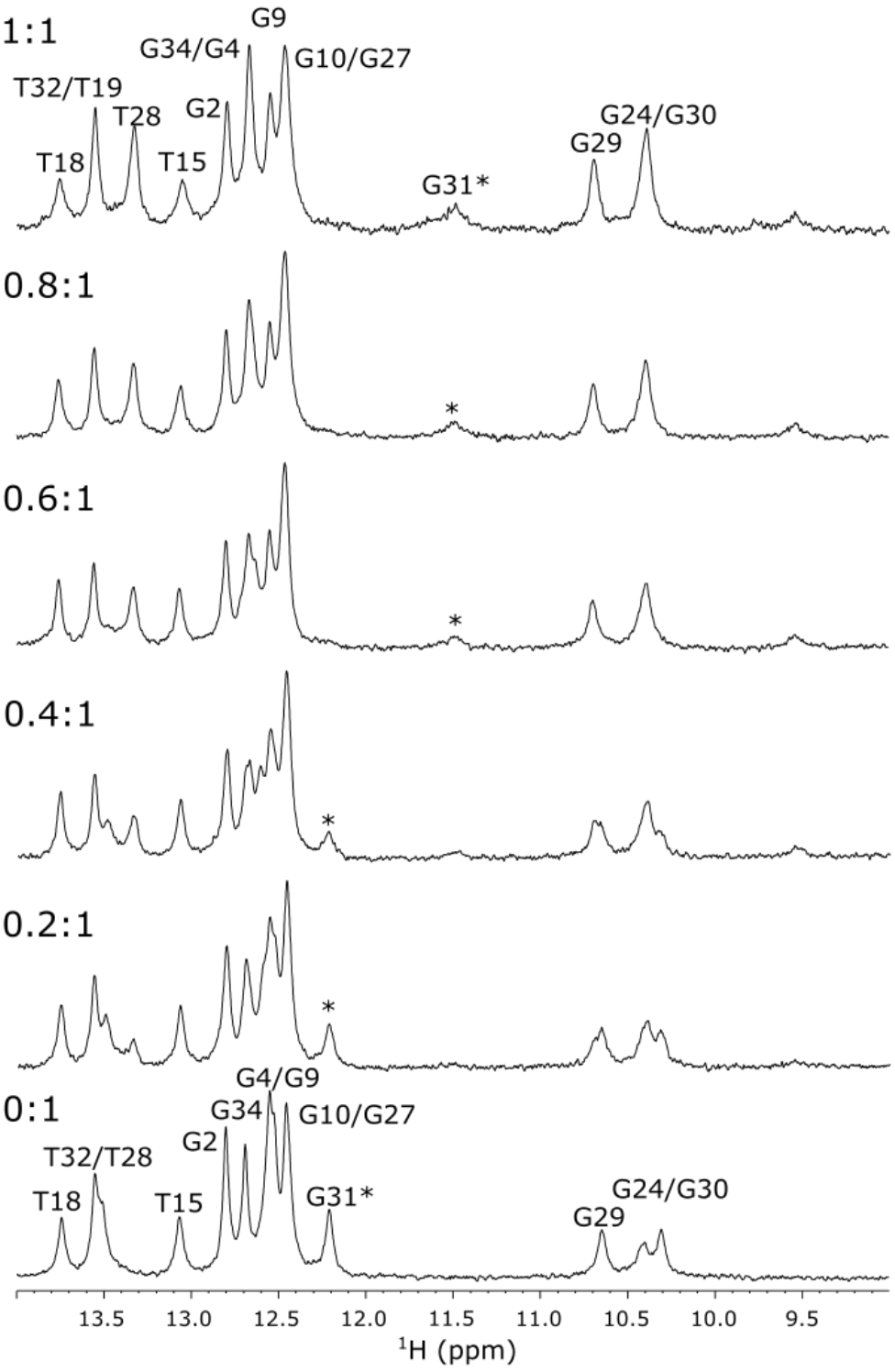

Figure 1.14. Titration of a cocaine-binding aptamer with amodiaquine. G31, whose signal is particularly indicative of binding, is marked with an asterisk. Amodiaquine was dissolved in DMSO-d6 (99.96%), and the concentration of DMSO at the 1:1 spectrum was about 2.5% (v/v). This titration was conducted in 10 mM NaH_2PO/Na_2HPO_4 (pH 7.4) 10% ^2H_2O, with an aptamer concentration of 200 µM. The molar ratios of ligand:aptamer are indicated.

An example of a titration of an aptamer where the number of imino protons increases with ligand binding is shown in Figure 1.15. Here, the imino protons in one stem of the MN19 cocaine-binding aptamer are not observed in the free form and appear as ligand is added [16], [17]. Presumably, in the free form stem 1 is unfolded, dynamic or loosely folded in the free state and folds or rigidifies in the bound state.

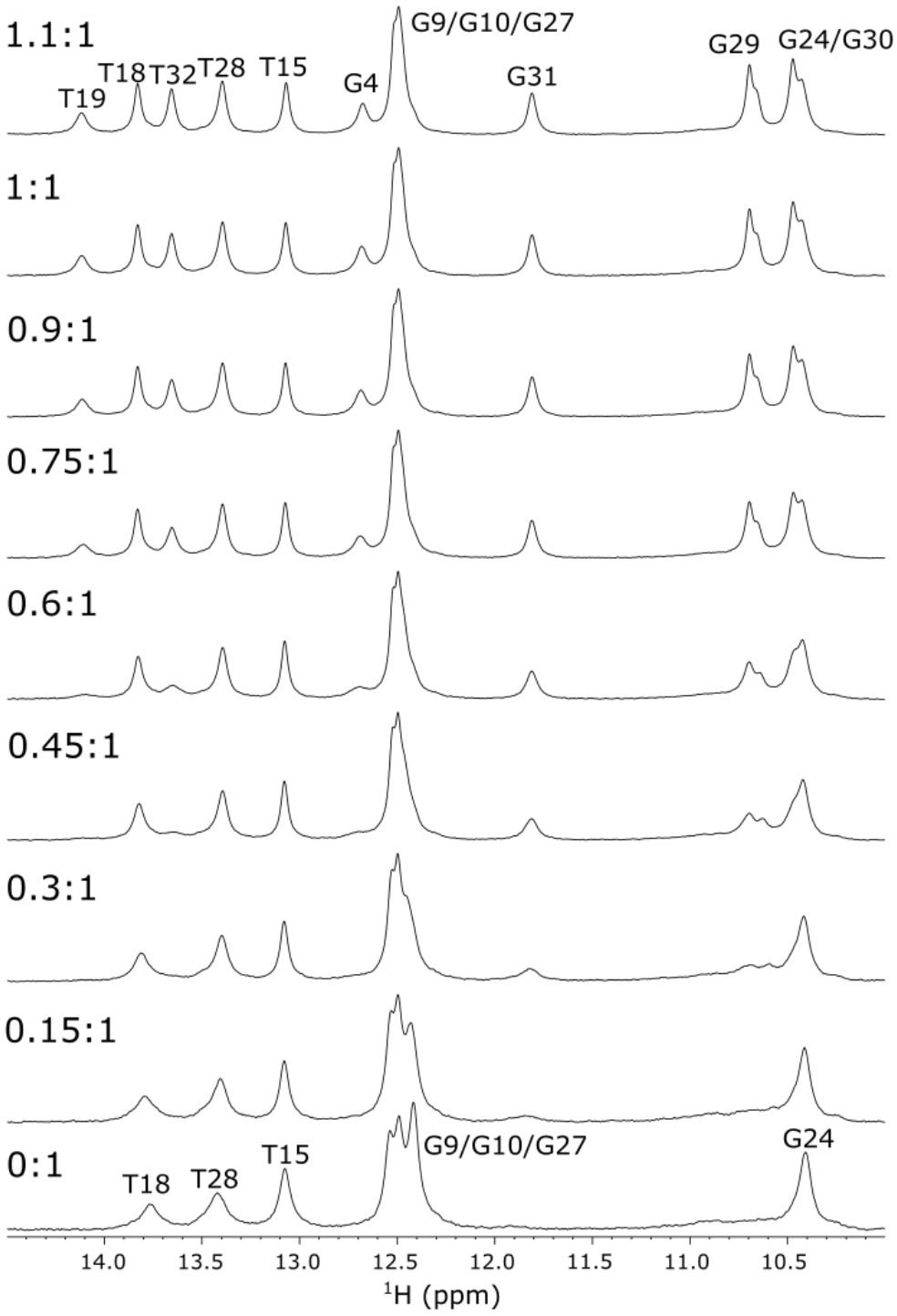

Figure 1.15. Titration of a cocaine-binding aptamer (MN19) with cocaine. As the amount of cocaine present in the sample increases, more peaks become visible (G4, T19, G29, G30, G31, T32) and the peaks present previously become sharper and more defined. This titration was conducted in 245 mM KCl, 5 mM KH_2PO_4/K_2HPO_4 (pH 6.8) 10% ^2H_2O, with an aptamer concentration of 1.5 mM. The molar ratios of ligand:aptamer are indicated on the left of each spectrum.

1.8.6 Thermal stability. A series of 1D ^{1}H spectra acquired as temperature is varied, a thermomelt, tracks how peaks in an aptamer change and the aptamer unfolds as the temperature increases. Starting at a low temperature, multiple spectra are acquired, increasing the temperature after each spectrum to see how the resonances change. Starting the series at 5 °C and increasing the temperature of the sample by 5 °C each time is adequate. An example is shown in Figure 1.16. If peaks disappear too quickly using the above scheme, starting the series at a lower temperature and using smaller temperature increments may be advantageous. An advantage of this technique over other techniques to monitor melting is that each imino proton can be tracked individually, allowing one to see if a global 2-state unfolding occurs or if different sections or helices of the aptamer unfold separately as the temperature increases. It is also possible that some peaks disappear before others due to them being more susceptible to exchange with water. As the temperature increases, the signal-to-noise ratio of the spectrum will decrease as the individual peaks broaden. It should be noted that the temperature that resonances disappear in the imino NMR spectrum is typically lower than the melt temperature determined using in other methods. A temperature scan with and without ligand present is a useful way to confirm binding, as the bound form of the aptamer will generally melt at a higher temperature.

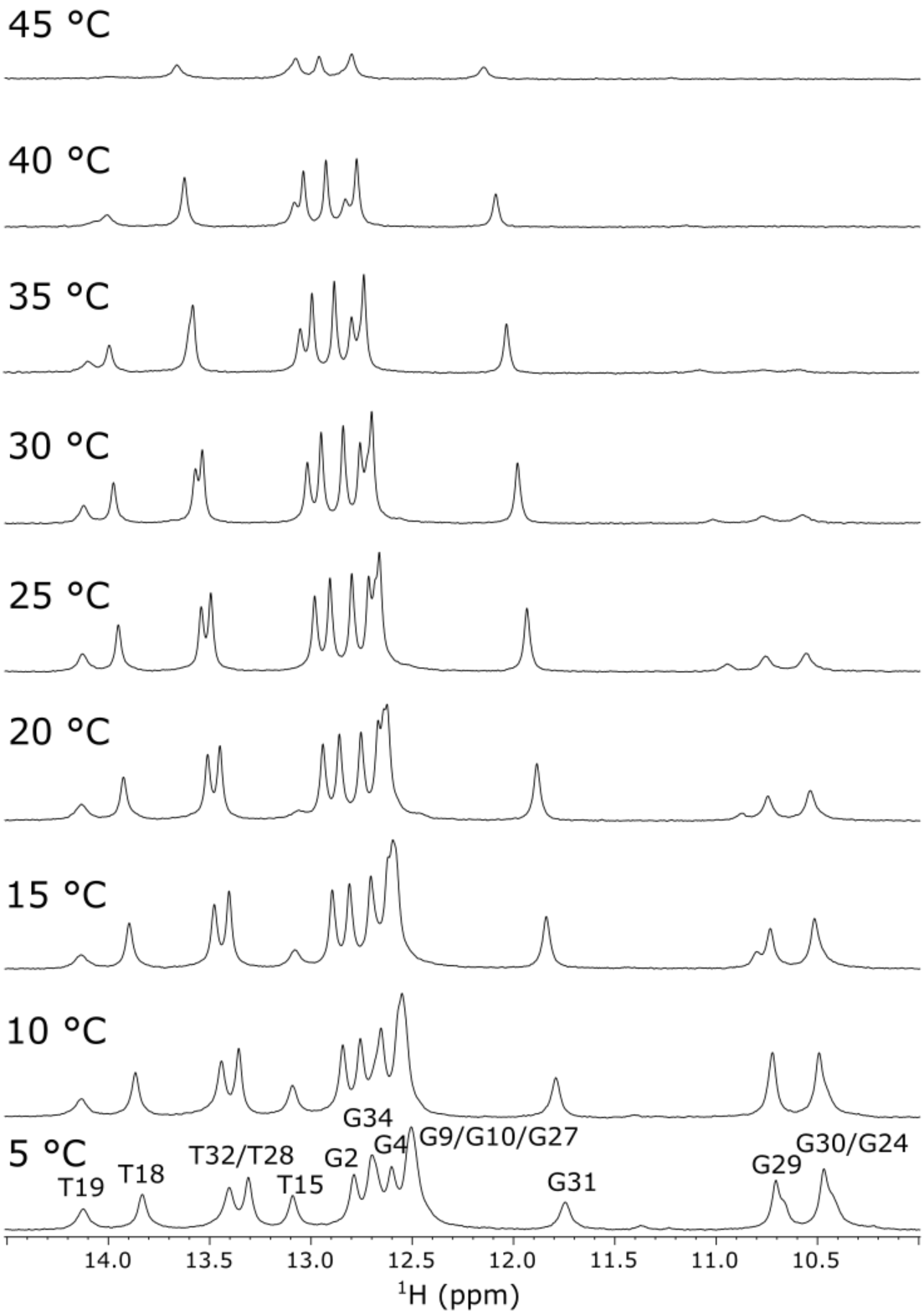

Figure 1.16. Temperature scan of a cocaine-binding aptamer bound to cocaine at a 1:1 ratio. The sample was in 245 mM KCl, 5 mM KH_2PO_4 /K_2HPO_4 (pH 6.8) 10% ^2H_2O, with an aptamer concentration of 1.0 mM.

1.9 Thesis Project.

The overall goal of this project is to use NMR spectroscopy to better understand how the structure of the cocaine-binding aptamer changes in response to ligand binding. Aptamers are often poorly understood and viewed as a black box. Using the cocaine-binding aptamer as a model system may help future aptamers be better understood. How different stimuli affect the cocaine-binding aptamer may inform how they would affect other similar aptamers. NMR spectroscopy is used as the main experimental technique as it allows atomic resolution data about a system to be acquired and is a nondestructive technique that allows for variables in a system to be changed during experiments. The projects in the thesis include studies of the dynamics in the cocaine-binding aptamer to better understand how the binding of a ligand can affect the stability of the individual base pairs within the aptamer. Characterization of off-target binding of the cocaine-binding aptamer to levamisole and three structurally related three-way junction-binding dyes was also investigated to see how these compare with both cocaine and quinine. As mentioned previously dyes can be useful in aptasensor system. As such more information about how an aptamer interacts with a set of dyes with various K_d values could be useful for future sensors. The binding affinity of levamisole was measured using NMR spectroscopy as it was too weak to be measured using other methods like ITC. This could be useful practically for aptamer-based cocaine biosensors due to the prevalence of levamisole in street cocaine. The binding site of these off-target ligands was found, and whether or not they interfered with the binding of cocaine or quinine. Additionally, the binding of the ochratoxin A binding aptamer to ochratoxin A was also investigated. While some structural information about the ochratoxin A aptamer was previously known, NMR spectroscopy was used to get a more complete idea of how this aptamer folds and behaves in the presence of its ligand.

Chapter 2 Methods and Materials

2.1 Preface

This chapter includes the methods used in the subsequent chapters

2.2 Aptamer Preparation

All DNA samples were obtained from Integrated DNA Technologies (IDT) as a dry powder with standard desalting. Sample identities were confirmed by mass spectrometry from the manufacturer, and further confirmed by NMR using previous samples as a guide. DNA samples were dissolved in ddH_2O exchanged against 1 M NaCl three times, and then exchanged against ddH_2O or buffer four times using Amicon style concentrators with a molecular weight cut off of 3 kDa. Aptamer samples were reduced to ~1000 μL in volume and then the concentration was determined using UV–Vis spectroscopy on a Varian Cary 100 Bio UV–Vis spectrophotometer by measuring the A260 and using the extinction coefficient provided by IDT.

2.3 Ligand Preparation

Cocaine, quinine, and levamisole were obtained from Sigma-Aldrich, while ochratoxin A, Dye-F, Dye-2Me, and Dye-5 were obtained from the Manderville lab at the University of Guelph. Stock solutions of cocaine, quinine, and levamisole were prepared by dissolving an appropriate amount of the compound in ddH_2O. A solution of ochratoxin A was prepared by dissolving an amount of powdered ochratoxin A into DMSO- d_6. Solutions of Dye-F, Dye-2Me, and Dye-5 were also prepared by dissolving an amount of powdered dye in DMSO-d_6. The addition of DMSO to NMR samples was tested by adding d_6 DMSO aliquots to an MN4 sample to see how the peaks changed. Peaks were not found to change significantly until the % v/v of DMSO reach ~5%.

2.4 NMR Experiment Setup

2.4.1 General. NMR experiments were conducted on a 600 MHz Bruker DRX Avance spectrometer equipped with a 1H–13C–15N triple-resonance probe. Samples were placed into a clean 0.5 mm NMR tube prior to being annealed. NMR tubes were cleaned with nitric acid to remove degrade any prior samples adhering to the walls of the tube. Afterward the NMR tubes were rinsed 4 times with 95% ethanol, and 4 times with ddH_2O. Once placed in the NMR tube, samples were annealed in a 95 °C water bath for 1 minute, and then placed in an ice water bath to favour intramolecular folding. Once annealed the samples were placed in the NMR an allowed to equilibrate at the NMR temperature for 5-10 minutes. All samples contained 10% ^2H_2O, to allow for the probe to lock onto the sample. Prior to experiments the NMR probe was manual tuned, and the NMR was shimmed either by manually adjusting the magnetic fields, or by applying a Z-only gradient shimming program and manually shimming the magnetic field afterward to ensure a high signal.

2.4.2 1D NMR Experiments. 1D NMR spectra were collected on samples using either excitation sculpting or WATERGATE to suppress the solvent signal from the water. Data was collected with a spectral width of ~22 ppm centered at 4.7 ppm. 1D spectra presented in the following chapters were collected using 32 dummy scans and 256 to 512 scans, with a delay of 1s was used between scans. Data was processed and view using TOPSPIN 3.7. 1D spectra were not zero filled. An exponential multiplication window function was used with an apodization value of 4 Hz. Spectra were phased to give a flat baseline.

2.5 Chapter 3 Methods

2.5.1 Data Collection. For both the MN4 and MN19 aptamers the original sample was divided in half before the NMR data for the free aptamer was acquired. Then cocaine was titrated in until a

1:1 complex was obtained using previously published titrations as a guide [17]. With the second half of the aptamer sample, quinine was titrated in to form a 1:1 complex, again, using previous titrations as a guide [73]. Sample volumes were from 550 to 600 μL, and concentrations of all samples of both MN4 and MN19 aptamers were 1.0 mM.

The imino hydrogen exchange rates were determined as outlined by the method of Lee and Pardi [74]. The apparent relaxation constant of water (R_{1w}), and the apparent relaxation constant of each imino proton (R_{1a}) was determined using a selective inversion recovery experiment employing a 180° shaped pulse to select either water or the imino region of the spectrum as appropriate. The peak intensities of the imino protons were measured using a water magnetization transfer experiment, using a 180° shaped pulse along the imino region. Twenty experiments were acquired using delay times of 5–100 ms.

2.5.2 Data analysis. The R_{1w} and R_{1a} values were obtained by measuring the intensity of either the water or imino peaks in the inversion recovery spectra and fitting the intensities to a single exponential curve. The intensities of the resonances in the magnetization transfer experiments were then measured and the data were fit to Eq. 1 using the Sigma Plot 11 software package (Systat Software) [74], [75]:

$$\frac{I(t)}{I_0} - 1 = -2\frac{k_{ex}}{R_{1w}-R_{1a}}\left(e^{-R_{1a}t} - e^{-R_{1w}t}\right) \qquad (1)$$

where *I(t)* is the peak intensity as a function of delay time, *Io* is the peak intensity with a delay time of 0 s, R_{1w} is the apparent relaxation rate constant of water, R_{1a} is the apparent relaxation rate constant of a particular nucleotide, k_{ex} is the exchange rate constant for the nucleotide, and *t* is the delay time in seconds. Once the constants (R_{1w} and R_{1a}) for the equation were obtained, k_{ex} was determined by rearranging Eq. 1 to isolate for k_{ex}.

2.6 Chapter 4 Methods

2.6.1 Data Collection. NMR experiments were conducted on a 600 MHz Bruker Avance spectrometer at temperatures from 5 °C to 45 °C. Spectra were acquired in either 245 mM KCl, 5 mM $KHPO_4$, pH 6.8 in 10% ^2H_2O, 90% H_2O (high-salt buffer with low catalyst concentration); or 120 mM KCl, 100 mM $KHPO_4$, pH 6.8 in 10% ^2H_2O, 90% H_2O (high-salt buffer with high catalyst concentration). NMR data were processed using TopSpin 3.7 (Bruker).

For both the MN4 and MN19 aptamers, an original sample was divided in half. Using one half of the sample, the NMR data for the free aptamer was acquired, then cocaine was titrated in to form a 1:1 complex, using previously published titrations as a guide [17]. With the second half of the aptamer sample, quinine was titrated in to form a 1:1 complex, again using previous titrations as a guide [73]. Sample volumes were 550 to 600 μL with the concentrations of MN4 samples in low catalyst concentration buffer were 1.0 mM and in high catalyst concentration buffer were 1.3 mM. For MN19, samples in low catalyst concentration buffer were 1.6 mM and in high catalyst concentration buffer were 1.5 mM.

The imino hydrogen exchange rates were determined as described by Lee and Pardi [74]. First, inversion-recovery experiments were performed to measure the R_{1a} and R_{1w} values. The water R_1 was measured using a DANTE pulse train designed so that the overall 90 degree pulse width was 90 μs. The peak intensities of the imino protons were measured using a water magnetization transfer experiment using a shaped 180° pulse along the imino region. To accomplish this a RE-BURP pulse shape of 965 μs was used. The pulse was centered in the range of 9-16 ppm and uniformly covered this region. The magnetization transfer experiments were conducted with 40 different delay times ranging from 0 ms to 500 ms, in a predetermined, non-sequential order in a manner as described earlier [76]. The order of temperature acquisition was

randomized between 5 °C and 45 °C. For the 10 ms and 120 ms delay times, measurements were acquired three times each in order to gauge the level of variability in the data.

2.6.2 Data Analysis The apparent relaxation constant of water (R_{1w}), and the apparent relaxation constant of each imino proton (R_{1a}) were obtained by measuring the intensity of either the water or imino peak in the inversion recovery spectra and fitting the intensity to a single exponential curve. The intensity of the resonances in the magnetization transfer experiments were then measured and the data were fit to Eq. 1 using Sigma Plot 11.0.

$$\frac{I(t)}{I_0} - 1 = -2\frac{k_{ex}}{R_{1w}-R_{1a}}\left(e^{-R_{1a}t} - e^{-R_{1w}t}\right) \quad (1)$$

where $I(t)$ is the peak intensity as a function of delay time, I_o is the peak intensity with a delay time of 0 ms, k_{ex} is the exchange rate constant for the nucleotide, and t is the delay time in seconds. Once the constants (R_{1w} and R_{1a}) for the equation were obtained, k_{ex} was determined by rearranging equation 1 to isolate for k_{ex}.

2.6.3 Determination of Enthalpy and Entropy of base pair dissociation. To obtain the enthalpy and entropy of base pair dissociation a method developed by Schwalbe and co-workers was used, where the exchange rates were determined as a function of temperature [77], [78]. At low temperatures, the measured exchange is dominated by NOE effects (the term d in equation 2) so to correct for this, the data was fit to Eq. 2 using Sigmaplot 11.0.

$$k_{ex} = \frac{1}{\frac{h}{k_b T}e^{\left(\frac{\Delta H_{TR} - T\Delta S_{TR}}{RT}\right)}\left(1+e^{\frac{\Delta H_{diss} - T\Delta S_{diss}}{RT}}\right)} + d \quad (2)$$

where k_{ex} was the calculated exchange rate constant from previous fitting, h is Planck's constant, k_b is Boltzmann's constant, T is the temperature in °K, ΔH_{TR} and ΔS_{TR} are the change in enthalpy and entropy of the open base pair, ΔH_{Diss} and ΔS_{Diss} are the change in enthalpy and entropy of the imino proton dissociating, and R is the gas constant. Once the k_{ex} values were corrected, the effect

of solvent catalysis on the exchange was found using k_{ex} values in the high catalyst concentration buffer, the low catalyst concentration buffer, and the nucleoside triphosphate exchange rates [78].

The calculated k_{ex} has contributions from both the base pair opening and the imino proton dissociation, and will be referred to as $k_{ex,net}$ from here on. To determine the $k_{ex,net}$ contribution of base pair opening, the ratio between $k_{ex,ext}$ and $k_{ex,int}$ was determined, where $k_{ex,ext}$ is the exchange rate constant of the imino proton dissociation and $k_{ex,int}$ is the exchange rate constant of the base pair dissociation. These two values are related as follows.

$$q = \frac{k_{ex,ext}}{k_{ex,int}} = \frac{k_{TR,ext}}{k_{TR,int}} \quad (3)$$

$k_{TR,ext}$ was obtained from previously published single nucleoside exchange rate experiments at 20 ºC [78] while q was determined using the $k_{ex,net}$ imino proton exchange rate data at 20 ºC from both the high catalyst concentration and low catalyst concentration data according to Steinert *et al.* [78]. The value of q was then used to find the $k_{TR,int}$ by Eq. 3.

After this, the data was fit to a linearized form of the Eyring equation.

$$ln\frac{k_{TR,int}}{T} = \frac{-\Delta H_{diss}}{RT} + ln\frac{k_b}{h} + \frac{\Delta S_{diss}}{R} \quad (4)$$

The slope of the line of best fit represents the enthalpy of the base pair dissociation (ΔH_{diss}), and the y-intercept represents the entropy of the base pair dissociation (ΔS_{diss}). The Gibbs free energy of base pair dissociation (ΔG_{diss}) was then determined using the relation $\Delta G_{diss} = \Delta H_{diss} - T\Delta S_{diss}$ where T is the temperature.

2.7 Chapter 5 Methods

2.7.1 NMR Spectroscopy. NMR experiments were conducted on a 600 MHz, 700 MHz, and 800 MHz Bruker Avance spectrometer at 5 °C to 55 °C in a manner described previously. Experiments run on the 800 MHz spectrometer were performed by Prof. Cameron Mackereth at the Université de Bordeaux. Spectra were acquired in 120 mM NaCl, 5 mM KCl, 20 mM $CaCl_2$, 10 mM d^{11}-Tris,

pH 8.0. Unless noted spectra were acquired in 90% $^{1}H_2O$- 10% $^{2}H_2O$ at 5 °C on the 600 MHz spectrometer. NMR data were processed using TopSpin 3.7 (Bruker).

2.7.2 1D ^{1}H NMR Titrations. OTA-1 was titrated with ochratoxin A until a 1:1 stoichiometric ratio of aptamer:ligand. The OTA-1 sample contained an aptamer concentration of 1.6 mM at 550 µL. Ochratoxin A was titrated into the sample in 0.1eq aliquots to a final ratio of 1:1 aptamer:ligand. The volume increased to 595 µL when the titration was finished, with a DMSO content of ~8.3%.

2.7.3 2D ^{1}H-^{1}H NOESY Experiment in H_2O. Two-dimensional $^{1}H-^{1}H$ NOESY experiments were performed on the ochratoxin A-bound OTA-1 sample with a mixing time (τ_m) of 200 ms. For this experiment the aptamer concentration was 1.0 mM with a ratio of aptamer:ligand of 1:1 respectively.

2.7.4 2D ^{1}H-^{1}H NOESY Experiment in D_2O. Two-dimensional $^{1}H-^{1}H$ NOESY experiments were performed on the ochratoxin A-bound OTA-1 sample with a mixing time (τ_m) of 200 ms on an 800 MHz NMR spectrometer. For this experiment the aptamer concentration was 2.0 mM in 120 mM NaCl, 5 mM KCl, 20 mM $CaCl_2$, 10 mM d^{11}-Tris, pH 8.0, 100% $^{2}H_2O$ at 20 °C. The ratio of aptamer:ligand in the sample was 1:1.

2.7.5 2D ^{1}H-^{1}H TOCSY Experiment. Two-dimensional $^{1}H-^{1}H$ TOCSY experiments were performed on the ochratoxin A-bound OTA-1 sample with a mixing time (τ_m) of 200 ms on an 800 MHz NMR spectrometer. For this experiment the aptamer concentration was 2.0 mM in 120 mM NaCl, 5 mM KCl, 20 mM $CaCl_2$, 10 mM d^{11}-Tris, pH 8.0, 100% $^{2}H_2O$ at 5 °C. The ratio of aptamer:ligand in the sample was 1:1.

2.7.6 2D ^{1}H-^{13}C HSQC Experiment. Two-dimensional $^{1}H-^{13}C$ HSQC experiments were performed on the ochratoxin A-bound OTA-1 sample with a coupling constant of 160 Hz to

optimize the signal from aliphatic proton-carbon bonds. These experiments were performed on a 700 MHz NMR spectrometer. For this experiment the aptamer concentration was 1.6 mM in 120 mM NaCl, 5 mM KCl, 20 mM $CaCl_2$, 10 mM d^{11}-Tris, pH 8.0, 100% ^2H_2O at 20 °C. The ratio of aptamer:ligand in the sample was 1:1.

2.7.7 Imino Proton Exchange Data Collection. Imino hydrogen exchange rate experiments were performed on a 1.25 mM ochratoxin A-bound OTA-1 sample. Data was acquired from 5 °C to 55 °C in 5 ° increments. The imino hydrogen exchange rates were determined as described by Lee and Pardi [74]. First, inversion-recovery experiments were performed to measure the R_{1a} and R_{1w} values. The water R_1 was measured using a DANTE pulse train designed so that the overall 90 degree pulse width was 90 μs. The peak intensities of the imino protons were measured using a water magnetization transfer experiment using a shaped 180 ° pulse along the imino region. To accomplish this a RE-BURP pulse shape of 965 μs was used. The pulse was centered in the range of 9-16 ppm and uniformly covered this region. The magnetization transfer experiments were conducted with 40 different delay times ranging from 0 ms to 500 ms, in a predetermined, non-sequential order in a manner as described earlier [76]. The order of temperature acquisition was randomized between 5 °C and 45 °C. For the 10 ms and 120 ms delay times, measurements were acquired three times each in order to gauge the level of variability in the data.

2.7.8 Imino Proton Exchange Data Analysis. The apparent relaxation constant of water (R_{1w}), and the apparent relaxation constant of each imino proton (R_{1a}) were obtained by measuring the intensity of either the water or imino peak in the inversion recovery spectra and fitting the intensity to a single exponential curve. The intensity of the resonances in the magnetization transfer experiments were then measured and the data were fit to Eq. 1 using Sigma Plot 11.0.

$$\frac{I(t)}{I_0} - 1 = -2\frac{k_{ex}}{R_{1w} - R_{1a}}\left(e^{-R_{1a}t} - e^{-R_{1w}t}\right) \quad (1)$$

where *I(t)* is the peak intensity as a function of delay time, I_o is the peak intensity with a delay time of 0 ms, k_{ex} is the exchange rate constant for the nucleotide, and *t* is the delay time in seconds. Once the constants (R_{1w} and R_{1a}) for the equation were obtained, k_{ex} was determined by rearranging equation 1 to isolate for k_{ex}.

2.8 Chapter 6 Methods

2.8.1 NMR Spectroscopy. NMR experiments were conducted on a 600 MHz Bruker Avance spectrometer at 5 °C in a manner described previously [79]. Spectra were acquired in 245 mM KCl, 5 mM $KHPO_4$, pH 6.8 in 10% ^2H_2O, 90% H_2O. NMR data were processed using TopSpin 3.7 (Bruker).

For both MN4 and MN19 aptamers, two samples were prepared from a common stock. Samples started at a concentration of 500 μM, and a volume of 550 μL. In one sample levamisole was titrated into the free aptamer until a molar ratio of 1:10 (aptamer:levamisole) was achieved. After this, cocaine was titrated into the sample to a final molar ratio of 1:10:2 for the MN4 (aptamer:levamisole:cocaine) sample and 1:10:3 for the MN19 (aptamer:levamisole:cocaine) sample. For the second sample for each aptamer, cocaine was titrated to a 1:1 molar ratio (aptamer:cocaine). Levamisole was then titrated into the cocaine-bound samples to a final ratio of 1:1:50 (aptamer:cocaine:levamisole).

To check the effect of pH on the interaction between levamisole and MN4, a sample of MN4 was split in half and exchanged into (i) a pH 6 buffer (245 mM KCl, 5 mM $KHPO_4$, pH 6.0 in 10% ^2H_2O/90% H_2O) and (ii) a pH 8 buffer (200 mM NaCl, 20 mM deuterated ammonium acetate, pH 8.0 in 10% ^2H_2O/90% H_2O). Each of these samples was titrated with levamisole to a final molar ratio of 1:10 (aptamer:levamisole).

2.8.2 Binding Affinity Calculations. The affinity of the aptamer-levamisole interaction was determined using standard methods of following the chemical shift perturbations of signals in the NMR spectrum [80]. The fraction bound (f_b) was fit as a function of ligand concentration to Eq. 5 below:

$$f_b = B_{max} \frac{[L]}{K_d + [L]} \quad (5)$$

Where B_{max} is theoretical maximum response, K_d is the dissociation constant and [L] is the concentration of levamisole present in the sample. The fraction bound at a given point was calculated using Eq. 6:

$$f_{bi} = \frac{\delta_i - \delta_o}{\delta_f - \delta_o} \quad (6)$$

Where f_{bi} is the fraction bound at a particular point during the titration, d_i is the current ^1H position of a particular resonance, d_0 is the initial ^1H position of the resonance in the absence of any ligand, and d_f is the final ^1H position of the resonance being used. f_{bi} should range from 0 in the free sample to 1 in the 1:10 aptamer:levamisole sample. This calculation also assumes that the aptamer is fully bound with an f_{bi} of 1 at the final titration point. For MN19 the same scheme as MN4 was used though peak intensity was used since many peaks in free MN19 are not visible due to the dynamic nature of the unbound MN19 aptamer. Nonlinear curve fits were performed using SigmaPlot 11.

2.9 Chapter 7 Methods

2.9.1 1D ^1H NMR Titrations. One-dimensional ^1H NMR spectra were acquired in 140 mM NaCl, 10 mM $Na_xH_yPO_4$ at pH 6.8 in 10% ^2H_2O/90% ^1H_2O at 5 °C in a manner described previously [76]. MN4-Dye-F titration was acquired with a 1.4 mM aptamer concentration at volume of 600 µL, while the MN4-Dye-2Me, MN4-Dye-5, and all MN19 titrations were acquired with a 500 µM aptamer concentration at a volume of 600 µL. For the NMR experiments, all the dyes were

dissolved in DMSO-d_6 (99.96%). The MN4-Dye-F titration was done to a ratio of 1:1 aptamer:ligand, while the MN4-Dye-2Me, MN4-Dye-5, and all MN19 titrations were done to a ratio of 1:2 aptamer:ligand. For all experiments the final DMSO content of the samples ranged from 1% to 5% (v/v).

2.9.2 2D ^{1}H-^{1}H NOESY Experiments. Two-dimensional ^{1}H−^{1}H NOESY experiments were performed on the Dye-F-bound, Dye-2Me-bound, and Dye-5-bound MN4 samples with a mixing time (τ_m) of 200 ms. For all these experiments the aptamer concentration was 1.4 mM and was conducted in 140 mM NaCl, 10 mM $Na_xH_yPO_4$ at pH 6.8 in 10% ^2H_2O/90% ^1H_2O at 5 °C. The ratio of aptamer:ligand in these experiments was 1:1, with an approximate DMSO content ranging from 3%-5%. Water suppression for all experiments was achieved using excitation sculpting.

2.9.3 1D ^{1}H NMR Competition Titrations. Quinine−Dye-F competition experiments were performed using a 500 μM sample of MN4 in the previously described NMR buffer. For these experiments, quinine and Dye-F were each separately dissolved in DMSO-d_6. First, Dye-F was titrated into MN4 until a final molar ratio of 1:1 aptamer: Dye-F. The final DMSO content was ∼2% v/v. Next, quinine was titrated into the same sample to a final molar ratio of 1:1:3 aptamer: Dye-F:quinine with an ∼5% v/v final DMSO content.

Cocaine-Dye-5 competition experiments were performed using a 500 μM sample of MN4 in the previously described NMR buffer. For these experiments cocaine was dissolved in ^1H_2O and Dye-5 was dissolved in DMSO-d_6. First, Dye-5 was titrated into MN4 until a final molar ratio of 1:1 aptamer:Dye-5. The final DMSO content was ∼1% v/v. Next, cocaine was titrated into the same sample to a final molar ratio of 1:1:15 aptamer:Dye-5:cocaine with an ∼1% v/v final DMSO content.

Chapter 3 Comparison of the Free and Ligand-Bound Imino Hydrogen Exchange Rates for the Cocaine-Binding Aptamer

3.1 Preface

All work presented in this chapter has been taken from the article below [76]

- **Churcher, Z.R.,** Neves, M.A.D., Hunter, H.N. and Johnson P.E. "**Comparison of the Free and Ligand-Bound Imino Hydrogen Exchange Rates for the Cocaine-Binding Aptamer.**" *Journal of Biomolecular NMR* 68, 33-39 (2017).

3.2 Introduction

Aptamers are nucleic acid molecules that have been selected to bind a particular ligand that can range from a small molecule to a cell. Aptamers typically bind with high affinity and selectivity, and they have been found to be useful in medical and analytical applications [81]– [85]. Understanding how aptamers interact with their ligands is an important question when implementing an aptamer in a biotechnology application. Measuring the hydrogen exchange rate constant (k_{ex}) for the imino proton of free and ligand-bound aptamers is a useful probe of how base pair dynamics change with ligand binding, as this exchange rate reflects the stability and solvent accessibility of base pairs [86]. The hydrogen exchange rate constant in nucleic acids is measured using water magnetization transfer experiments and has been previously employed in studying both DNA and RNA duplex and aptamer molecules [74], [75], [87], [88].

The cocaine-binding aptamer is a widely used model system for studying aptamer function and biotechnology applications of aptamers [59], [89]– [94]. The aptamer was originally selected by Stojanovic *et al*. [52], [58] to bind cocaine, but not any of the common cocaine metabolites. Unusually, this aptamer binds quinine 50-fold tighter than cocaine [54], [56], [73]. Structurally, the cocaine-binding DNA aptamer consists of three stems centered around a three-way junction [17]). The two variants of the cocaine-binding aptamer studied here are MN4 and MN19 (Fig. 3.1).

MN4 is a sequence variant of the originally reported cocaine-binding aptamer that binds more tightly to cocaine, while MN19 is a variant of MN4, where the length of stem 1 has been reduced to three base pairs. The MN19 aptamer is most commonly utilized in biotechnology applications, as it has a ligand-induced folding mechanism. In the unbound state, MN19 is poorly structured or unstructured, and the aptamer becomes folded concurrently with ligand binding [17], [58].

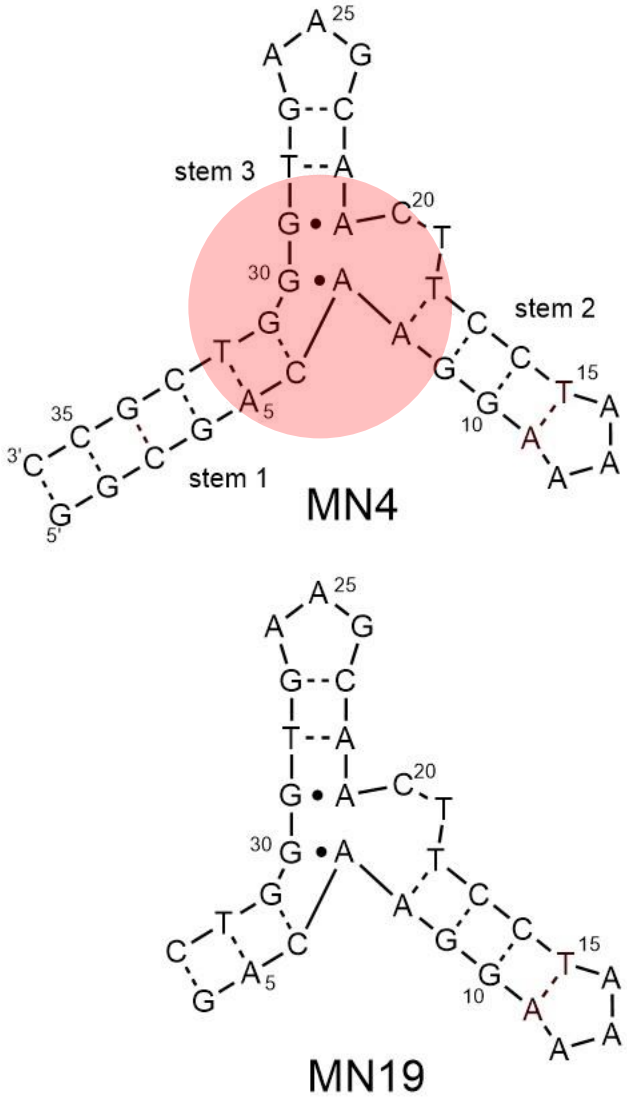

Figure 3.1 Secondary structure of the MN4 and MN19 cocaine-binding aptamers used in this study. For ease of comparison both aptamers follow the same numbering scheme. Highlighted in MN4 is the location of the high affinity ligand-binding site.

In this study, the k_{ex} values of the imino protons is measured in both the MN4 and MN19 aptamers in their free, cocaine-bound, and quinine-bound states. Base pairs at the ligand-binding site have reduced k_{ex} values in both their quinine and cocaine-bound forms. The k_{ex} values of nucleotides away from the binding site are minimally affected by ligand binding suggesting a decrease in base pair dynamics at the binding site is occurring, but that a reduction in k_{ex} values is not felt throughout the molecule.

3.3 Results and discussion

3.3.1 NMR spectroscopy. Resonance assignments for the imino regions of both MN4 and MN19, free, cocaine-bound and quinine-bound states were obtained based on previous studies (Fig. 3.2) [17], [73]. The spectra shown here are very similar to what was reported previously. Imino resonance intensity was measured as a function of time using semi-selective inversion recovery experiments for both MN4 and MN19 in their free, cocaine-bound and quinine-bound states. Due to peak overlap, it was not possible to independently measure the intensity of every imino or even the same imino resonances in different aptamer states. For example, G4, G9, G10 and G27 all overlap together or with another resonance in this group, except for cocaine-bound MN4, where G4 appears as a separate resonance (Fig. 3.2). The intensity of ten different imino resonances from the 15-guanine and thymine nucleotides in MN4 (not including G1) was measured. Of these ten, six different nucleotides were measured across the free, cocaine-bound and quinine-bound states.

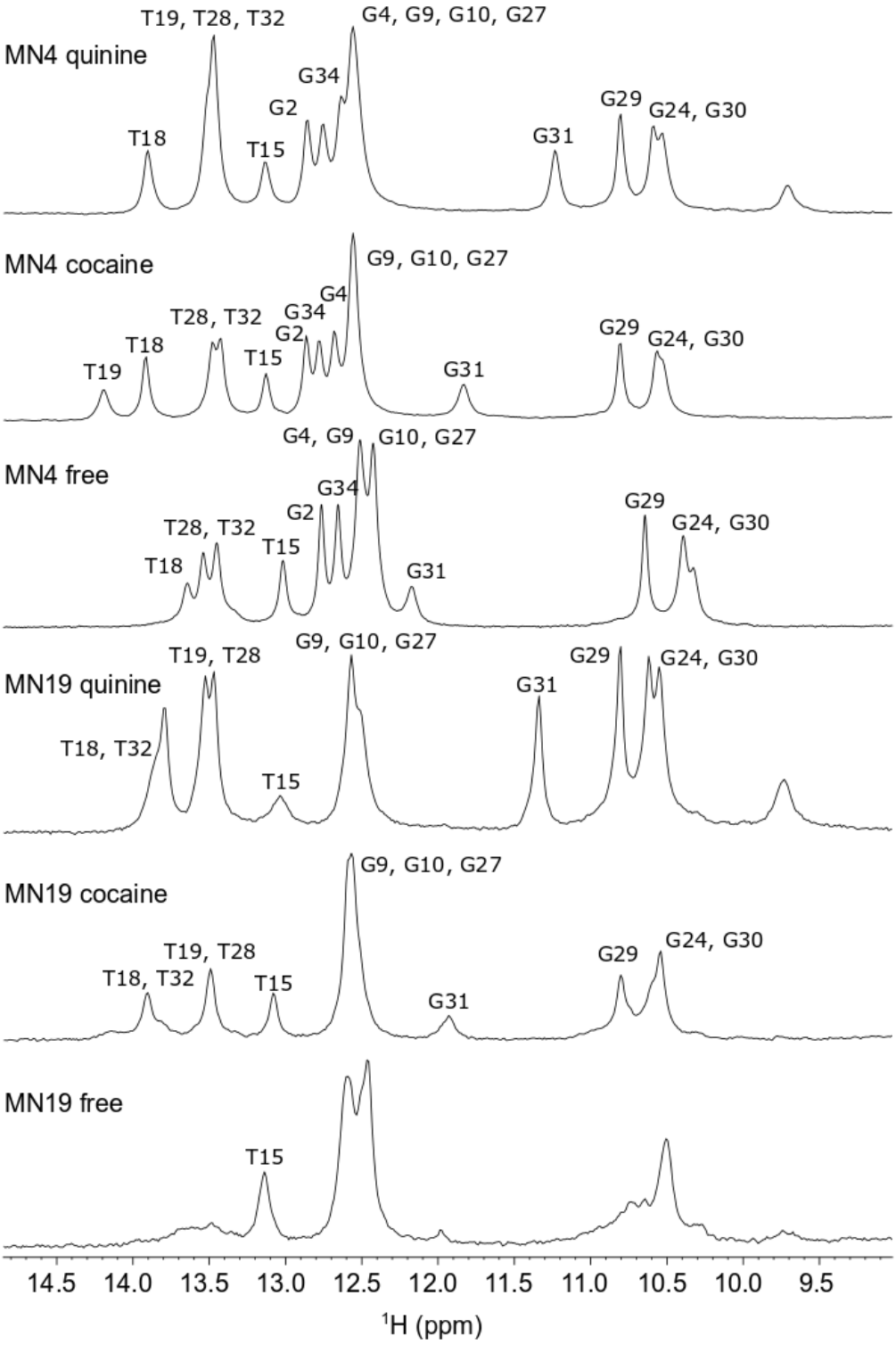

Figure 3.2. Downfield imino region of the 1D-^{1}H NMR spectra of MN4 and MN19 cocaine-binding aptamers free and bound to cocaine and quinine. Spectra were acquired at 5 °C in 10% $^{2}H_2O$, 90% H_2O.

20 1D spectra were obtained at different delay times in order to fit the intensity decay and obtain k_{ex} values. Figure 3.3 shows ten selected spectra of the MN4 cocaine-bound state. Fast decaying nucleotides such as T15 produce a negative signal by the last decay time while slower decaying signals (T19, G29) still have a positive intensity with the same delay time. Decay curves for all measured peaks are shown Figure 3.4 and Figure 3.5, with the error bars representing the standard deviation of the measurement. Take for example, the decay cure used to obtain the k_{ex} values for G29 in MN4 (Figure 3.4). For this nucleotide, the imino resonance in the free state decays to a greater degree than in the quinine and cocaine-bound states. The two bound states decay in a similar manner. The error in the normalized peak intensity in the decay curve was obtained from measuring the peak height in two separate experiments and obtaining a standard deviation. In general, the data presented in Fig. 3.4 agree with Eq. 1 producing an average R^2 value of 0.96 with a range of 0.81–0.99. Exchange rate constants for MN4 and MN19 are given in Table 3.1.

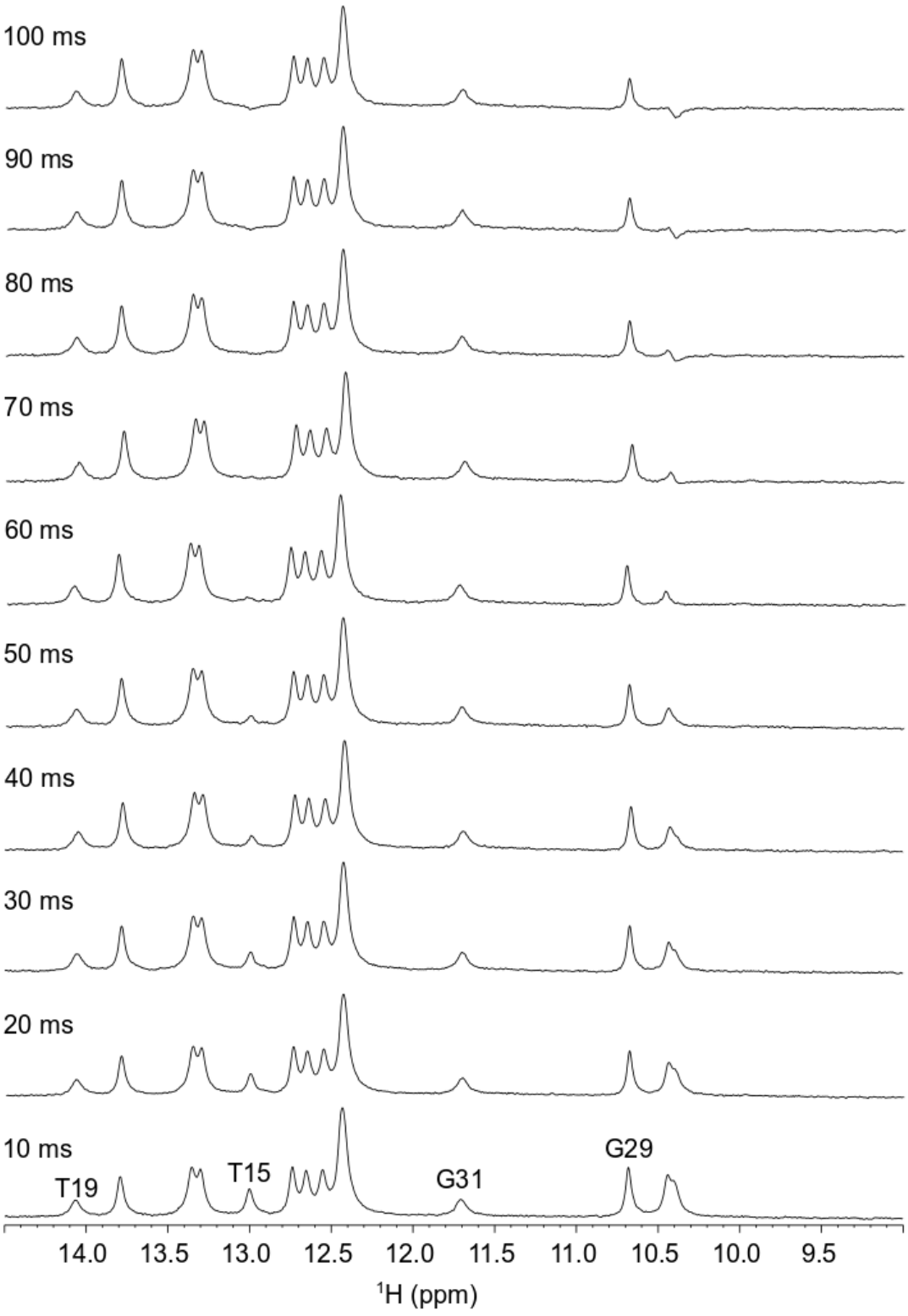

Figure 3.3 1D spectra of the water magnetization transfer experiment for the imino protons in the MN4 bound to cocaine sample. Delay times range from 10 to 100 ms. Selected nucleotides are numbered.

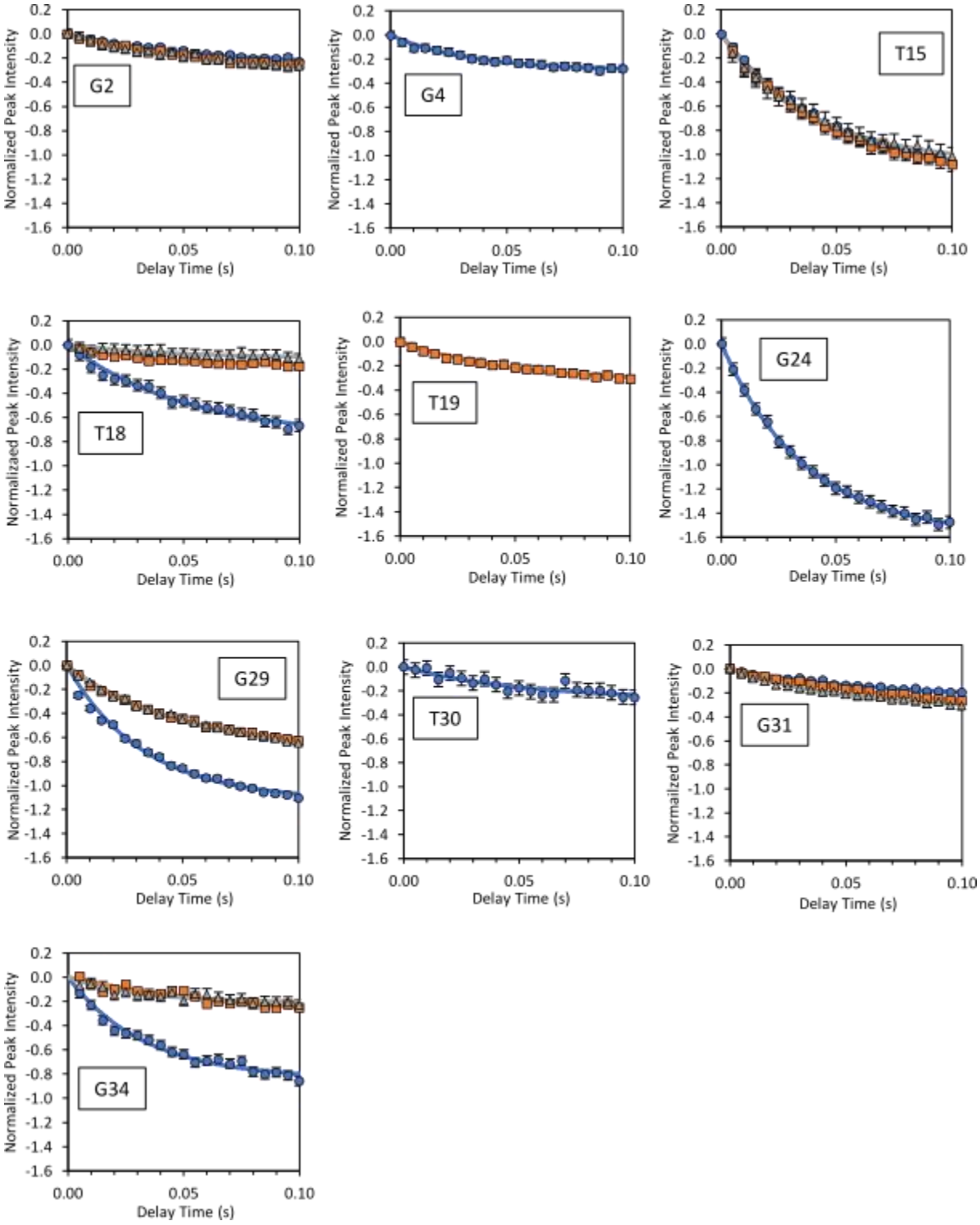

Figure 3.4 Intensity of the imino resonances in MN4 as a function of delay time. *Blue circles* are from free MN4, *grey triangles* are from the quinine-bound MN4 and *orange squares* are from the cocaine-bound MN4. The *line* represents the best fit to Eq. 1. The intensities are normalized.

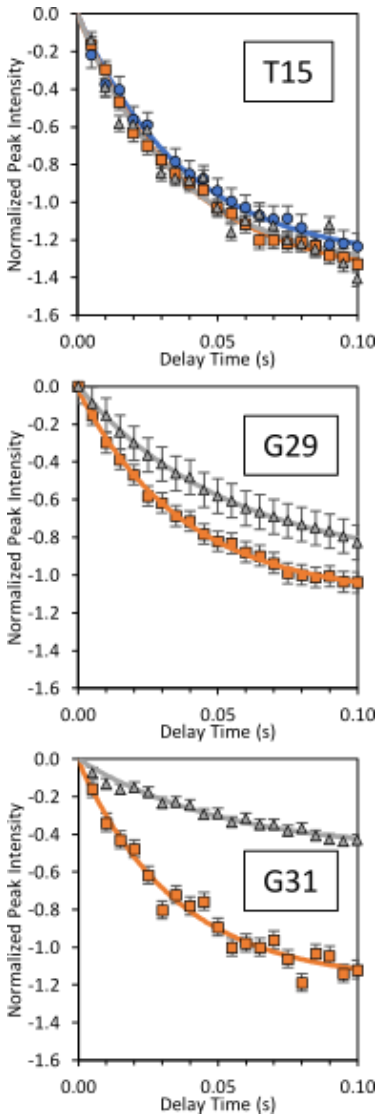

Figure 3.5 Intensity of the imino resonances in MN19 as a function of delay time. *Blue circles* are from free MN19, *grey triangles* are from the quinine-bound MN19 and *orange squares* are from the cocaine-bound MN19. The *line* represents the best fit to Eq. 1. The intensities are normalized.

3.3.2 Hydrogen exchange rate constants. The values of hydrogen exchange rate constants of the imino protons in the MN4 aptamer reflect the position of the nucleotide in the secondary structure of the aptamer (Fig. 3.1; Table 3.1). In the free MN4 aptamer the nucleotides with the lowest exchange rate constants are G2 and G34 with k_{ex} values of (1.9 ± 0.6) and (2.2 ± 0.6) s^{-1}, respectively, and are located in the middle of a stem. The nucleotide with the largest exchange rate

constant is G24 (36.3 ± 8.5) s^{-1}, and it is located in the loop of stem 3. Between these extremes are G29 and G30, the guanine residues that comprise the tandem GA mismatch (k_{ex} values of (17.0 ± 2.1) and (21.8 ± 3.2) s^{-1}, respectively), and residues located at the end of stems such as T15 (12.8 ± 1.3), T18 (7.5 ± 1.6) and G31 (12.7 ± 1.8) s^{-1}.

Table 3.1. Hydrogen exchange rate constants (s^{-1}) of the imino protons for the free and bound MN4 and MN19 aptamers.[a]

Residue	MN4			MN19		
	Free	Cocaine	Quinine	Free	Cocaine	Quinine
G2	1.9 ± 0.6	2.3 ± 0.8	3.6 ± 0.6	-	-	-
G4	-	4.3 ± 0.7	-	-	-	-
T15	12.8 ± 1.3	13.5 ± 0.8	18.2 ± 2.5	18.2 ± 2.5	18.6 ± 3.6	19.1 ± 4.7
T18	7.5 ± 1.6	3.0 ± 0.9	1.1 ± 0.9	-	-	-
T19	-	2.7 ± 2.0	-	-	-	-
G24	36.3 ± 8.5	-	-	-	-	-
G29	17.0 ± 2.1	7.5 ± 0.8	7.2 ± 0.9	-	14.5 ± 1.6	8.9 ± 1.3
G30	21.8 ± 3.2	-	-	-	-	-
G31	12.7 ± 1.8	2.1 ± 1.9	3.5 ± 1.2	-	20.1 ± 3.3	4.7 ± 1.3
G34	2.2 ± 0.6	2.7 ± 0.6	2.9 ± 0.7	-	-	-

[a] All data acquired at 5 °C in 10% ^2H_2O, 90% H_2O. The uncertainty represents the error in the fit of the data.

The hydrogen exchange rates of the imino protons were analyzed in order to determine the effect of ligand binding at the individual base pair level. For resonances whose k_{ex} values were measured in more than one state, the values are shown graphically in Fig. 3.6, and their average ligand-bound increase or decrease are depicted in Fig. 3.7. With cocaine binding T18, G29 and G31 display a large reduction in k_{ex} values. These three nucleotides are located at the MN4 high affinity binding site. The cocaine-binding aptamer has two ligand binding sites, a high affinity site involving nucleotides at the three-way junction and the end of stem 1 abutting the three-way junction. A second, lower affinity site mostly involves nucleotides located in stem 2 [95]. In this

study, given the amount of ligand added and the K_d difference between the two sites, only the high affinity site is significantly populated.

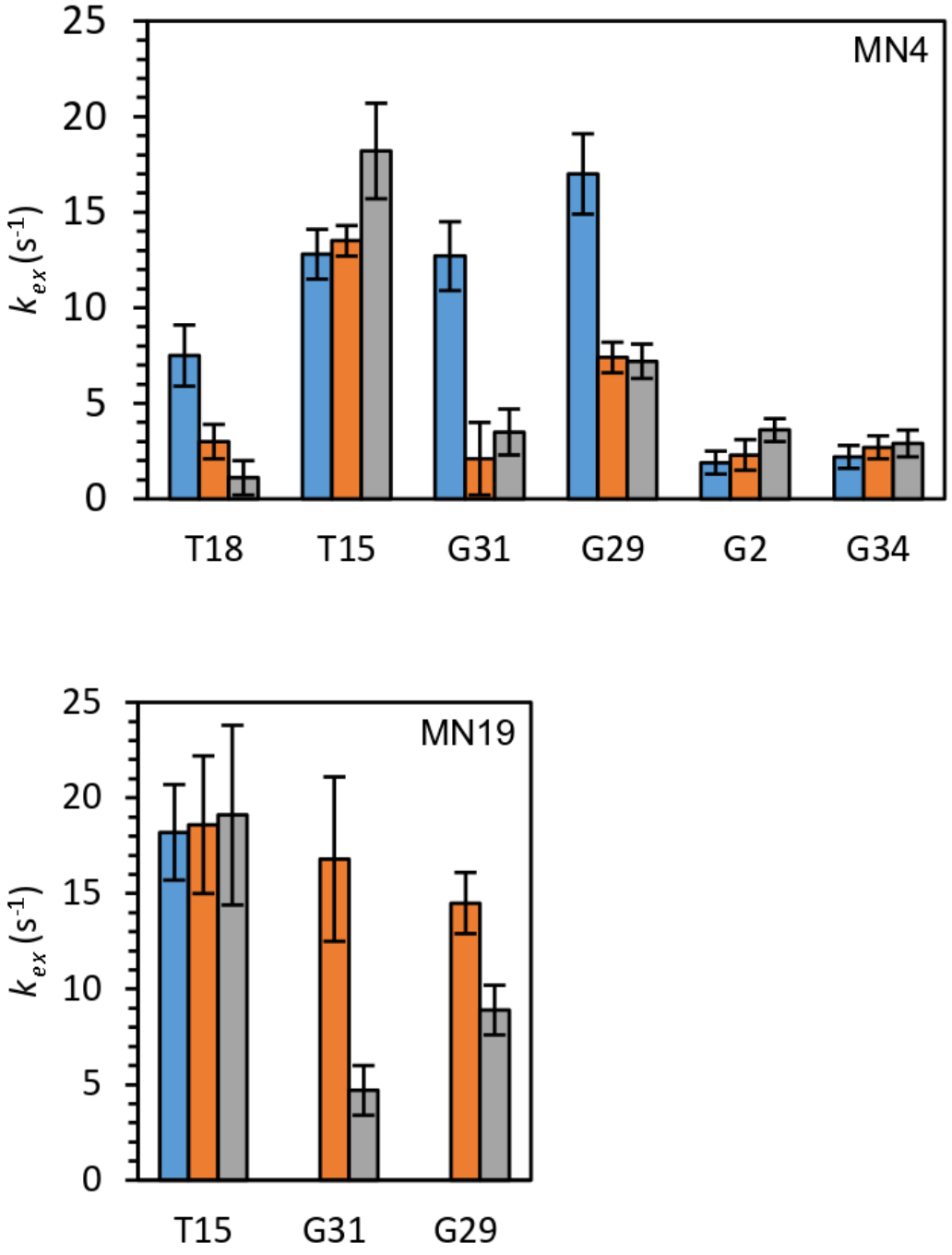

Figure 3.6 Comparison of the imino exchange rates in MN4 (top) and MN19 (bottom). In blue are data for free aptamer, in orange are data for cocaine-bound aptamer and in grey are data for the quinine-bound aptamer. Only nucleotides with data from more than one state are shown.

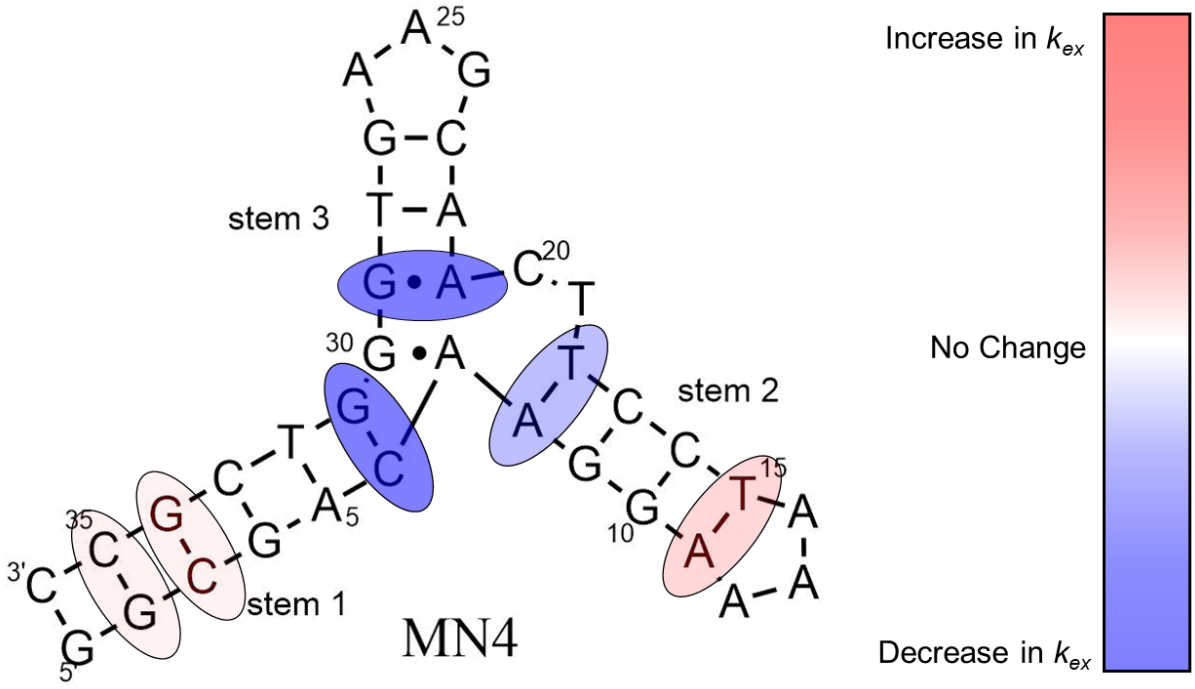

Figure 3.7 Change in imino exchange rate upon ligand binding mapped onto the MN4 secondary structure. A greater intensity of blue corresponds to a greater reduction in the imino exchange rate with ligand binding. A greater intensity of red corresponds to a greater increase in the imino exchange rate with ligand binding.

In contrast to the reduction in k_{ex} for nucleotides at the high affinity site, the k_{ex} value of T15, located away from the high affinity binding site at the end of stem 2, is unchanged with cocaine binding and remains high at (12.8 ± 1.3) s^{-1} in the free and (13.5 ± 0.8) s^{-1} in the cocaine-bound states. The k_{ex} values of G2 and G34, also located away from the binding site are unchanged and remain low when cocaine bound. T19 which is at the centre of the high-affinity binding site, and only observed as an isolated peak in the cocaine-bound MN4 complex, has a low k_{ex} value (2.7 ± 2.0) s^{-1} and within the uncertainty range for its adjacent nucleotide T18 despite it being in the dinucleotide bulge (Fig. 3.1). Finally, k_{ex} value of G4 in the cocaine-bound MN4 complex was found to be (4.3 ± 0.7) s^{-1}. This value is slightly higher than the nucleotides G2 and G34 in stem 1, but certainly not a fast-exchanging residue.

The effects of quinine binding on the k_{ex} values of MN4 are similar to what was seen with cocaine binding (Table 3.1; Fig. 3.6). All the k_{ex} values that can be measured in both bound states are within the error range of each other, with the exception of T15. The nucleotides T18, G29 and G31, are located at the high-affinity site that experience a significantly decreased k_{ex} value for cocaine binding, display an analogous behavior when quinine is bound. The k_{ex} value of T15 remains high when quinine is bound and even increases significantly compared to the free and cocaine-bound states though only slightly greater than the uncertainty in the values.

For MN19, the data set is very limited due to overlapping signals. In the free state, MN19 is thought to be loosely structured or unfolded [17], [58], [73] and of the approximately five imino protons detected only the imino proton of T15 is able to assigned (Fig. 3.2). In the cocaine and quinine-bound states, the expected number of imino protons for the MN19 secondary structure shown in Fig. 3.1 are detected. However, only the k_{ex} values for the imino resonances of G29 and G31 in addition to T15 are measured due to signal overlap. The k_{ex} values of T15 are similar in all three states of MN19 (Fig. 3.6; Table 3.1). For G29 and G31, both residues are at the high affinity site, the k_{ex} values are lower in the quinine-bound state than the cocaine-bound state, possibly, reflecting the higher affinity of MN19 for quinine. For both nucleotides, the k_{ex} values are higher in MN19 than what was observed in MN4 indicating that this aptamer is more dynamic than MN4 and consistent with MN19 having a lower melting point (T_m) than MN4 in both the cocaine and quinine-bound forms [94].

The reduction in k_{ex} values with ligand binding observed here for residues at the ligand-binding site is consistent with previous aptamer-ligand studies. A free aptamer versus protein-bound aptamer study of the macugen-$VEGF_{165}$ interaction showed that the free aptamer had many residues whose imino protons were not observed due to a high exchange rate in the free state. In

the bound state, many of these protons were observable and the k_{ex} values were less than 1.5 s^{-1} [75] . Even with the binding of a small organic molecule, a reduction in k_{ex} values at the ligand-binding site is still seen. Other studies on riboswitches, though not involving measuring k_{ex} rates but instead small-angle X-ray scattering (SAXS) based studies, have also shown that many riboswitches can become more compact with ligand binding. However, this phenomenon is not observed in all cases [96]. In MN4, the tandem GA mismatch at the three-way junction has a lower k_{ex} rate in the ligand-bound forms than in the free state. This reduction in mobility might be necessary for binding given than the replacement of the G29-A21 base pair with a GC base pair greatly reduces cocaine affinity [55], [97] though structural changes may also play a role.

3.4 Concluding Remarks

Using magnetization transfer experiments, the k_{ex} values of imino protons in the MN4 and MN19 cocaine-binding aptamers have been measured in the free, cocaine-bound and quinine-bound states. With ligand binding a significant reduction in the k_{ex} values for nucleotides T18, G29 and G31 located at the binding site in the aptamer was observed. Only minor changes in the k_{ex} values of imino protons located away from the binding site was seen. This trend of a reduction of imino proton k_{ex} values at the binding site upon ligand binding has been seen before in the macugen-$VEGF_{165}$ complex [75], the AMP-RNA aptamer complex and the AMP-DNA aptamer complex [88] and appears to be a general feature in aptamer-ligand interactions.

Chapter 4: **Reduction in Dynamics of Base Pair Opening upon Ligand Binding by the Cocaine-Binding Aptamer**

4.1 Preface

Most work presented in this chapter has been published in the article listed below [98]

- **Churcher, Z.R.,** Garaev, D.M., Hunter, H.N. and Johnson, P.E. **"**Reduction in Dynamics of Base Pair Opening upon Ligand Binding by the Cocaine-Binding Aptamer". *Biophysical Journal*, 119, 1147-1156 (2020). [98]

4.2 Introduction

Understanding how aptamers function is important in their designed development in biotechnology applications as well as obtaining a better understanding of how aptamers function in nature. However, few aptamers to date have been thoroughly characterized. One aptamer that has been particularly well studied is the cocaine-binding DNA aptamer [52], [59], [89], [91], [99]– [101]. The cocaine-binding aptamer has a three-way junction structure formed around a tandem AG base pair (Fig. 4.1) with its high affinity binding site located at the junction [17]. This aptamer is distinctive in that its mode of binding changes from being largely pre-formed to having a ligand-induced structure switching mechanism as the length of stem 1 is shortened from 6 base pairs (MN4; Fig. 4.1) to 3 base pairs (MN19; Fig. 4.1) [17], [102]. The exact nature of the ligand-induced structure switching mechanism in MN19 is not known and could result from a reduction of dynamics of pre-formed base pairs or whole scale folding of a region or helix of MN19.

The cocaine-binding aptamer is also unusual in that it has high specificity for cocaine and not common cocaine metabolites [52], [58], [94], [103], [104] whereas the aptamer has high binding affinity, tighter than for cocaine, to quinine and quinine-based antimalarial compounds [54], [57], [73], [104]– [106]. Another unusual feature of this aptamer is that it binds two copies

of its ligand in an independent manner in low NaCl conditions. At NaCl concentrations of greater than 75 mM only one ligand is bound [95]. The experiments presented in this chapter use buffer conditions of 120 mM and 245 mM KCl where both MN4 and MN19 bind one molecule of cocaine or quinine.

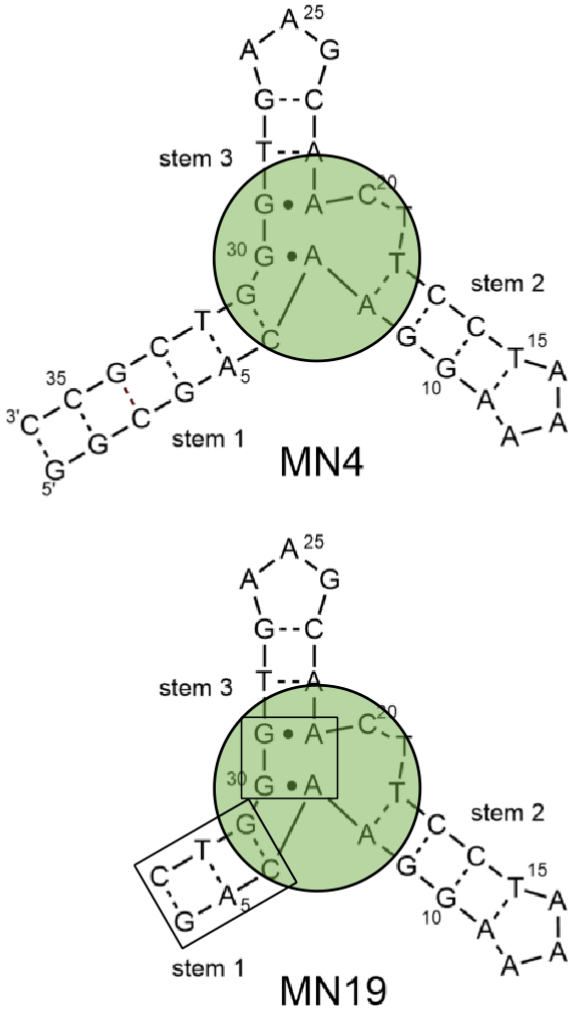

Figure 4.1: Secondary structure of MN4 and MN19. Circled is the high affinity ligand-binding site. Boxed in MN19 are the base pairs in which imino protons are not observed in the free form because of rapid exchange. For ease of comparison, both aptamers follow the same numbering scheme.

One aspect of biomolecules that has become increasingly important is how their function is related to their mobility or dynamics [107], [108]. Dynamics has been well-studied in proteins but relatively less is known about how dynamics and function are related in nucleic acids [109]–

[113]. One method to study the dynamics in nucleic acids is by measuring the exchange rate constant (k_{ex}) of the imino protons in the base pairs with the bulk solvent [114]. Previous studies have reports k_{ex} values between 1 s^{-1} and 124 s^{-1} being detected by this method [115] with an upper exchange limit of 400 s^{-1} given for detection of an imino proton [75]. A recent approach developed by the Schwalbe lab is to measure the k_{ex} values as a function of temperature in order to obtain the thermodynamic parameters of base pair opening [77], [78], [116].

In the previous chapter, the k_{ex} values of the imino protons in free, cocaine and quinine-bound cocaine-binding aptamer at a single temperature, 5 ºC [76] were measured, with changes in the k_{ex} values with ligand binding being observed. Here the k_{ex} values of the imino protons in MN4 and MN19 were measured as a function of temperature in their free, cocaine-bound, and quinine-bound states to allow for a more in-depth understanding of how the dynamics differ between the two aptamers in the different ligand-bound states. With ligand binding in MN19 there is a reduction in dynamics in stem 1 and at the ligand-binding site, while for MN4 there is a reduction in dynamics that is localized to nucleotides at the ligand-binding site. In addition, the experiments presented here were done using two different buffer conditions for MN4 in order to determine the enthalpy, entropy and free energy of base pair opening as a function of ligand binding. The data shows that only the base pairs near the binding site increase in free energy and strengthen with ligand binding.

4.3 Results

4.3.1 Imino proton k_{ex} measurements. ^{1}H NMR spectra of the MN4 and MN19 cocaine-binding aptamer constructs (Fig. 4.1) in the free, cocaine-bound and quinine-bound states were highly similar to previously work from the Johnson lab (Figure 4.2 & 4.3) and ^{1}H imino assignments were obtained by consulting previous works [76].

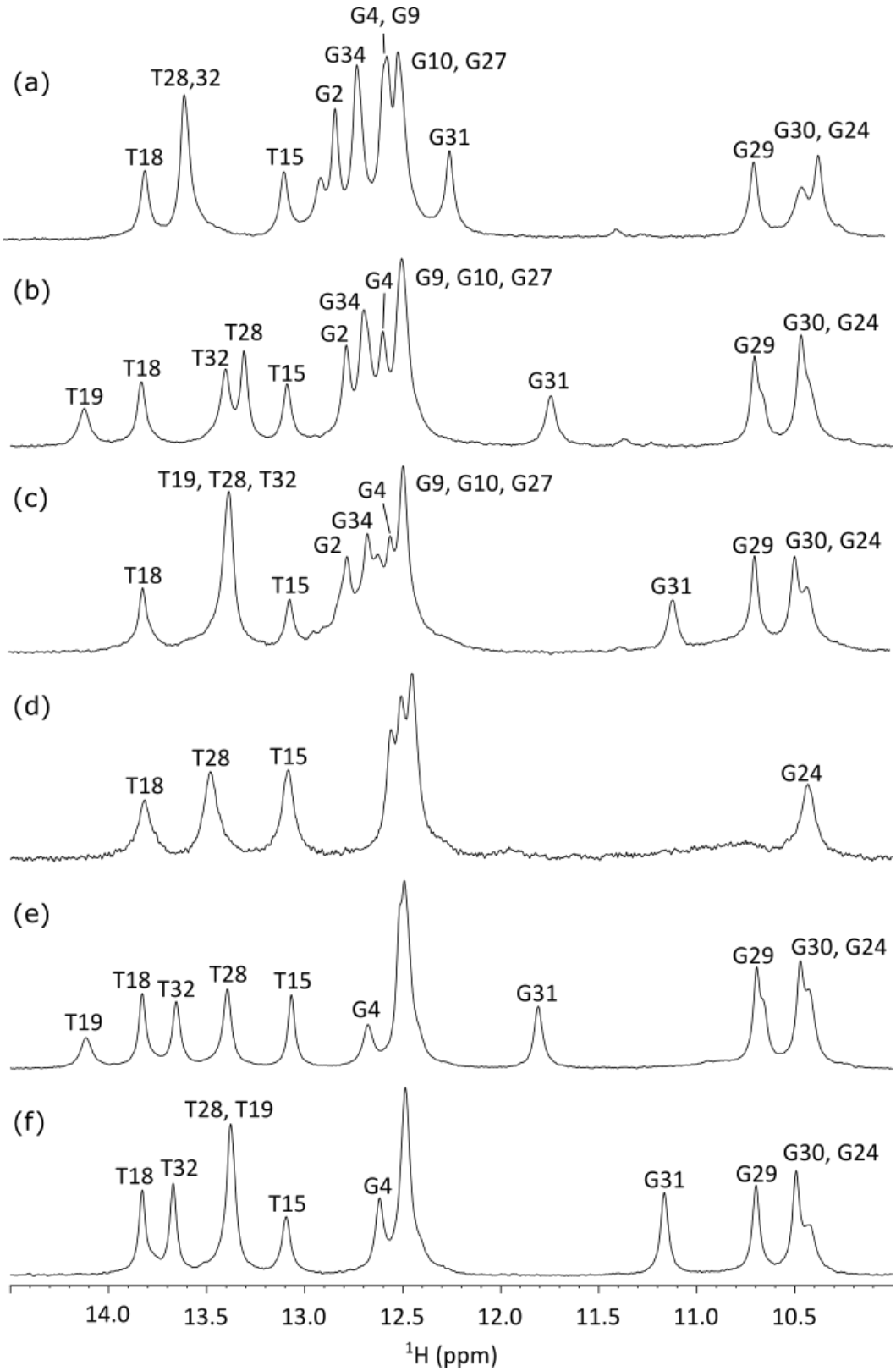

Figure 4.2: Sample spectra of MN4 (a) free, (b) cocaine-bound and (c) quinine-bound. MN19 (d) free, (e) cocaine-bound and (f) quinine-bound. Spectra acquired in 5 mM $KHPO_4$, 245 mM KCl pH 6.8, 10% ^2H_2O/90% H_2O.

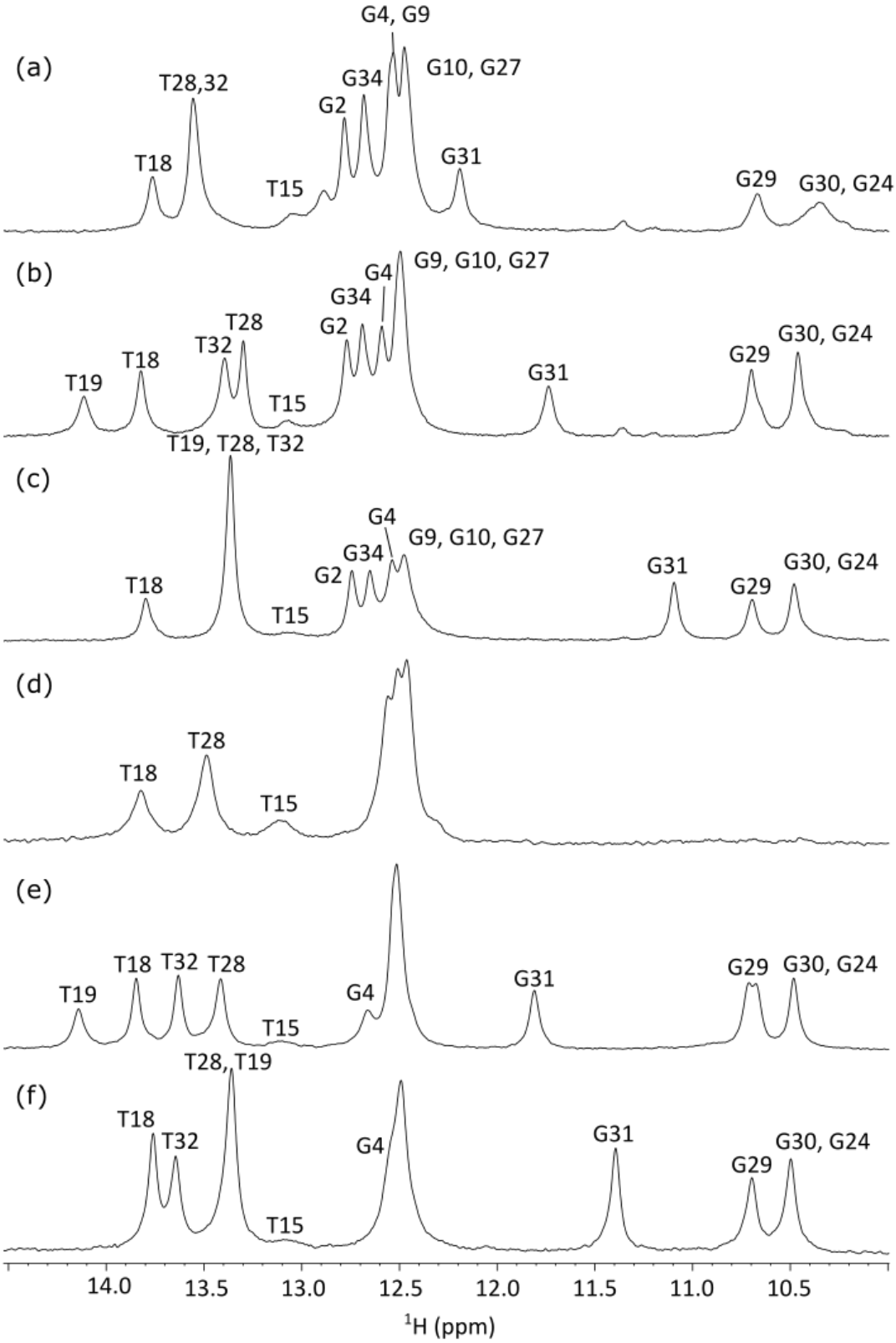

Figure 4.3: Sample spectra of MN4 (a) free, (b) cocaine-bound and (c) quinine-bound. MN19 (d) free, (e) cocaine-bound and (f) quinine-bound. Spectra acquired in 120 mM $KHPO_4$, 100 mM, KCl pH 6.8, 10% ^2H_2O/90% H_2O.

NMR spectra were acquired every 5° between 5 °C and 45 °C in order to observe the effect of temperature on the dynamics of the aptamer. For each aptamer-ligand combination, the R_{1w} and R_{1a} values were measured using inversion recovery experiments. Next, the imino resonance intensity was measured as a function of delay time after perturbation of the water signal using the magnetization transfer experiments with forty-four 1D spectra obtained with delay times varying from 5 ms to 500 ms (Fig. 4.4a). The peak intensity of these spectra was measured and fit to an intensity curve to obtain exchange rate constants (Fig. 4.4b). Three separate experiments were acquired at both 10 ms and 120 ms and are essentially overlapped in this plot showing very close repeatability of this analysis. The measured k_{ex} values are found in Tables 4.1, 4.2, 4.3 and 4.4. ^{1}H imino NMR spectra of the MN4 and MN19 in their free and ligand-bound states at the temperatures these experiments were conducted at can be found in Figures 4.5 and 4.6. Plots of k_{ex} values as a function of temperature in low catalyst concentration buffer are found in Fig. 4.7 while plots of k_{ex} values as a function of temperature in high catalyst concentration buffer are in Fig. 4.8.

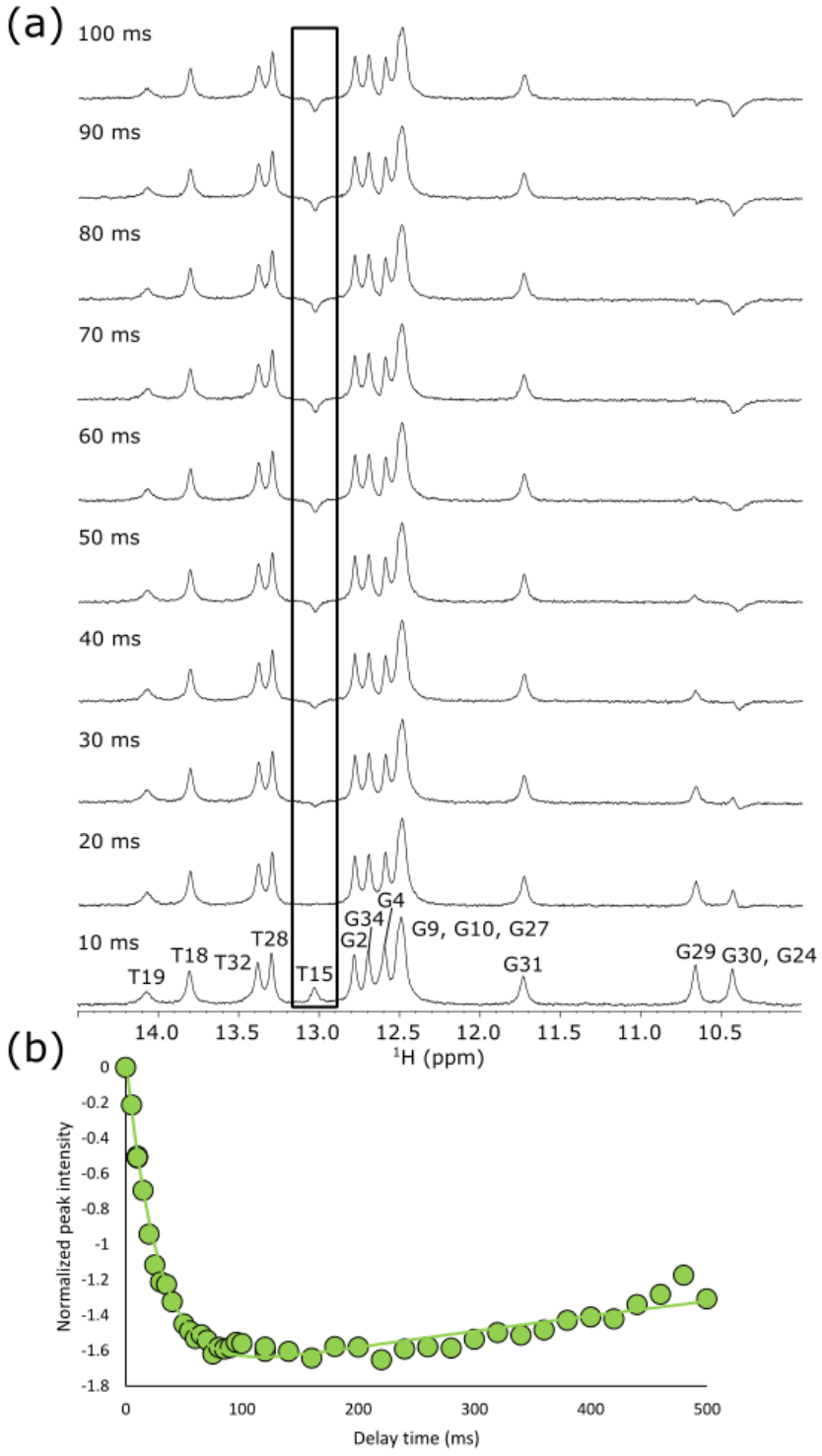

Figure 4.4: 1D ^{1}H spectra of (a) the magnetization transfer experiment showing the imino proton resonances for cocaine-bound MN4 at 10 °C. (b) The normalized peak intensity, $I(t)/I_0$, of cocaine-bound T15 in MN4 at 10 °C (boxed peak in part (a)). Shaded circles represent the raw data acquired from the NMR experiments, while the line shows the fit of the data to equation 1 to determine the k_{ex} values. The R^2 value for this fit is 0.98.

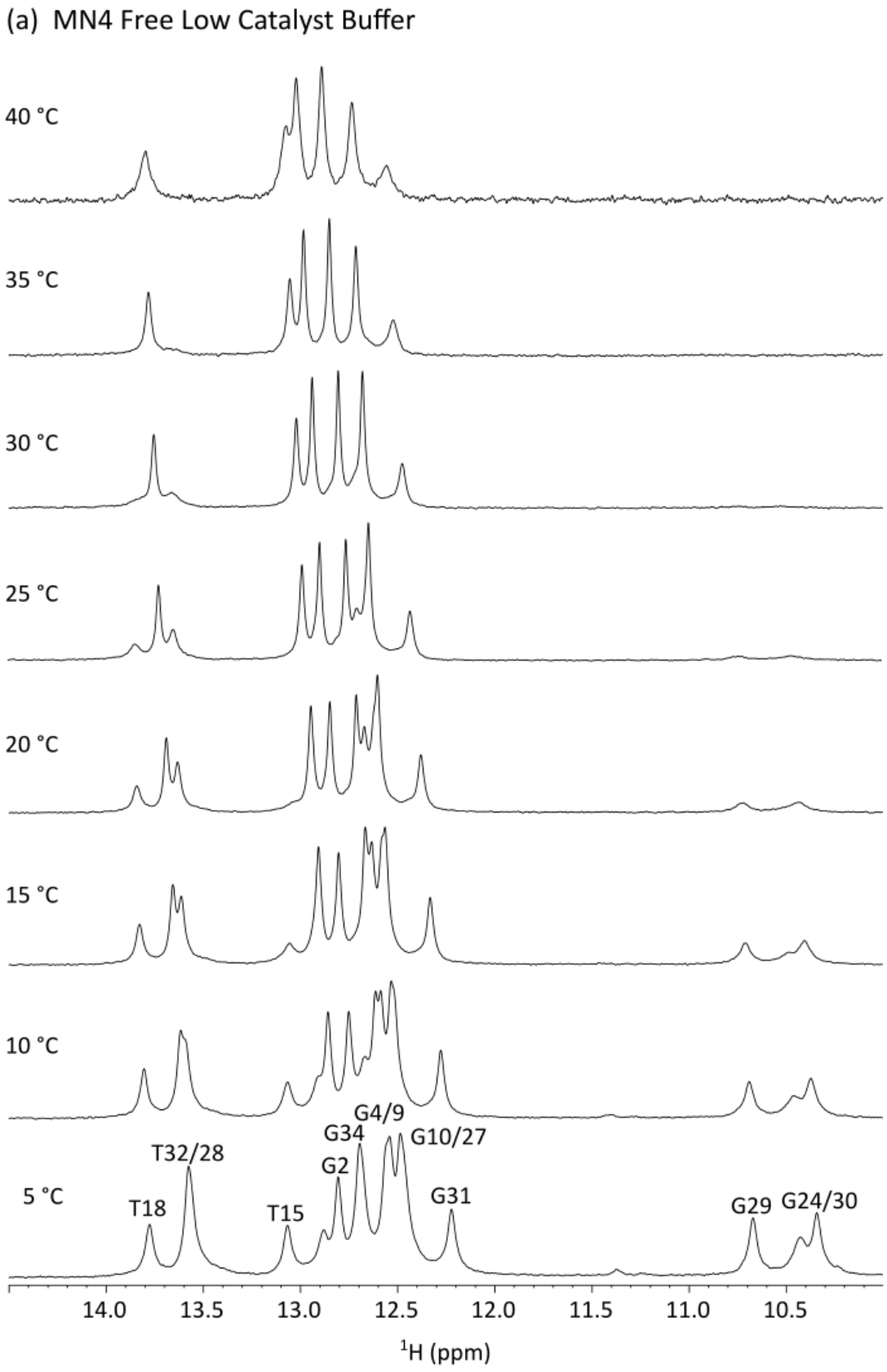
(a) MN4 Free Low Catalyst Buffer
40 °C
35 °C
30 °C
25 °C
20 °C
15 °C
10 °C
5 °C
T18
T32/28
T15
G2
G34
G4/9
G10/27
G31
G29
G24/30
14.0
13.5
13.0
12.5
12.0
11.5
11.0
10.5
^{1}H (ppm)

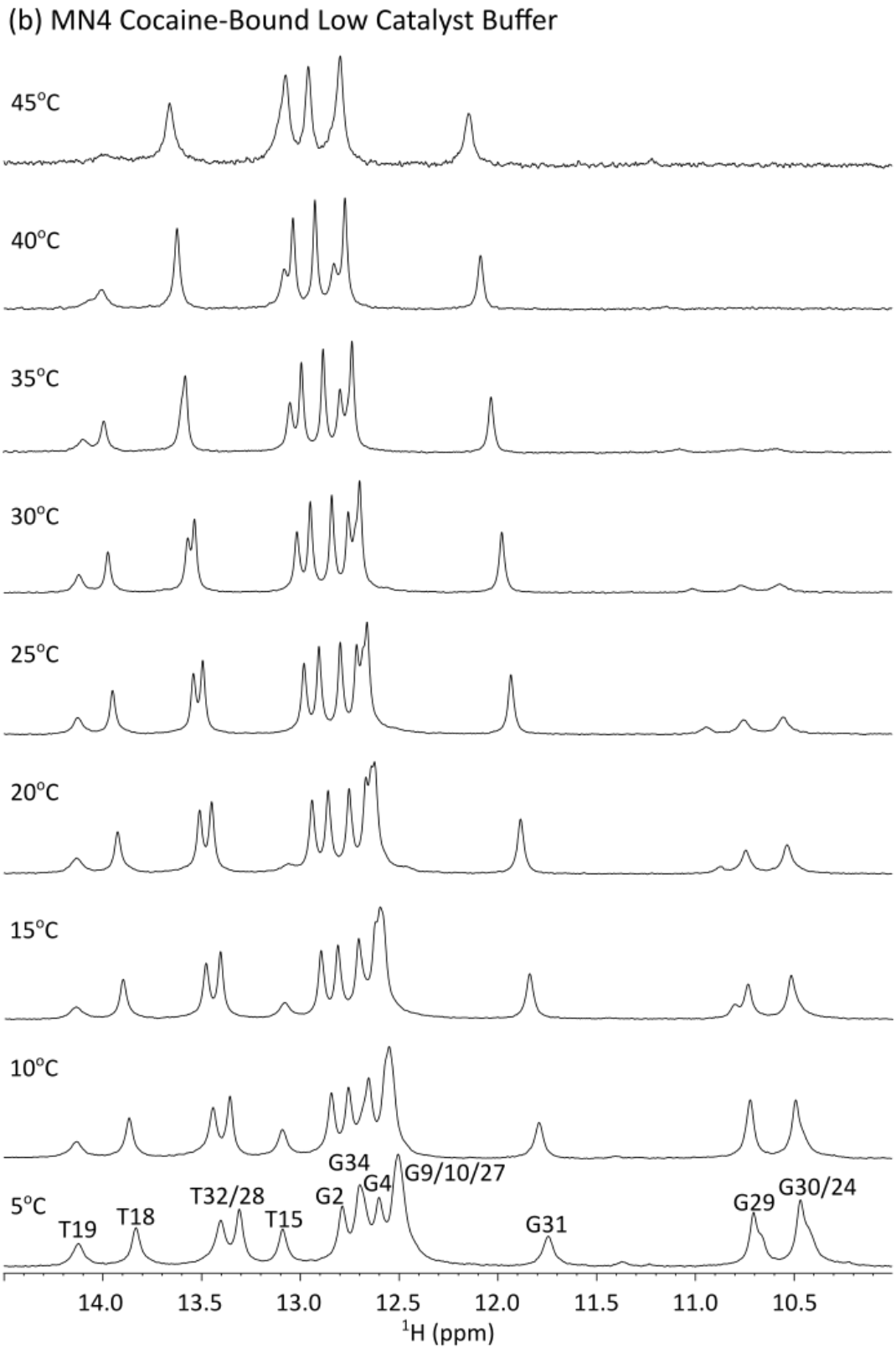
(b) MN4 Cocaine-Bound Low Catalyst Buffer
45°C
40°C
35°C
30°C
25°C
20°C
15°C
10°C
5°C
T19
T18
T32/28
T15
G2
G34
G4
G9/10/27
G31
G29
G30/24
14.0
13.5
13.0
12.5
12.0
11.5
11.0
10.5
^{1}H (ppm)

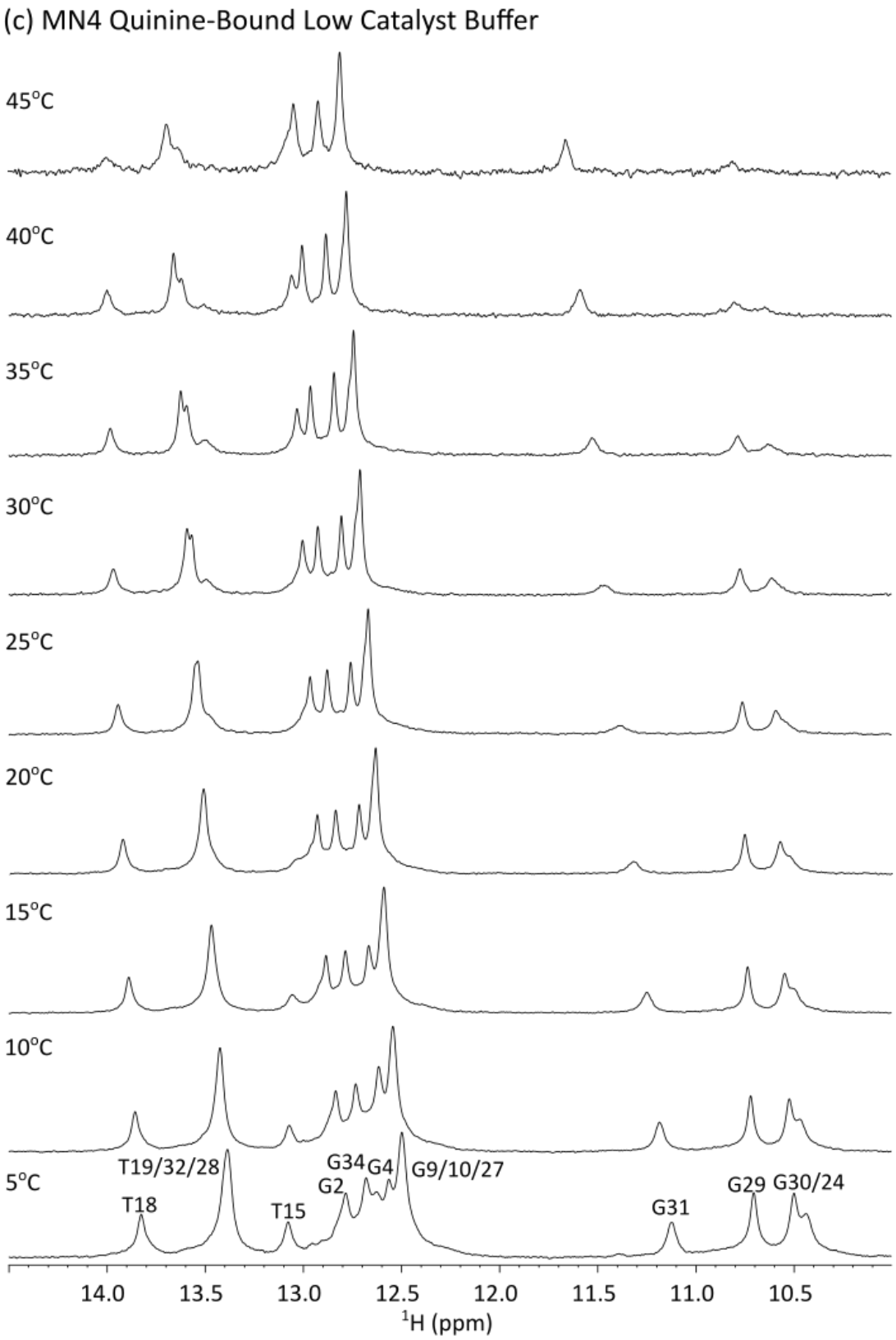
(c) MN4 Quinine-Bound Low Catalyst Buffer
45°C
40°C
35°C
30°C
25°C
20°C
15°C
10°C
5°C
T19/32/28
T18
T15
G34
G2
G4
G9/10/27
G31
G29
G30/24
14.0
13.5
13.0
12.5
12.0
11.5
11.0
10.5
^{1}H (ppm)

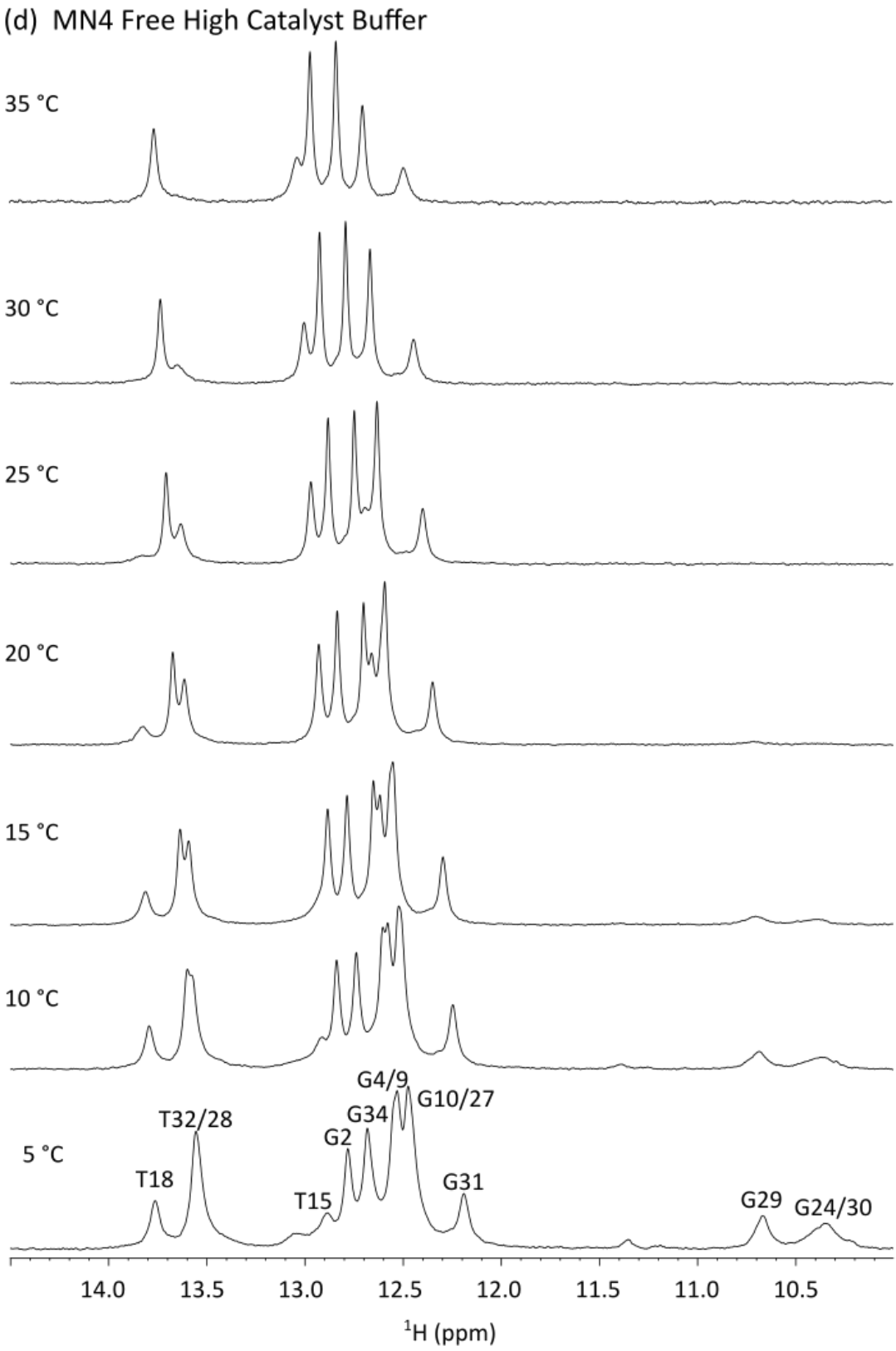
(d) MN4 Free High Catalyst Buffer
35 °C
30 °C
25 °C
20 °C
15 °C
10 °C
5 °C
T18
T32/28
T15
G2
G34
G4/9
G10/27
G31
G29
G24/30
14.0
13.5
13.0
12.5
12.0
11.5
11.0
10.5
^{1}H (ppm)

(e) MN4 Cocaine-Bound High Catalyst Buffer

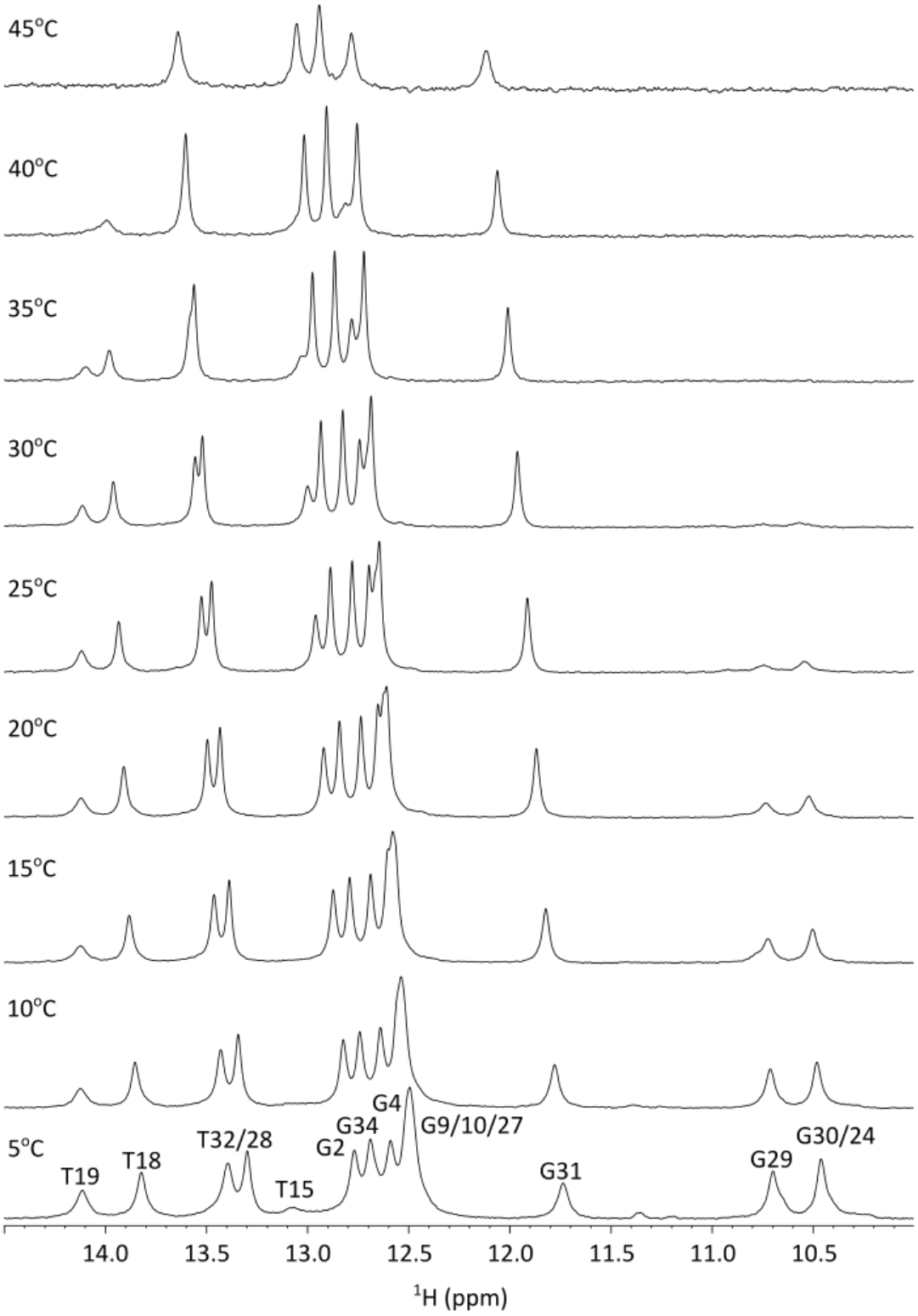

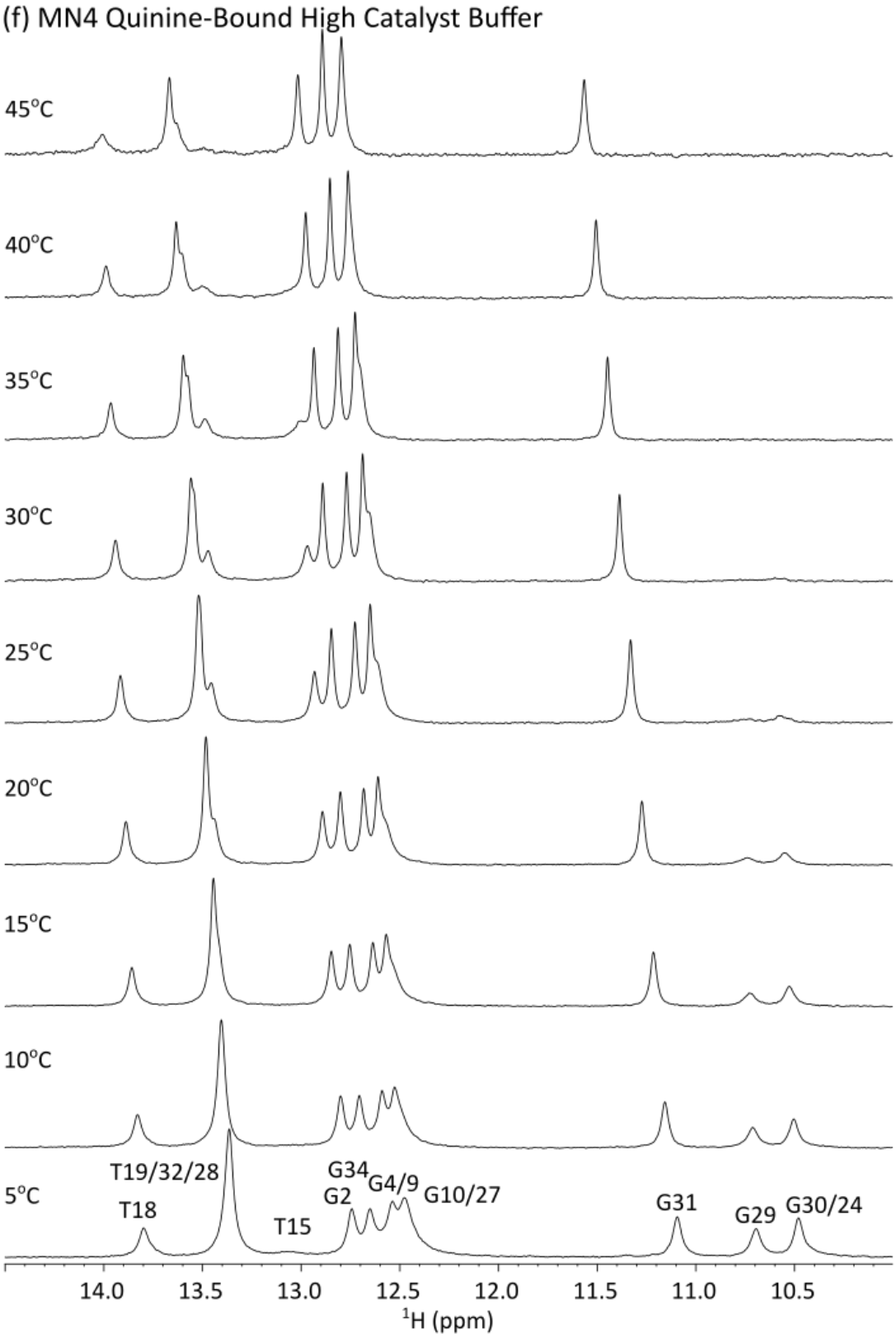
(f) MN4 Quinine-Bound High Catalyst Buffer
45°C
40°C
35°C
30°C
25°C
20°C
15°C
10°C
5°C
T19/32/28
T18
T15
G34
G2
G4/9
G10/27
G31
G29
G30/24
14.0
13.5
13.0
12.5
12.0
11.5
11.0
10.5
¹H (ppm)

Figure 4.5: 1D ^{1}H spectra of all temperatures for which data of MN4 was collected. The temperature series are MN4 free (a), cocaine-bound (b), and quinine-bound (c) in low catalyst buffer, and MN4 free (d), cocaine-bound (e), and quinine-bound (f) in high catalyst buffer.

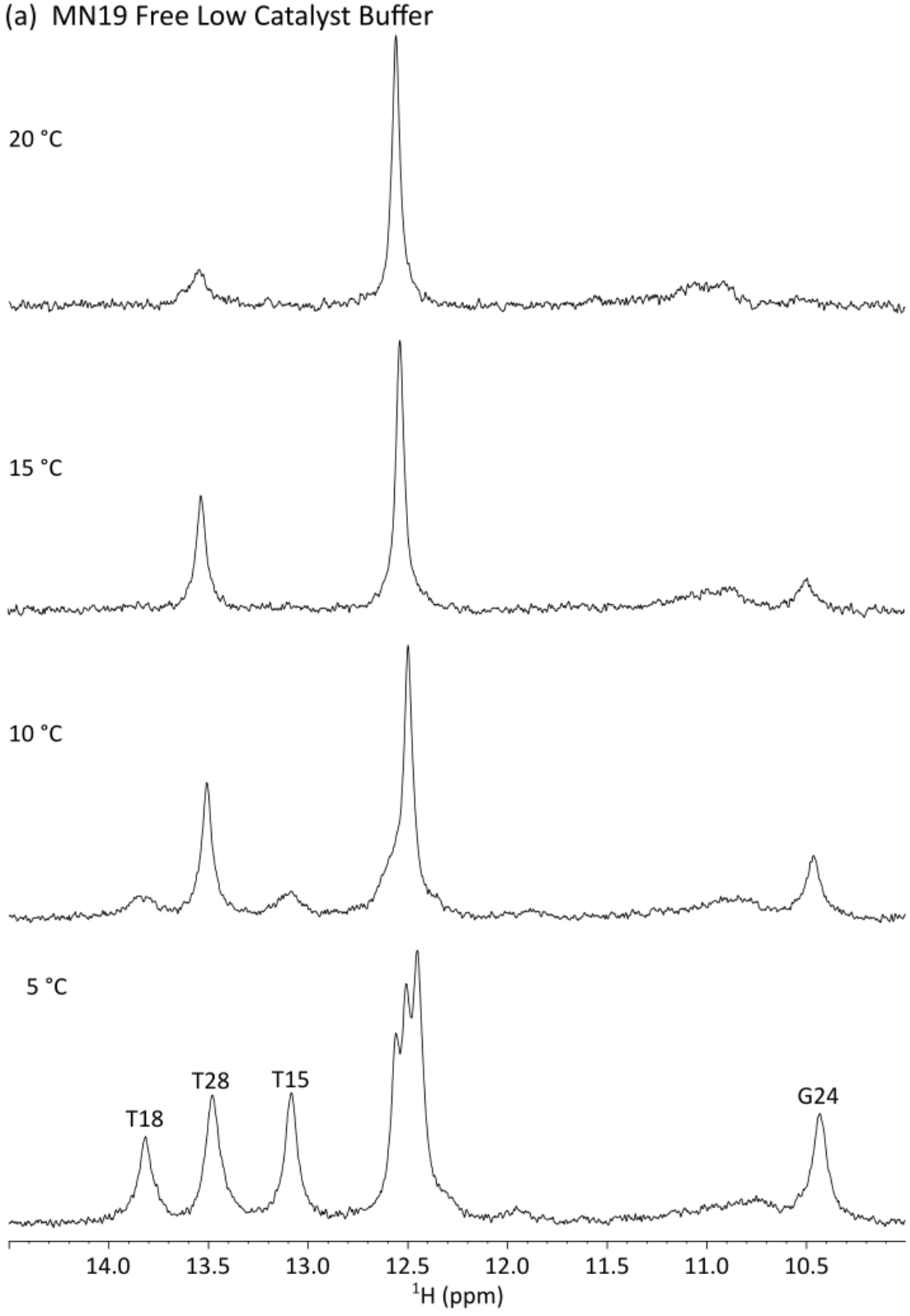
(a) MN19 Free Low Catalyst Buffer
20 °C
15 °C
10 °C
5 °C
T18
T28
T15
G24
14.0
13.5
13.0
12.5
12.0
11.5
11.0
10.5
^{1}H (ppm)

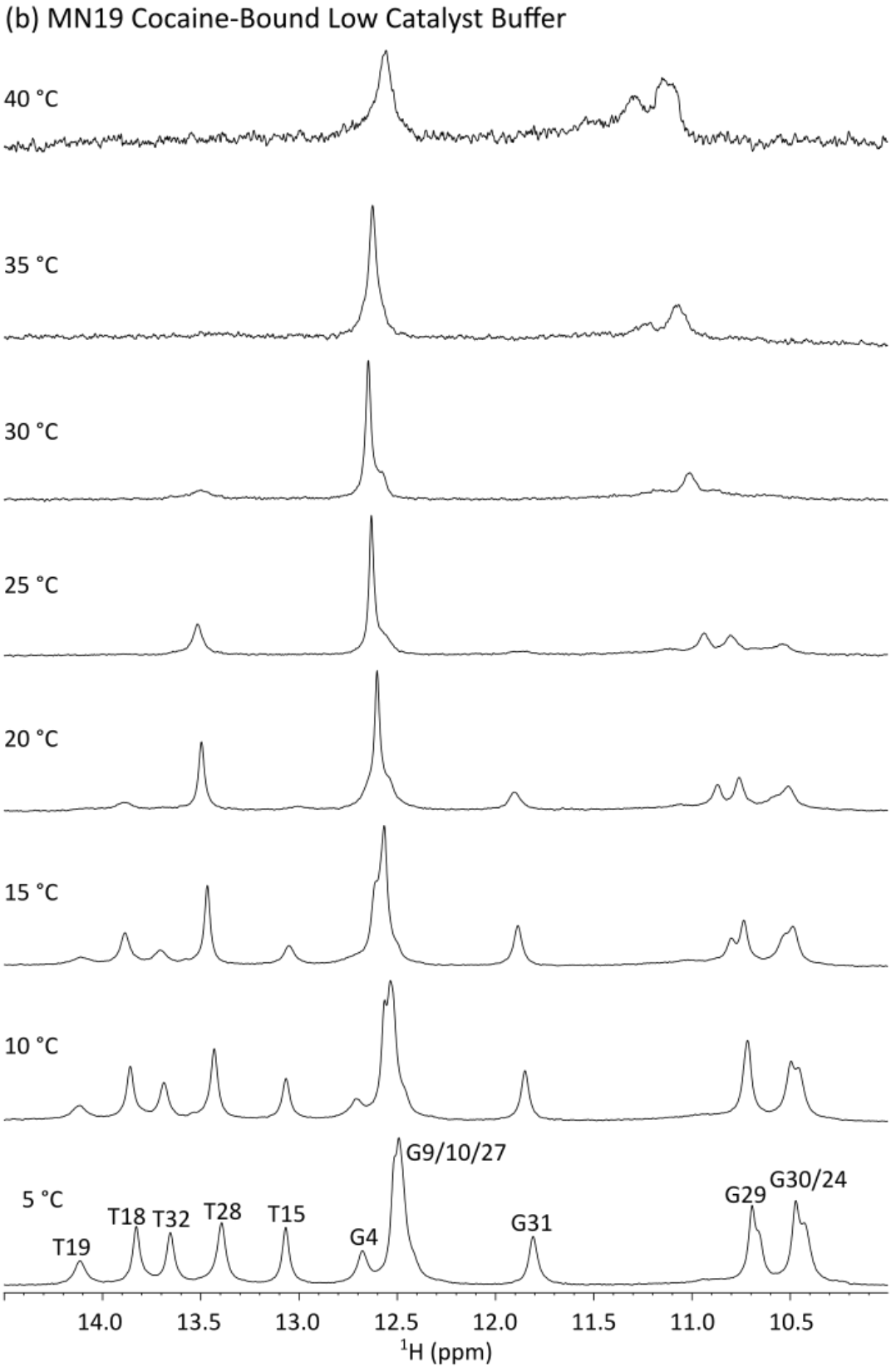
(b) MN19 Cocaine-Bound Low Catalyst Buffer
40 °C
35 °C
30 °C
25 °C
20 °C
15 °C
10 °C
5 °C
T19
T18
T32
T28
T15
G4
G9/10/27
G31
G29
G30/24
14.0
13.5
13.0
12.5
12.0
11.5
11.0
10.5
^{1}H (ppm)

(c) MN19 Quinine-Bound Low Catalyst Buffer

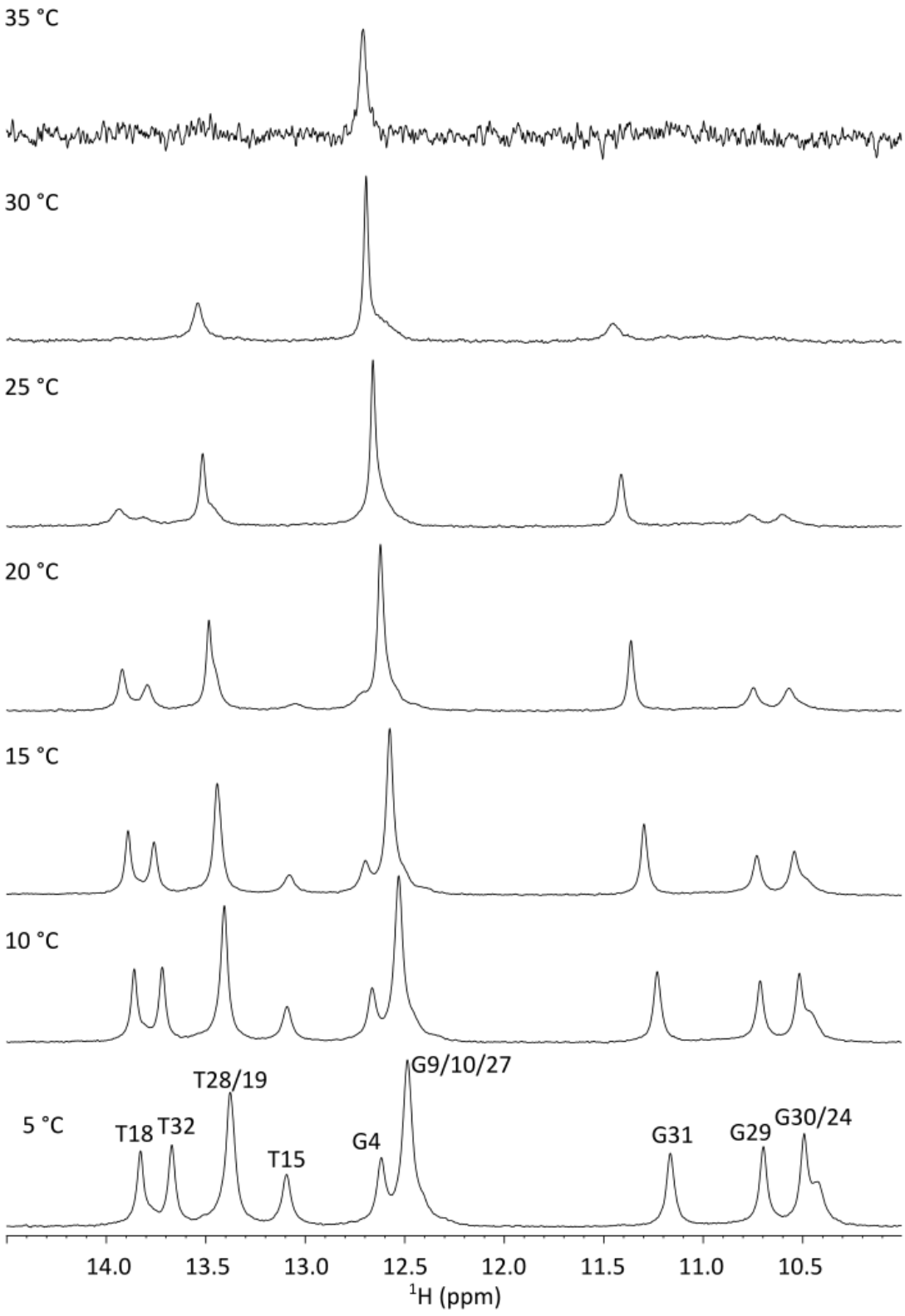

(d) MN19 Free High Catalyst Buffer

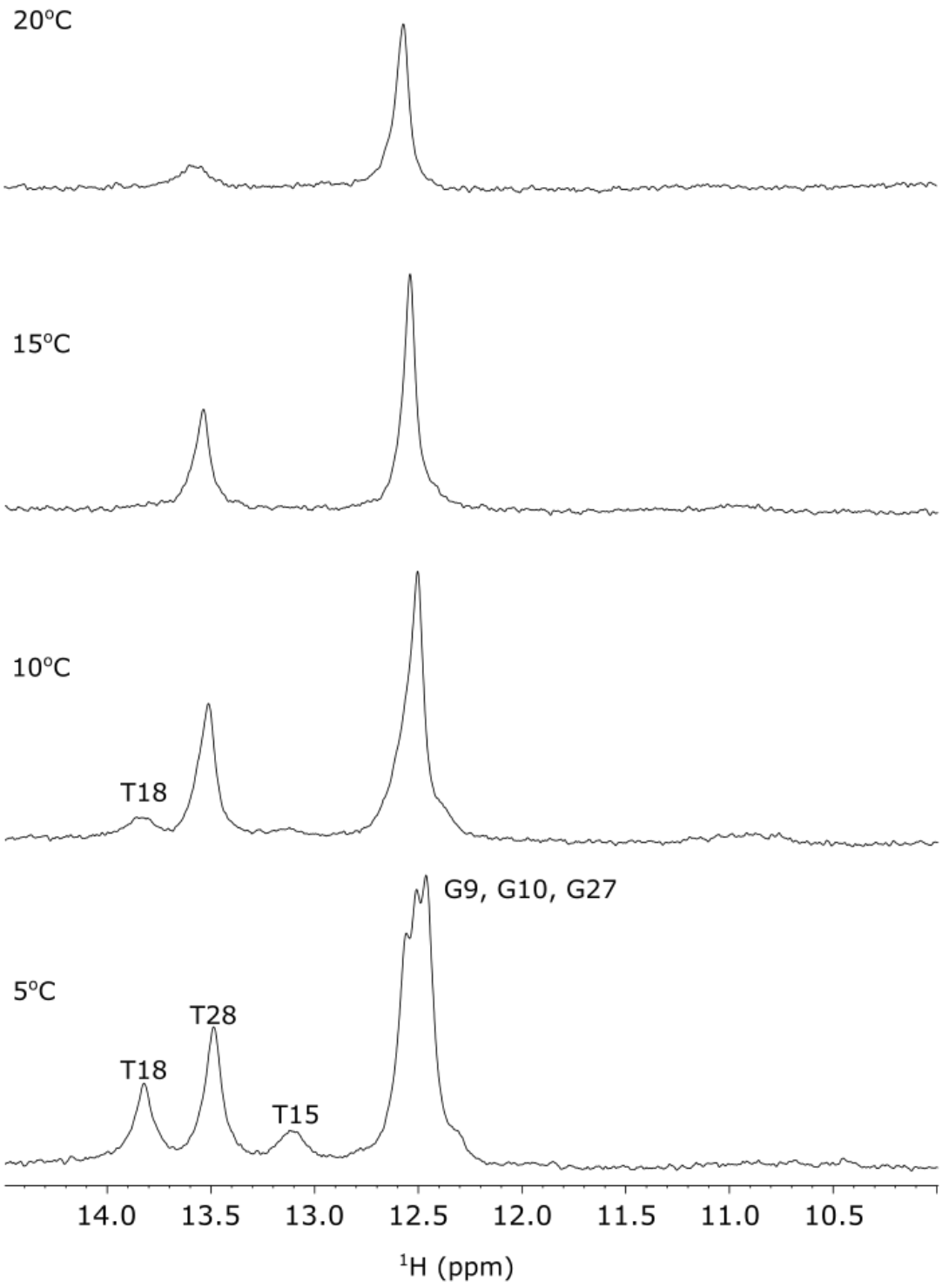

(e) MN19 Cocaine-Bound High Catalyst Buffer

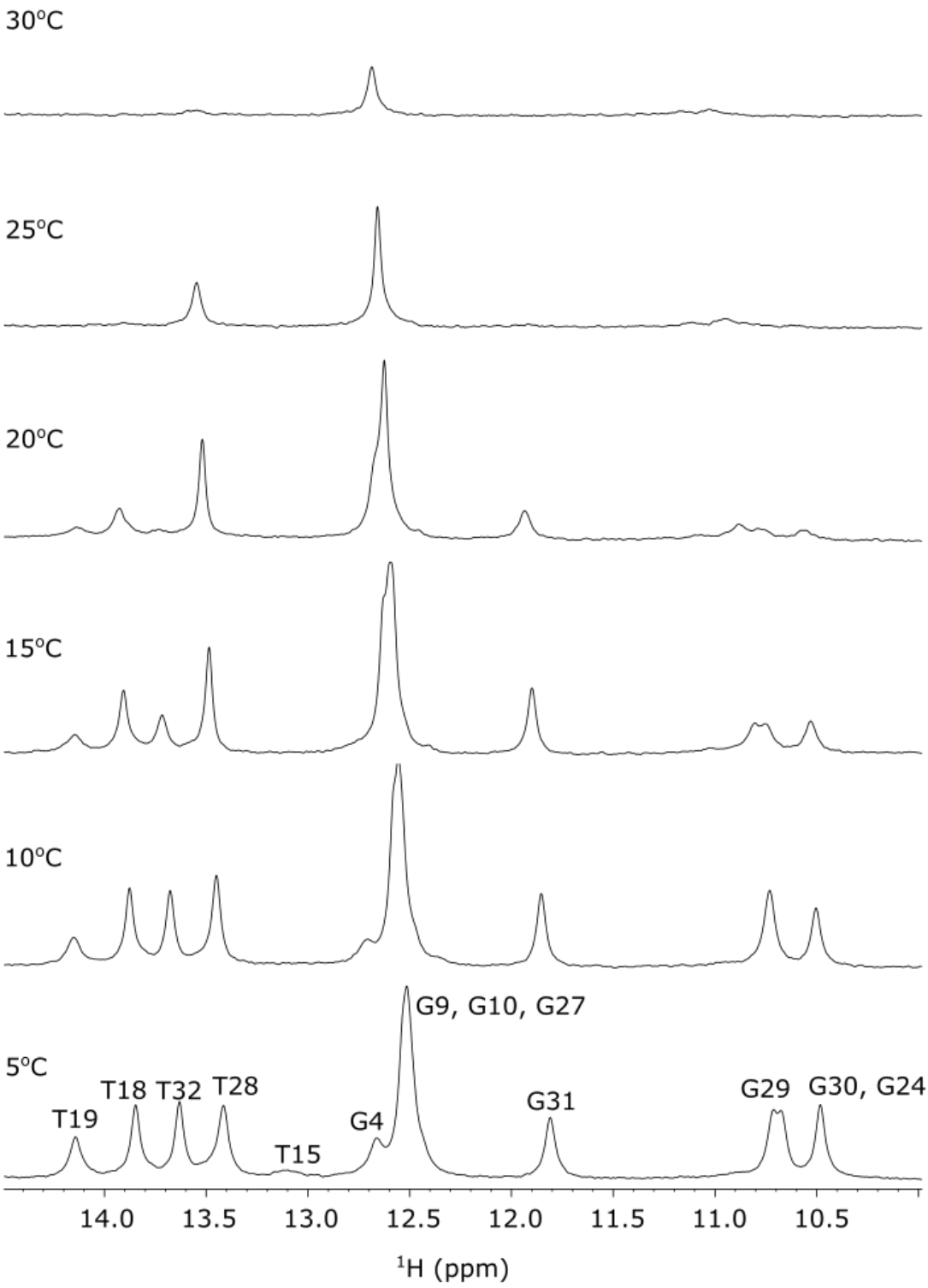

(f) MN19 Quinine-Bound High Catalyst Buffer

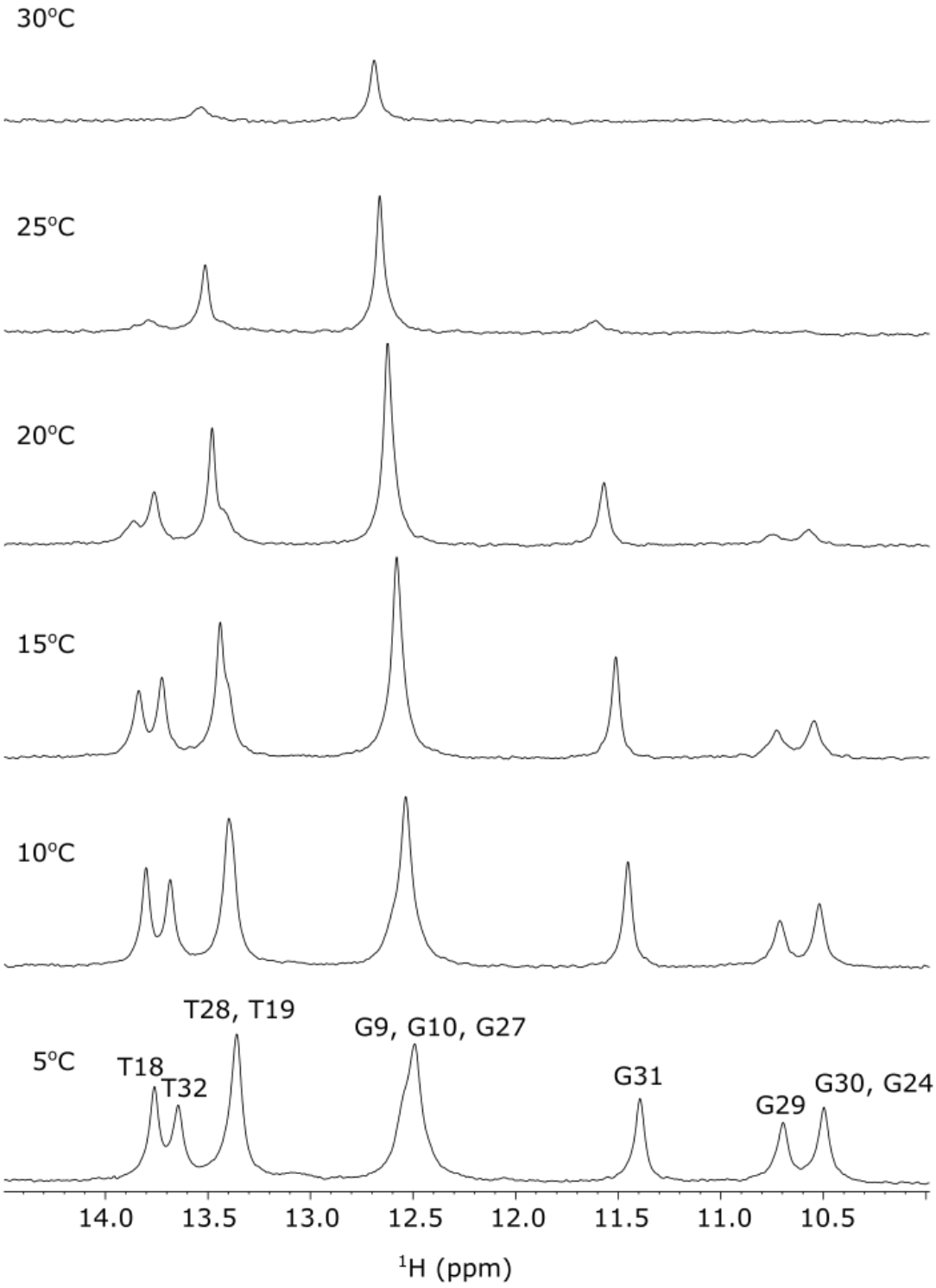

Figure 4.6: 1D ^{1}H spectra of all temperatures for which data of MN19 was collected. The temperature series are MN19 free (a), cocaine-bound (b), and quinine-bound (c) in low catalyst buffer, and MN19 free (d), cocaine-bound (e), and quinine-bound (f) in high catalyst buffer.

Table 4.1 Hydrogen exchange rate constants (s^{-1}) of the imino protons for the free and ligand-bound MN4 aptamer as a function of temperature.[1]

Temperature (°C)	Residues											
Free Aptamer	G2	G4	T15	T18	T19	G24	T28	G29	G30	G31	T32	G34
5	3±3	-	21±2	6±1	-	38±4	-	29±3	40±4	3±2	-	6±2
10	3±2	-	40±4	13±2	-	67±6	-	50±6	65±8	4±1	-	3±1
15	5±2	-	62±9	19±3	-	-	6±1	(7±1)x10^1	-	3.8±0.8	2±2	1.7±0.9
20	6±1	-	-	38±2	-	-	13.3±0.6	-	-	7±1	3.6±0.7	3±5
25	5±1	-	-	(7±1)x10^1	-	-	24±3	-	-	13±3	7±1	2±4
30	9±2	-	-	-	-	-	45±7	-	-	25±2	11±2	5±6
35	18±4	-	-	-	-	-	-	-	-	(4±1)x10^1	18±9	6±8
40	37±3	-	-	-	-	-	-	-	-	90±7	57±6	23±1
Cocaine-bound Aptamer	G2	G4	T15	T18	T19	G24	T28	G29	G30	G31	T32	G34
5	4±3	4±1	21±2	1±3	3±3	-	2±2	14±2	-	4±2	2±2	-
10	2±3	7±2	33±3	2±3	3±4	-	2±2	15±1	-	2±2	2±3	2±2
15	3±3	7±3	(6±1)x10^1	3±3	8±2	-	3±4	25±7	-	4±5	4±3	2±5
20	3±2	1.2±0.8	-	3±2	7±2	-	4±2	51±7	-	2±2	4±2	1±2
25	5±1	3±2	-	5.7±0.7	14±2	-	5±1	77±7	-	2±1	5±2	1±2
30	9±1	2±2	-	11±1	23±3	-	8±1	(15±4)x10^1	-	4±2	8±2	2±3
35	16±2	3±3	-	13±1	49±6	-	-	-	-	7±1	-	4±2
40	27±2	3±2	-	54±6	-	-	-	-	-	12±2	-	6.6±0.7
45	-	2±2	-	-	-	-	-	-	-	43±4	-	-
Quinine-bound Aptamer	G2	G4	T15	T18	T19	G24	T28	G29	G30	G31	T32	G34
5	2±2	-	15±2	2±3	-	23±2	-	8±1	13±1	4±4	-	4±1
10	2±4	-	25±3	2±5	-	38±4	-	12±2	17±3	3±3	-	3±3
15	3±2	3±2	41±6	2±3	-	44±5	-	15±1	25±2	3±3	-	2±3
20	4±2	2±2	53±8	4±3	-	64±9	-	20±2	37±3	5±4	-	2±3
25	8±3	2±3	-	5±3	-	-	-	32±8	-	7±4	-	3±3
30	11±2	2±4	-	8±4	24±5	-	10±2	45±8	-	6±8	6±1	5±4
35	16±3	3±3	-	13±5	(4±1)x10^1	-	17±2	(7±2)x10^1	-	10±4	10±2	6±2
40	26±3	5±3	-	29±5	(6±2)x10^1	-	32±4	(11±2)x10^1	-	16±3	13±3	10±1
45	-	11±3	-	(8±4)x10^1	-	-	(6±1)x10^1	-	-	33±8	22±3	-

[1]Data acquired in 245 mM KCl, 5 mM $KHPO_4$, pH 6.8 in 10% ^2H_2O, 90% H_2O. The uncertainty represents the error in the fit of the data.

Table 4.2 Hydrogen exchange rate constants (s^{-1}) of the imino protons for the free and ligand-bound MN19 aptamer as a function of temperature.[1]

Temperature (°C)	Residues									
Free Aptamer	G4	T15	T18	T19	G24	T28	G29	G30	G31	T32
5	-	31±3	12±2	-	51±4	8±2	-	-	-	-
10	-	(6±2)x10^1	29±8	-	68±6	11±1	-	-	-	-
15	-	-	-	-	-	20±1	-	-	-	-
20	-	-	-	-	-	45±8	-	-	-	-
Cocaine-bound Aptamer	G4	T15	T18	T19	G24	T28	G29	G30	G31	T32
5	17±1	14.4±0.5	1±7	3±1	21.1±0.7	1±3	7.0±0.6	11.2±0.5	3±1	3±1
10	25±2	24±1	3±1	6±1	29.8±0.7	3±2	9.1±0.4	17.9±0.9	3±1	7.0±0.9
15	-	44±2	6.2±0.5	14±3	37±1	4.8±0.9	18±2	31±3	12.8±0.1	14±1
20	-	-	18±3	-	-	8.1±0.4	25±1	67±3	27±2	-
25	-	-	-	-	-	22±1	51±2	(13±2) x10^1	-	-
Quinine-bound Aptamer	G4	T15	T18	T19	G24	T28	G29	G30	G31	T32
5	10.1±0.5	17.9±0.7	1±2	-	37±2	-	14.8±0.5	16.9±0.8	1±5	2±2
10	17.2±0.8	33±2	1±1	-	55±3	-	23.6±0.7	24±1	1±3	3.2±0.8
15	30±2	58±3	2±2	-	-	-	36±2	40±2	3±1	6.2±0.5
20	-	-	5.9±0.6	-	-	-	62±4	67±4	7.0±0.3	16.1±0.7
25	-	-	23±2	-	-	-	(11±1) x10^1	(12±1)x10^1	21.2±0.7	39±5
30	-	-	-	-	-	-	-	-	(8±1)x10^1	-

[1]Data acquired in 245 mM KCl, 5 mM $KHPO_4$, pH 6.8 in 10% ^2H_2O, 90% H_2O. The uncertainty represents the error in the fit of the data.

Table 4.3 Hydrogen exchange rate constants (s^{-1}) of the imino protons for the free and ligand-bound MN4 aptamer as a function of temperature.[1]

Temperature (°C)	Residues								
Free Aptamer	G2	T15	T18	T19	T28	G29	G31	T32	G34
5	1±3	(5±1)x10[1]	12.9±0.9	-	-	72±7	4.6±0.7	9.9±0.9	-
10	4.0±0.6	(4±1)x10[1]	28±2	-	-	(13±3)x10[1]	4.5±0.4	1.9±0.7	-
15	4.6±0.7	-	38±4	-	4.0±0.6	(13±4)x10[1]	7.8±0.6	4.0±0.6	4.6±0.7
20	9±1	-	(9±1)10[1]	-	16.0±0.6	-	11.7±0.7	2±1	5±2
25	16±1	-	(12±4)x10[1]	-	33±1	-	20.9±0.9	1±1	8.6±0.6
30	34±2	-	-	-	(7±2)x10[1]	-	35±2	4.0±0.3	15.9±0.5
35	42±8	-	-	-	-	-	77±9	12.2±0.8	30±2
Cocaine-bound Aptamer	G2	T15	T18	T19	T28	G29	G31	T32	G34
5	3.4±0.6	(12±2)x10[1]	1.4±0.9	1±3	1.3±0.4	25±1	-	0.9±0.9	-
10	2.5±0.7	-	1.4±0.9	2.3±0.8	1.0±0.7	34±2	1±5	0.3±0.6	0.9±0.5
15	3.5±0.5	-	2.2±0.6	4.0±0.5	2.3±0.3	59±6	0±1	0.2±0.5	0.6±0.3
20	7.1±0.9	-	3.4±0.4	(1±2)x10[1]	4±1	(11±2)x10[1]	1.0±0.2	1.1±0.5	0.7±0.7
25	15±3	-	6±2	13±2	8±2	-	1.6±0.3	1.4±0.3	1.4±0.4
30	30±3	-	15±1	29±2	13.0±0.8	-	3.5±0.8	4±2	2.8±0.5
35	57±6	-	36±2	(6±1)x10[1]	-	-	6.6±0.6	-	4.3±0.6
40	-	-	(10±1)x10[1]	-	-	-	15±1	-	9.1±0.6
45	-	-	-				57±7	-	39±3
Quinine-bound Aptamer	G2	T15	T18	T19	T28	G29	G31	T32	G34
5	3±2	-	2±2	-	-	34±3	2±1	-	4±2
10	3±2	-	1±2	-	-	54±5	2±1	-	1±2
15	5±1	-	1±3	-	-	(9±1)x10[1]	1±1	-	2±1
20	9.4±0.9	-	2±2	-	-	(15±3)x10[1]	1±4	-	1±2
25	18.8±0.9	-	3±2	-	-	-	1±2	-	2±2
30	24±2	-	6±1	-	-	-	1±1	-	4±1
35	-	-	11±1	-	-	-	2±2	-	4±1
40	-	-	25±1	-	-	-	5±1	-	6.5±0.9
45	-	-	78±7	-	-	-	14.1±0.9	-	18±2

[1] Data acquired in 120 mM KCl, 100 mM $KHPO_4$, pH 6.8 in 10% ^1H_2O, 90% H_2O. The uncertainty represents the error in the fit of the data.

Table 4.4. Hydrogen exchange rate constants (s^{-1}) of the imino protons for the free and ligand-bound MN19 aptamer as a function of temperature.[1]

Temperature (°C)	Residues							
Free Aptamer	G4	T15	T18	T19	T28	G29	G31	T32
5	-	$(11 \pm 2)x10^1$	31 ± 3	-	9 ± 1	-	-	-
10	-	-	$(6 \pm 1)x10^1$	-	21 ± 2	-	-	-
15	-	-	-	-	43 ± 4	-	-	-
20	-	-	-	-	$(8 \pm 1)x10^1$	-	-	-
Cocaine-bound Aptamer	G4	T15	T18	T19	T28	G29	G31	T32
5	30 ± 3	-	1 ± 1	1 ± 6	2 ± 1	27 ± 2	3 ± 1	4 ± 1
10	44 ± 8	-	2 ± 1	3 ± 2	3 ± 1	35 ± 2	6 ± 1	9.6 ± 0.4
15	-	-	12 ± 3	14 ± 2	14 ± 4	57 ± 5	19 ± 1	37 ± 5
20	-	-	27 ± 4	33 ± 5	10 ± 2	49 ± 7	64 ± 8	-
25	-	-	-	-	32 ± 3	61 ± 9	-	-
Quinine-bound Aptamer	G4	T15	T18	T19	T28	G29	G31	T32
5	-	-	5 ± 1	-	-	35 ± 2	6 ± 2	2 ± 1
10	-	-	9 ± 1	-	-	52 ± 5	4 ± 1	2 ± 2
15	-	-	20 ± 1	-	-	80 ± 7	8 ± 1	3.7 ± 0.4
20	-	-	62 ± 4	18 ± 3	7.5 ± 0.4	$(15 \pm 3)x10^1$	26 ± 1	17 ± 1
25	-	-	-	-	24 ± 2	-	$(10 \pm 1)x10^1$	60 ± 8
30	-	-	-	-	83 ± 7	-	-	-

[1]Data acquired 120 mM KCl, 100 mM $KHPO_4$, pH 6.8 in 10% ^2H_2O, 90% H_2O. The uncertainty represents the error in the fit of the data.

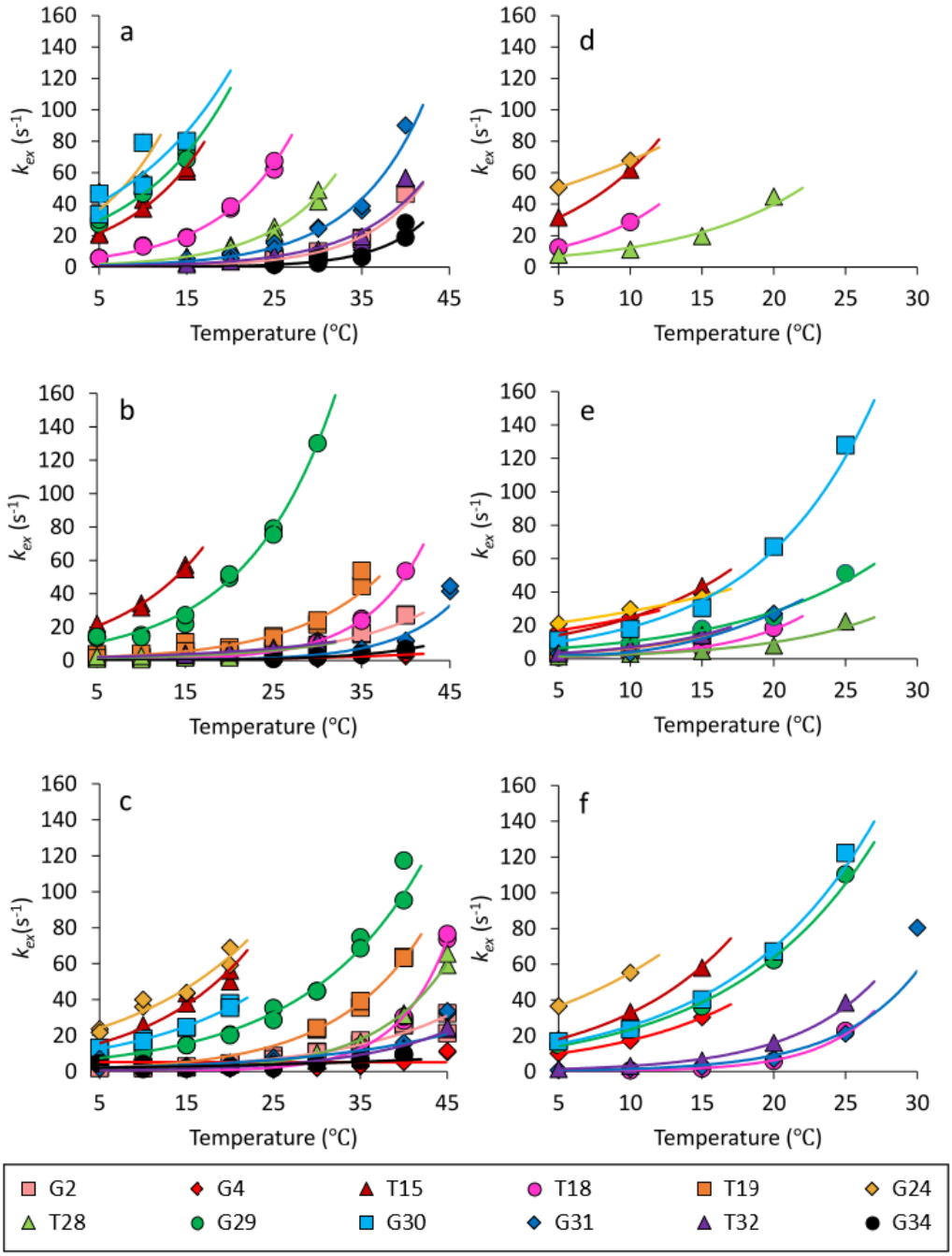

Figure 4.7: k_{ex} data as a function of temperature for MN4 (a) free, (b) cocaine-bound and (c) quinine bound and MN19 (d) free, (e) cocaine-bound and (f) quinine-bound. All data were acquired in 5 mM $KHPO_4$, 245 mM KCl, pH 6.8. The bases are shown in the following scheme: G2, pink squares; T4, red diamonds; T15, dark red triangles; T18, magenta circles; T19, orange squares; G24, yellow diamonds; T28, lime triangles; G29, green circles; G30, aqua squares; G31, blue diamonds; T32, purple triangles; and G34, black circles. Multiple points at the same temperature for the same nucleotide represent the results from independent analysis of the same dataset.

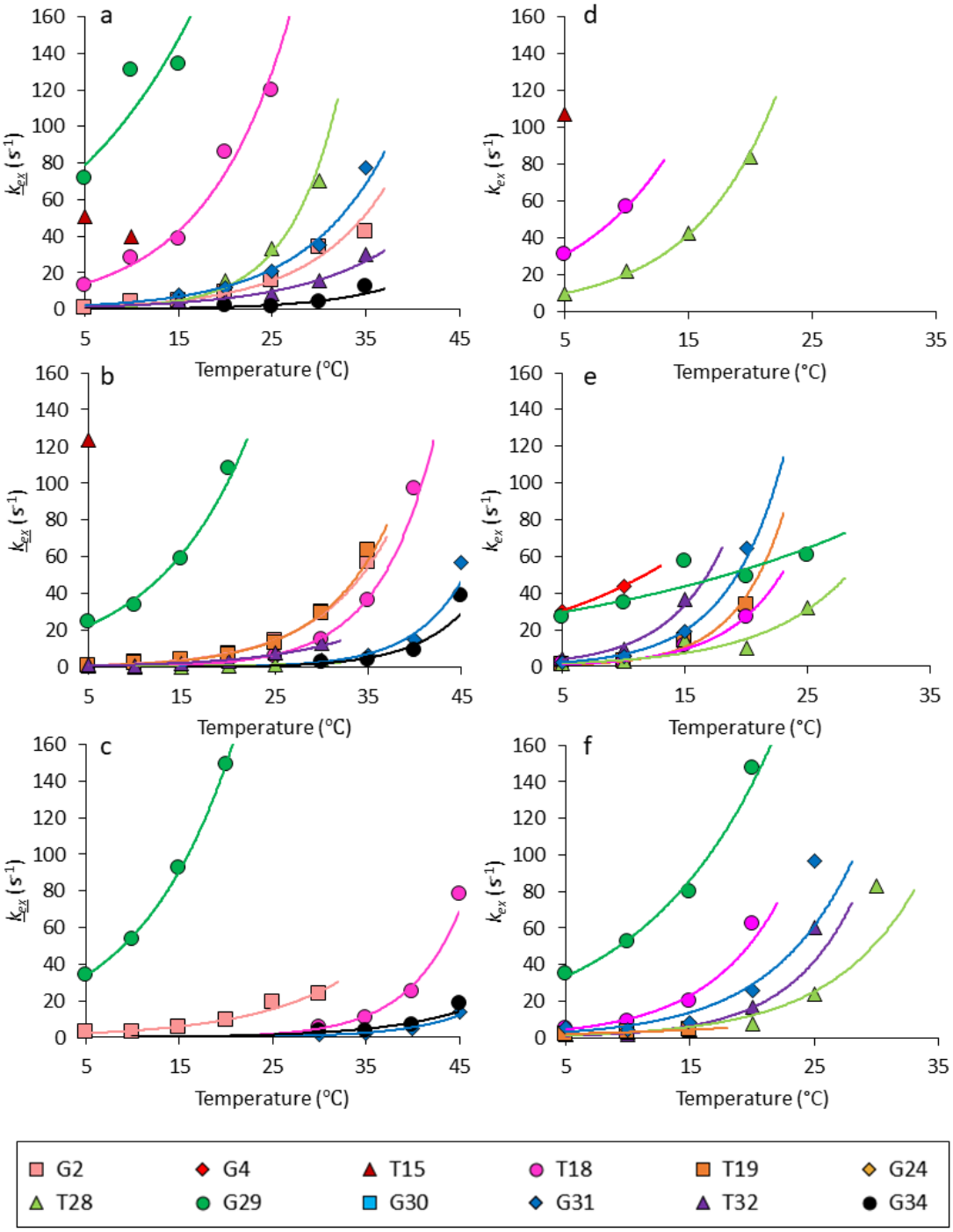

Figure 4.8: k_{ex} data as a function of temperature for MN4 (a) free, (b) cocaine-bound and (c) quinine bound and MN19 (d) free, (e) cocaine-bound and (f) quinine-bound. All data were acquired in 120 mM $KHPO_4$, 100 mM KCl, pH 6.8. The bases are shown in the following scheme: G2, pink squares; T4, red diamonds; T15, dark red triangles; T18, magenta circles; T19, orange squares; G24, yellow diamonds; T28, lime triangles; G29, green circles; G30, aqua squares; G31, blue diamonds; T32, purple triangles; and G34, black circles. Multiple points at the same temperature for the same nucleotide represent the results from independent analysis of the same dataset.

4.3.2 Entropy and Enthalpy of base pair dissociation. Imino ^{1}H k_{ex} values for free, cocaine-bound, and quinine-bound MN4 and MN19 were measured at different temperatures and in both high catalyst concentration and low catalyst concentration buffers in order to calculate the enthalpy (ΔH_{diss}), entropy (ΔS_{diss}) and the free energy (ΔG_{diss}) of base pair opening by fitting these data directly to the Eyring equation [78]. Data are presented in Table 4.5 for MN4 and Table 4.6 for MN19 and plotted in Fig. 4.9 for MN4 and Figure 4.10 for MN19.

Table 4.5. Calculated enthalpy (J mol^{-1}), entropy (J mol^{-1} ^{o}K^{-1}) and free energy at 15 ^{o}C (J mol^{-1}) of dissociation for bases in MN4. [1]

		Residues							
		G2	T18	T19	T28	G29	G31	T32	G34
Free Aptamer	ΔH_{diss} (x10^4)	12±2	12±1	-	11±2	10±2	8.4±0.8	19±2	21±5
	ΔS_{diss} (x10^1)	15±7	18±4	-	14±6	13±5	5.4±3	40±7	45±17
	ΔG_{diss} (x10^3)	75±2	65.0±0.2	-	68.3±0.8	61.4±0.2	68.8±0.4	77.8±0.2	84±3
Cocaine -bound	ΔH_{diss} (x10^4)	12±2	13.9±0.3	12±2	25±1	9.6±0.8	23±1	17±9	13.9±0.6
	ΔS_{diss} (x10^1)	17±5	21±1	16±5	57±5	11±3	51±4	32±31	19±2
	ΔG_{diss} (x10^3)	74±1	77.6±0.3	74±1	83.6±0.7	64.0±0.4	85±1	78±4	83.9±0.4
Quinine-bound	ΔH_{diss} (x10^4)	7.0±0.8	16.7±0.5	-	-	9.7±0.9	14±6	-	7.6±0.4
	ΔS_{diss} (x10^1)	0±3	31±2	-	-	11±3	13±2	-	4.1±0.2
	ΔG_{diss} (x10^3)	69.6±0.7	78.2±0.5	-	-	64.0±0.4	77±4	-	75.9±0.3

[1]The uncertainty represents the error in the fit of the data in ΔH_{diss} and ΔS_{diss} and is propagated to ΔG_{diss} by calculating the quadrature of the errors and adjusting for covariance.

Table 4.6. Calculated enthalpy (J mol^{-1}), entropy (J mol^{-1} $^\circ$K^{-1}) and free energy at 15 °C (J mol^{-1}) of dissociation for bases in MN19[1].

		Residues				
		T18	T28	G29	G31	T32
Free Aptamer	ΔH_{diss} (x10^4)	-	14.3±0.1	-	-	-
	ΔS_{diss} (x10^1)	-	27.4±0.3	-	-	-
	ΔG_{diss} (x10^3)	-	64.28±0.01	-	-	-
Cocaine-bound	ΔH_{diss} (x10^4)	16±1	16±2	10.3±0.8	11±1	-
	ΔS_{diss} (x10^1)	31±4	31±8	13±3	17±4	-
	ΔG_{diss} (x10^3)	66.6±0.2	69.7±0.8	65.0±0.2	64.6±0.1	-
Quinine-bound	ΔH_{diss} (x10^4)	19.8±0.4	-	8.54±0.06	20.02±0.08	12.8±0.6
	ΔS_{diss} (x10^1)	44±1	-	8.0±0.2	45.1±0.3	21±2
	ΔG_{diss} (x10^3)	69.8±0.1	-	62.33±0.02	70.40±0.04	68.7±0.2

[1]The uncertainty represents the error in the fit of ΔH_{diss} and ΔS_{diss} and is propagated to ΔG_{diss} by calculating the quadrature of the errors and adjusting for covariance.

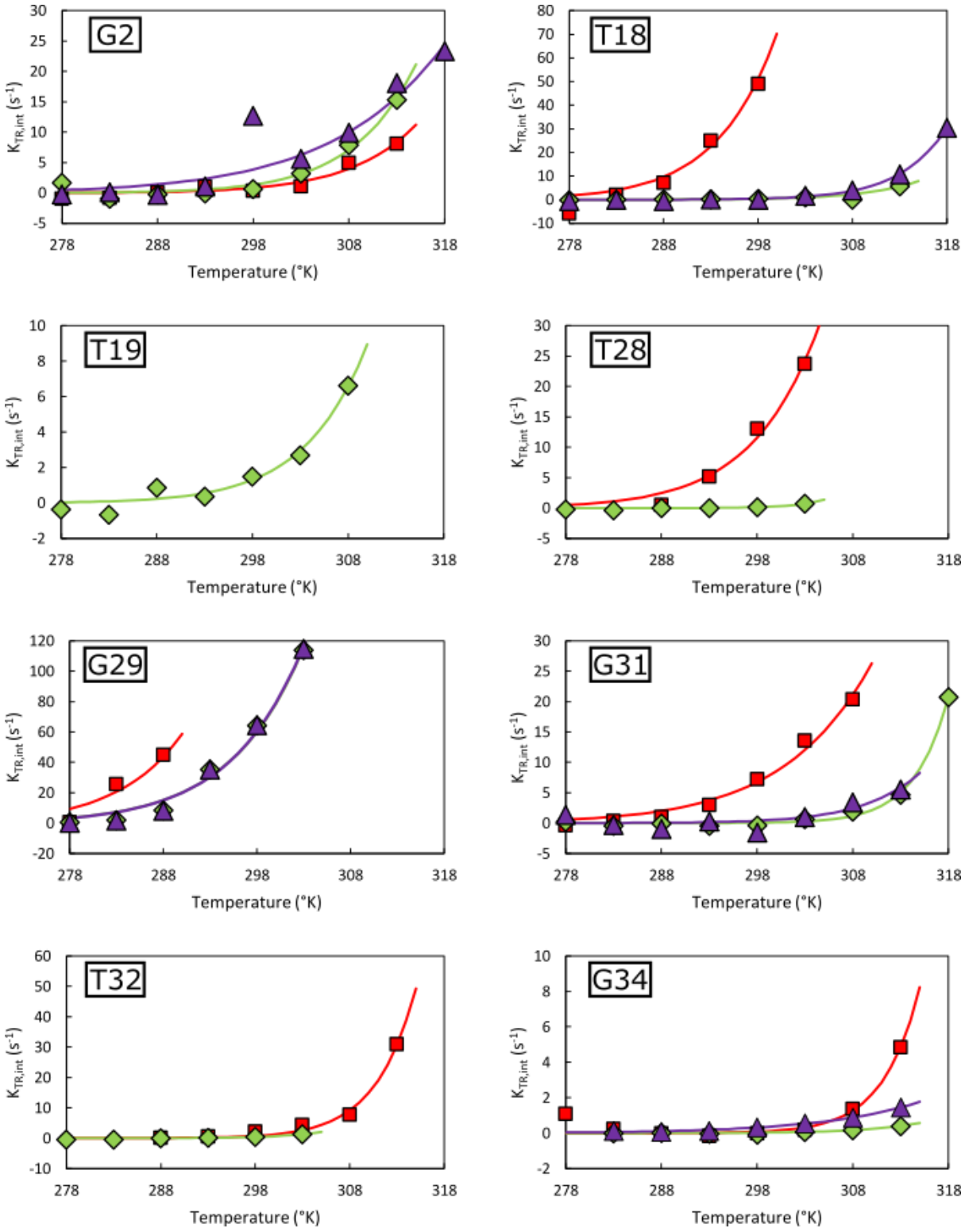

Figure 4.9: Plot of the exchange rate for G2, T18, T19, T28, G29, G31, T32, and G34 in MN4 to the Eyring equation. The free aptamer is shown with red squares, the cocaine-bound aptamer is shown with green diamonds, and the quinine-bound aptamer is shown with purple triangles.

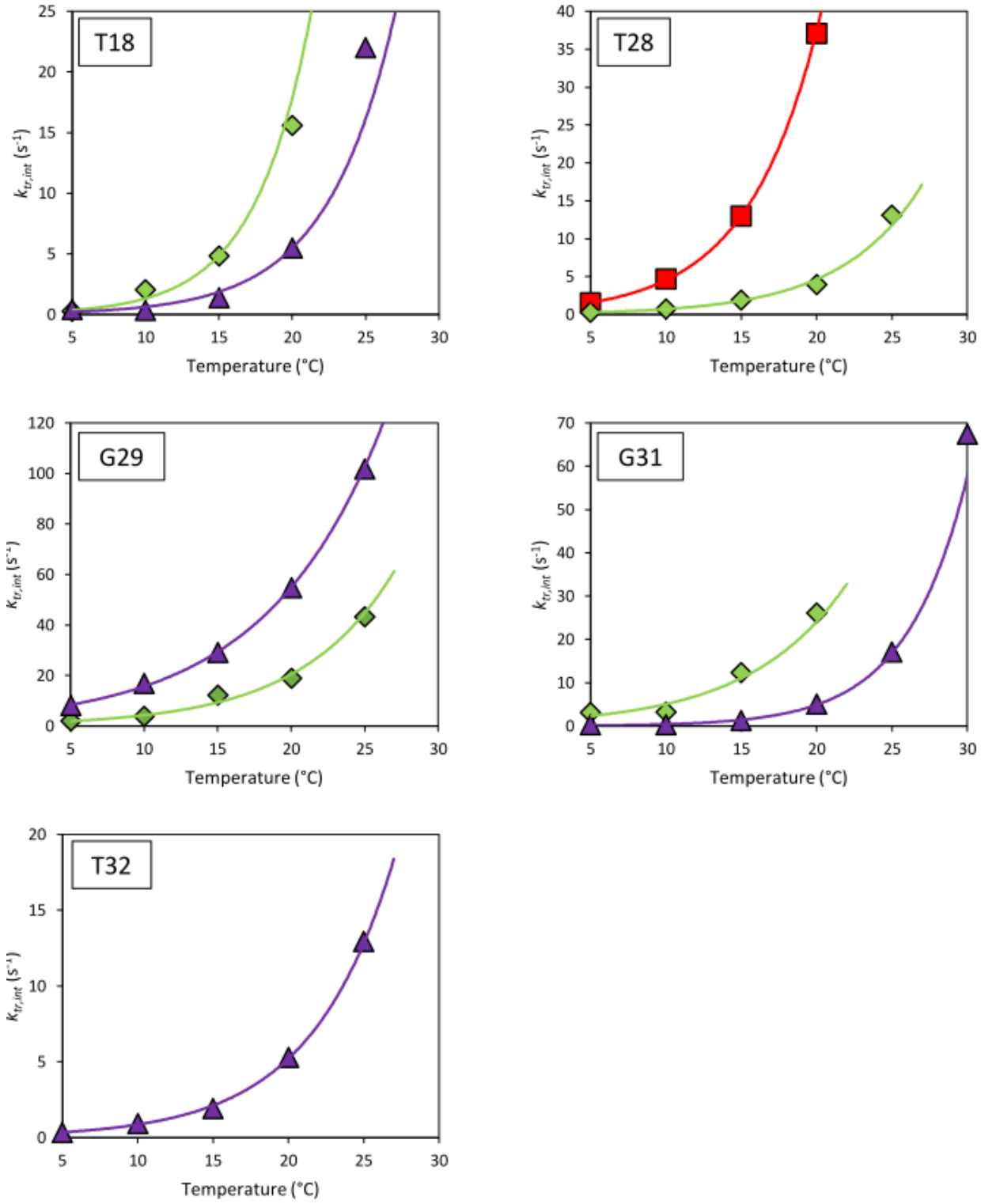

Figure 4.10. Eyring plots for T18, T28, G29, G31, and T32 in MN19 in the free, cocaine-bound, and quinine bound aptamers. The free aptamer is shown with red squares, the cocaine-bound aptamer is shown with green diamonds, and the quinine-bound aptamer is shown with purple triangles.

The values of ΔH_{diss} and ΔS_{diss} (Table 4.5) vary among the different bases in the free and ligand-bound forms of MN4 with ΔH_{diss} values ranging from 70 to 250 kJ mol^{-1} and ΔS_{diss} values ranging from 0 to 570 J mol^{-1} $^{o}K^{-1}$. The values of ΔH_{diss} and ΔS_{diss} (Table 4.6) in free and ligand-bound forms of MN19 also vary among the different bases. The ΔH_{diss} range from 85.4 to 200.2 kJ mol^{-1} and the S_{diss} values range from 80 to 274 2 kJ mol^{-1} . The ΔH_{diss} and ΔS_{diss} values appear to be linearly correlated (Fig. 4.11 for MN4 and Figure 4.12 for MN19) as also observed in previous studies using this method [77], [78], [116].

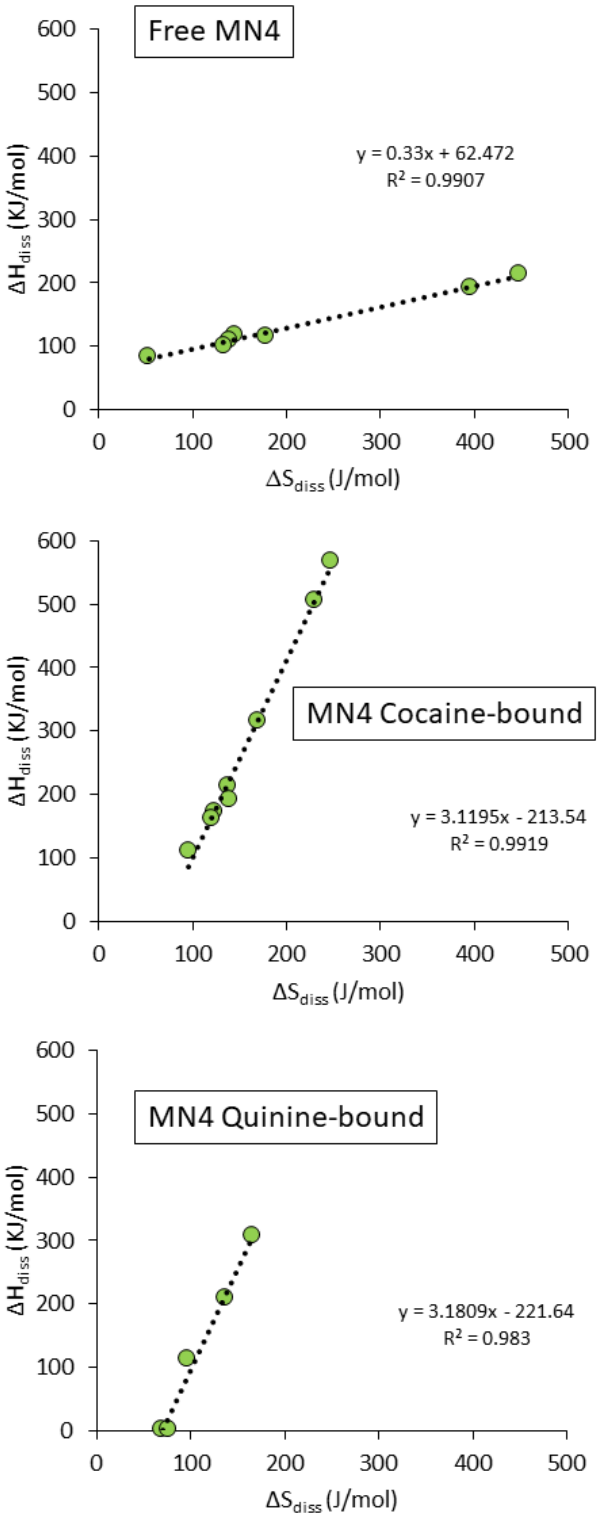

Figure 4.11. Entropy-Enthalpy correlations plots of ΔS_{diss} and ΔH_{diss} of bases in MN4 free, cocaine-bound, and quinine-bound. ΔS_{diss} and ΔH_{diss} terms were generated from k_{ex} data acquired in high and low catalyst concentration buffer. Plots were fit to the linear equation y=mx+b, and fit results are shown on the plots.

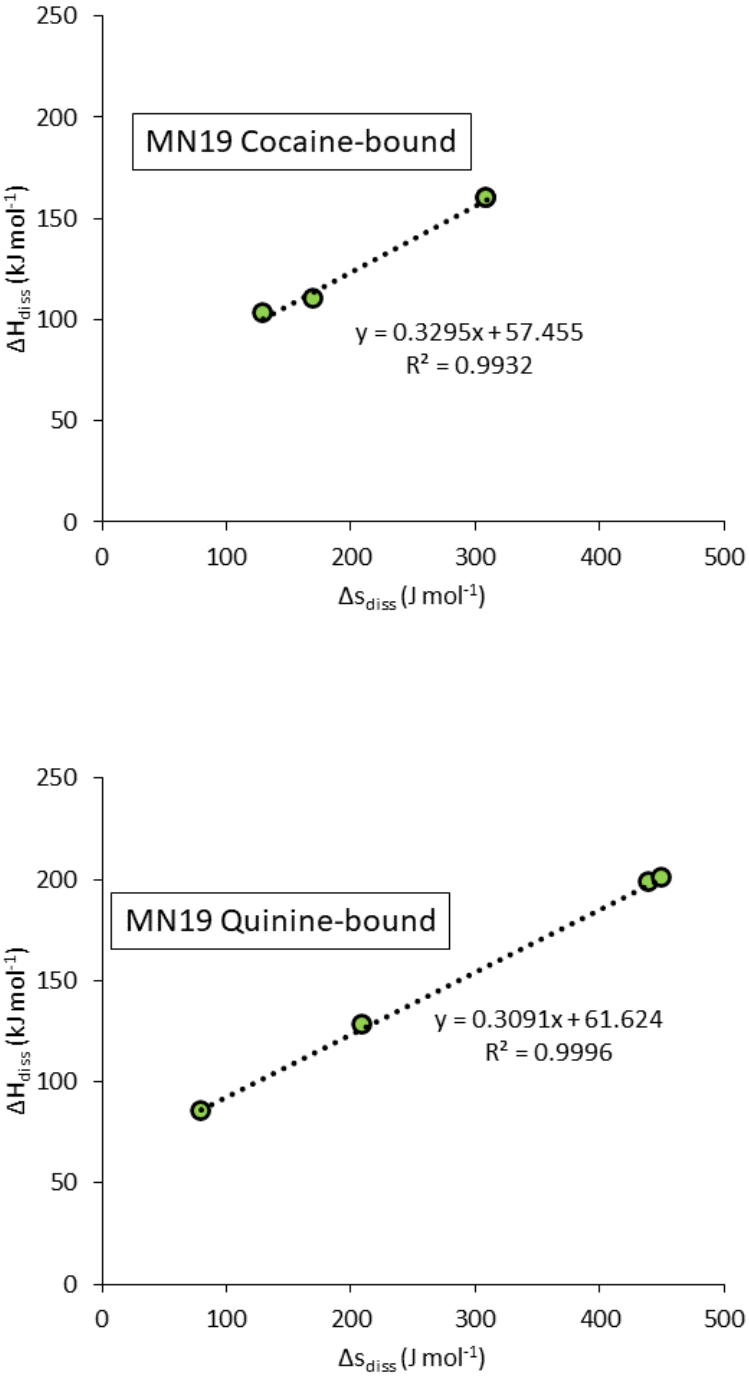

Figure 4.12. Entropy-Enthalpy correlations plots of ΔS_{diss} and ΔH_{diss} of bases in MN19 cocaine-bound, and quinine-bound. ΔS_{diss} and ΔH_{diss} terms were generated from k_{ex} data acquired in high and low catalyst concentration buffer. Plots were fit to the linear equation y=mx+b, and fit results are shown on the plots.

The ΔG_{diss} values are presented in Table 4.4 and 4.5 and range from 61.4 to 85 kJ mol^{-1} for MN4 and range from 64.28 to 70.40 kJ mol^{-1} for MN19. For free MN4 the largest ΔG_{diss} values,

corresponding to the strongest base pairs, belong to the Watson-Crick GC base pair G34 followed by the Watson-Crick AT base pair T32. For the cocaine-bound MN4 the largest ΔG_{diss} value belongs to G31 followed by G34. For quinine-bound MN4, the largest ΔG_{diss} value belongs to the Watson-Crick AT base pair T18. In all three forms of MN4, the lowest measured ΔG_{diss} value, indicating the weakest base pair, belongs to G29, a nucleotide that is in a non-Watson-Crick AG base pair.

Upon ligand binding there is a uniform trend among the ΔG_{diss} values where the base pairs closest to the ligand binding site (T18, T28, G29, G31 and T32; Fig. 4.1) become larger, indicating they become stronger. For the base pairs furthest from the ligand-binding site (G2, G34) their ΔG_{diss} values decrease, indicating these base pairs are weaker when the aptamer is ligand bound. The $\Delta\Delta G_{diss}$ values between bound and free MN4 are tabulated in Table 4.6. No clear trend seems to exist in changes in ΔH_{diss} and ΔS_{diss} values with ligand binding among the different bases in MN4. This is exemplified by G31 where ΔH_{diss} and ΔS_{diss} increase for cocaine and quinine binding while for T18 ΔH_{diss} and ΔS_{diss} change much less (Table 4.4). A similar analysis of the $\Delta\Delta G_{diss}$ values for MN19 was not possible. T28 was the only resonance that produced a ΔG_{diss} value, and it can only be compared with the cocaine-bound ΔG_{diss} as T28 was not analyzable in the quinine-bound MN19.

Table 4.7 Difference in calculated free energy of dissociation (kJ mol^{-1}) between free and ligand-bound bases in MN4 at 15 °C.

		Residues						
		G2	T18	T28	G29	G31	T32	G34
Cocaine binding	$\Delta\Delta G_{diss}$	-0.9±2	12.6±0.4	15±1	2.5±0.4	16±1	1±5	0±3
Quinine binding	$\Delta\Delta G_{diss}$	-6±2	13.2±0.6	-	2.6±0.4	9±4	-	-8±3

4.4 Discussion

The hydrogen exchange rates of the imino protons in the MN4 aptamer correspond to their placement within the helices in the aptamer with residues at the ends having higher k_{ex} values than residues in the middle of stems. For example, G2 and G34, which are located in the middle of stem 1 (Fig. 1), have low k_{ex} values of (3 ± 2) s^{-1} and (3 ± 1) s^{-1}, respectively, at 10 ºC in the free MN4 aptamer, while T18 and T15, located at the edges of stem 2, have higher k_{ex} values of (13 ± 2) s^{-1} and (40 ± 4) s^{-1} respectively at the same temperature in the free MN4 aptamer (Table 4.1). G29 and G30, the A-G mismatches at the core of the aptamer, have high k_{ex} values of (50 ± 6) s^{-1} and (65 ± 8) s^{-1} at 10 °C in the free MN4 aptamer. These trends match data reported in the previous chapter as well as data from reports from other groups [75], [76], [116].

The NMR data presented here on free MN19 gives new insights into the nature of the structure of the unbound MN19 aptamer. Free MN19 is thought to be loosely structured and is predicted to undergo ligand-induced folding [103]. In the ^{1}H NMR of free MN19 acquired here, in the presence of low catalyst concentration buffer (245 mM KCl, 5 mM $KHPO_4$, pH 6.8), more resonances for free MN19 were observed than seen in the previous chapter (Fig. 4.2 d). The imino protons of T18, T28, T15, and G24 all had observable signals, as well as a group of overlapped signals from G9, G10 and G27. There were no observable signals from residues in stem 1 or the two AG base pairs. This demonstrates that in free MN19, stem 2 and 3 are structured and it is stem 1 and the AG base pairs that become structured with ligand binding. This is in agreement with the model proposed by Sigurdsson and coworkers [117].

k_{ex} values for imino proton in the free MN19 aptamer (Table 4.2 and 4.4; Fig. 4.7 d-f and 4.8 d-f). For all the nucleotides the were measured and are in both free MN4 and free MN19 (T15, T18, G24, T28), these nucleotides have higher k_{ex} values at the same temperature in MN19.

Additionally, the imino proton NMR signal disappears at lower temperatures in free MN19 compared with free MN4 (Fig. 4.7 and 4.8). This implies that the folded regions of the unbound MN19 aptamer are more dynamic than the same regions in free MN4. Again, this is consistent with MN19 undergoing ligand-induced folding starting from a partially unfolded or flexible state. Increasing the temperature increases the k_{ex} values of imino protons in all forms of both MN4 and MN19, but the rate of increase depends on the position of the nucleotide within the aptamer. Residues buried within the aptamer, or stabilized by interactions with the ligand, increase their k_{ex} values more slowly than those found on the periphery of the aptamer (Fig. 4.13). For example, in cocaine-bound MN4, G2, located near the end of stem 1, increased from $(4 \pm 3)\ s^{-1}$ at 5 °C to $(27 \pm 2)\ s^{-1}$ at 40 °C, while G4, which is located further into stem 1, remains fairly constant with a k_{ex} value of $(4 \pm 1)\ s^{-1}$ at 5 °C and a k_{ex} value of $(3 \pm 2)\ s^{-1}$ at 40 °C. T15 and T18 are located at opposite ends of stem 2, with T18 being located close to the ligand-binding site. Here, T15 increases from $(21 \pm 2)\ s^{-1}$ at 5 °C to $(6 \pm 1) \times 10^{1}\ s^{-1}$ at 15 °C in the cocaine-bound MN4 aptamer. This residue is not seen in higher temperature data sets as it exchanges with the solvent too quickly to be observed. T18 however, has a k_{ex} value of $(1 \pm 3)\ s^{-1}$ at 5 °C and remains fairly constant at 15 °C with a value of $(3 \pm 3)\ s^{-1}$ and does not match the exchange rate of T15 at 15°C until T18 reaches 40 °C where it has a k_{ex} value of $(54 \pm 6)\ s^{-1}$. This non-uniform increase in k_{ex} values as temperature increases is consistent with what was seen previously in the hsp17 RNA thermometer [116].

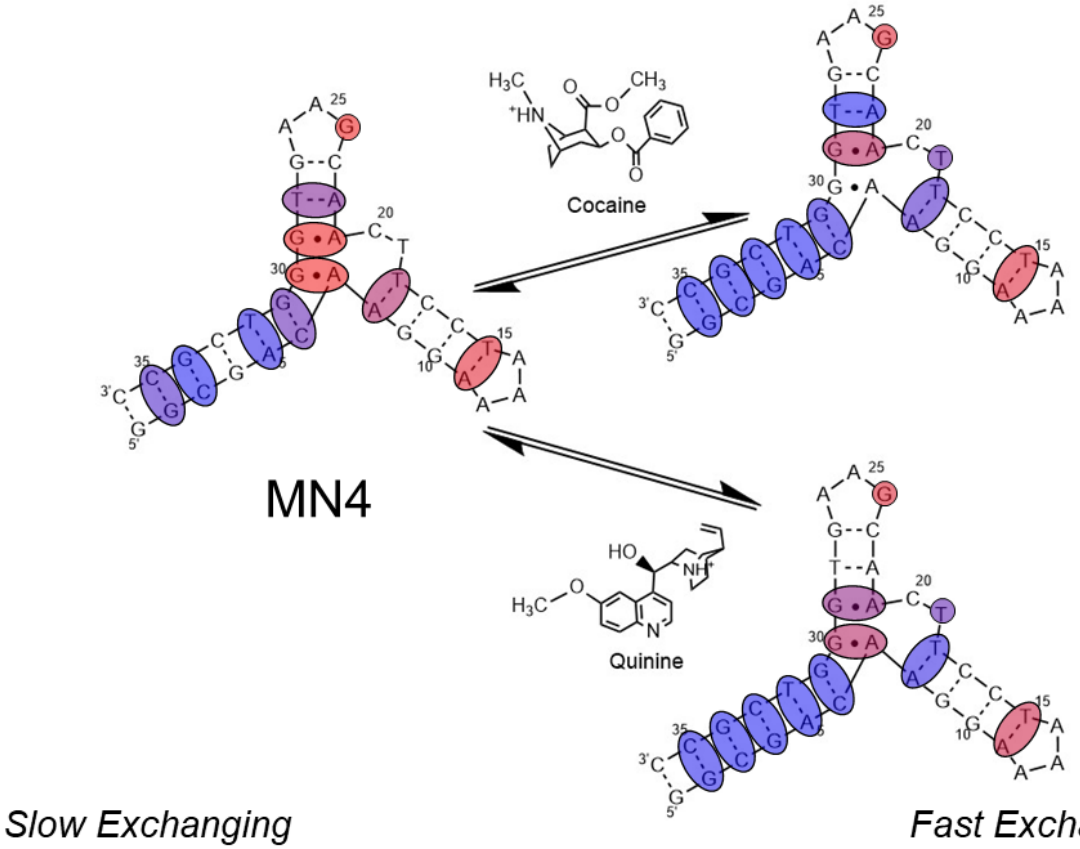
Cocaine
MN4
Quinine
Slow Exchanging
Fast Exchanging

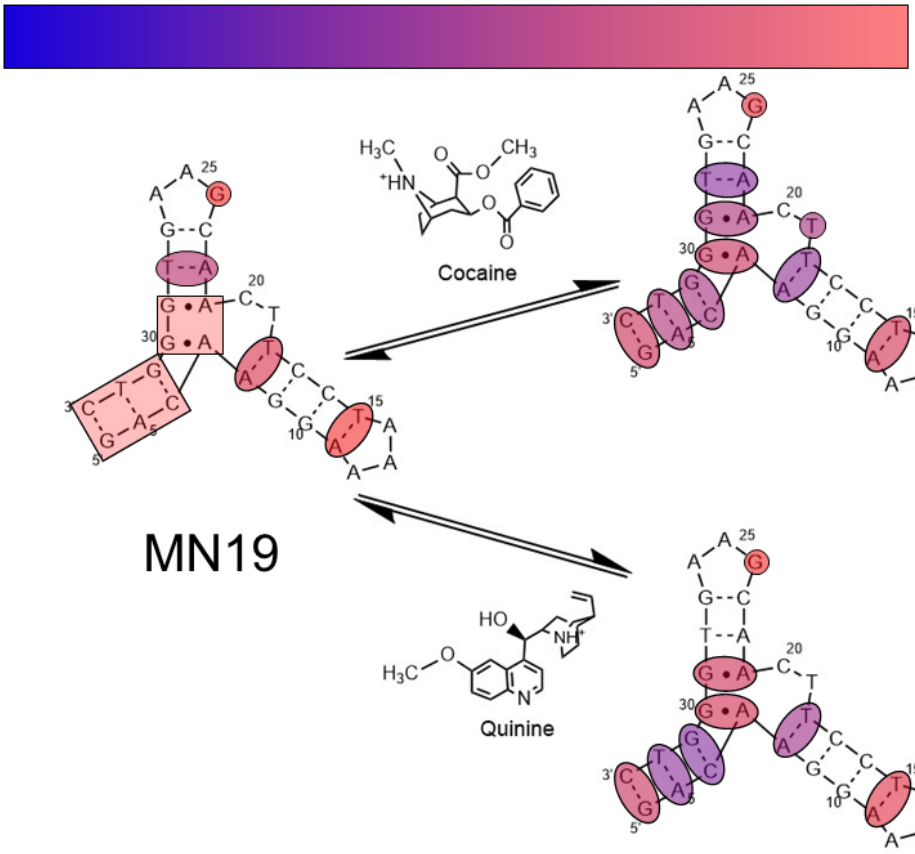
Cocaine
MN19
Quinine

Figure 4.13 (previous page) Secondary structure diagram of MN4 and MN19 highlighting the dynamics of the free, cocaine-bound, and quinine-bound aptamers. Base pairs are shaded on a scale of red to purple to blue, depending on what temperature the imino proton in that base pair reached a k_{ex} value of 40 s^{-1} based on the fit line of the k_{ex} values (Fig. 4). Bases that started with a k_{ex} value of 40 s^{-1} or higher at 5 °C, were shaded 100% red (255 red, on an RGB scale). Bases that do not reach a k_{ex} value of 40 s^{-1} at 45 °C, were shaded 100% blue (255 blue, on an RGB scale). Other bases were shaded purple (shaded so that the sum of the red and blue sliders on a RGB scale was 255), depending on when the k_{ex} value for its imino proton reached a value of 40 s^{-1}. Imino protons that reached that value at a lower temperature are shaded darker red, and imino protons that reached that value at higher temperatures are shaded darker blue. Bases that are shaded in a pale red box are unobserved in the free NMN19 due to rapid exchange.

The addition of ligand reduced the exchange rate constants of imino protons close to the binding site, but it has little effect on resonances distant from the binding site. For example, G29 is located at the binding site of the aptamer, its k_{ex} value reduces from (50 ± 6) s^{-1} in the free state of MN4 at 10 °C to 15 ± 1 s^{-1} in the cocaine-bound MN4 aptamer also at 10 °C, and 12 ± 2 s^{-1} in the quinine-bound MN4 aptamer at the same temperature. Other resonances such as T15 and G34, which are far removed from the binding site, differ little in their k_{ex} values, with (40 ± 4) s^{-1} and (4 ± 1) s^{-1} respectively in the free state of MN4 at 10 °C, (33 ± 3) s^{-1} and (2 ± 2) s^{-1} respectively in the cocaine-bound MN4 at 10 °C, and (25 ± 3) s^{-1} and (3 ± 3) s^{-1} respectively in the quinine-bound MN4 at 10 °C. This demonstrates that the changes in dynamics observed in MN4 at the time scale monitored by k_{ex} values are localized to the binding site and are not felt globally throughout the molecule.

When comparing quinine and cocaine-bound MN4, experiments by both the Johnson lab and outside groups have shown that quinine binds approximately 50 fold tighter than cocaine [54], [73], [100], [104], [118]– [120]. When looking at the k_{ex} values of quinine and cocaine-bound MN4 there is generally little to no observable difference between these two bound aptamers at low temperatures. As the temperature increases, the k_{ex} values of some nucleotides (T15, T18, G29) in the tighter binding quinine sample do not increase as fast as in the cocaine-bound sample. In the

quinine-bound MN4 ^{1}H NMR spectra there are more peaks visible at higher temperatures than seen in the cocaine-bound spectrum (Fig. 4.5 and 4.6). This demonstrates that the tighter binding ligand does not result in significantly decreased k_{ex} values until the sample is at temperatures approaching where its ^{1}H NMR signal disappears.

At 5 °C the k_{ex} values for residues in bound MN19 have similar values as in bound MN4 (Tables 4.1 and 4.2). However, where these two ligand-bound aptamers differ is that as the temperature increases, the k_{ex} values increase more rapidly in MN19 and their peaks in the NMR data disappear sooner in MN19 than in MN4. This observation is consistent with both the cocaine- and quinine-bound forms of MN19 being a more dynamic version of the cocaine-binding aptamer and undergoing a structure switching binding mechanism. It is also consistent with ligand-bound MN19 being less thermally stable than ligand-bound MN4 [17], [58], [94], [102]–[104], [121]. For example at 5 °C in the cocaine-bound aptamers, T15 has a k_{ex} of (14.4 ± 0.5) s^{-1} in MN19 and a k_{ex} value of (21 ± 2) s^{-1} in MN4, T28 has a k_{ex} of (1 ± 3) s^{-1} in MN19 and a k_{ex} of (2 ± 2) s^{-1} in MN4, and G29 has a k_{ex} of (7.0 ± 0.6) s^{-1} in MN19 and a k_{ex} of (14 ± 2) s^{-1} in MN4. What does differ is that residues in MN19 disappear faster than their counterparts in MN4. For the cocaine-bound aptamers, T18 disappears after 20 °C in MN19 compared with 40 °C in MN4. T19 disappears after 15 °C in MN19 compared with 35 °C in MN4, and G31 disappears after 20 °C in MN19 versus 45 °C in MN4 (Tables 4.1 and 4.2; Fig. 4.7).

Ligand binding by aptamers is generally thought to result in aptamers becoming more structured, which should result in a reduction of motion or dynamics in the aptamer [113], [122]. Previous imino ^{1}H exchange rate studies on the $VEGF_{165}$-targeting aptamer (Macugen) and the AMP-RNA aptamer both show a large reduction in dynamics upon binding at the ligand binding site, which in both these aptamers is a loop or bulge region that is unstructured in the free state

[75], [87]. In this study, for both MN4 and MN19, there is a reduction in k_{ex} values at the ligand-binding site upon cocaine and quinine binding. This might be expected for MN19 where signals from stem 1 are not observed in the free aptamer and only appear in the ligand-MN19 complex. For MN4, the base pairs in this aptamer are formed in the free state, and this aptamer also shows a reduction in dynamics upon ligand binding. This demonstrates that even aptamers with no large-scale change in base pairing have reduced dynamics with ligand binding and suggest this may be a general feature of aptamer function and does not depend on the formation of new base pairs with ligand binding.

The observation that in MN4 the base pairs close to the ligand-binding site strengthen with both cocaine and quinine binding complements the reduction in dynamics, as indicated by reduced k_{ex} values. Together, these data lead to a binding model for MN4 where both cocaine and quinine addition leads to a reduction of dynamics and base pair strengthening near the binding site, despite the base pairs in this aptamer being pre-formed. It is a possibility that a strengthening of base pairs upon ligand binding is a common trait in aptamers but will require further studies to confirm.

4.5 Concluding Remarks

k_{ex} values were measured for the imino protons in MN4 and MN19 in their free, cocaine-bound, and quinine-bound states as a function of temperature. In addition, from data acquired in two different buffers, the $\Delta H_{diss,}$ ΔS_{diss} and ΔG_{diss} values for base pair dissociation in MN4 were also determined. For MN19, with ligand binding a reduction in k_{ex} values of iminos both near the binding site and in stem 1 was observed. This is consistent with its ligand induced-folding mechanism where stem 1 folds or becomes more rigid with ligand binding. In MN4, upon ligand binding, a localized reduction of k_{ex} values for imino protons near the binding site was observed, but not this did not occur elsewhere in the aptamer. Additionally, from the ΔG_{diss} values, base pairs

near the ligand-binding site in MN4 strengthened with both cocaine and quinine binding. This means that both a pre-folded aptamer and an aptamer loosely folded in the free state undergo a reduction in dynamics upon ligand binding.

Chapter 5: **Characterization and Dynamics Study of the Ochratoxin A-binding aptamer via ^{1}H-NMR**

5.1 Introduction

Ochratoxin A is common food contaminating mycotoxin produced by certain *penicillium* and *aspergillus* fungi [123]. These fungi can also produce ochratoxins B and C, but ochratoxin A is the most widely produced and well-studied toxin of the three. It is chemically stable and often found in pork and grain, but can also be found in coffee, wine, and dried fruits [124]. Due to its stability, ochratoxin A can survive processing and make its way to consumers [123]. Ochratoxin A mainly effects the kidneys but can also cause damage to the liver, brain, immune system, and has been shown to be carcinogenic in animals [125]. Ochratoxin A exposure can cause Focal Segmental Glomerulosclerosis (FSGS) in kidneys [126]. FSGS causes a scarring in the kidneys and leads to significant protein lose through the urine. This damage cannot be repaired and in severe cases people may have to undergo kidney transplants. Ochratoxin A has been shown the be ability to cross from mother to offspring through the placenta in animal studies, and additionally ochratoxin A has been found in breast milk [127]– [129]. In mouse studies, ochratoxin A was shown to cause oxidative damage to the brain, and *in vitro* studies of ochratoxin A showed that neuron cells incubated with ochratoxin A were damaged in a dose dependent manner. Ochratoxin A has a tolerable dose of 5 ng/kg per day or ~300 ng per day in the average adult so even small amounts of ochratoxin A in food can have an impact on health [125]. Canada does not actively test for ochratoxin A, but a survey of grain products in Canadians cities from 2018-2019 showed 99.8% of samples contained less than the 3 ppb of ochratoxin A which is the limit for ochratoxin A in food products [130]. However, 45% of samples tested did contain some level of ochratoxin A. Europe does actively test for ochratoxin A. A 2002 EU report testing the amount of ochratoxin A

in various grain found that only ~0.95% of samples tested were above the 5 ppb limit for ochratoxin A [131]. Testing for ochratoxin A is currently done using an ELISA based assay.

A number of DNA aptamers that bind to ochratoxin A were selected by Cruz-Aguado and Penner in 2008 [132]. Their goal was to obtain an aptamer that binds selectively to ochratoxin A, while not binding to other structurally related compounds such as N-acetylphenylalanine or warfarin. According to initial results, the aptamer generated bound ochratoxin A with a K_d of 0.36 μM. The same aptamer also bound ochratoxin B ~100 times weaker than its intended ligand, with the difference between these two molecules being 1 chlorine group. The authors also noted that the aptamer's ability to bind ochratoxin A was dependent on the presence of divalent cations, with magnesium and calcium being tested. The authors believed that the ochratoxin A was forming a complex with the ion neutralizing the negative charge of the ligand, by neutralizing this charge the aptamer is more easily able to bind ochratoxin A. They also showed that the presence of calcium induced strong aptamer-ligand association, and that the presence of the monovalent cations sodium and potassium did not increase binding strength in the same way.

In 2012, Penner and colleagues were able to use this aptamer as the basis for an ochratoxin A sensor and able to analytically detect the presence of ochratoxin A in wheat samples [133]. This was done using time-resolved fluorescence (TRF) spectroscopy and tracking the interaction between an ochratoxin A-terbium complex. Wheat samples were extracted using an acetonitrile/water extraction solvent and passed through an aptamer-affinity column to capture the ochratoxin A. Ochratoxin A was eluted from the column, then the samples were measured using TRF spectroscopy. This was done for 29 wheat samples, with varying ochratoxin A concentrations, and the measured amount of ochratoxin A was consistent with the amount measured using HPLC-fluorescence methods. This method had a detection limit of 0.5 μg/kg which is far below the EU

regulatory limit for ochratoxin A. As in the 2008 paper, this detection system was much less sensitive to ochratoxin B and did not provide false positives from structurally related compounds [132], [133].

Penner and colleagues were not the only scientists that used this aptamer to create ochratoxin sensing platforms. In 2021 Xie and colleagues used the aptamer to create a "one-pot" affinity column using polymerization of the aptamer to the column initiated by UV light [134]. They showed this method was still able to detect ochratoxin A, even in samples containing the related compound ochratoxin B. Shuang *et al*. used this aptamer to build a label free aptasensor using electrochemical detection methods, with the goal of being able to detect ochratoxin A in wine [135]. The scientists immobilized particles with the conjugated aptamer to a graphene surface electrode. The binding of ochratoxin A to the aptamers of the surface of the particles impedes the electron transfer of the electrode, which changed as a function of the amount of ochratoxin A in the sample. He and colleagues used the aptamer to create a colourmetric sensor for the detection of ochratoxin A [136]. The aptamer was conjugated to gold nanorods, and when the aptamer was bound to ochratoxin A this caused a blueshift of the gold nanorod surface that was visible in solution to the eye.

In 2017, the Manderville lab at the University of Guelph released a paper characterizing the main aptamer from Penner and Cruz-Aguado [137]. They studied a truncated version of the ochratoxin A binding aptamer that was the minimum binding core sequence from the previous paper. Using a combination of fluorescence techniques and CD spectroscopy it was discovered that the aptamer was a two tetrad G-quadruplex, with 3 lateral loops, and an anti-parallel backbone. More specifically, they also determined which guanine bases in the aptamer sequence made up the G-quadruplex, along with the syn/anti configuration of those bases. This was done by using a set

of aptamers each containing an 8-thienyl-2'dG (ThdG) base in place of one of the guanines, and then using UV-Vis spectroscopy to tracking the melting temperature of the resulting sample and comparing it with the melting temperature of the wild type aptamer. They were also able to use the intrinsic fluorescence of the ochratoxin A to track its binding to the aptamer. The structure of the aptamer based on this data, along with the structure of ochratoxin A can be found in Figure 5.1

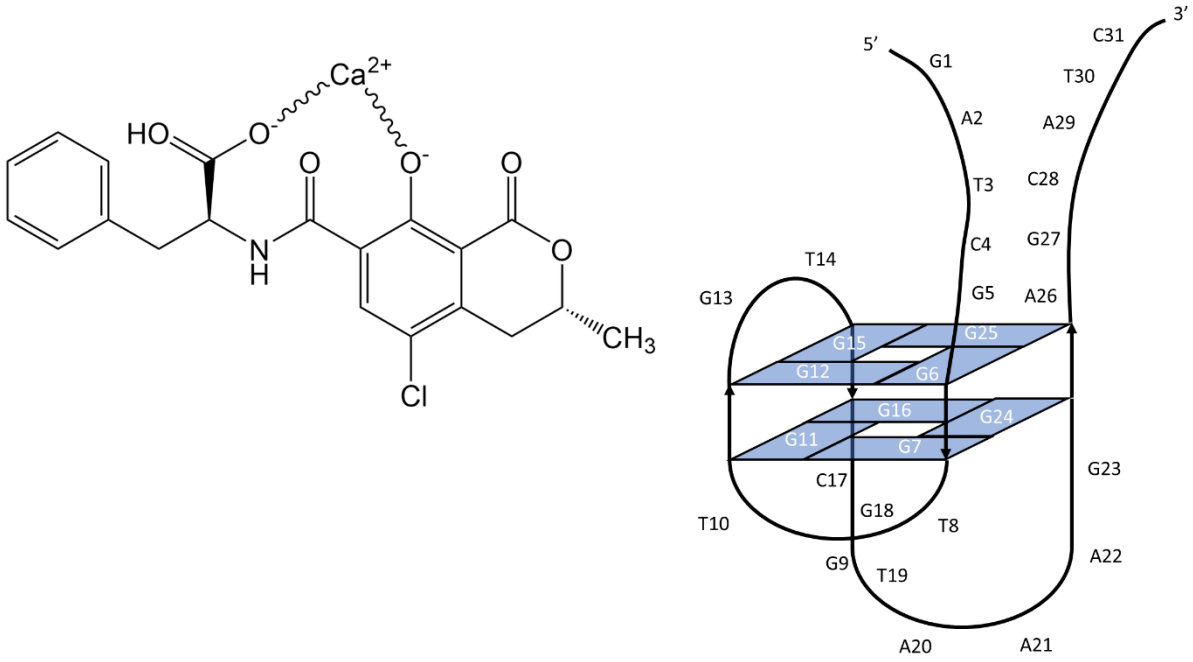

Figure 5.1: Structure of ochratoxin A with its predicted coordinated calcium (left) and the secondary structure of OTA-1 as predicted by the Manderville lab (right).

The goal of this chapter was to build upon the knowledge of the aptamer that the Manderville group published in 2017, mainly using NMR techniques. Trying to answer questions such as, where does the ligand bind on the aptamer? What nucleotides in the aptamer and important for proper folding and binding of the aptamer? And what is the structure of the aptamer-ligand complex?

5.2 Results

5.2.1 Imino Proton Assignments A ^{1}H-NMR spectrum of the free OTA-1 aptamer was acquired, and ligand was titrated into the aptamer sample to a 1:1.1 molar ratio of aptamer to ligand (Figure 5.2). What is interesting to note is that as soon as a small amount of ligand is added (~20%) the guanine residues in the G-Quadruplex form, as opposed to shifting more as additional ligand is added. Some peaks do change chemical shift as the ligand concentration increase, but these are all resonances of the Watson-Crick region in the ^{1}H NMR spectrum. These Watson-Crick base pairs are interesting as the initial quadruplex structure did not show any Watson-Crick base pairs, but ~5 resonances belonging to Watson-Crick imino protons can be seen. It is also worth noting is that it is predicted that the G-Quadruplex contained 2 G-quartets, whereas there are ~11 imino resonances for the non-Watson-Crick base pairs.

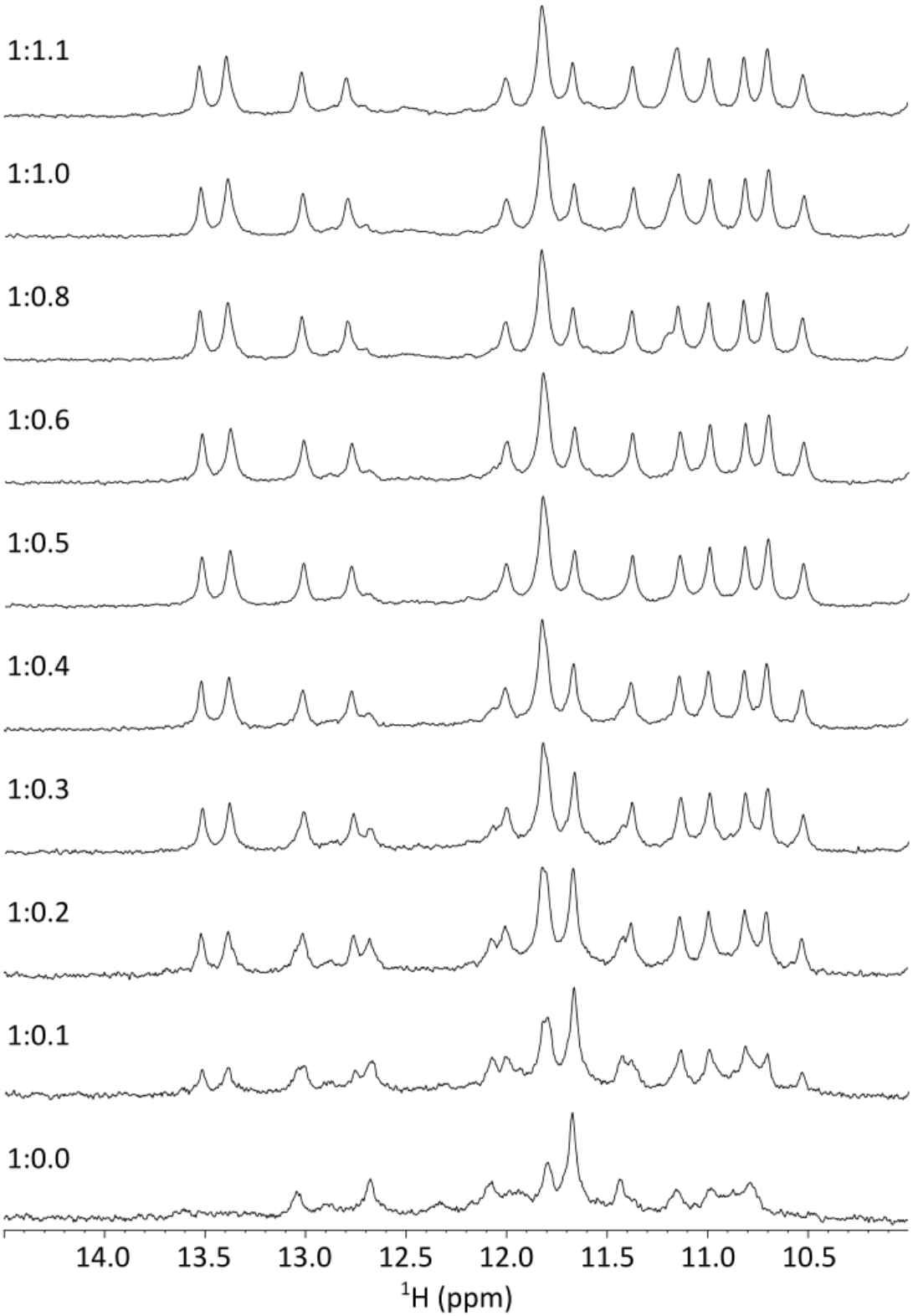

Figure 5.2: Titration of ochratoxin A into the OTA-1 aptamer. Ratios above show the relative amount of aptamer:ligand. Data acquired with a 1.25 mM aptamer sample in 120 mM NaCl, 20 mM $CaCl_2$, 5 mM KCl, 10 mM $^{2}H_{11}$-Tris, pH 8, 90% $^{1}H_2O$-10% $^{2}H_2O$ at 5 °C.

To assign the identities of the imino protons, a series of selectively labelled ^{13}C and ^{15}N labelled samples were prepared. In each of these sample only two nucleotides were selectively labelled, one nucleotide was a guanine, and the other was another non-guanine nucleotide. This allowed for unambiguous assignments of the imino protons. The labelled nucleotides in the samples were G6 & A20, G7 & T14, G11 & T3, G12 & A21, G13 & T8, G15 & A22, G16 & C4, G23 & C28, G24 & T10, and G25 & T19. This accounts for 20 of the 31 nucleotides in the aptamer including all the guanines present in the quadruplex. 1D spectra of the labelled samples were acquired to assign as many imino protons as possible, then a ^{1}H-^{1}H NOESY of the bound aptamer was acquired to confirm the identities of the rest of the resonances (Figure 5.3). This data also contains NOE signals that show the presence of noncanonical base pairs outside of the quadruplex. The imino protons of G5 and T14 show a strong NOE to each other suggesting a G-T base pair. The nucleotides are both found above the top tetrad in the aptamer. The imino protons of G9 and G23 NOE to each other but G9 is found the in Watson-Crick region for guanine, while G23 is found in the non-Watson-Crick region for guanines. G23 and G9 are likely not in a stand G-G base pair as if this was the case both imino proton resonances would appear more upfield and have a much stronger NOE linking them. Finally, T10 has an observable imino proton, so it must be stabilized by interaction within the aptamer. Figure 5.4 shows an updated secondary structure including the helix. The extra non-Watson-Crick imino protons belong to bases that are being stabilized through interactions with the quadruplex. An updated assigned ^{1}H spectrum of the bound OTA-1 can be found in Figure 5.5.

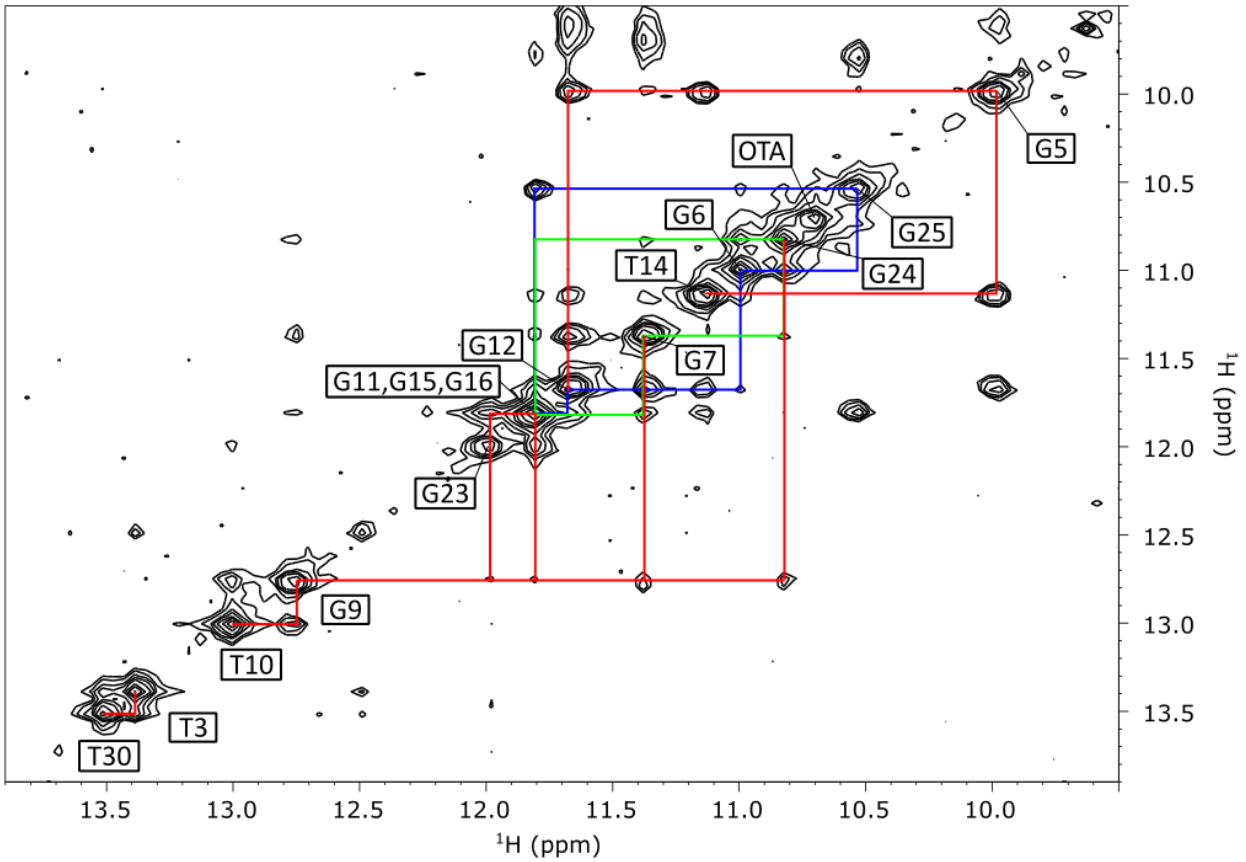

Figure 5.3. ^{1}H-^{1}H NOESY showing the imino proton region of the ligand-bound OTA-1. Blue lines show the NOE pattern between the bases in the top tetrad. Green lines show the NOE pattern between bases in the bottom tetrad. Red lines show the NOE patterns between bases outside the quadruplex structure. Data acquired with a 1.0 mM aptamer sample in 120 mM NaCl, 20 mM $CaCl_2$, 5 mM KCl, 10 mM $^2H_{11}$-Tris, pH 8, 90% ^1H_2O-10% ^2H_2O at 5 °C.

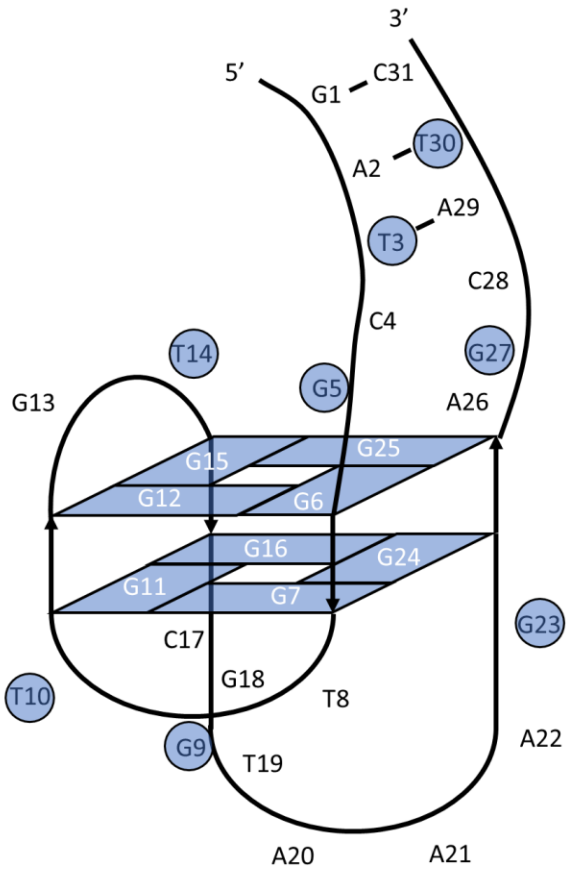

Figure 5.4: Updated OTA-1 secondary structure based on acquired NOE data. The difference from the initial structure is the formation of a small helix with the 5' and 3' tails of the sequence. Blue shaded bases show which nucleotides have observable imino proton signals.

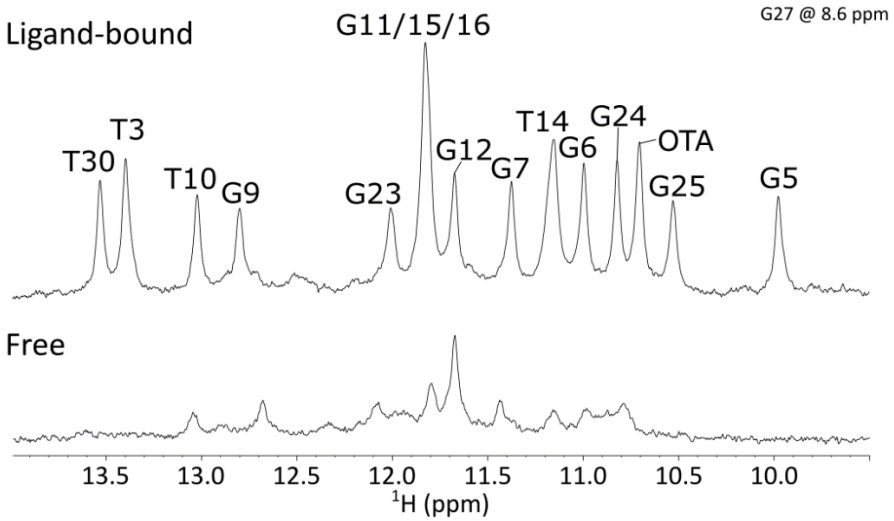

Figure 5.5: 1D spectra of the OTA-1 aptamer free and ligand-bound. Data acquired with a 1.25 mM aptamer sample in 120 mM NaCl, 20 mM $CaCl_2$, 5 mM KCl, 10 mM $^2H_{11}$-Tris, pH 8, 90% ^1H_2O-10% ^2H_2O at 5 °C.

5.2.2 Nucleotide base ^{1}H assignments A goal of this NMR data analysis was to use NOESY spectra in H_2O and D_2O to generate NOE restraints to help create a 3D structure of the aptamer-ligand complex. This was assisted using HSQC data of the specifically labeled samples in order to make assignments of specific atoms throughout the aptamer to identify NOE cross peaks in the two NOESY spectra. The first step was to assign as many H1' to H6/H8 correlations as possible. In duplex DNA and quadruplex structures, the H1' of a nucleotide's sugar base will see the H6 (for cytosine and thymines) or H8 (for guanine and adeninies) or its own nucleotide, and the next nucleotide in the DNA sequence. It is possible to trace the backbone of the aptamer and breaks in this NOE pattern can also be useful in that they might show areas of the aptamer that are disordered or have geometries that would not allow for this NOE cross peak to exist. The assignments of these cross peaks can be seen in Figure 5.6.

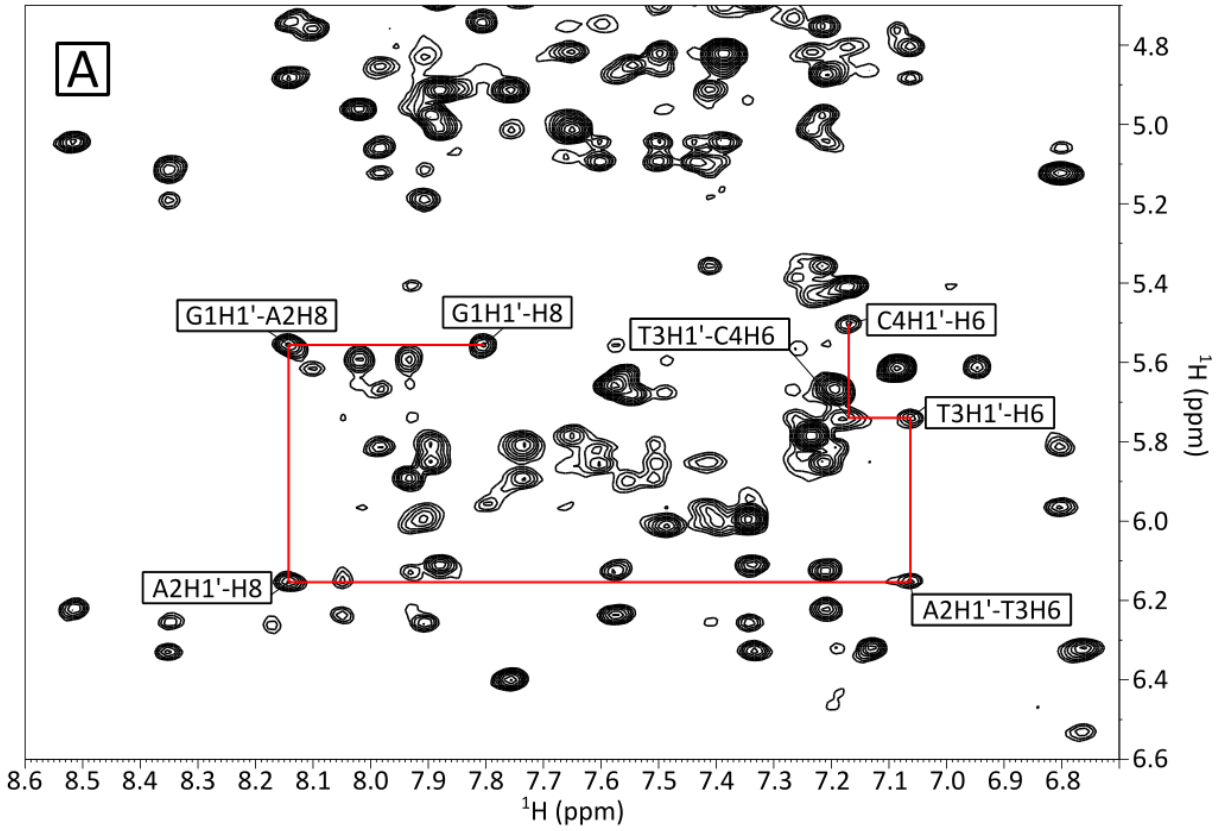
A
G1H1'-A2H8
G1H1'-H8
T3H1'-C4H6
C4H1'-H6
T3H1'-H6
A2H1'-H8
A2H1'-T3H6
^{1}H (ppm)
^{1}H (ppm)

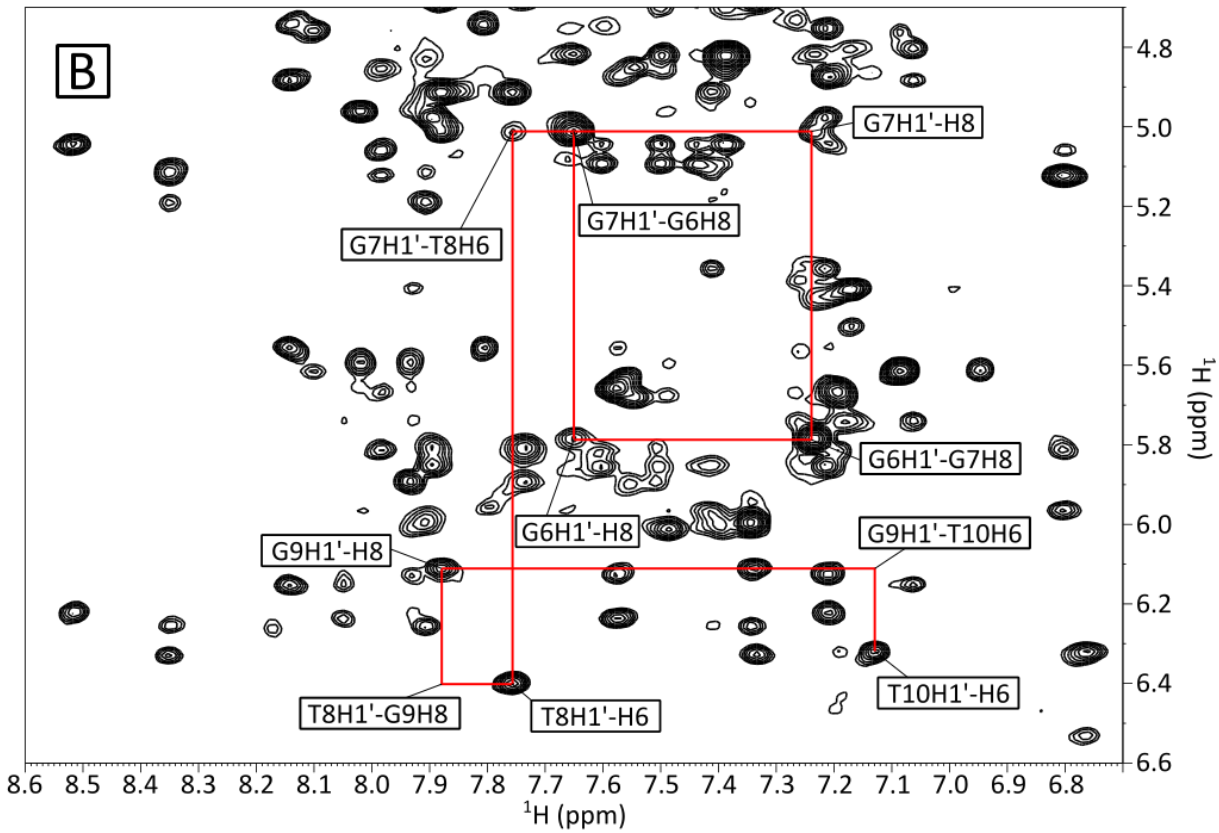
B
G7H1'-H8
G7H1'-G6H8
G7H1'-T8H6
G6H1'-G7H8
G6H1'-H8
G9H1'-H8
G9H1'-T10H6
T10H1'-H6
T8H1'-G9H8
T8H1'-H6
^{1}H (ppm)
^{1}H (ppm)

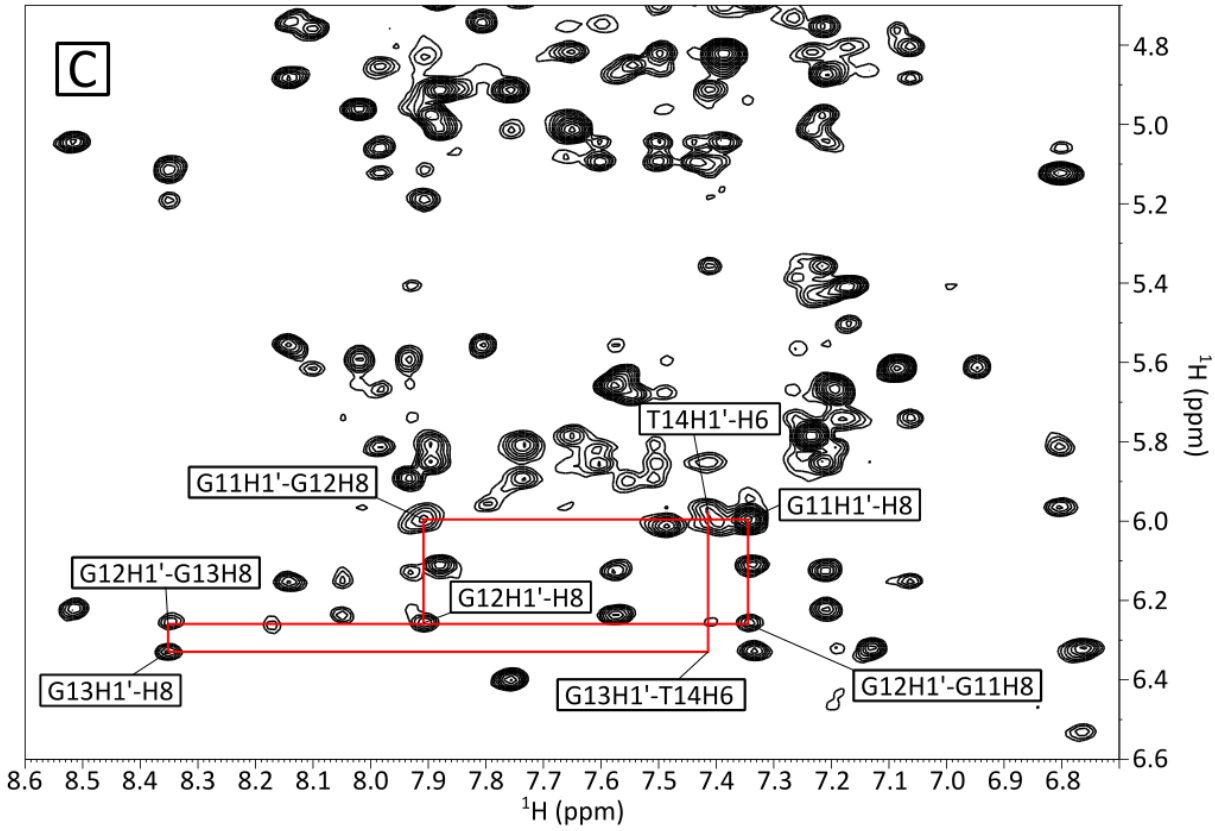
C
T14H1'-H6
G11H1'-G12H8
G11H1'-H8
G12H1'-G13H8
G12H1'-H8
G13H1'-H8
G13H1'-T14H6
G12H1'-G11H8
8.6 8.5 8.4 8.3 8.2 8.1 8.0 7.9 7.8 7.7 7.6 7.5 7.4 7.3 7.2 7.1 7.0 6.9 6.8
^{1}H (ppm)
4.8 5.0 5.2 5.4 5.6 5.8 6.0 6.2 6.4 6.6
^{1}H (ppm)

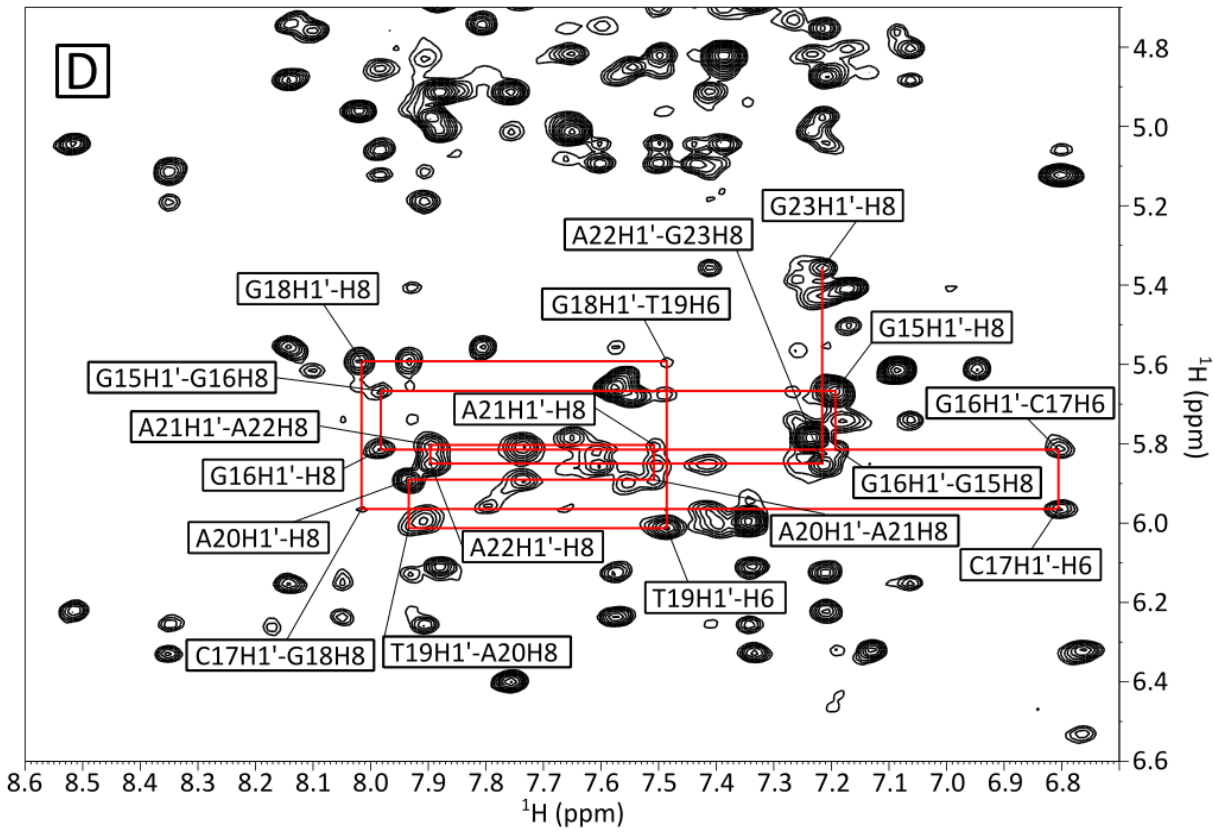
D
G23H1'-H8
A22H1'-G23H8
G18H1'-H8
G18H1'-T19H6
G15H1'-H8
G15H1'-G16H8
A21H1'-H8
G16H1'-C17H6
A21H1'-A22H8
G16H1'-H8
G16H1'-G15H8
A20H1'-H8
A22H1'-H8
A20H1'-A21H8
C17H1'-H6
T19H1'-H6
C17H1'-G18H8
T19H1'-A20H8
8.6 8.5 8.4 8.3 8.2 8.1 8.0 7.9 7.8 7.7 7.6 7.5 7.4 7.3 7.2 7.1 7.0 6.9 6.8
^{1}H (ppm)
4.8 5.0 5.2 5.4 5.6 5.8 6.0 6.2 6.4 6.6
^{1}H (ppm)

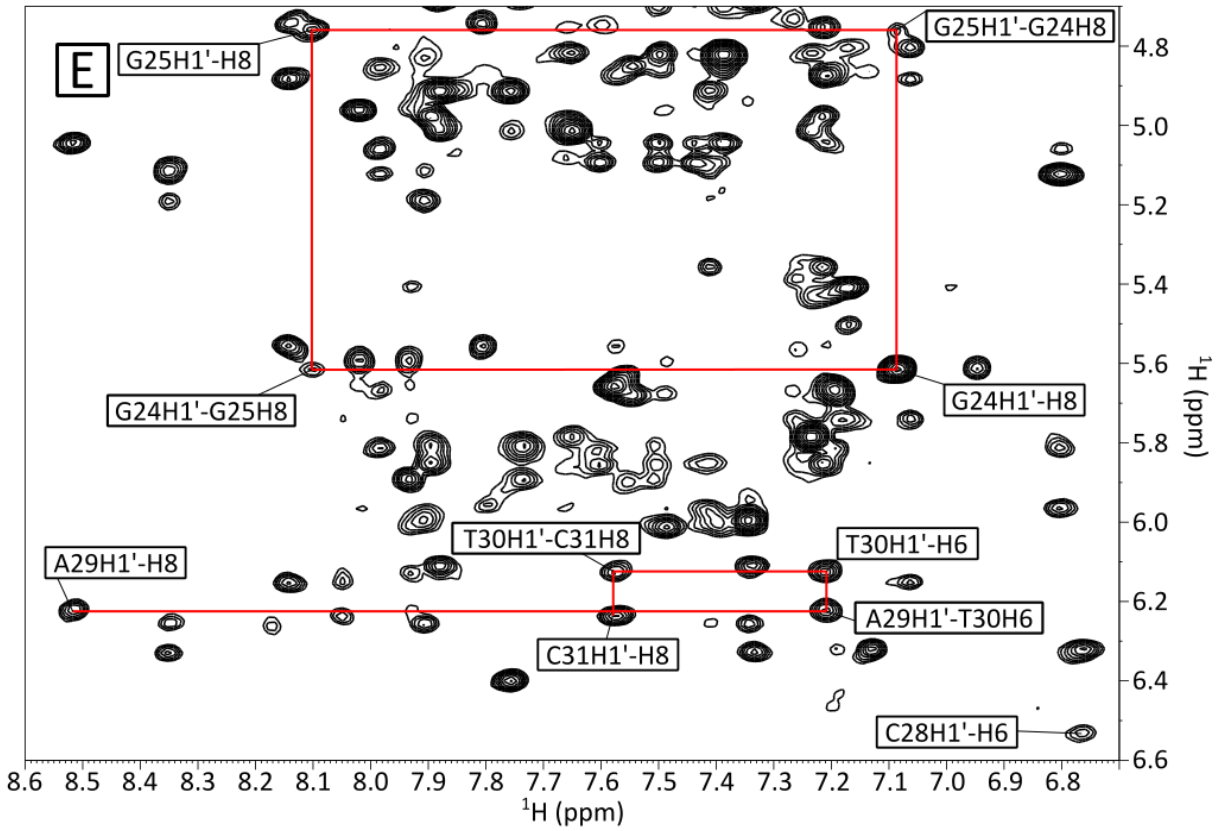

Figure 5.6: ^{1}H-^{1}H NOESY of the ligand-bound OTA-1 aptamer showing the aromatic-anomeric walk between the H1' on the sugar and the H6/H8 on the nucleobase. A shows G1 to C4, B shows G6 to T10, C shows G11 to T14, D shows G15 to G23, and E shows G24 to C31. The walk is not continuous in 100% of cases. Experiment conducted on a 2.0 mM aptamer sample in 120 mM NaCl, 20 mM $CaCl_2$, 5 mM KCl, 10 mM $^2H_{11}$-Tris, pH 8, 100% ^2H_2O at 5 °C.

While assigning these H1' and H6/H8 resonances there were some places where the NOE pattern was discontinuous. Starting at G1 it was possible to trace the pattern to the C4H1'-H6 NOE, suggesting that G5 is not sitting directly below C4 in a standard helix (Figure 5.6 a). The pattern does not start again until G6. Since there is not an NOE from the H1 of G5 to the H1 of G6 this supports the idea that G5 isn't sitting flat on top of G6. Within the tetrad there are two paths that can be used to trace from G6 to G7 as there is both a G6H1'-G7H8 correlation and a G7H1'-G6H8 NOE. This is consistent with G-Quadruplexes in a syn-anti base orientation [138]. The NOE pattern breaks after T10H1'-H6 as there is no distinct visible NOE linking T10 to G11. This could

be due to how T10 is positioned in the loop relative to G11 which is in a G-tetrad above (Figure 5.6 b).

The NOE pattern resumes starting at G11 and is continuous until T14 (Figure 5.6 c). The G11 to G12 NOEs are similar to the G6 to G7 NOEs in that there are two possible paths, which is consistent with the literature [138]. There is no NOE linking T14 to G15 which like with T10 and G11 is where the DNA bases go back to being in a G-Tetrad. Starting at G15 however there is a long NOE pattern tracing from G15 all the way to G23 which suggests some kind of organized structure in the seven-nucleotide loop from C17 to G23 (Figure 5.6 d). From G15 to G16 there again are two paths to trace similar to the previous two guanines stretches. The NOE pattern break between G23 and G24 at the interface between the G-tetrad.

G24 and G25 are linked by a similar NOE pattern observed in the previous guanine in a G-tetrad. After this the NOE walk becomes discontinuous until G29 (Figure 5.6 e). There is no NOE linkage from G25 to A26 nor from C28 to A29. The pattern remains uninterrupted from A29 to C31. There is also no G27 NOE resonance in this area either. This suggests these bases are in positions that would put the various protons on these nucleotides out of NOE range. The NOE pattern is traceable from A29 to C31 (Figure 5.6 e) suggesting these 3 nucleotides are likely in a helix.

After these backbone assignments were made, the remaining protons in the nucleotide portion of each base were assigned. The H1 of guanines and H3 of thymines had been previously assigned from the specifically labelled samples and $^{1}H_2O$ NOESY as these are the imino protons. The H2 resonances found on adenines were assigned by finding an NOE cross peak from the nucleotide's H2 to its own H1' or the H1'in a neighboring nucleotide (Figure 5.7). These resonances have a unique ^{13}C chemical shift, so it is possible to isolate which resonances

specifically belong to the H2 protons. Unfortunately, with the current assignments not all of these protons could be assigned unambiguously. The H2 resonance of A26 was not assignable with this data at this time. H5 resonances found on cytosines were assigned using a TOCSY and searching for the H5-H6 correlations (Figure 5.8). These correlations are in an uncluttered region of the TOCSY and should only have 1 cross peak per cytosine, making them easy to identify and assigned. The H7 resonances found on thymines were assigned by looking for TOCSY cross peaks between H6 and H7 (Figure 5.9). These resonances are also in an uncluttered region of the TOCSY like the H5-H6 correlations.

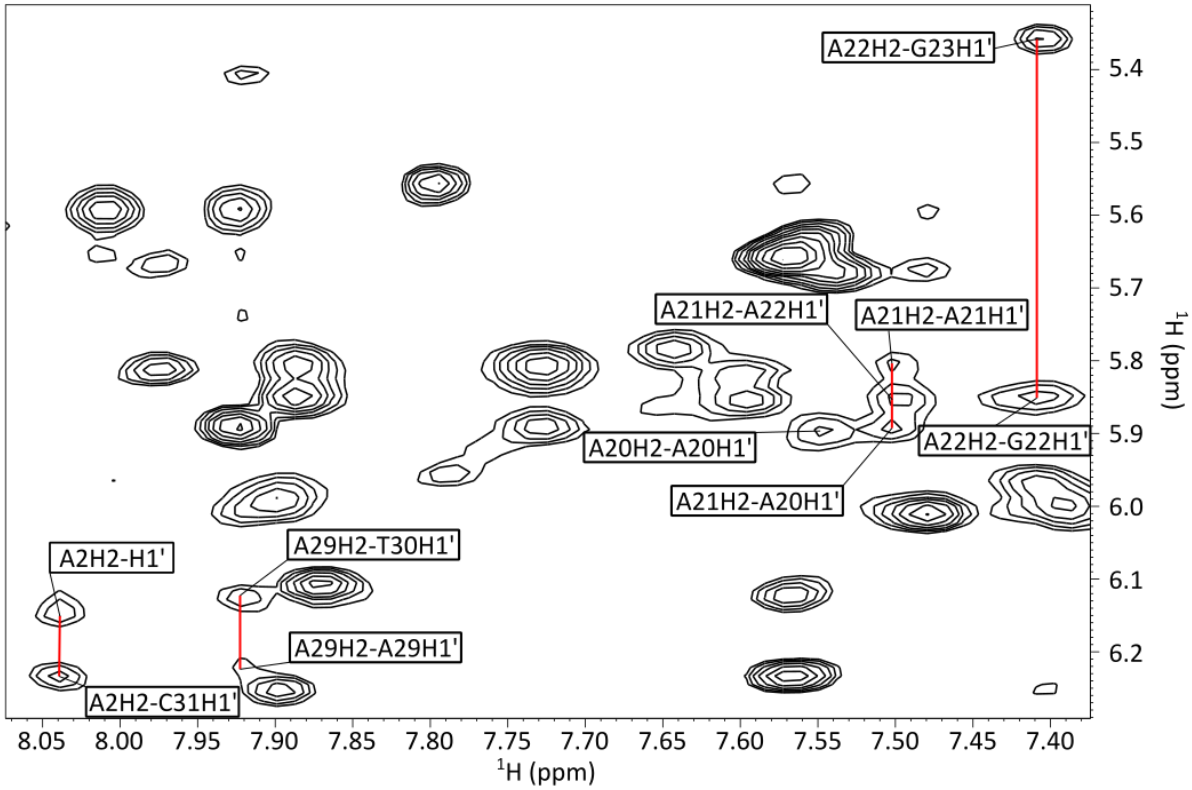

Figure 5.7: NOESY spectrum assigning the H2 resonances of the adenine nucleotides. Data acquired with a 2.0 mM aptamer sample in 120 mM NaCl, 20 mM $CaCl_2$, 5 mM KCl, 10 mM $^2H_{11}$-Tris, pH 8, 100% ^2H_2O at 5 °C.

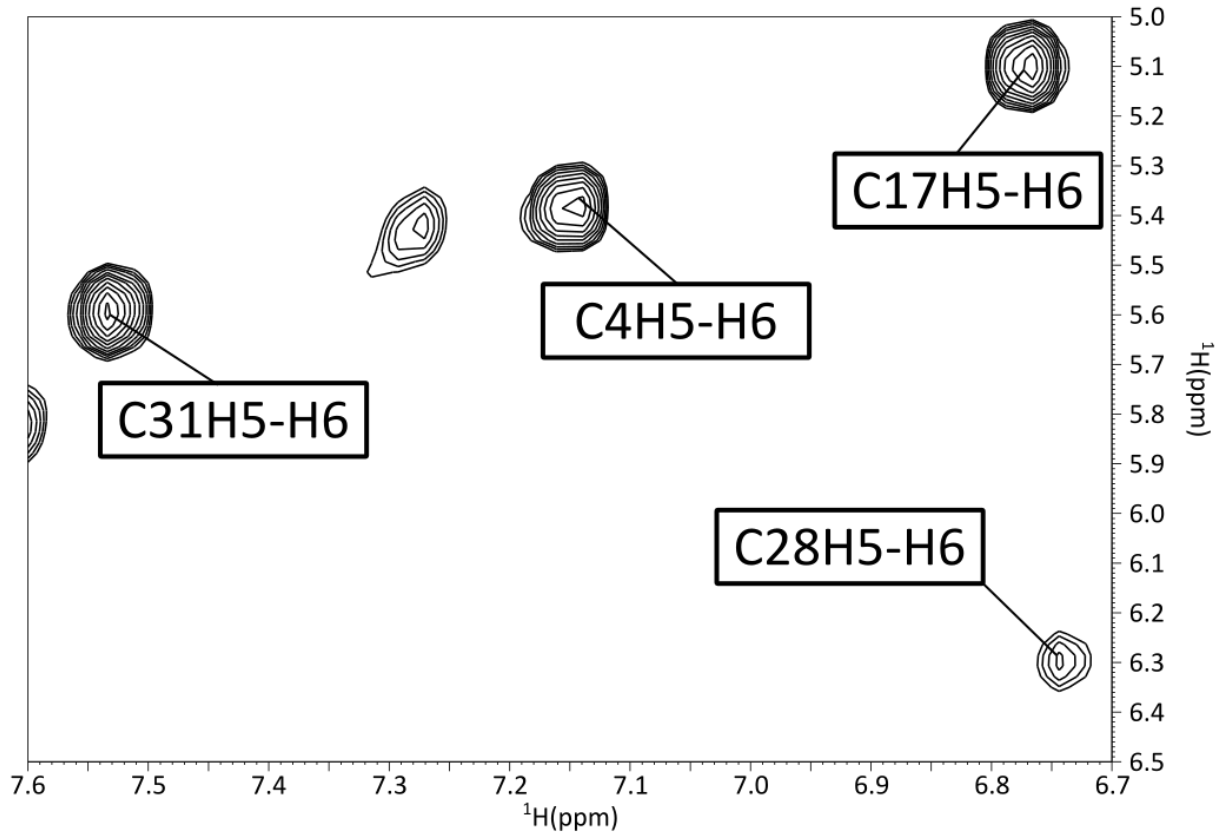

Figure 5.8: TOCSY spectrum assigning the H5 resonances of the cytosine nucleotides. Data acquired with a 2.0 mM aptamer sample in 120 mM NaCl, 20 mM $CaCl_2$, 5 mM KCl, 10 mM $^2H_{11}$-Tris, pH 8, 100% ^2H_2O at 5 °C.

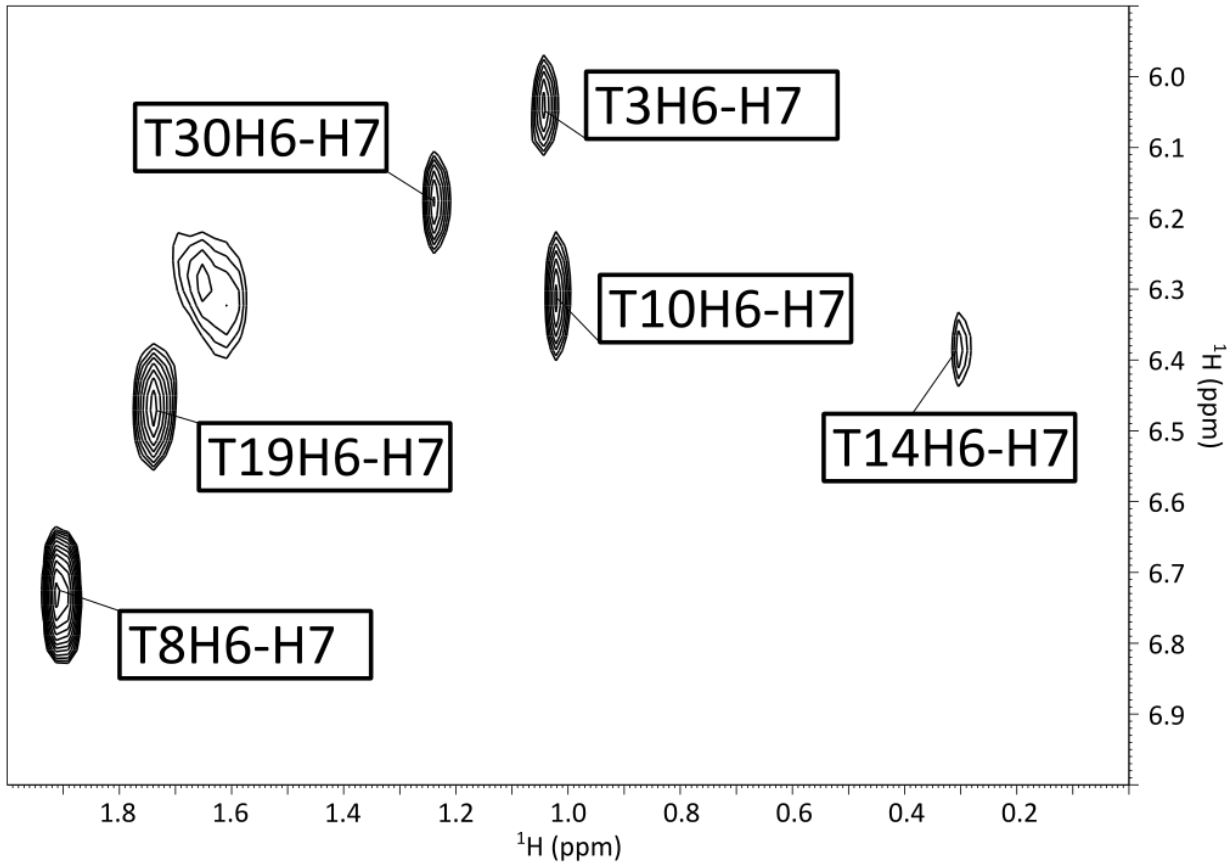

Figure 5.9: TOCSY spectrum assigning the H7 resonances of the thymine nucleotides. Data acquired with a 2.0 mM aptamer sample in 120 mM NaCl, 20 mM $CaCl_2$, 5 mM KCl, 10 mM $^2H_{11}$-Tris, pH 8, 100% ^2H_2O at 5 °C.

5.2.3 Binding site investigation. An ^{1}H-^{13}C HSQC of the ligand-bound OTA-1 was acquired. This spectrum showed which of the methyl resonances present belong to thymines on the aptamer and which resonance belongs to the methyl group on the ligand (Figure 5.10). The methyls belonging to thymine all have a similar ^{13}C chemical shift of ~81-82 ppm, whereas the ligand methyl has a different ^{13}C chemical shift ~89.5 ppm. Of the seven methyl resonances, the second resonance going from upfield to downfield in the ^{1}H chemical shift belongs to the ligand. Looking at the data from the ^{1}H-^{1}H NOESY again and focusing on the methyl-imino region (Figure 5.11), the ligand methyl proton is interacting with methyl group on the thymine of T3 (Figure 5.4). In addition, the

amide proton in the ochratoxin A shows small NOEs to the methyl groups of T3 and T30. These initial interactions place the binding site of the ligand near the helix of the aptamer (Figure 5.12).

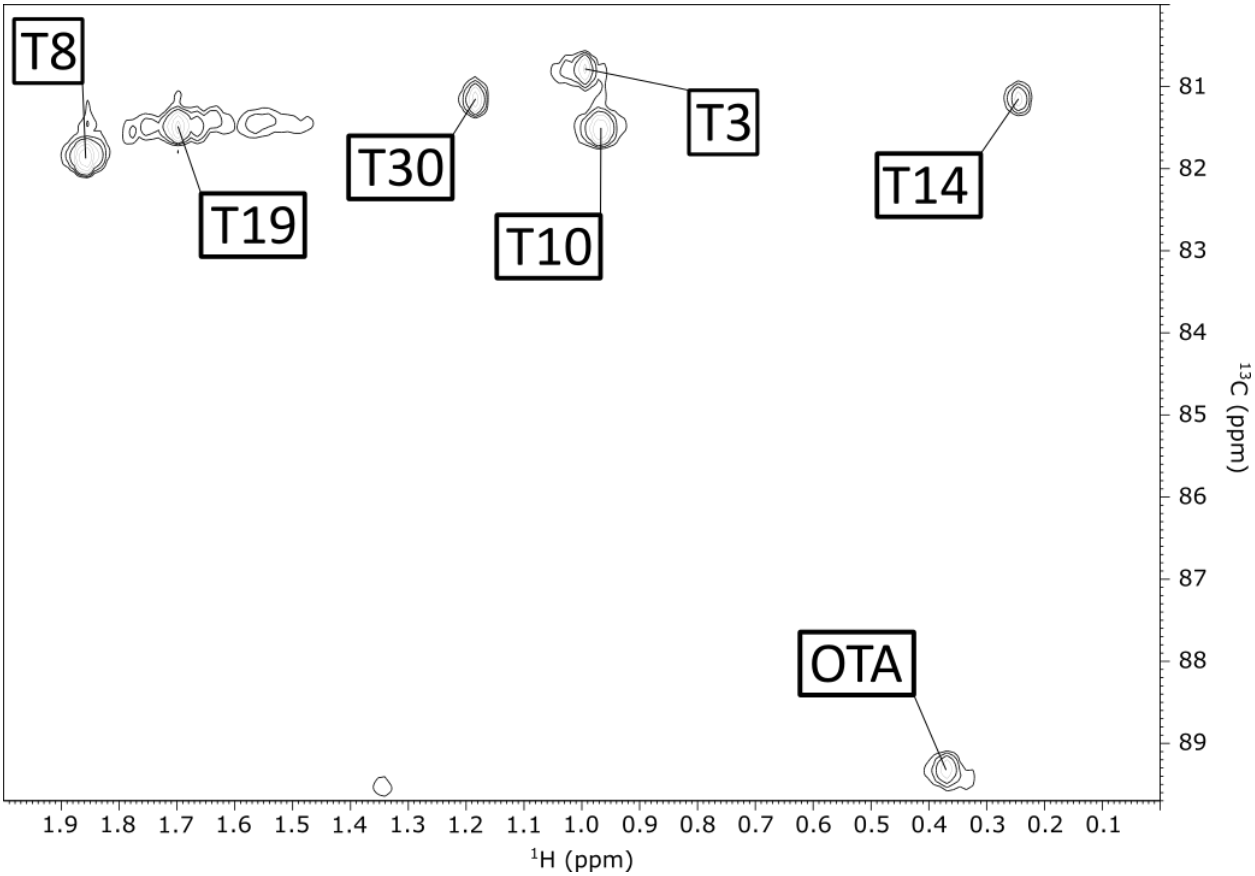

Figure 5.10: HSQC spectrum showing the methyl resonances of the thymine nucleotides and the methyl resonance on ochratoxin A. Data acquired with a 1.6 mM aptamer sample in 120 mM NaCl, 20 mM $CaCl_2$, 5 mM KCl, 10 mM $^{2}H_{11}$-Tris, pH 8, 90% $^{1}H_2O$-10% $^{2}H_2O$ at 5 °C.

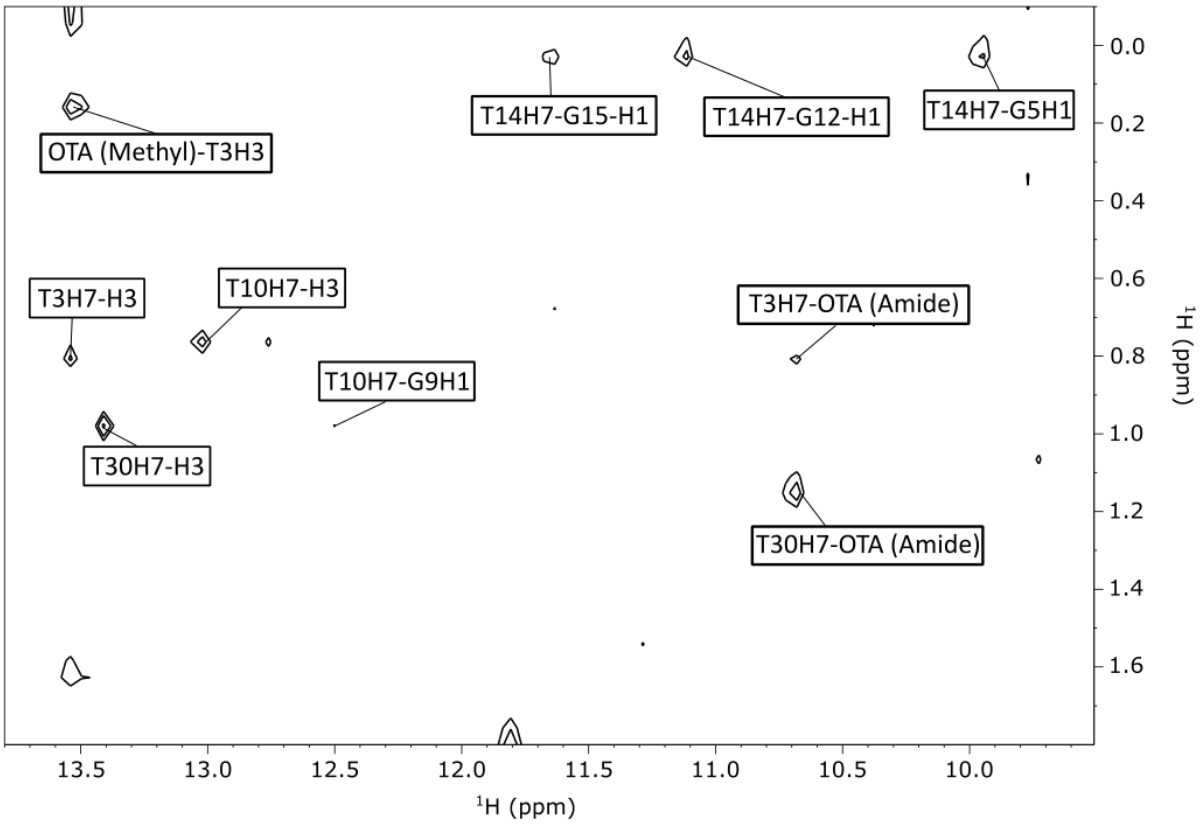

Figure 5.11. ^{1}H-^{1}H NOESY showing the imino-methyl proton region of the ligand-bound OTA-1. Labelled are the imino-methyl resonances on the aptamer and the methyl-amide resonances between the aptamer and the ligand. Data acquired with a 1.0 mM aptamer sample in 120 mM NaCl, 20 mM $CaCl_2$, 5 mM KCl, 10 mM $^{2}H_{11}$-Tris, pH 8, 90% $^{1}H_2O$-10% $^{2}H_2O$ at 5 °C.

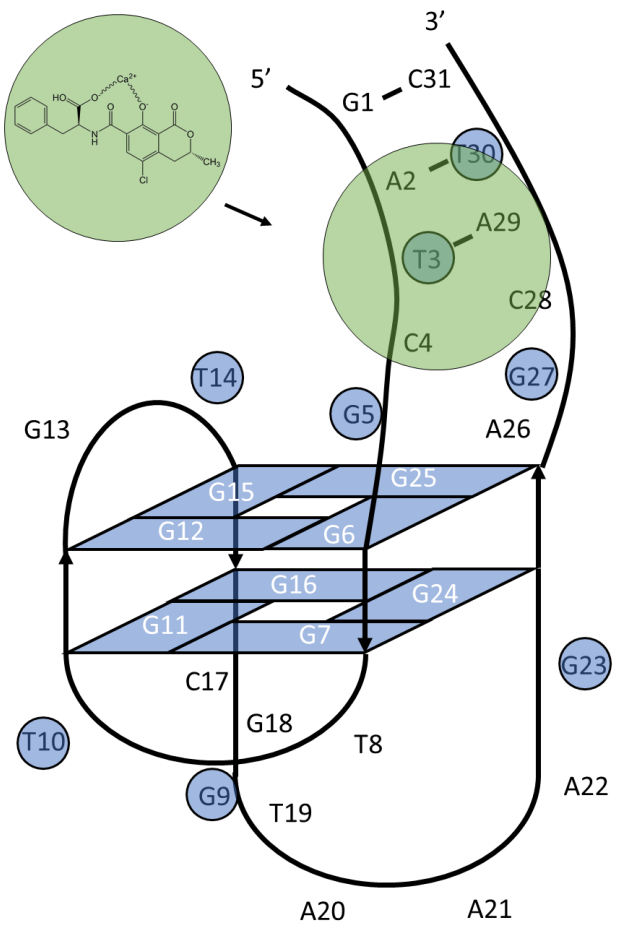

Figure 5.12. Secondary structure of the OTA-1 aptamer representing where the approximate binding site of the ochratoxin A ligand should be. The green circle on the aptamer represents where the ligand binds based on the available NOE data.

5.2.4 Imino Proton Exchange study An imino proton exchange study of the ligand-bound OTA-1 aptamer was conducted similar to chapter 4. NMR spectra were acquired from 5 °C to 55 °C at 5° intervals in order to observe the effect of temperature on the dynamics of the aptamer. R_{1w} and R_{1a} values were measured using inversion recovery experiments. The imino resonance intensity was measured as a function of delay time from 5 ms to 500 ms, with the 10 ms and 120 ms time interval data being measured in triplicate to observe the variability in the data. The measured k_{ex} values are found in table 5.1. A temperature series of the data acquired for the ligand-bound OTA-1 aptamer can be found in Figure 5.13. and plots of the k_{ex} data can be found in Figure 5.14. The

dynamics of this ligand-bound OTA-1 are shown visually in Figure 5.15 Due to the buffer requirements of the OTA-1 aptamer to fold properly, a full analysis of the data to obtain the thermodynamic parameters of base pair opening as was conducted in chapter 4 was not conducted here. The buffer conditions used in chapter 4 to obtain ΔH, ΔS, and ΔG of base pair opening could not be used with OTA-1. Without being able to vary a catalyst concentration and measure the resulting changes in k_{ex} calculating the ΔH, ΔS, and ΔG is not possible. In addition, these experiments were only performed on the ligand-bound aptamer as the spectrum of the free OTA-1 appears to be several different quadruplex structures superimposed over one another.

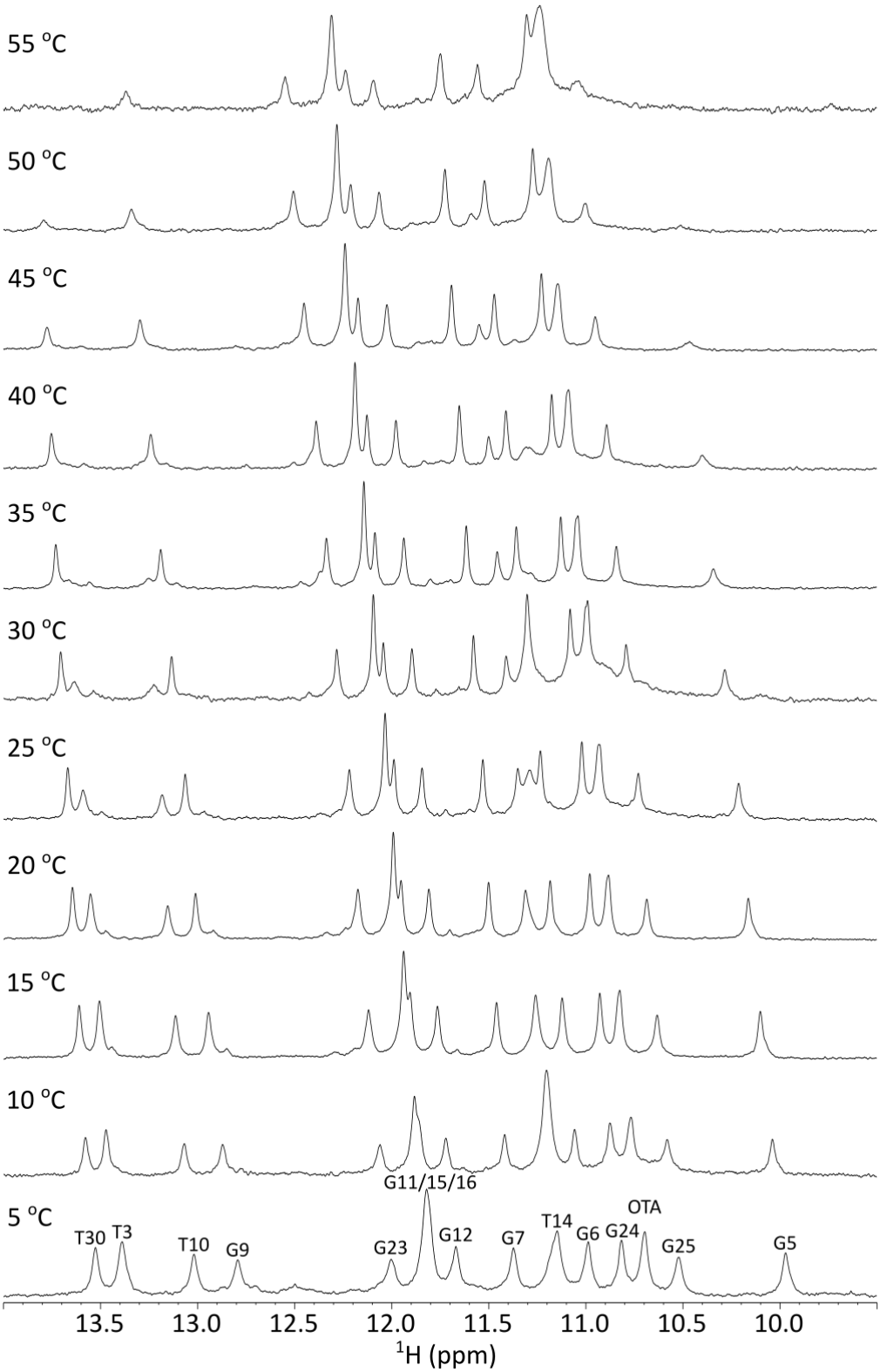

Figure 5.13: 1D ^{1}H spectra of all temperatures for which data of OTA-1 was collected. The temperature series were collected with a 1.25 mM aptamer sample in 120 mM NaCl, 20 mM $CaCl_2$, 5 mM KCl, 10 mM $^2H_{11}$-Tris, pH 8, 90% ^1H_2O-10% ^2H_2O.

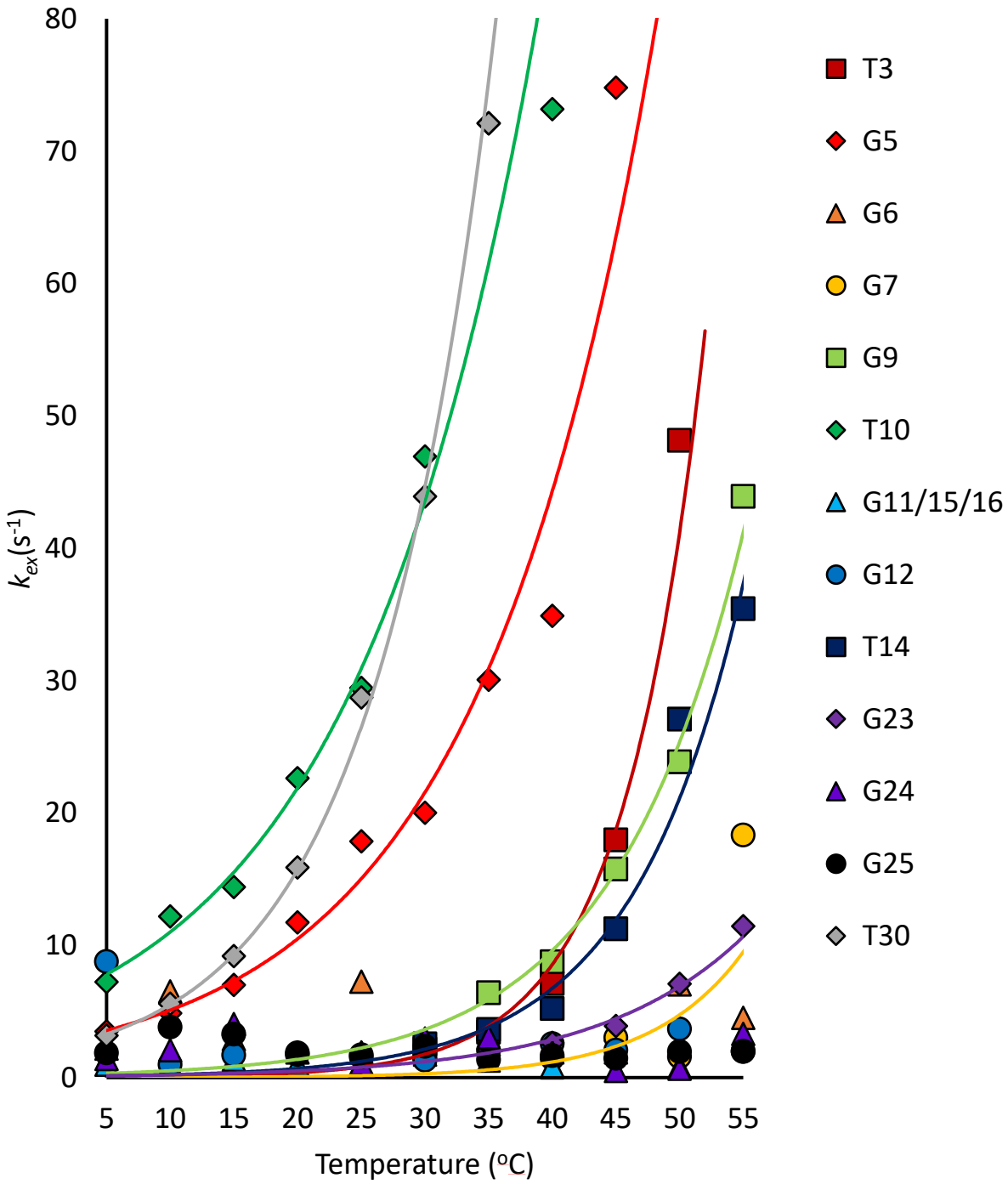

Figure 5.14: k_{ex} data as a function of temperature for the ligand-bound OTA-1. All data were collected with a 1.25 mM aptamer sample in 120 mM NaCl, 20 mM $CaCl_2$, 5 mM KCl, 10 mM $^2H_{11}$-Tris, pH 8, 90% ^1H_2O-10% ^2H_2O. The bases are shown in the following scheme: T3, dark red squares; G5, red diamonds; G6, orange triangles; G7, yellow circles; G9, lime green squares; T10, green diamonds; G11/G15/G16, aqua triangles; G12, blue circles; T14, dark blue squares; G23, purple diamonds; G24, dark purple triangles; G25, black circles; and T30, grey diamonds.

Table 5.1. Hydrogen exchange rate constants (s^{-1}) of the imino protons for the ligand-bound OTA-1 aptamer as a function of temperature.[1]

	Residues												
Temperature (°C)	T3	G5	G6	G7	G9	T10	G11/15 /16	G12	T14	G23	G24	G25	T30
5	1±5	3±2	2±2	2±2	2±2	7±1	1±4	9±4	5±2	3±1	1±2	2±3	3±1
10	2±2	4±2	7±3	2±2	2±4	12±1	1±4	1±7	2±3	3±3	2±2	4±3	6±1
15	2±4	7±1	3±2	1±7	3±1	14±1	1±3	2±2	3±2	5±2	4±2	3±3	9±1
20	2±4	11±2	1±3	2±4	4±3	23±2	1±9	2±3	3±4	2±5	2±2	2±5	16±2
25	2±3	17±2	7±5	1±5	4±3	29±2	2±1	2±2	3±2	1±4	1±2	2±3	29±2
30	2±7	20±2	3±2	2±2	4±4	47±5	2±2	1±5	3±5	2±5	3±2	2±3	44±5
35	3±1	30±2	2±2	1±5	5±2	72±6	1±2	2±5	4±7	2±3	3±2	1±9	72±6
40	7±2	35±5	1±7	1±2	9±4	73±10	1±3	2±3	5±2	3±3	2±2	2±3	-
45	18±3	75±9	4±3	3±3	16±3	-	2±2	2±2	11±4	4±2	1±1	1±2	-
50	48±6	-	7±3	2±3	24±2	-	1±2	4±2	27±2	7±2	1±6	2±3	-
55	-	-	5±3	18±6	44±5	-	3±1	2±4	35±8	11±2	3±2	2±3	-

[1]Data acquired in 120 mM NaCl, 20 mM $CaCl_2$, 5 mM KCl, 10 mM $^2H_{11}$-Tris, pH 8, 90% ^1H_2O-10% ^2H_2O. The uncertainty represents the error in the fit of the data.

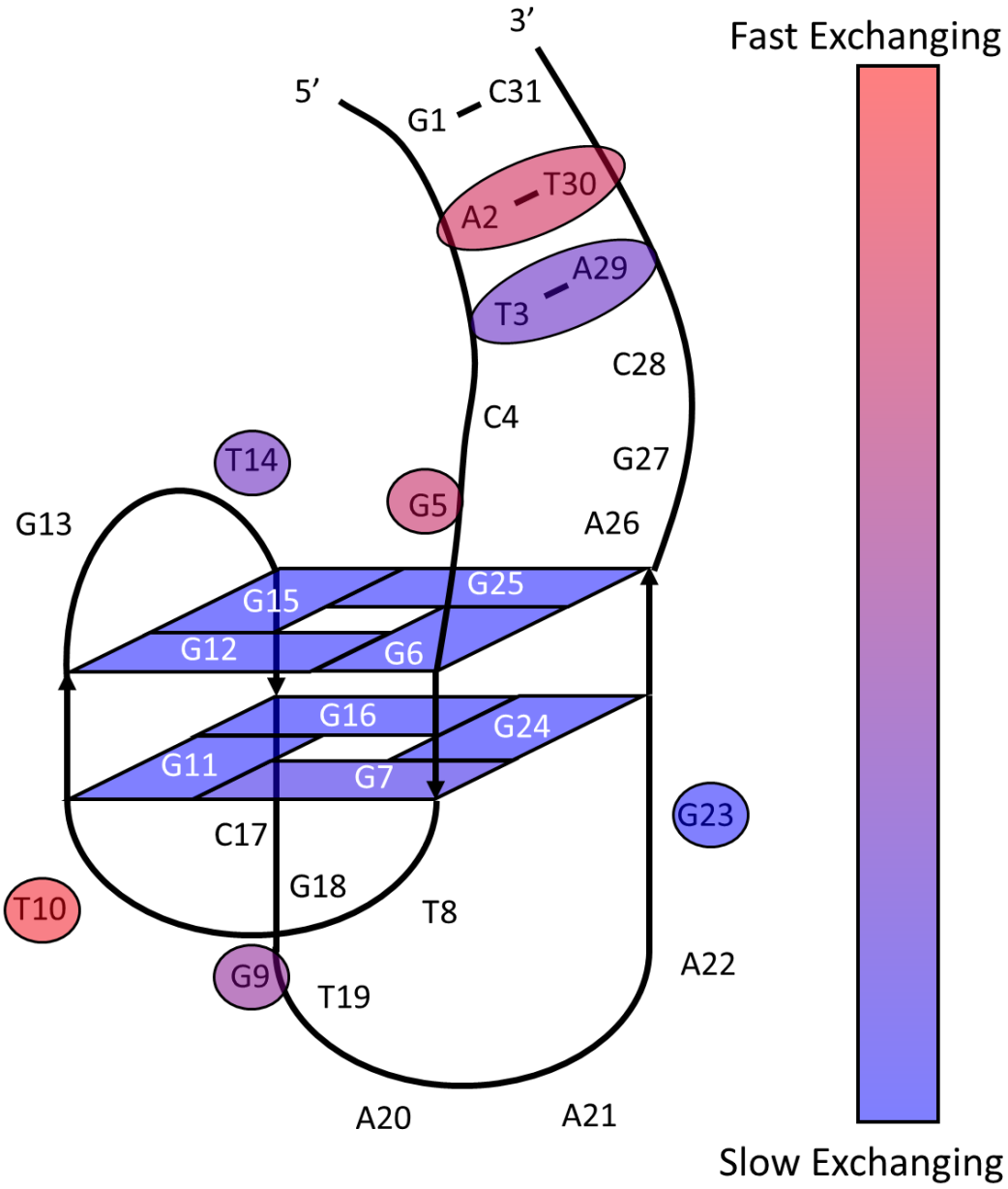

Figure 5.15: Secondary structure diagram of OTA-1 highlighting the dynamics of the ligand-bound aptamer. Base pairs are shaded on a scale of red to purple to blue, depending on what temperature the imino proton in that base pair reached a k_{ex} value of 40 s^{-1} based on the fit line of the k_{ex} values (Fig. 5.13). Bases that started with a k_{ex} value of 10 s^{-1} or higher at 5 °C, were shaded 100% red (255 red, on an RGB scale). Bases that do not reach a k_{ex} value of 10 s^{-1} at 45 °C, were shaded 100% blue (255 blue, on an RGB scale). Other bases were shaded purple (shaded so that the sum of the red and blue sliders on a RGB scale was 255), depending on when the k_{ex} value for its imino proton reached a value of 10 s^{-1}. Imino protons that reached that value at a lower temperature are shaded darker red, and imino protons that reached that value at higher temperatures are shaded darker blue.

The imino protons in OTA-1 can be grouped into a few broad groups, the imino protons close to the binding site, the imino protons belonging to bases in the G-tetrads, and the imino protons belonging to bases underneath the quadruplex. The imino protons belonging to bases near the binding site are T3, G5, T14, and T30. G1 exchanges too quickly to be measured in this type of experiment, even though it should fall under the previous category. The imino protons belonging to bases in the G-tetrads are G6, G7, G11, G12, G15, G16, G24, and G25. The imino protons beneath the quadruplex are G9, T10, and G23.

For the imino protons close to the binding site, they start with a low k_{ex} value at 5 °C and begins to increase as the temperature increases. The rate of temperature increase is not uniform and the k_{ex} value of imino protons in less dynamic bases increases at higher temperatures. T30 is the most terminal imino protons that is visible, G1 is the terminal base pair but that proton is not visible in any spectra in any temperature studied. T30 is very dynamic compared to other imino protons in the aptamer, with a kex value of (3 ± 1 s^{-1}) at 5 °C which immediately increases at 10 °C, until a kex value of (72 ± 6 s^{-1}) at 35 °C, which is its last visible data point. T3 follows a similar pattern to T30, but because it is farther away from the terminal base pair, it is less dynamic. T3 start with a low k_{ex} value of (1 ± 5 s^{-1}) and remain fairly consistent until ~ 40 °C when the k_{ex} value increases to (7 ± 2 s^{-1}) and is visible until 50 °C with a k_{ex} value of (48 ± 6 s^{-1}). G5 and T14 form the non-Watson-Crick G-T base pair, and their k_{ex} values follow are not always the same. Both G5 and T14 start with a low k_{ex} value of (3 ± 2 s^{-1}) and (5 ± 2 s^{-1}) at 5 °C respectively. G5 appears to be more dynamics, as its k_{ex} values begins to increase around 15 °C, while in T14 the k_{ex} values doesn't start to increase until 45 °C. The G5 resonance is visible until 45 °C where it has a k_{ex} value of (75 ± 9 s^{-1}), whereas T14 is visible until the last temperature point at 55 °C, with a k_{ex} value of (35 ± 8 s^{-1-}).

The k_{ex} values of the imino protons found in the G-tetrads all follow a very similar pattern. The k_{ex} values of these imino protons starts low at 5 °C and stays low up to 55 °C and in most cases don't significantly change. The resonances for the imino protons of G11, G15, and G16 are overlapped, making it impossible to accurately measure these imino protons. G6 and G24 both follow the above trend, with kex values of (2±2 s^{-1}) and (1±2 s^{-1}) respectively at 5 °C, and kex values of (5±3 s^{-1}) and (3±2 s^{-1}) at 55 °C. G7 is slightly more dynamic than the other bases in the tetrads. The imino proton of G7 has a k_{ex} value of (2±2 s^{-1}) at 5 °C, but increases to (18±6 s^{-1}) at 55 °C.

There are 3 imino protons located outside of the binding site and g-tetrads with resonances that are visible. These imino protons belong to G9, T10 and G23. G9 and G23 are adjacent to the bottom tetrad, while T10 is in the middle of a tri-loop. At 5 °C the k_{ex} value for G23 is (3±1 s^{-1}) and remains consistent until 50 °C when the kex value increase to (7±2 s^{-1}) and increases again at 5 5°C to (11±2 s^{-1}). G9 is more dynamic than G23. At 5 °C G9 has a k_{ex} value of (2±2 s^{-1}) but starts to increase at 40 °C to (9±4 s^{-1}) and is visible until 55 °C with a k_{ex} value of (44±5 s^{-1}). These bases are likely stabilized by stacking interactions from the quadruplex above, which is why they both appear less dynamic than most of the imino protons in the bases near the binding site. At 5 °C, T10's k_{ex} value is (7±1 s^{-1}), and its k_{ex} value follows a similar trend to T30 as it begins to increase in value immediately as the temperature rises. T10 is visible until 40 °C, where it has a k_{ex} value of (73±10 s^{-1}). T10 is the most dynamic imino proton there is data for in this aptamer.

5.3 Concluding Remarks

The structure of OTA-1 was investigated using ^{1}H NMR. This led to the discovery of an ill-defined free state that folds into a very well-structured aptamer with a small amount of ligand present. Imino proton resonances were assigned for this aptamer which led to the discovery of

three Watson-Crick base pairs forming at the 5'/3' end of the aptamer. Non canonical Watson-Crick base pairs were also seen between G5 and T14, and G9 and G23. This information was previously unknown. After this, the H1', and H6 or H8 resonances for the nucleotides in the aptamer were assigned. This included nucleotides G1 to G4, G6 to G25, and C28 to C31. Next, the H2, H5, and H7 resonances of the nucleotides were assigned as completely as possible, with the H2 of A26 being unable to be assigned. These assignments could be used to help generated a 3D model of the aptamer-ligand complex in the future. Even from these preliminary assignments it is possible to see that the ligand is binding at the top of the aptamer, near the Watson-Crick base pairs (Figure 5.12). Using magnetization transfer NMR techniques discussed previously the k_{ex} values of the imino protons in the ligand-bound aptamer were measured. The imino protons found outside the main quadruplex are much more dynamic than those found within the quadruplex, even though the quadruplex isn't the binding site of ochratoxin A. This is different than the cocaine-binding aptamer where the ligand binding site is the least dynamic section of the aptamer. When comparing these two aptamers, the ochratoxin A-binding aptamer is much less dynamic than the cocaine-binding aptamer. The k_{ex} values of OTA-1 are smaller than in MN4 or MN19, and the resonances remain visible at higher temperatures.

Chapter 6: **Off target ligand-binding of levamisole to the primary ligand-binding site in the Cocaine-Binding Aptamer**

6.1 Preface

All work presented in this chapter has been published in the article listed below [139]

- Shoara, A.A., Churcher, Z.R., Slavkovic, S. and Johnson, P.E. "Weak Binding of Levamisole by the Cocaine-Binding Aptamer Does Not Interfere with an Aptamer-based Detection assay." *ACS Omega,* 6, 24209-24217 (2021).

6.2 Introduction

Levamisole (Fig. 6.1) is an anti-parasitic worm medicine first discovered in 1966 and manufactured by Janssen. Levamisole is an imidazothiazole derivative that functions by interacting with the nematode nicotinergic acetylcholine receptor, which are a set of ligand-gated ion channels required for synaptic action [140]– [142]. This interaction prevents male worms from properly using their reproductive muscles and limiting their ability to reproduce. It was also approved by the FDA in the 1970's and 1980's for therapy in patients with rheumatoid arthritis and in 1990 for combination treatment of colorectal cancer [140], [143]. Prescription of levamisole to humans for parasitic infections in North America was stopped in 1996 due to its severe side effects [144]. Some of the side effects of levamisole use can include dizziness, headache, vomiting, and abdominal pain, and it was not recommended to be used by patients that are breast feeding or in their third trimester of pregnancy [140], [145], [146].

Besides its intended purposes, levamisole is also often used as an adulterant in street cocaine samples (Figure 6.1). There are two main reasons for this, the first is that it helps to bulk out a cocaine sample making it appear that there is more cocaine power present. The second is that it can have a synergistic effect with the cocaine, producing a stronger result than the cocaine by itself [147]. Approximately 90% of street cocaine samples contain an adulterant, while 65% of

those samples contain levamisole [148]. Lacing cocaine with levamisole can lead to side effects not often seen with levamisole, in chronic cocaine users. Agranulocytosis is more present in people who ingest levamisole from contaminated cocaine [140], [149], [150], than it is from people who ingest levamisole for its intended purposes. Agranulocytosis leads to a decrease in granulocytes in the body, causing a reduction in neutrophil counts. Patients can recover upon discontinuing exposure to levamisole [140]. Cases of leukoencephalopathy have also been reported with people who frequently ingested levamisole contaminated cocaine [140], [151], [152]. In leukoencephalopathy, cerebral neurons are demyelinated causing weakness, confusion, and can be potentially fatal. Another side effect from cocaine related levamisole ingestion is vasculitis [140], [153], [154], or the inflammation of veins, arteries, and other blood vessels. The presence of levamisole can also create false positives in quick colorimetric tests performed outside labs on street samples, which are then investigated using more selective methods such as gas chromatography, mass spectrometry, and/or flame ionization detection, potentially wasting valuable lab time and resources [155].

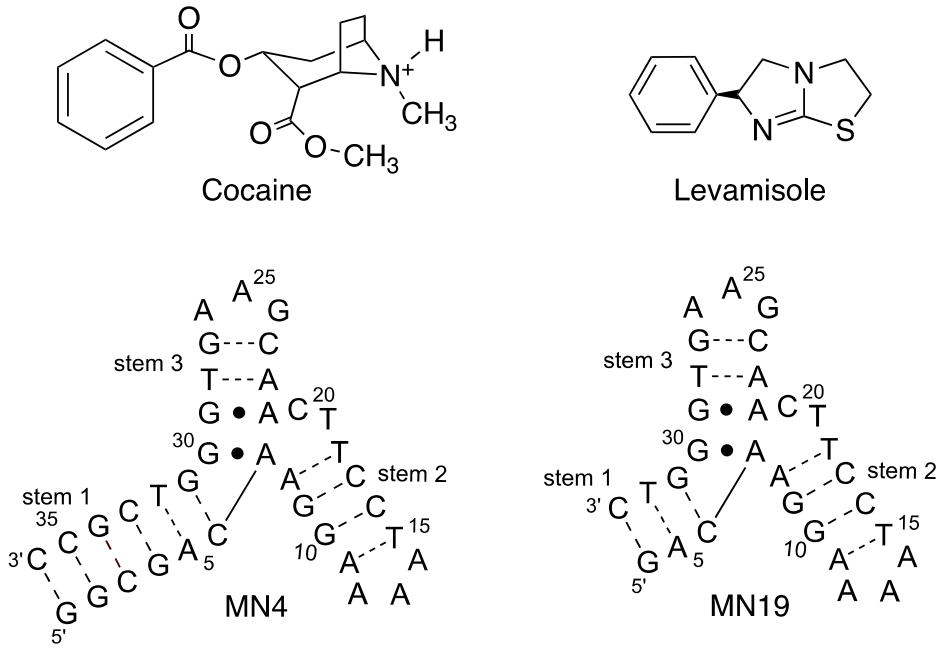

Figure 6.1: Structures of the cocaine-binding aptamers MN4 and MN19 as well as the compounds levamisole and cocaine. Nucleotides in both constructs are numbered in the same manner as in MN4. Dashes between nucleotides indicate Watson−Crick base pairs while dots indicate non-Watson−Crick base pairs.

If levamisole is present in cocaine acquired from outside a reputable distributor, is it possible that the cocaine binding aptamer might bind to levamisole as well? Off target ligand-binding is a feature of certain aptamer sequences that is well documented [156]. This is seen in the ability of the ATP aptamer to binding to ADP, AMP, adenosine and adenine, and is also seen in an RNA GTP aptamer binding to several structurally related compounds [18], [156], [157]. Off target ligand binding is not limited to structurally related ligands. The cocaine-binding aptamer itself is quite promiscuous with the ability to bind to a host of other ligands not structurally related to cocaine [56], [57]. This ability to bind a host of other ligands is seen in both the long stem 1 variant of the cocaine-binding aptamer (MN4, Fig. 6.1) and the short stem 1 variant (MN19, Fig. 6.1).

Aptamer-ligand interactions can depend on several different factors. Aptamers are often selected using specific buffers or using specific conditions which can help facilitate interaction. In

addition, there can be differences in the strength of aptamer-ligand interaction depending on if the aptamer in question is floating free in solution or attached to a surface. This can lead to discrepancies in K_d values reported to help determine the strength of interaction [158]– [161]. It can be important to test binding of aptamer-ligand pairs using a variety of different experimental techniques, as one technique may provide important data that others miss. Isothermal Titration Calorimetry (ITC), UV-Vis Spectroscopy, Fluorescence techniques, and Nuclear Magnetic Resonance Spectroscopy (NMR) can all be useful for probing K_d values at a variety of concentration ranges. NMR in particular can be useful for probing weak interactions in the high micromolar to millimolar range [162].

In this chapter NMR is used to characterize the binding of the cocaine-binding aptamer with levamisole. ITC, UV thermal melts, and fluorescence had been used previously to check for the interaction of MN4 and levamisole, but no interaction was seen[1]. NMR was then used to check for any interaction between MN4 and levamisole, and once binding was observed NMR was used to characterize the interaction in both MN4 and MN19.

6.3 Results and Discussion

6.3.1 Levamisole binding to MN4 detected using NMR methods. Binding of levamisole to the MN4 aptamer was investigated using ITC and UV-Vis methods. Using these methods an interaction between the MN4 aptamer and levamisole was not seen. In addition, the presence of levamisole did not prevent the detection of cocaine via the photochrome aptamer switch assay (PHASA) [139].

The binding of levamisole to the cocaine binding aptamer was detected using NMR methods. Levamisole was titrated into a sample of the MN4 aptamer and monitored by recording

[1] These experiments were performed by Sladjana Slavkovic and Aron Shoara from the Johnson lab. Their results can be seen in the initial reference for this chapter.

1D ^{1}H NMR spectra (Figure 6.2(a)). Chemical shift changes of the imino protons as levamisole was added indicates that levamisole is being bound by the MN4 aptamer. Levamisole binds MN4 in fast exchange on the NMR timescale where the population-weighted chemical shift is observed and indicates relatively weak binding affinity compared to tighter binding ligands such as cocaine and quinine that bind in slow exchange on the NMR timescale [17], [73]. The positions of the imino proton resonances were tracked as a function of levamisole concentration in order to determine the K_d value by fitting the chemical shift changes to equation 2.6. The results of these fits are shown in Figure 6.2(b). Four different imino protons were tracked and their individual K_d values are summarized in Table 6.1. The average K_d value for MN4 binding levamisole is (0.5 ± 0.1) mM.

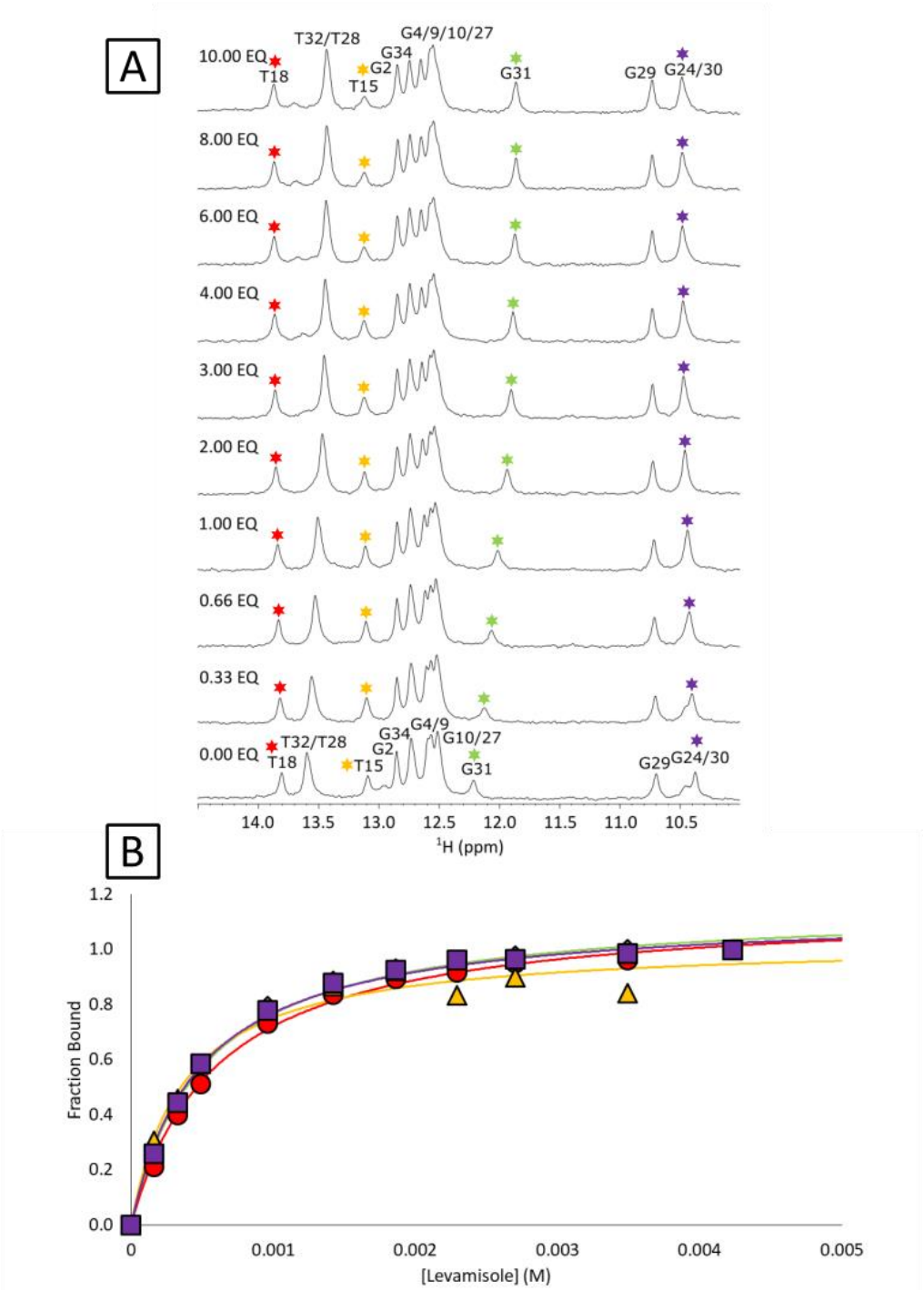

Figure 6.2. Levamisole binding by MN4 monitored by one-dimensional ^{1}H NMR. (a) The imino proton region of MN4 titrated with levamisole. Imino resonances marked with colored stars were used to determine the binding affinity. (b) The overlayed plots of the imino protons fit to the equation that describes 1:1 binding of levamisole and MN4. Solid line represents the fit and the data by the colored symbols. The color of the symbol and fit line match the peaks indicated with the same color in part (a). Experiments were conducted at 5 °C with a 500 μM DNA aptamer sample, in 245 mM KCl. 5 mM $K_xH_yPO_4$ pH 6.8 with 10% $^{2}H_2O$.

Table 6.1. K_d values for levamisole binding the cocaine-binding aptamers MN4 and MN19 as determined by NMR-based chemical shift perturbation.

Nucleotide	MN4 (pH 6.8) K_d (mM)	MN4 (pH 6.0) K_d (mM)	MN4 (pH 8.0) K_d (mM)	MN19 (pH 6.8) K_d (mM)
T15	0.37 ± 0.06	0.37 ±0.03	-	-
T18	0.61 ±0.04	0.37 ±0.06	-	0.9 ±0.2
G29	-	-	-	2.7 ±0.3
G30	0.48 ±0.03	-	-	-
G31	0.51 ±0.04	0.32 ±0.04	0.42 ±0.05	1.7 ±0.3
T32	-	0.32 ±0.05	0.34 ±0.05	-
Average	0.5 ±0.1	0.35 ±0.03	0.38 ±0.05	1.7 ±0.9

Error in the K_d value for individual bases is from the error in fit. The error in the average is the standard deviation of the values used to calculate the average.

Insight into the location of the levamisole binding site is gained by looking at the nucleotides whose chemical shifts move most with ligand biding. These residues are, in order of decreasing magnitude: G31, G30, G4, T18, G29, T15 and G34. With the exception of G4, four of the five nucleotides that change chemical shift most are at or adjacent to the three-way junction (Figure 6.1). This finding matches the location in the MN4 aptamer for cocaine, quinine and amodiaquine binding [17], [57], [73]. For all cocaine-binding aptamer and ligands studied to date, the nucleotide whose chemical shift changes the most is that of G31. This result indicates that levamisole shares the same binding site as the other ligands for the MN4 aptamer.

To see if levamisole and cocaine compete for the same binding site, the levamisole-bound MN4 sample was then titrated with cocaine. In this titration (Figure 6.3), by the stage where two molar equivalents of cocaine were added, signals indicative of the cocaine-bound MN4, such the downfield T19 imino, indicate that cocaine is bound, and levamisole is displaced. This indicates that cocaine and levamisole compete at the same site for binding MN4.

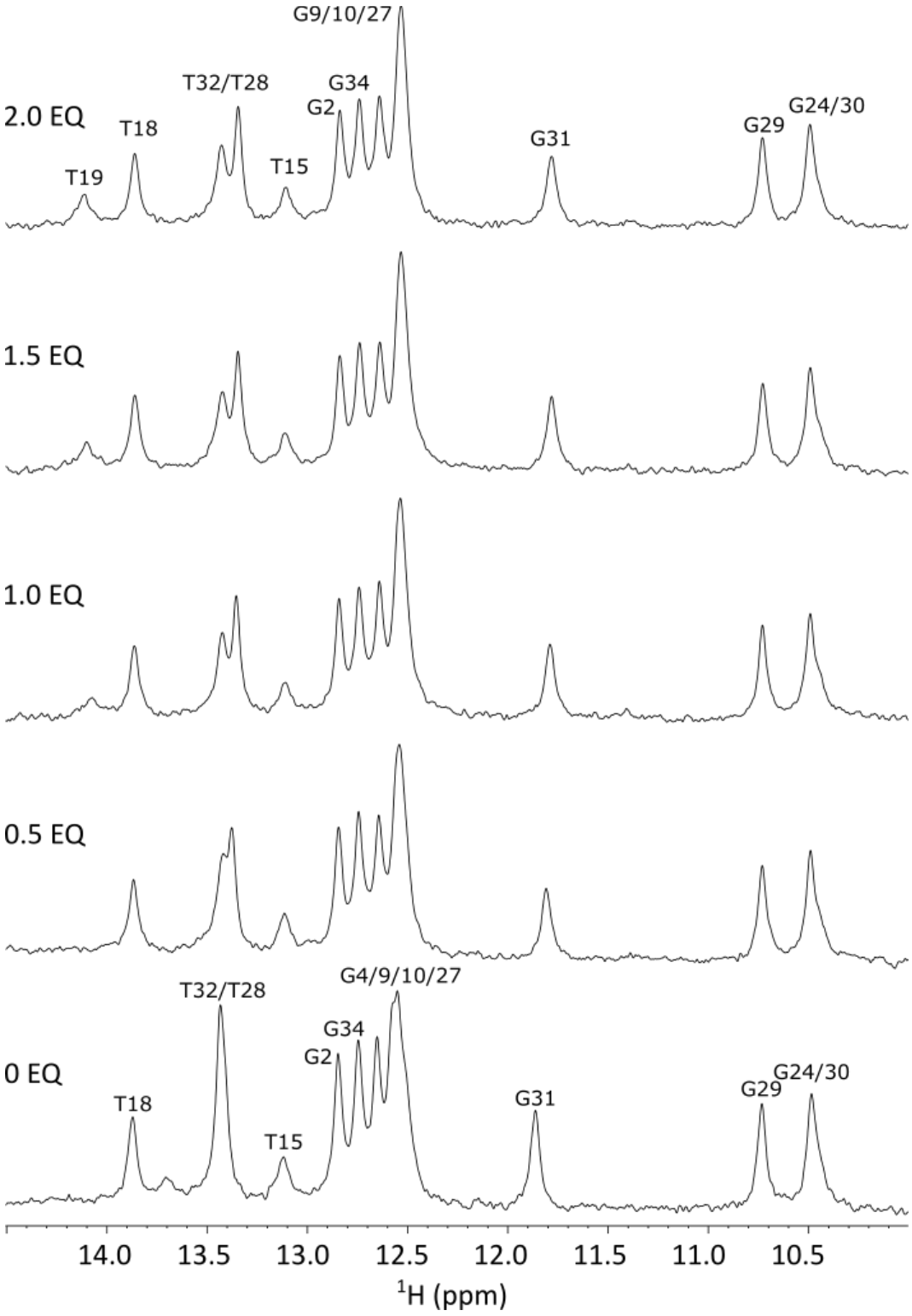

Figure 6.3. Levamisole displacement by cocaine in MN4 monitored by one-dimensional ^{1}H NMR. The imino proton region of levamisole-bound MN4 titrated with cocaine. Experiments were conducted at 5 °C with a 500 μM DNA aptamer sample, in 245 mM KCl. 5 mM $K_xH_yPO_4$ pH 6.8 with 10% ^2H_2O.

Next the competitive binding of cocaine and levamisole was confirmed by titrating levamisole into a 1:1 molar ratio sample of MN4 bound to cocaine. A sample of MN4 was titrated with cocaine to a 1:1 molar ratio. Then, this sample was titrated with levamisole to see if the levamisole could compete off the bound cocaine (Figure 6.4). In this experiment, it took ~50 molar equivalents of levamisole to compete off the 1 equivalent of cocaine from MN4. The competitive binding is best shown by the disappearance of the T19 peak with levamisole binding. This large excess of levamisole is consistent with its weak binding affinity compared with that of cocaine.

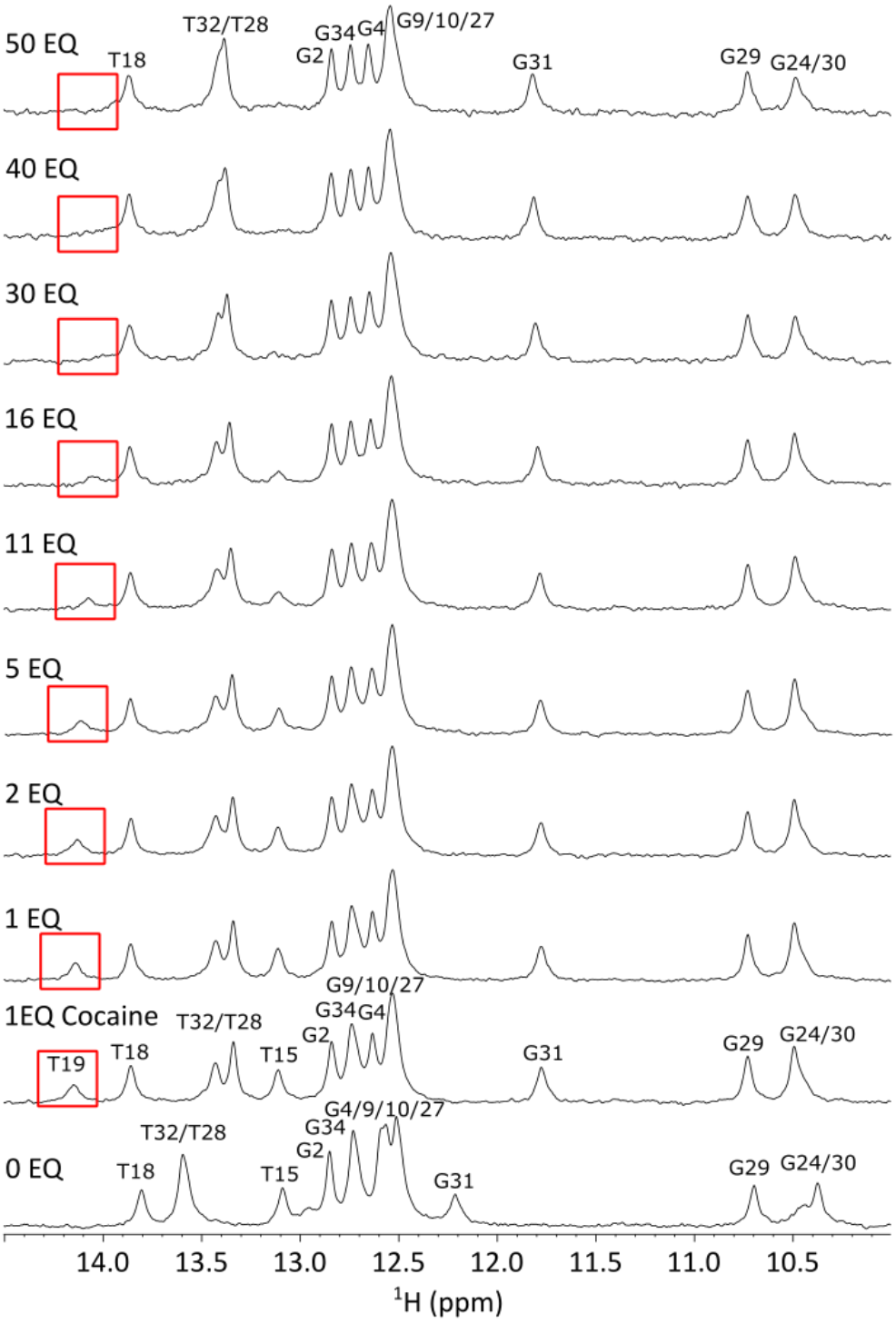

Figure 6.4. Cocaine displacement by levamisole in MN4 monitored by one-dimensional ^{1}H NMR. The imino proton region of cocaine-bound MN4 titrated with levamisole. The red box tracks the disappearance of T19 as cocaine is displaced by levamisole. Experiments were conducted at 5 °C with a 500 μM DNA aptamer sample, in 245 mM KCl. 5 mM $K_xH_yPO_4$ pH 6.8 with 10% ^2H_2O.

6.3.2 Detection of non-specific Levamisole binding to DNA. To confirm that levamisole binding by MN4 is not simply weak non-specific binding to DNA the binding of levamisole to two control sequences for the aptamer was investigated. In the first control (MN4-rando) the sequence of MN4 was randomized, but the nucleotide composition was kept constant. For the second control, the SS1 sequence was used, where the two AG base pairs (A7/G30 and A21/G29) were switched to be GA base pairs (G7/A30 and G21/A29) as shown in Figure 6.1. SS1 has previously been used as a negative control for cocaine and quinine binding as it interacts very weakly with these ligands with binding in the 0.5-1 mM range [163]. Titrations of levamisole monitored by NMR spectroscopy were performed for MN4-rando and SS1 under the same conditions as for MN4. As seen in Figures 6.5 & 6.6 the addition of levamisole produced no changes in chemical shift of the imino signals that would indicate levamisole binding. Some small changes in peak height were observed that can be attributed to a slight dilution of the sample as ligand solution is added. Together, these data show that levamisole does not bind the examined DNA molecules indicating that levamisole binding by MN4, though weak, is a result of a specific interaction.

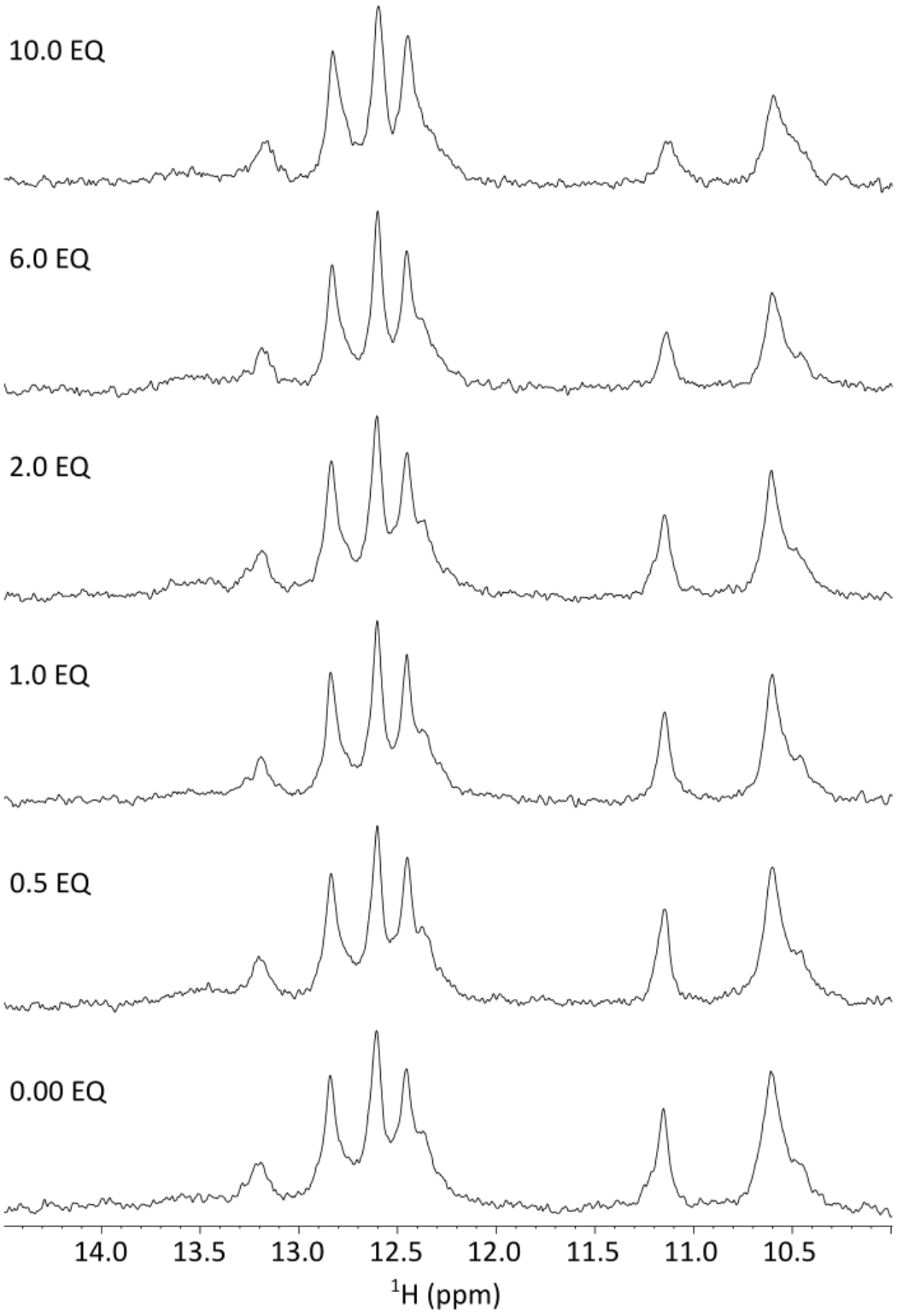

Figure 6.5. Addition of levamisole to the MN4-rando DNA sequence monitored by one-dimensional ^{1}H NMR. Experiments were conducted at 5 °C with a 500 μM DNA aptamer sample, in 245 mM KCl, 5 mM $K_xH_yPO_4$ pH 6.8 with 10% ^2H_2O.

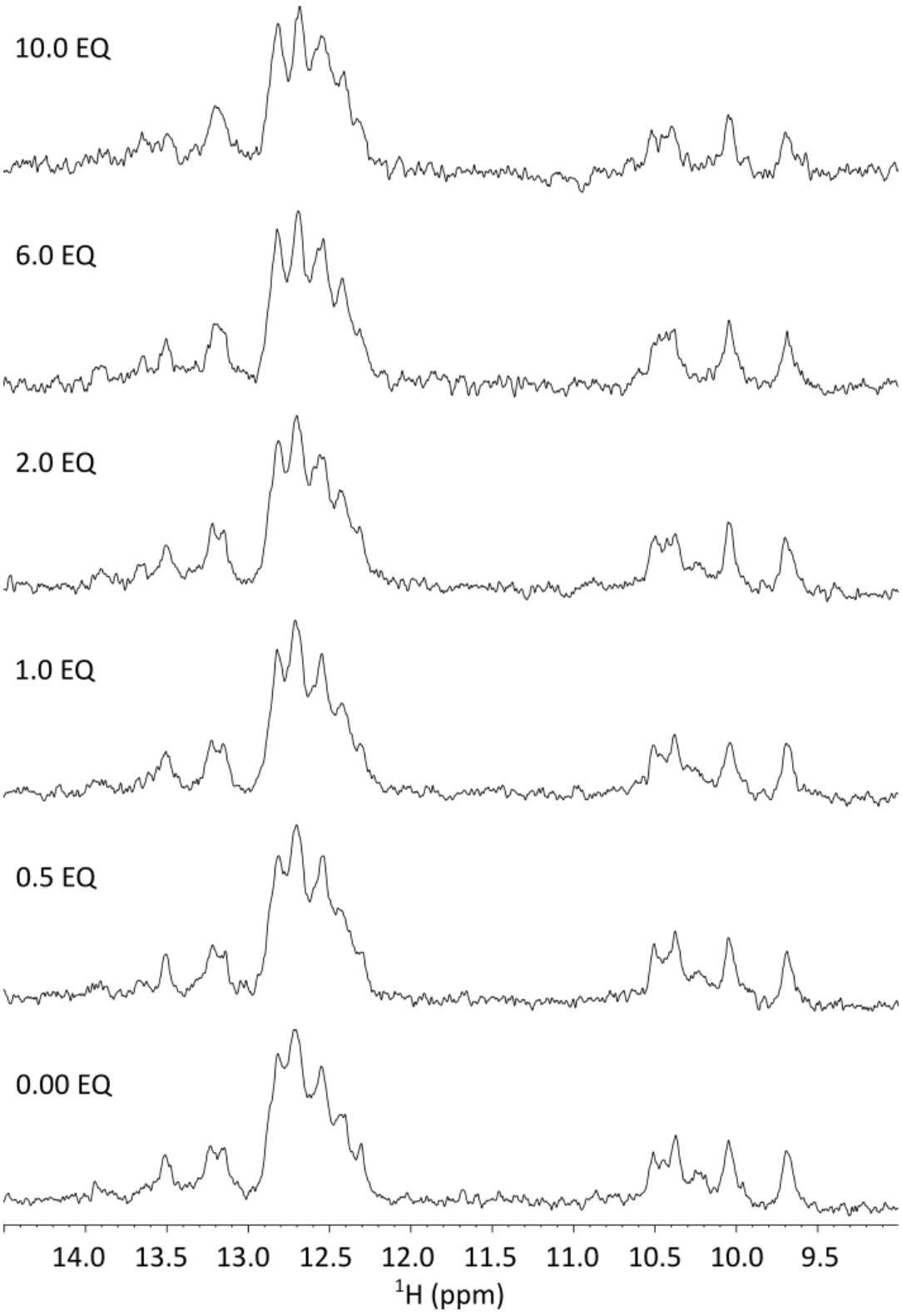

Figure 6.6. Addition of levamisole to the SS1 DNA sequence monitored by one-dimensional ^{1}H NMR. Experiments were conducted at 5 °C with a 500 μM DNA aptamer sample, in 245 mM KCl, 5 mM $K_xH_yPO_4$ pH 6.8 with 10% ^2H_2O.

6.3.3 Levamisole binding to MN19 detected using NMR methods. Given the weak binding of levamisole to MN4, the short stem 1 cocaine-bind aptamer variant MN19 was also investigated to see if this aptamer experienced ligand induced folding in the presence of levamisole like it does with other ligands such as cocaine and quinine. A titration of MN19 with levamisole was monitored by 1D ^{1}H NMR spectra and is shown in Figure 6.7(a). Again, changes in chemical shifts of imino signals as levamisole is added indicate binding is occurring. The positions of the imino proton resonances were tracked as a function of levamisole concentration to determine the K_d value for the interaction by fitting to equation 6 in chapter 2 (Figure 6.7(b)). The K_d values of three imino signals were averaged to provide an average K_d value for levamisole binding MN19 of (1.7 ± 0.9) mM (Table 6.1). This weaker ligand binding by MN19 is consistent with MN19 binding weaker to other known cocaine-binding aptamer ligands such as cocaine and quinine [102].This is attributed to some of the binding free energy being used to fold the aptamer, with the remaining binding free energy being detected as an apparent K_d that is weaker than for MN4, an aptamer that does not need to use some of the binding free energy to fold.

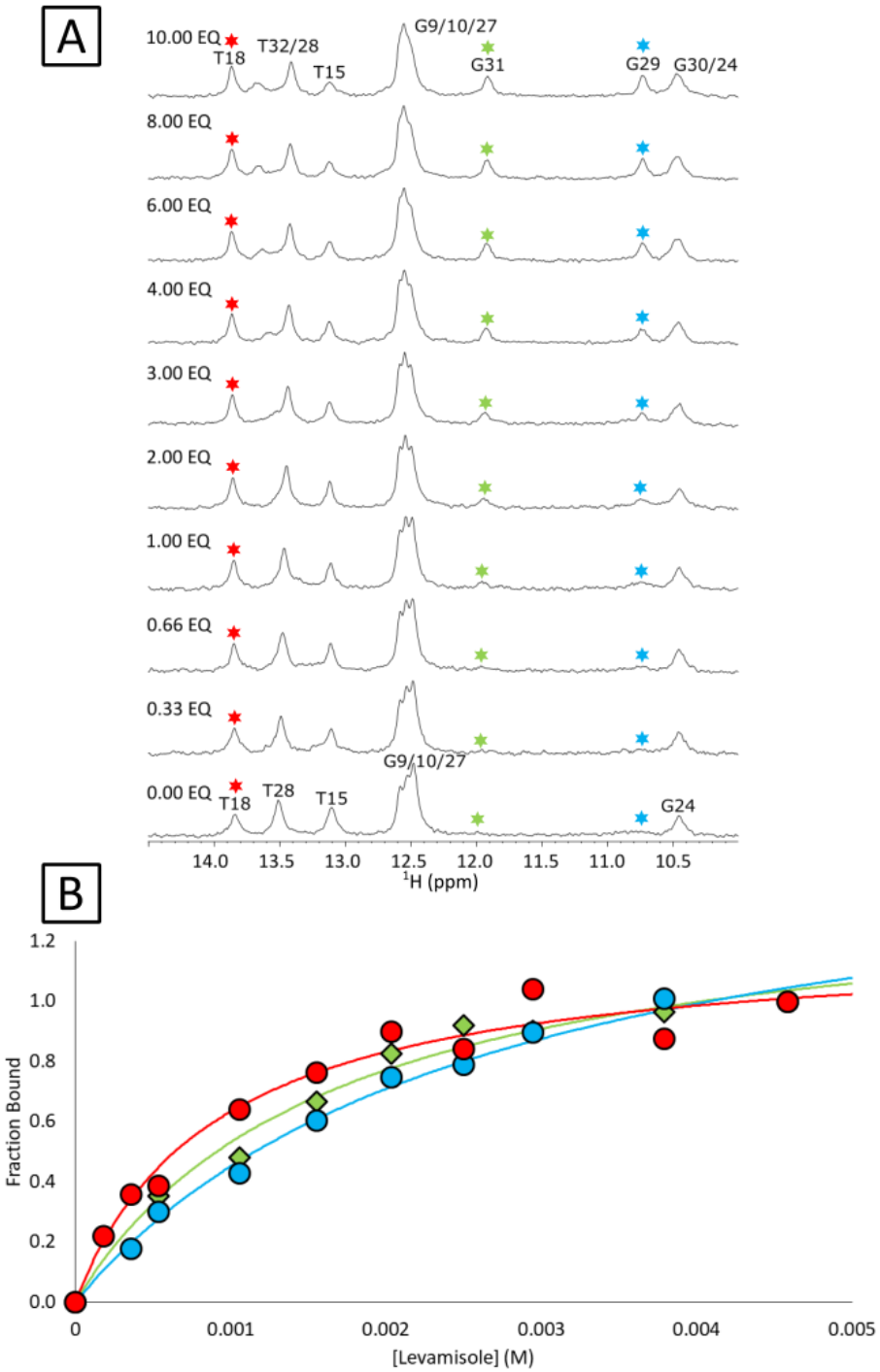

Figure 6.7. Levamisole binding by MN19 monitored by one-dimensional ^{1}H NMR. (a) The imino proton region of MN19 titrated with levamisole. Imino resonances marked with colored stars were used to determine the binding affinity. (b) The overlayed plots of the imino protons fit to the equation that describes 1:1 binding of levamisole and MN19. Solid line represents the fit and the data by the colored symbols. The color of the symbol and fit line match the peaks indicated with the same color in part (a). Experiments were conducted at 5 °C with a 500 μM DNA aptamer sample, in 245 mM KCl, 5 mM $K_xH_yPO_4$ pH 6.8 with 10% ^2H_2O.

A competition binding experiment was then conducted to see if levamisole and cocaine compete for the same binding site in MN19. First, the MN19-levamisole complex was titrated with cocaine (Figure 6.8) and signals indicative of the MN19-cocaine complex, such as the downfield T19 and the distinct T28 and T32 signals that are overlapped in the MN19 levamisole complex, were seen by a 2:1 molar ratio of cocaine:levamisole. Cocaine was also titrated into MN19 (Figure 6.9) with the NMR spectrum being identical to what has been seen and assigned previously [17], [76], [98]. This complex was then titrated with levamisole to a final molar ratio of levamisole to cocaine of 50:1 (Figure 6.9). By a ratio of approximately 30-50:1, the peaks indicative of cocaine-bound MN19 (particularly T19, T32, T28 and G4) were replaced with their levamisole-MN19 counterparts. Together, these experiments show that in MN19, as seen in MN4, levamisole and cocaine compete for the same binding site in the aptamer.

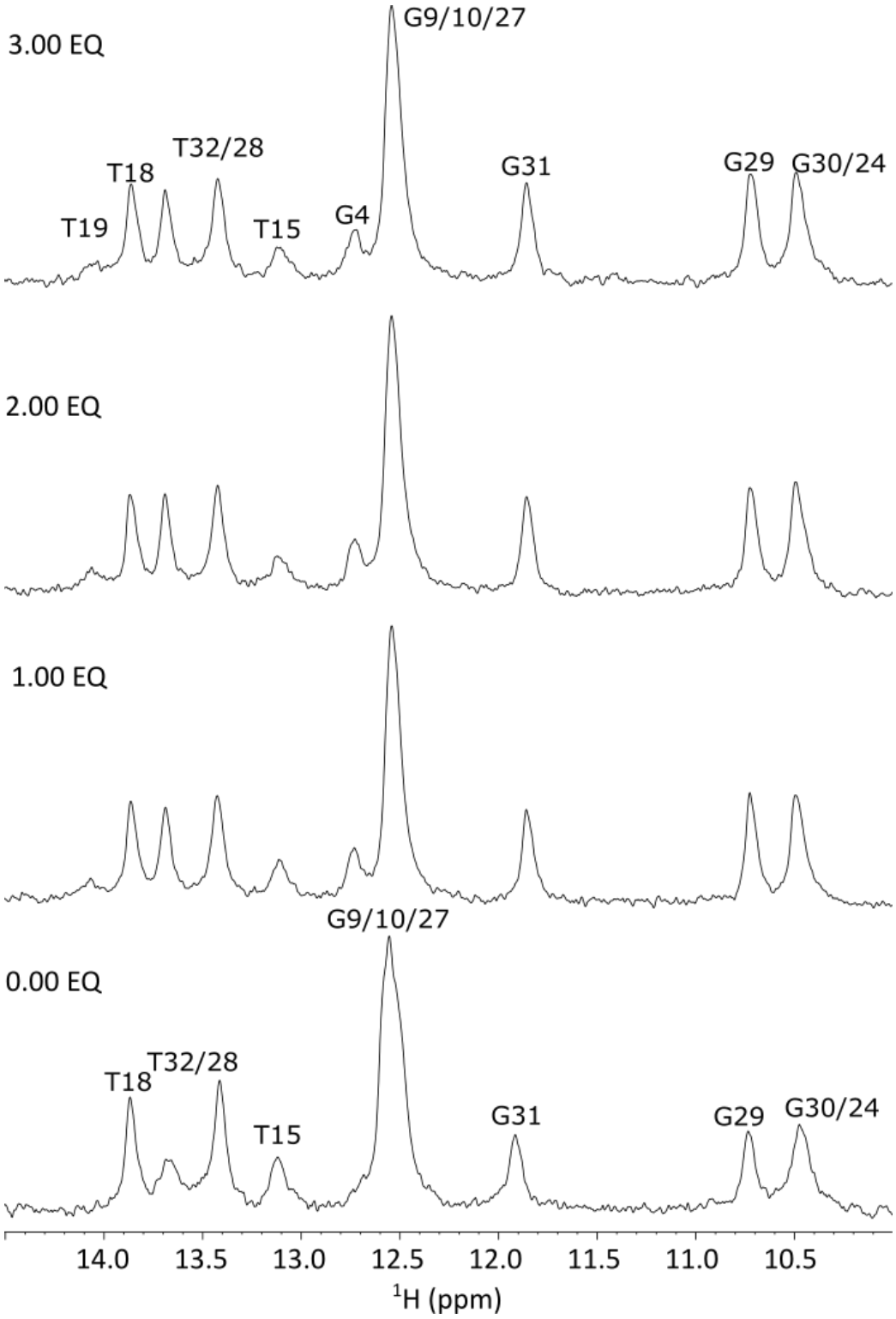

Figure 6.8. Levamisole displacement by cocaine in MN19 monitored by one-dimensional ^{1}H NMR. The imino proton region of levamisole-bound MN19 titrated with cocaine. Experiments were conducted at 5 °C with a 500 μM DNA aptamer sample, in 245 mM KCl, 5 mM $K_xH_yPO_4$ pH 6.8 with 10% ^2H_2O.

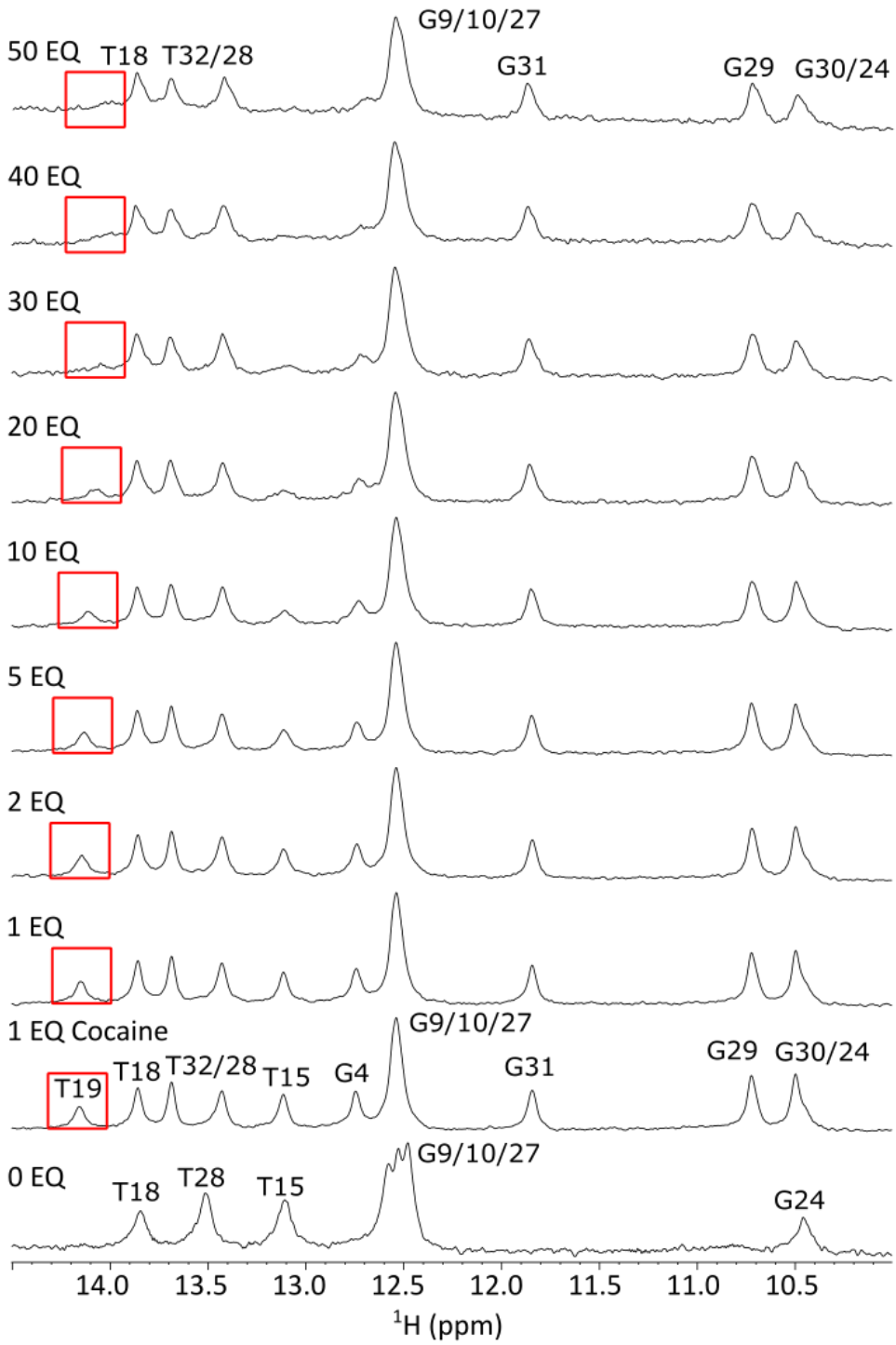

Figure 6.9. Cocaine displacement by levamisole in MN19 monitored by one-dimensional ^{1}H NMR. The imino proton region of cocaine-bound MN19 titrated with levamisole. The red box tracks the disappearance of T19 as cocaine is displaced by levamisole. Experiments were conducted at 5 °C with a 500 μM DNA aptamer sample, in 245 mM KCl, 5 mM $K_xH_yPO_4$ pH 6.8 with 10% ^2H_2O.

6.3.4 Effect of pH on the binding of MN4 and Levamisole. The pH dependence of the binding of levamisole by the MN4 aptamer was investigated by repeating the MN4-levamisole NMR titrations in a pH 6 and a pH 8 buffer. This was done as the pKa value of the tertiary amine in levamisole is ~7 and initial titrations were performed at pH 6.8 (Figures 6.2-6.4,6.7-6.9). This could potentially mean approximately half of the levamisole is protonated and half neutral. First, a titration of MN4 with levamisole was conducted in a pH 6 buffer (Figure 6.10(a)). At this pH, the imino spectra of free MN4 and levamisole-bound MN4 are essentially identical to the spectra acquired at pH 6.8. To determine the K_d of this interaction, the positions of several imino protons was tracked as a function of levamisole concentration and fit to equation 2.6 (Figure 6.10(b)) with the average K_d value being (0.35 ± 0.03) mM (Table 6.1). This affinity is very close to being within the error range for the value obtained at pH 6.8.

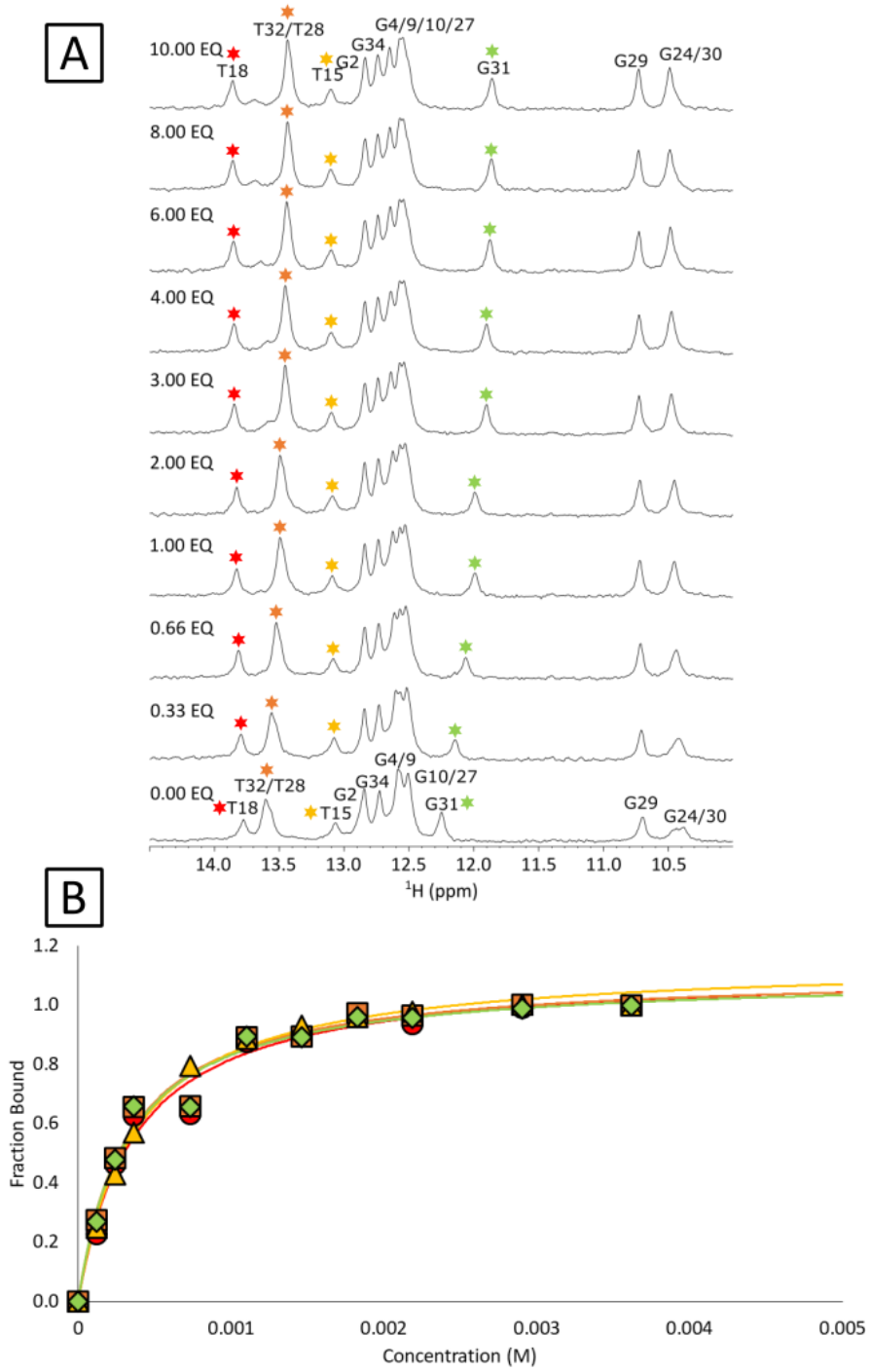

Figure 6.10. Levamisole binding by MN4 at pH 6.0 monitored by one-dimensional ^{1}H NMR. (a) The imino proton region of MN4 titrated with levamisole. Imino resonances marked with colored stars were used to determine the binding affinity. (b) The overlayed plots of the imino protons fit to the equation that describes 1:1 binding of levamisole and MN4. Solid line represents the fit and the data by the colored symbols. The color of the symbol and fit line match the peaks indicated with the same color in part (a). Experiments were conducted at 5 °C with a 500 µM DNA aptamer sample, in 245 mM KCl, 5 mM $K_xH_yPO_4$ pH 6.0 with 10% $^{2}H_2O$.

A titration of MN4 with levamisole in a pH 8 buffer was then performed (Figure 6.11(a)). At this pH value, the imino protons of several nucleotides, including T15, G29, G24 and G30 are not observable, likely due to a change in hydrogen exchange rate at this pH. Binding was still observed and the imino proton resonance positions of G31 and T32/T28 were tracked as a function of levamisole concentration and fit to equation 2.6 (Figure 6.11(b)). The values of these fits can be seen in Table 6.1 and the average K_d value at pH 8 is (0.38 ± 0.05) mM. The measured K_d values obtained at pH 8 agree within the uncertainty. Within the pH 6 to pH 8 range tested, there does not appear to be an appreciable difference in the K_d of the MN4 and levamisole interaction indicating that binding is not dependent on the protonation state of the tertiary amine or that the pK_a value of this atom is significantly different from predicted.

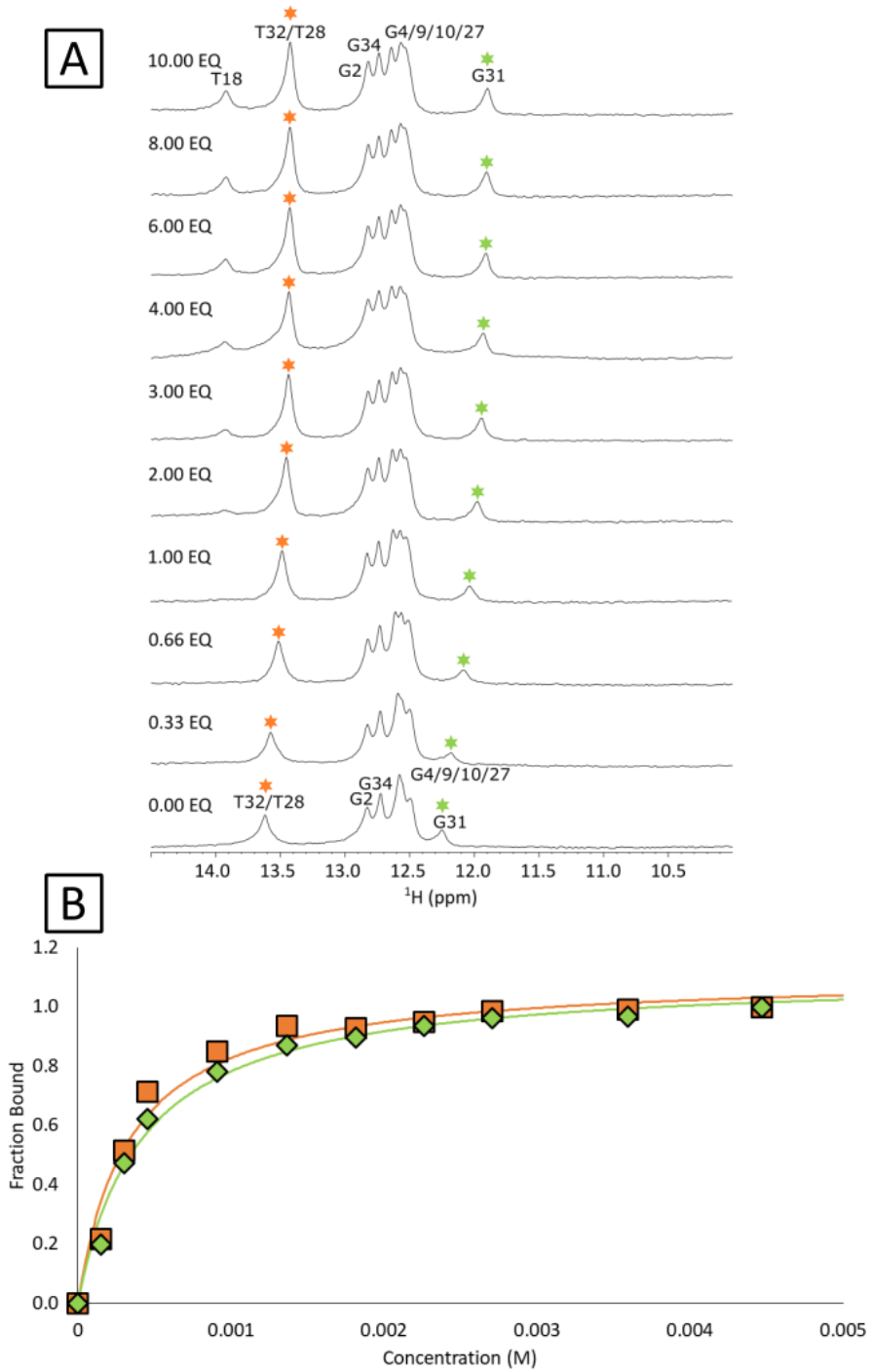

Figure 6.11. Levamisole binding by MN4 at pH 8.0 monitored by one-dimensional ^{1}H NMR. (a) The imino proton region of MN4 titrated with levamisole. Imino resonances marked with colored stars were used to determine the binding affinity. (b) The overlayed plots of the imino protons fit to the equation that describes 1:1 binding of levamisole and MN4. Solid line represents the fit and the data by the colored symbols. The color of the symbol and fit line match the peaks indicated with the same color in part (a). Experiments were conducted at 5 °C with a 500 µM DNA aptamer sample, in 200 mM NaCl, 20 mM NH_4^+ pH 8.0 with 10% $^{2}H_2O$.

6.4 Concluding Remarks

In this chapter the question of whether levamisole binds to the cocaine-binding aptamers MN4 and MN19 was investigated. The question is interesting as levamisole is a common adulterant of cocaine sample and can cause harm when someone uses the adulterated substance. In addition, levamisole can also interfere with electrochemical detection methods for cocaine. Weak binding of levamisole was seen for both MN4 and MN19 (Table 6.1) as seen in the change in the imino ^{1}H signals in the aptamer (Figures 6.2 and 6.7). Both levamisole and cocaine contain both aromatic and aliphatic ring structure, though the aliphatic ring structures between the two molecules are significantly different. Cocaine is a bit larger than levamisole and could form more hydrogen bond due to the presence of the ester groups within the molecule. This might allow cocaine to sit more nicely in the binding pocket of the aptamer and interact with more nucleotides. This interaction of levamisole with the cocaine-binding aptamer while weak is still specific to this aptamer and not a result of non-specific interaction. Because this interaction is so weak, it should not interfere with aptamer-based assays. This was tested using the PHASA assay in the published study, which was able to detect cocaine in the presence of levamisole[2].

[2] These experiments were performed by Aron Shoara in the Johnson lab and discussed here to clarify results. These results can be seen in the initial reference for this chapter.

Chapter 7: **Characterization of the interactions of three-way junction dyes to the Cocaine-Binding Aptamer**

7.1 Preface

Some work presented in this chapter has been published in the article listed below.

- Van Riesen A. J., Le J., Slavkovic S., **Churcher Z. R.,** Shoara A. A., Johnson P. E., and Manderville R. A. "Visible Fluorescent Light-up Probe for DNA Three-Way Junctions Provides Host-Guest Biosensing Applications." *ACS Applied Biomaterials.* **4 (9)**, 6732-6741 (2021) [164].

7.2 Introduction

DNA three-way junctions (TWJs) are a type of structure where three duplex stems make a Y-shaped intersection with a hydrophobic core [165]. This structural motif can be used as a druggable target and has been used to cause apoptosis in cancer cells [166]. This structure is important for building DNA nanostructures [167], [168] and can be used as the ligand binding site in aptamers.

Several dyes already exist that bind to other DNA structures such as duplex DNA and G-quadruplexes. These types of dyes can be used to create aptasensor systems, where the light up probe does not require chemical modification of the aptamer [168], [169]. Some of these dyes include thiazole orange [170], thioflavin T [171], and SYBR Green I [172]. These dyes have a very low fluorescence quantum yield in the free state, but they light up upon binding to DNA. This is due to the ability of the dye to rotate easily in the free state but becomes more rigid in the bound state [173]. Dyes that bind three-way junctions are rare but some of these include blue cyanine (Cy7) [103], naphthyridine (ATMND [59]), and calix[3]carbazole [174]. These dyes need to be able to recognize the Y-shaped binding pocket, and ideally can be displaced upon binding of a ligand. This displacement would allow a signal to be seen upon ligand binding using fluorescence.

Dye-F is a TWJ-binding fluorescent dye (Figure 7.1), which after being synthesized was found to bind to three-way junction in DNA. The dye itself is composed of a N-methyl-

benzothiazolium (Btz) linked to an ortho-fluoro-phenol (FPh) by a vinyl linkage. The Btz group acts as a DNA binding motif for fluorescent probes [170]–[172], [175] and the FPh group acts as a pH indicator [176] favoring the phenolate form at pH 7.4. This also allows the dye to switch to a quinone methide form in non-polar solvents or when binding to a three-way junction.

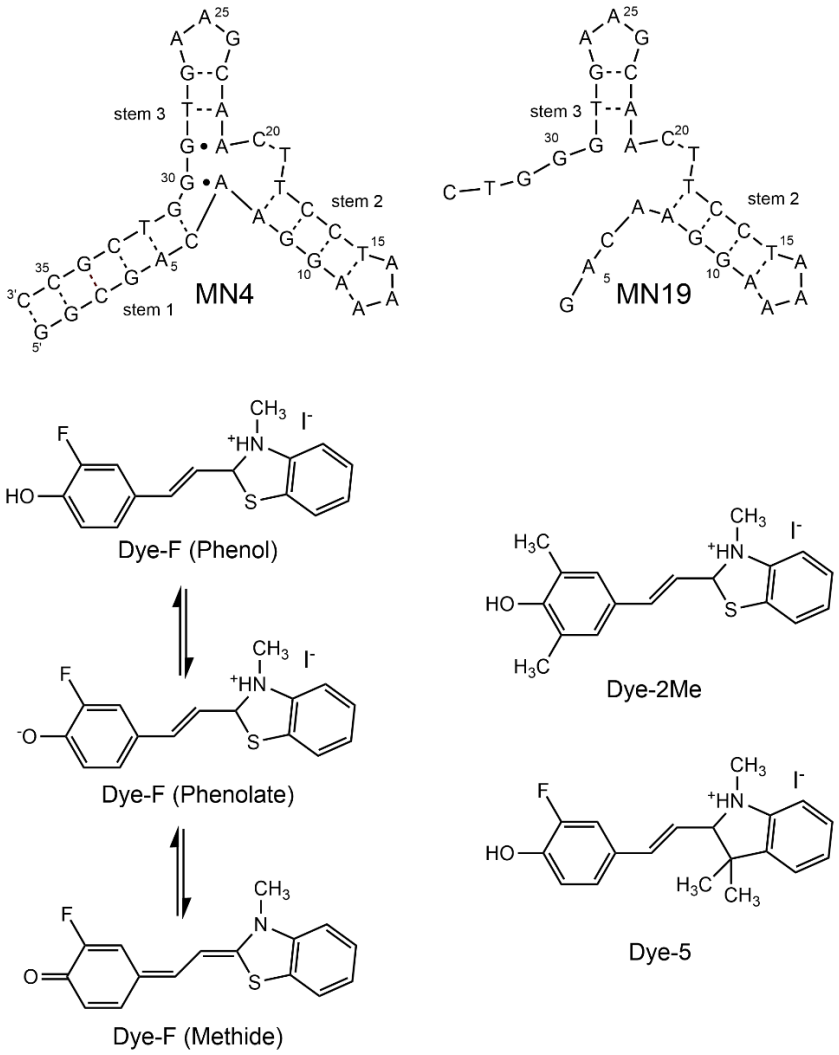

Figure 7.1. Secondary structure of MN4 and MN19, and chemical structures of Dye-F, Dye-2Me, and Dye-5. On the left shows Dye-F as it transitions from its phenol to its methide forms, this reaction is also possible for Dye-2Me and Dye-5. For ease of comparison, both aptamers follow the same numbering scheme. Bases that are linked by dashes are Watson-Crick base pairs, while bases linked by dots are non-Watson-Crick base pairs.

The cocaine-binding aptamer consists of three stems centered around a TWJ. [17], [103], [177] This TWJ is used as the ligand binding site for cocaine and other ligands which were not

selected for, such as quinine [73], amodiaquine [57], artemisinin, and levamisole [139]. It is worth noting that the aptamer can bind to some of these ligands with a higher affinity than cocaine. The specific cocaine-binding aptamer constructs used here are MN4 and MN19 (Figure 7.1). MN4 has a longer stem 1 which causes the aptamer construct to be less dynamic and more structured in the absence of any ligand, while MN19 has a short stem 1 which causes this construct to be more dynamic and less structured in its free state. In this chapter, ^{1}H NMR spectroscopy is used to characterize the binding of Dye-F and two derivative dyes (Figure 7.1) to both MN4 and MN19, in order to see if these three-way junction specific dyes interact with the cocaine-binding aptamer in a similar manner to its ligands.

7.3 Results and Discussion

7.3.1 Dye-F binds specifically to TWJ DNA structures[3]. Using a variety of methods Dye-F was found to bind MN4 and the cholic acid-binding aptamer (CABA). Using ITC the K_d of Dye-F binding to MN4 was measured to be 0.42 μM at 15 °C. This is tighter than the K_d of MN4 for cocaine (5.5 μM), but not as tight as for quinine (0.21 μM). ITC was also used to quantify the the K_d of CABA for Dye-F (9 μM) which is tighter than the K_d of CABA for cholic acid (24 μM). Dye-F is fluorescent, and its fluorescence increased upon binding to a TWJ. This increase was ~180-fold with CABA and ~734-fold for MN4. This increase in fluorescence was not seen with Dye-F when added to duplex and quadruplex oligonucleotide systems.

7.3.2 TWJ Binding Specificity by Dye-F and Target-Mediated Displacement. To provide information on the location of the binding site of Dye-F in the MN4 aptamer, dye binding was monitored using 1D ^{1}H NMR spectroscopy. The imino proton region of MN4 is displayed in Figure 7.2. The free MN4 sample looks very similar to previously reported spectra [76], [98]. As

[3] Results in this section were obtained by other authors in the referenced paper. The results have been included here to help clarify the properties of Dye-F.

Dye-F was titrated into the MN4 sample some of the imino proton resonances shifted, consistent with ligand binding. The identities of the imino proton resonances for the Dye-F-bound MN4 were confirmed using a 2D NOESY spectroscopy (Figure 7.3). The connectivity observed with Dye-F-bound MN4 is the same as that observed in previous MN4 NOESY experiments with different ligands such as cocaine and quinine [17], [98] indicating that MN4 forms a similar structure to these when bound to Dye-F.

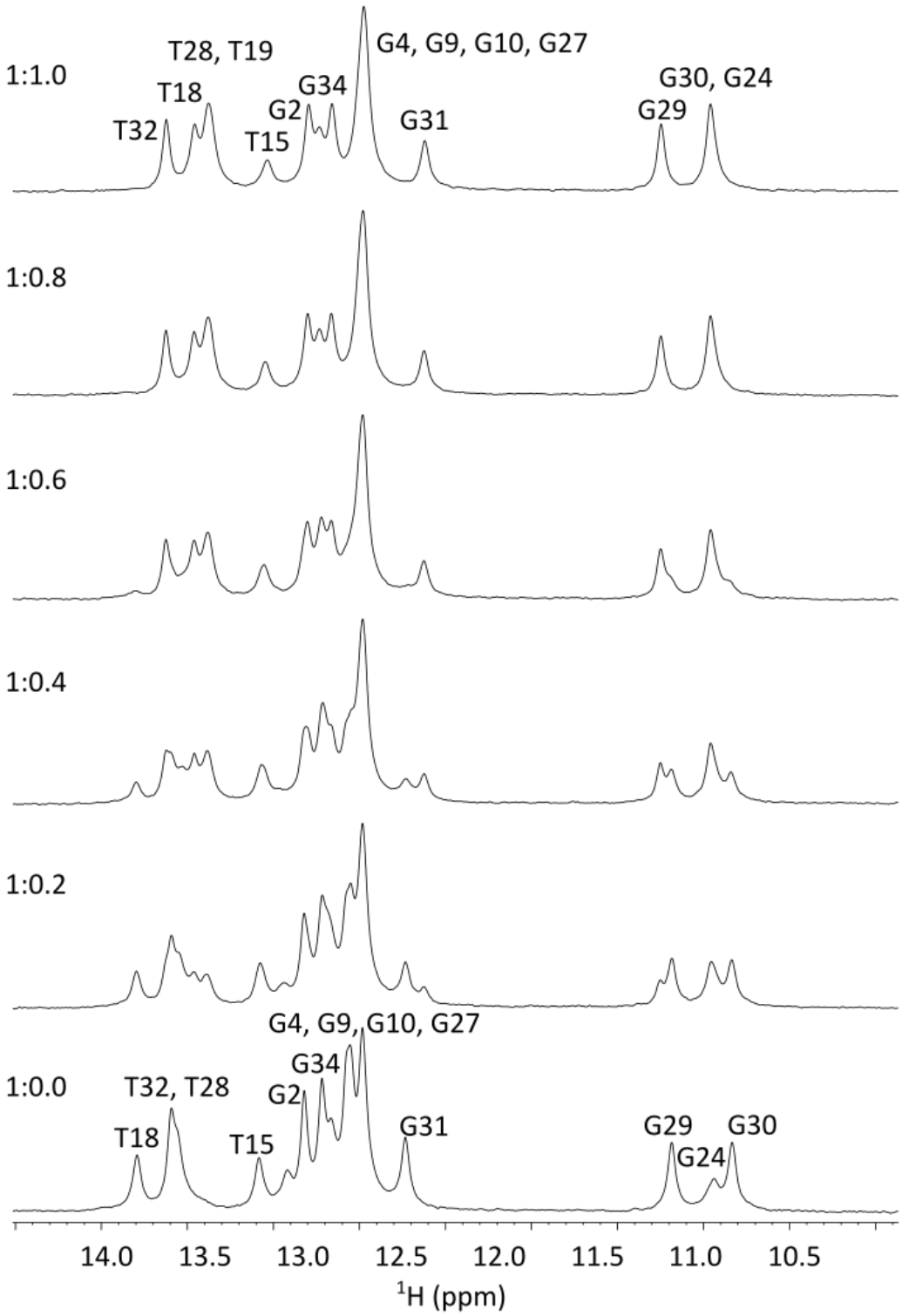

Figure 7.2. One-dimensional ^{1}H NMR spectra showing the titration of Dye-F into the MN4 cocaine binding aptamer. Spectra show the imino proton resonances of the NMR spectra. Ratios on the spectrum denote the molar ratio of aptamer to Dye-F. Spectra were acquired with an MN4 concentration of 1.4 mM in 140 mM NaCl, 10 mM $Na_xH_yPO_4$, pH 6.8, 10% ^2H_2O–90% H_2O at 5 °C.

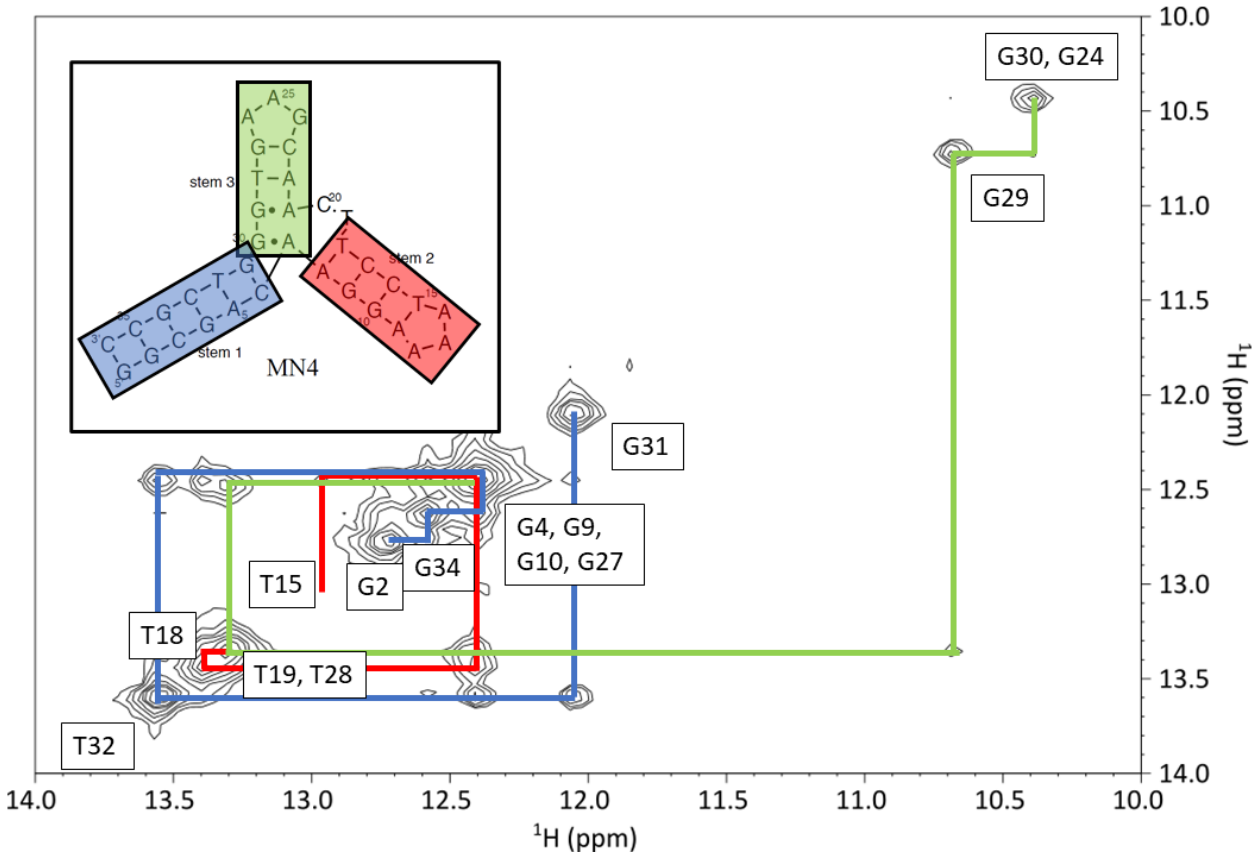

Figure 7.3. 2D ^{1}H–^{1}H NOESY spectrum of the Dye-F-bound MN4 cocaine-binding aptamer. Spectrum shows the imino-imino cross peaks used to assign the Dye-F-bound MN4 aptamer. Spectra were acquired with an MN4 concentration of 1.4 mM in 140 mM NaCl, 10 mM $Na_xH_yPO_4$, pH 6.8, 10% ^2H_2O–90% H_2O at 5 °C.

The position of the imino protons in MN4 between the free and the Dye-F-bound MN4 and their change in chemical shift is provided in Figure 7.4. The imino protons that change chemical shift most with Dye-F binding are T18, T28, G30, and G31 (Figure 7.1). These four resonances are all located at or adjacent to the TWJ of the aptamer, which is the high-affinity binding site for cocaine and quinine. The resonances that shift most with Dye-F binding are very similar to the resonances that shift most with cocaine binding (G31, T32, T28, and G30) and quinine binding (G31, T18, G24, and G30) [98], suggesting TWJ binding by the dye.

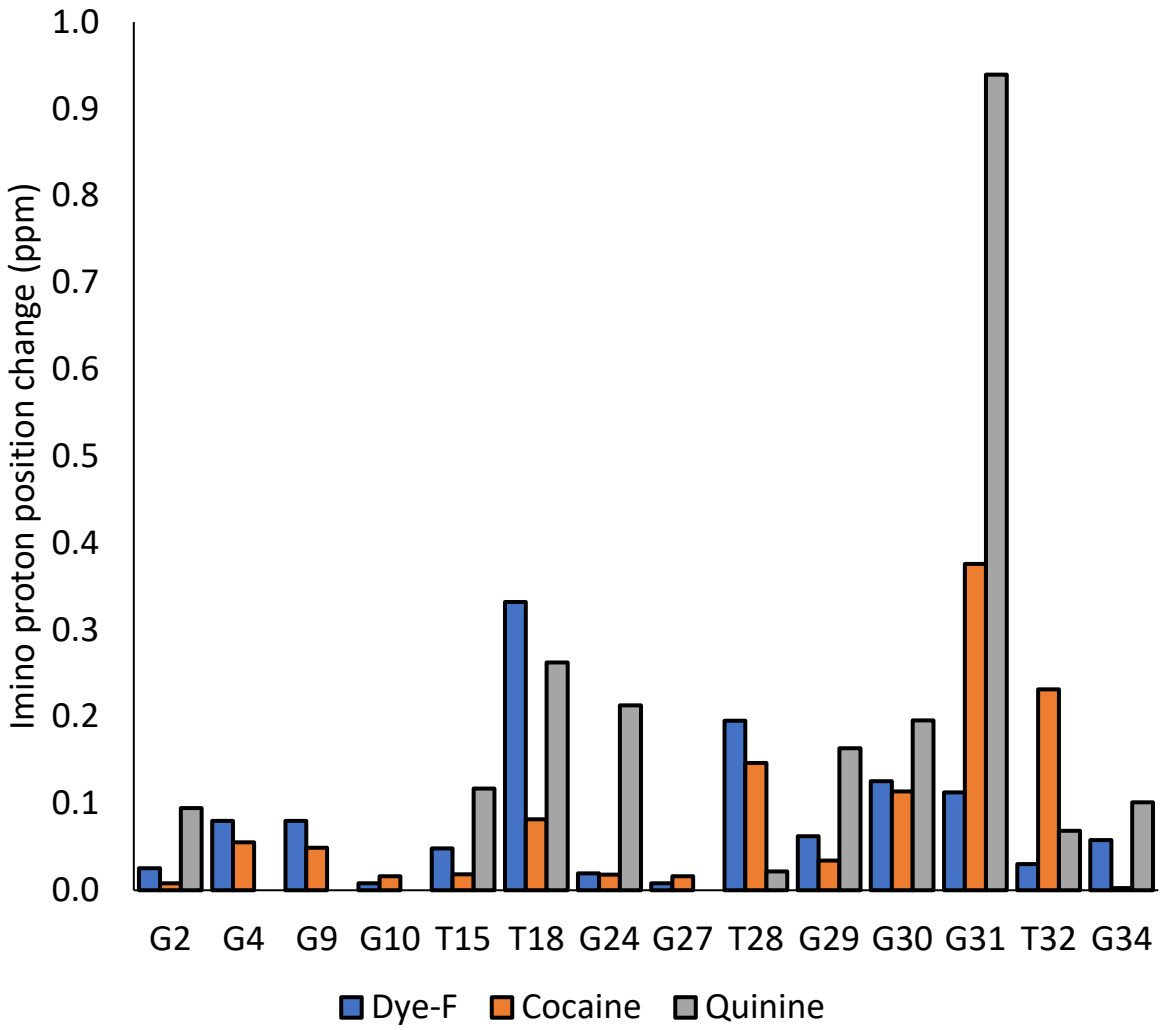

Figure 7.4. Histogram showing the change in 1H NMR chemical shift between free and bound MN4 cocaine-binding aptamer $\left|(\delta_{bound} - \delta_{free})\right|$. This comparison was done for MN4 bound to Dye-F (blue), cocaine (orange), and quinine (grey).

Quinine was also titrated into a sample of MN4−Dye-F and tracked with 1D ^{1}H NMR to see if the two ligands compete for the same binding site (Figure 7.5). In quinine-bound MN4 (top spectrum, Figure 7.5), the position of the G31 imino proton resonance is indictive of quinine binding and appears at 11.1 ppm in the bound aptamer [73], while in Dye-F MN4 the G31 proton is located downfield at 12.2 ppm (1:1:0.00 spectrum). As quinine was added to the Dye-F-bound sample, the G31 imino resonance associated with the Dye-F-bound aptamer began to decrease in intensity and the upfield resonance associated with quinine-bound aptamer began to appear

(indicated by red dot in Figure 7.5) as the two states are in slow exchange on the NMR time scale. The downfield G31 resonance continued to shrink in intensity and the upfield resonance grew in intensity as quinine was added until a ratio of 1:1:1 MN4:Dye-F:quinine, at which point the Dye-F-bound G31 peak had disappeared. The peaks in the final titration point are broadened when compared with the original Dye-F-bound MN4 or a sample of quinine-bound MN4. Similar broadening was observed in previous NMR competition experiments between cocaine and quinine [73]. Thus, the NMR experiments confirm competitive displacement of MN4-bound Dye-F by quinine.

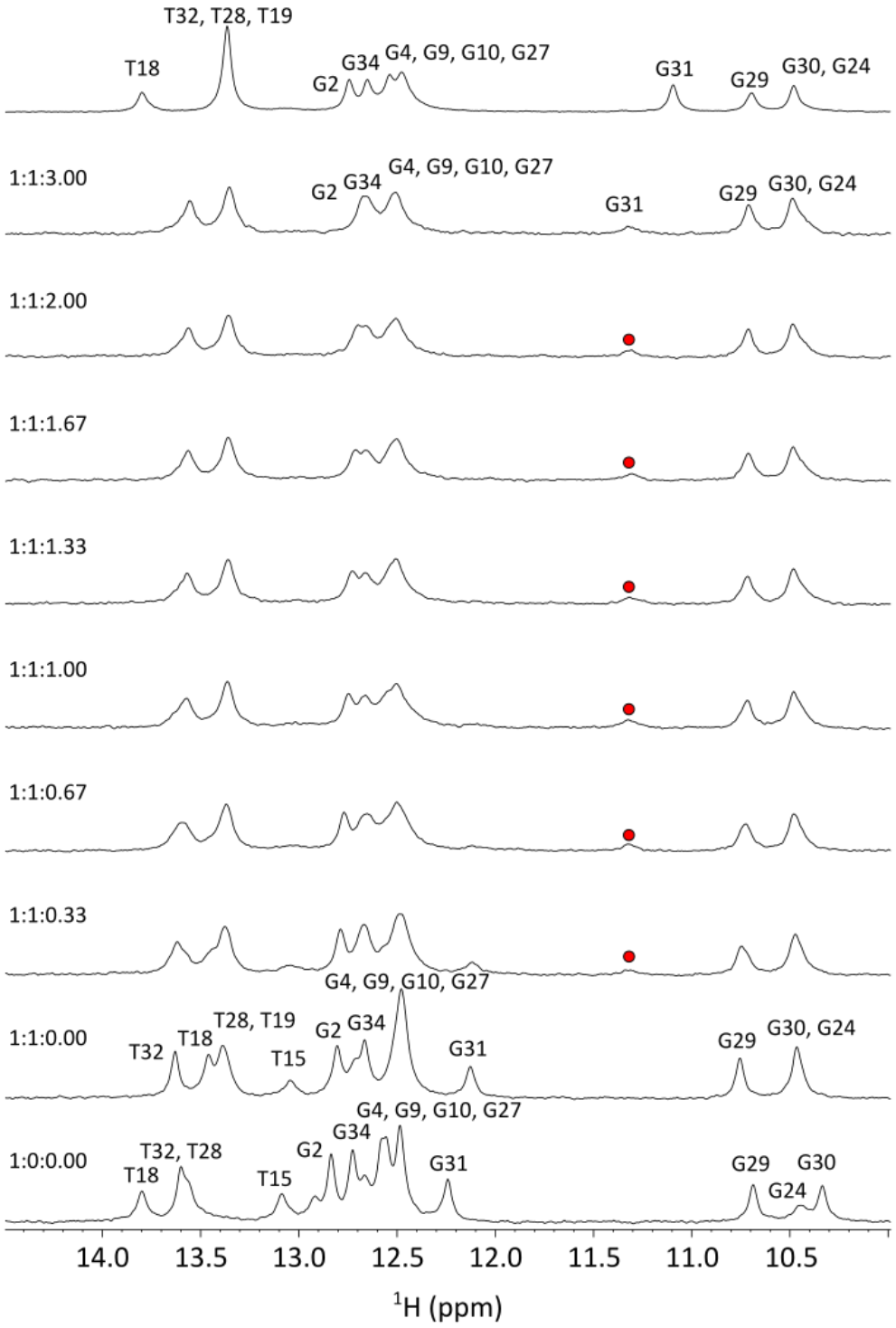

Figure 7.5. ^{1}H NMR spectra showing the imino proton resonances during a titration of Dye-F and quinine into a sample of the MN4 aptamer. Ratios on the left-hand side show the molar ratio of aptamer:Dye-F:quinine. Top spectrum shows a reference spectrum of MN4 bound to quinine in the absence of Dye-F. Spectra were acquired with an MN4 concentration of 1.4 mM in 140 mM NaCl, 10 mM $Na_xH_yPO_4$, pH 6.8, 10% ^2H_2O−90% H_2O at 5 °C. Emergence of the G31 resonance for quinine-bound MN4 is highlighted by the red dot.

7.3.3 Derivative dyes of Dye-F also bind to MN4. After the binding of the original Dye-F was characterized, a set of dyes based on the original were synthesized in order to investigate their potential binding properties. These derivative dyes were investigated initially using ITC[4] to determine which ones bind to MN4, and two dyes were picked to investigate further in the NMR. These dyes are called Dye-2Me and Dye-5 (Figure 7.1). Dye-2Me differs from the original dye in that the single fluorine group relative to the phenol group has been replaced by two methyl groups, one of each ortho position (Figure 7.1). For Dye-5 the structure differs from the original in the benzothiazolium group where the sulfur atom has been replaced with a carbon with two methyl groups attached (Figure 7.1). Dye-2Me binds to MN4 tighter than the original dye with a K_d of 0.04 μM, while Dye-5 binds to MN4 weaker than the original dye and weaker than cocaine with a K_d of 8.1 μM both at 5 °C.

1D ^{1}H NMR spectroscopy was used to track the imino proton resonances of MN4 as Dye-2Me was added to the DNA. This titration can be seen in Figure 7.6. The free state looked the same as the previous MN4 sample, and the positions of the imino proton resonances were tracked throughout the titration. A 2D ^{1}H-^{1}H NOESY was done on the Dye-2Me-bound MN4 sample to confirm the identities of the imino proton resonances. The connectivity pattern was similar to what was seen with Dye-F and other previous ligands. This indicates that the structure of the ligand-bound MN4 does not differ greatly between these two dyes. This NOESY can be seen in Figure 7.7.

[4] Experiments performed by Sladjana Slavkovic from the Johnson lab, added here to further clarify results. Data in section 7.3.3 and 7.3.4 has not yet been published.

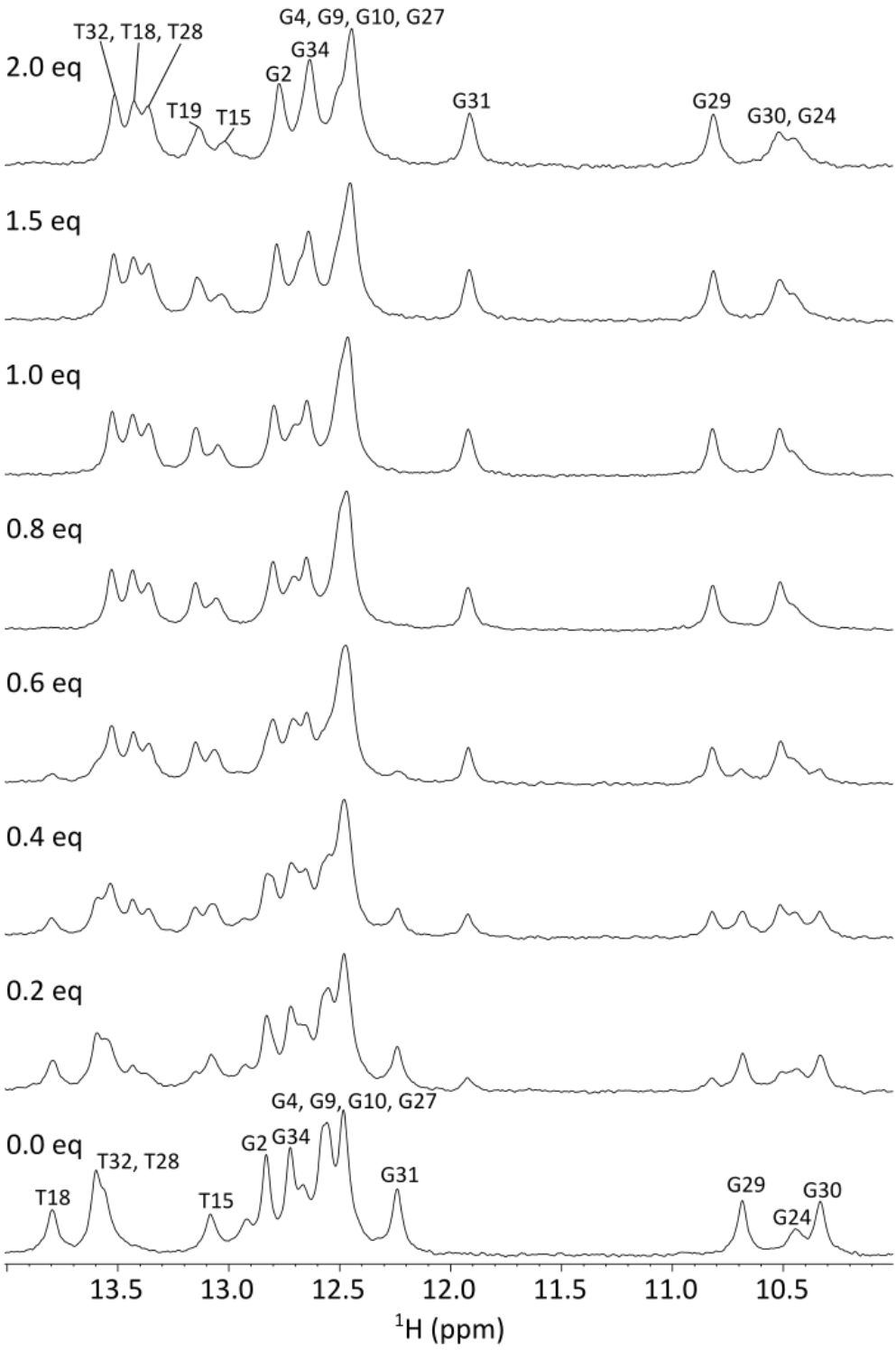

Figure 7.6. One-dimensional ^{1}H NMR spectra showing the titration of Dye-2Me into the MN4 cocaine-binding aptamer. Spectra show the imino proton resonances of the NMR spectra. Ratios on the spectrum denote the molar ratio of aptamer to Dye-2Me. Spectra were acquired with an MN4 concentration of 500 μM in 140 mM NaCl, 10 mM $Na_xH_yPO_4$, pH 6.8, 10% ^2H_2O−90% H_2O at 5 °C.

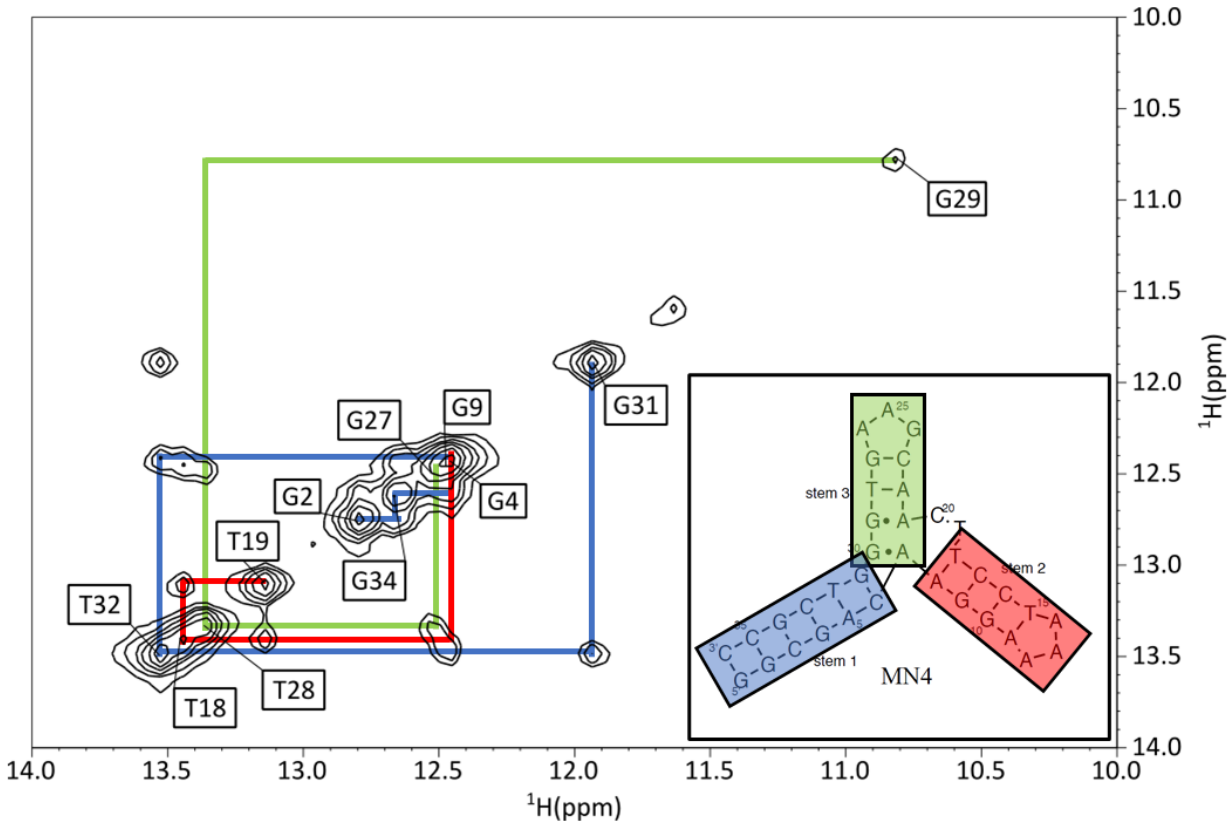

Figure 7.7. 2D ^{1}H–^{1}H NOESY spectrum of the Dye-2Me-bound MN4 cocaine-binding aptamer. Spectrum shows the imino-imino cross peaks used to assign the Dye-2Me-bound MN4 aptamer. Spectra were acquired with an MN4 concentration of 1.4 mM in 140 mM NaCl, 10 mM $Na_xH_yPO_4$, pH 6.8, 10% ^2H_2O–90% H_2O at 5 °C.

1D ^{1}H NMR spectroscopy was also used to track the imino proton resonances of MN4 as Dye-5 was added to the DNA. This titration can be seen in Figure 7.8. The free state looked the same as the previous MN4 sample. Again, a 2D ^{1}H-^{1}H NOESY was performed on the Dye-5-bound MN4 sample to confirm the identities of the imino protons. This connectivity pattern was similar to what was seen with the previous dyes, again indicating that the structure of the dye-bound MN4 does not differ greatly. This NOESY can be seen in Figure 7.9

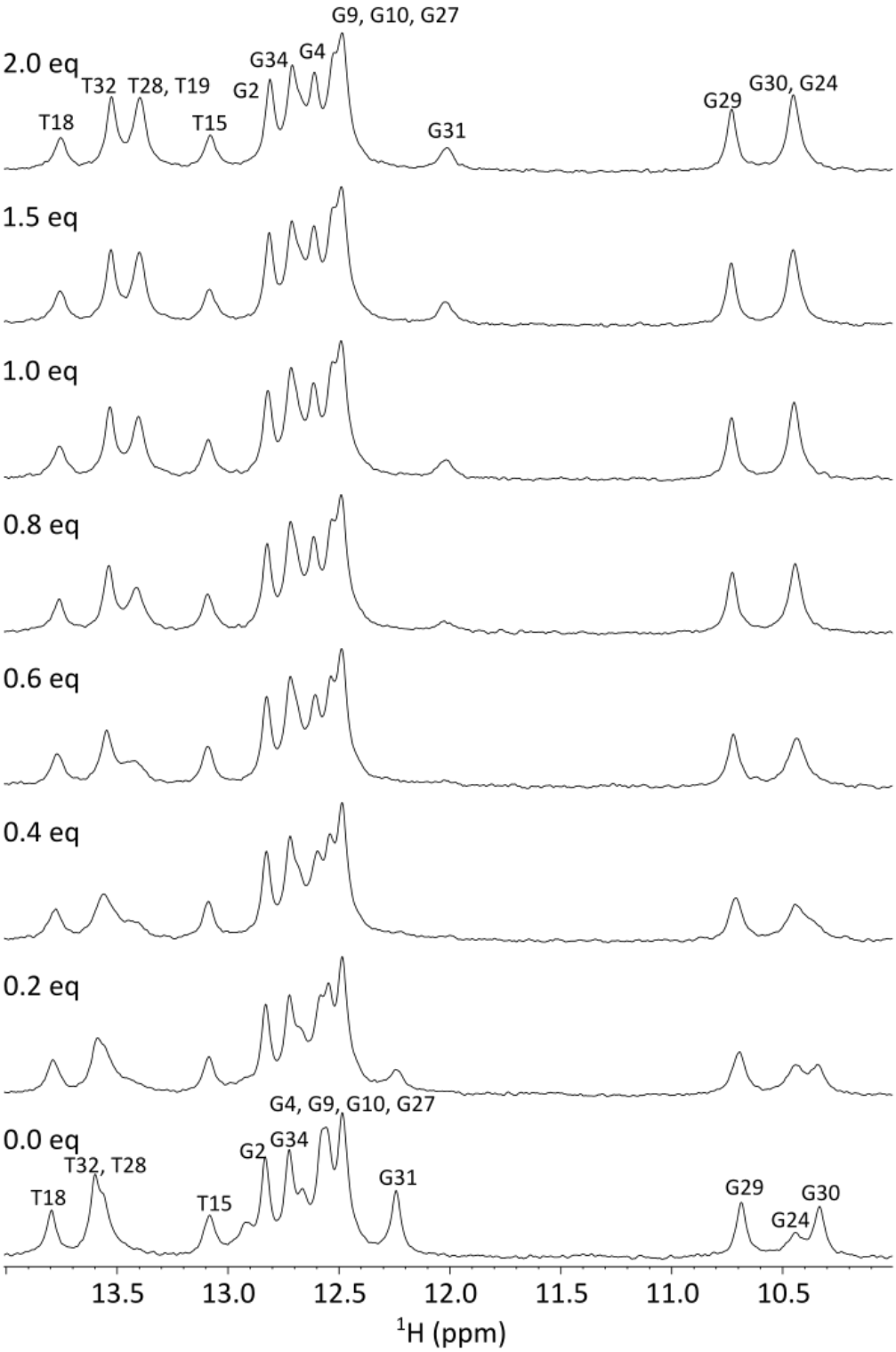

Figure 7.8. One-dimensional ^{1}H NMR spectra showing the titration of Dye-5 into the MN4 cocaine binding aptamer. Spectra show the imino proton resonances of the NMR spectra. Ratios on the spectrum denote the molar ratio of aptamer to Dye-5. Spectra were acquired with an MN4 concentration of 500 μM in 140 mM NaCl, 10 mM $Na_xH_yPO_4$, pH 6.8, 10% ^2H_2O−90% H_2O at 5 °C.

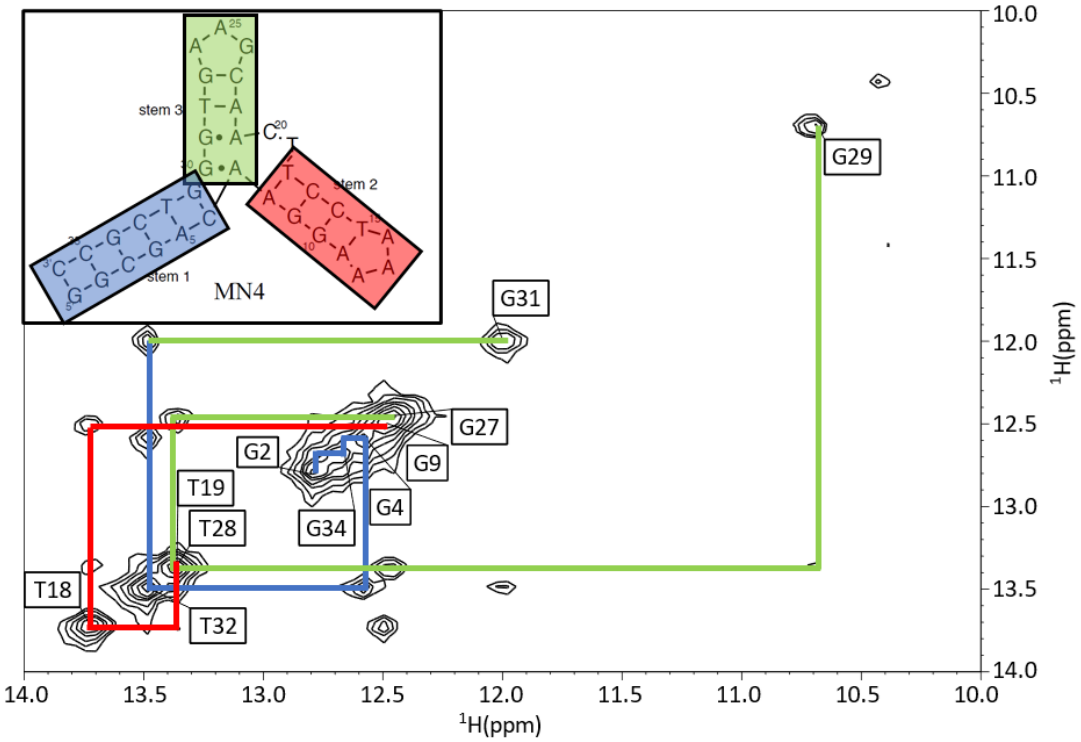

Figure 7.9. 2D ^{1}H–^{1}H NOESY spectrum of the Dye-5-bound MN4 cocaine-binding aptamer. Spectrum shows the imino-imino cross peaks used to assign the Dye-5-bound MN4 aptamer. Spectra were acquired with an MN4 concentration of 1.4 mM in 140 mM NaCl, 10 mM $Na_xH_yPO_4$, pH 6.8, 10% ^2H_2O–90% H_2O at 5 °C.

Cocaine was added to the Dye-5-bound MN4 sample to try and displace the bound dye. This titration was tracked using ^{1}H NMR to see if a spectrum similar to that of MN4 bound to cocaine could be achieved. This titration can be seen in Figure 7.10. Like with the MN4-Dye-F-Quinine titration the position of G31 was tracked. The position of G31 in cocaine-bound MN4 is ~11.6 ppm, while in the Dye-5-bound MN4 the position of G31 is ~12.0 ppm Upon addition of 1 equivalent of cocaine to the Dye-5-bound sample G31 moved upfield toward the cocaine-bound position. Another characteristic imino proton resonance for cocaine-bound MN4 is the presence of T19 at ~14.1 ppm. This resonance does not show up in the spectrum of the free aptamer. After the addition of 10.0 equivalents of cocaine to the Dye-5-bound MN4 sample, the resonance of T19 could be seen. At this point the spectrum of the MN4-Dye-5-cocaine sample highly resembled that of the MN4-cocaine spectrum.

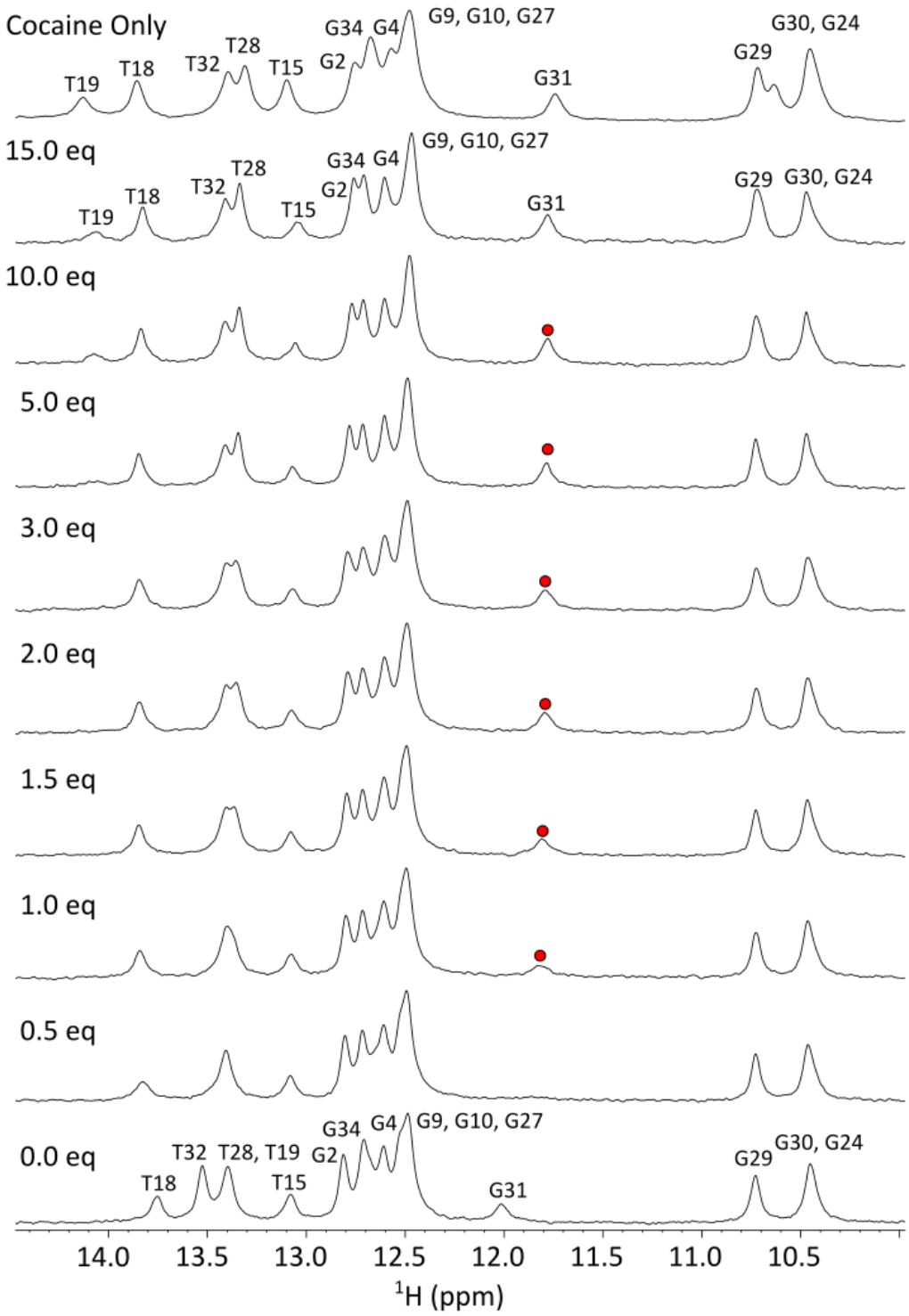

Figure 7.10. ^{1}H NMR spectra showing the imino proton resonances during a titration of Dye-5 and cocaine into a sample of the MN4 aptamer. Ratios on the left-hand side show the molar ratio of aptamer:Dye-5:cocaine. Top spectrum shows a reference spectrum of MN4 bound to cocaine in the absence of Dye-5. Spectra were acquired with an MN4 concentration of 500 μM in 140 mM NaCl, 10 mM $Na_xH_yPO_4$, pH 6.8, 10% ^2H_2O−90% H_2O at 5 °C. Emergence of the G31 resonance for cocaine-bound MN4 is highlighted by the red dot.

The position of the imino proton resonances as the dyes were added was tracked using ^{1}H NMR. A histogram showing the absolute change in imino proton resonance position between the free and bound aptamer can be seen in Figure 7.11. Like with Dye-F, the imino proton resonances with the largest chemical shift changes are in the resonances around the three-way junction. These include T18, T28, G30, and G31. T18 is the resonance that changes position the most with both Dye-F and Dye-2Me, while G31 is the resonance that changes position the most with the binding of Dye-5 and with cocaine. T28 is adjacent to the three-way junction and is a resonance that changes its position a relatively large amount with ligand binding. For Dye-F and Dye-5, it is the resonance that changes its position the second greatest and for Dye-2Me is the third greatest. This is evidence that Dye-2Me and Dye-5 and binding in a similar manner to Dye-F and cocaine.

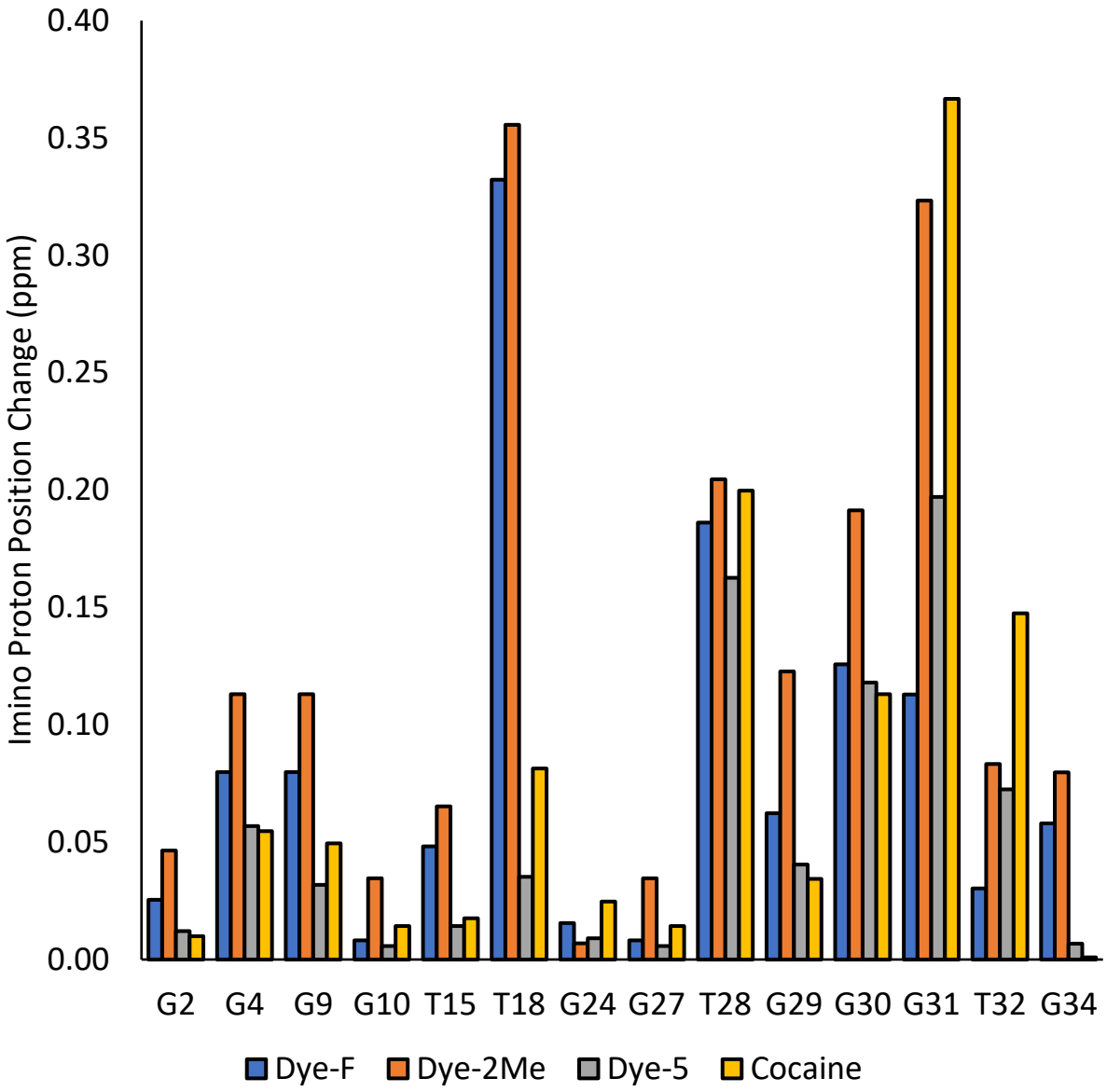

Figure 7.11. Histogram showing the change in ^{1}H NMR chemical shift between free and bound MN4 cocaine-binding aptamer $|(\delta_{bound} - \delta_{free})|$. This comparison was done for MN4 bound to Dye-F (blue), Dye-2Me (orange), Dye-5 (grey), and Cocaine (yellow).

7.3.4 Dye-F and Derivative dyes also bind and fold MN19. Next ^{1}H NMR spectroscopy was used to determine if Dye-F, Dye-2Me, and Dye-5 would bind to MN19. Each dye was titrated into a sample of MN19 as the imino proton resonances were monitored using ^{1}H NMR spectroscopy. These titrations can be seen in Figure 7.12 for MN19 & Dye-F, Figure 7.13 for MN19 & Dye-2Me, and Figure 7.14 for MN19 & Dye-5.

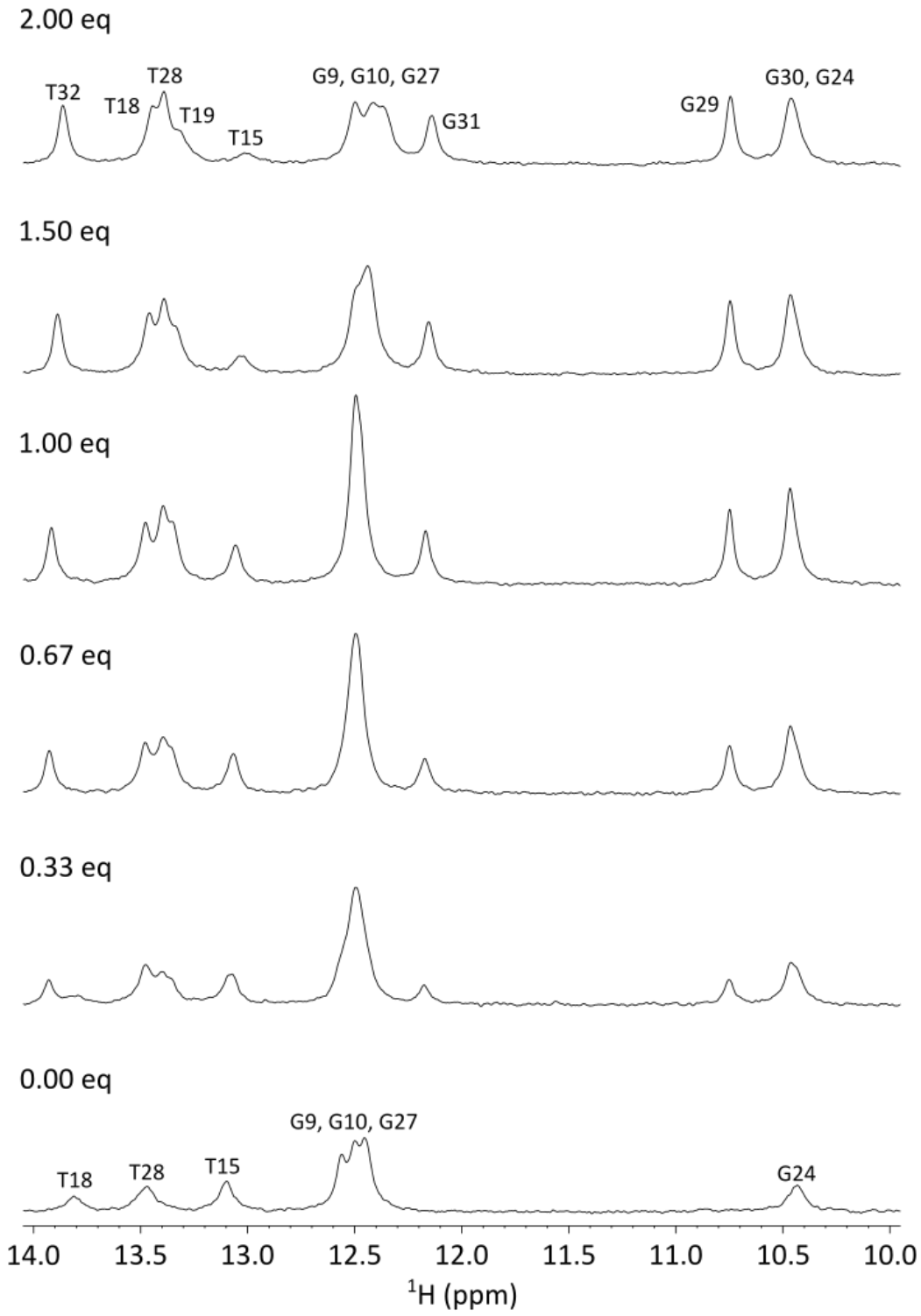

Figure 7.12. One-dimensional ^{1}H NMR spectra showing the titration of Dye-F into the MN19 cocaine binding aptamer. Spectra show the imino proton resonances of the NMR spectra. Ratios on the spectrum denote the molar ratio of aptamer to Dye-F. Spectra were acquired with an MN4 concentration of 500 μM in 140 mM NaCl, 10 mM $Na_xH_yPO_4$, pH 6.8, 10% ^2H_2O−90% H_2O at 5 °C.

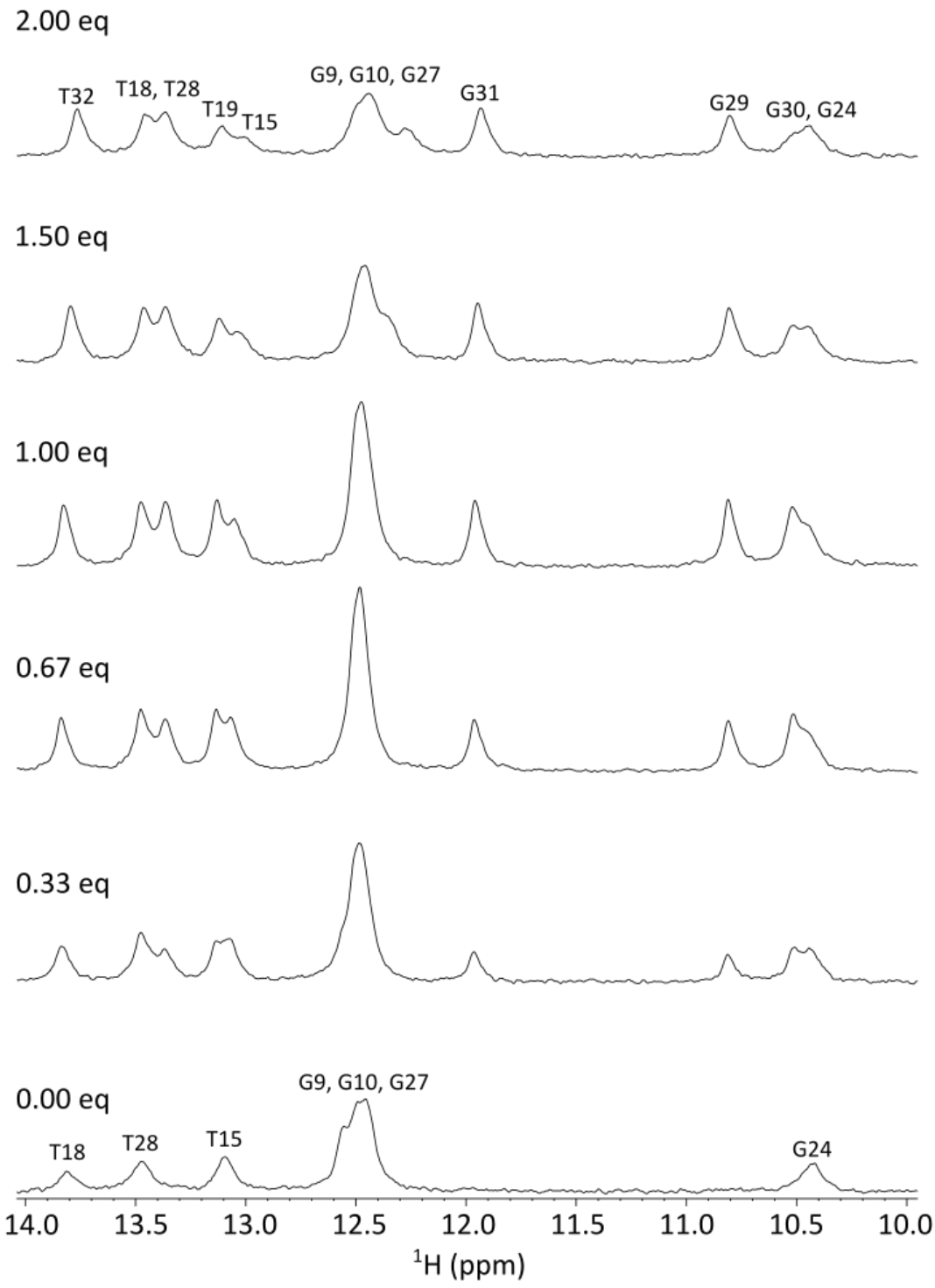

Figure 7.13. One-dimensional ^{1}H NMR spectra showing the titration of Dye-2Me into the MN19 cocaine binding aptamer. Spectra show the imino proton resonances of the NMR spectra. Ratios on the spectrum denote the molar ratio of aptamer to Dye-2Me. Spectra were acquired with an MN4 concentration of 500 μM in 140 mM NaCl, 10 mM $Na_xH_yPO_4$, pH 6.8, 10% ^2H_2O–90% H_2O at 5 °C.

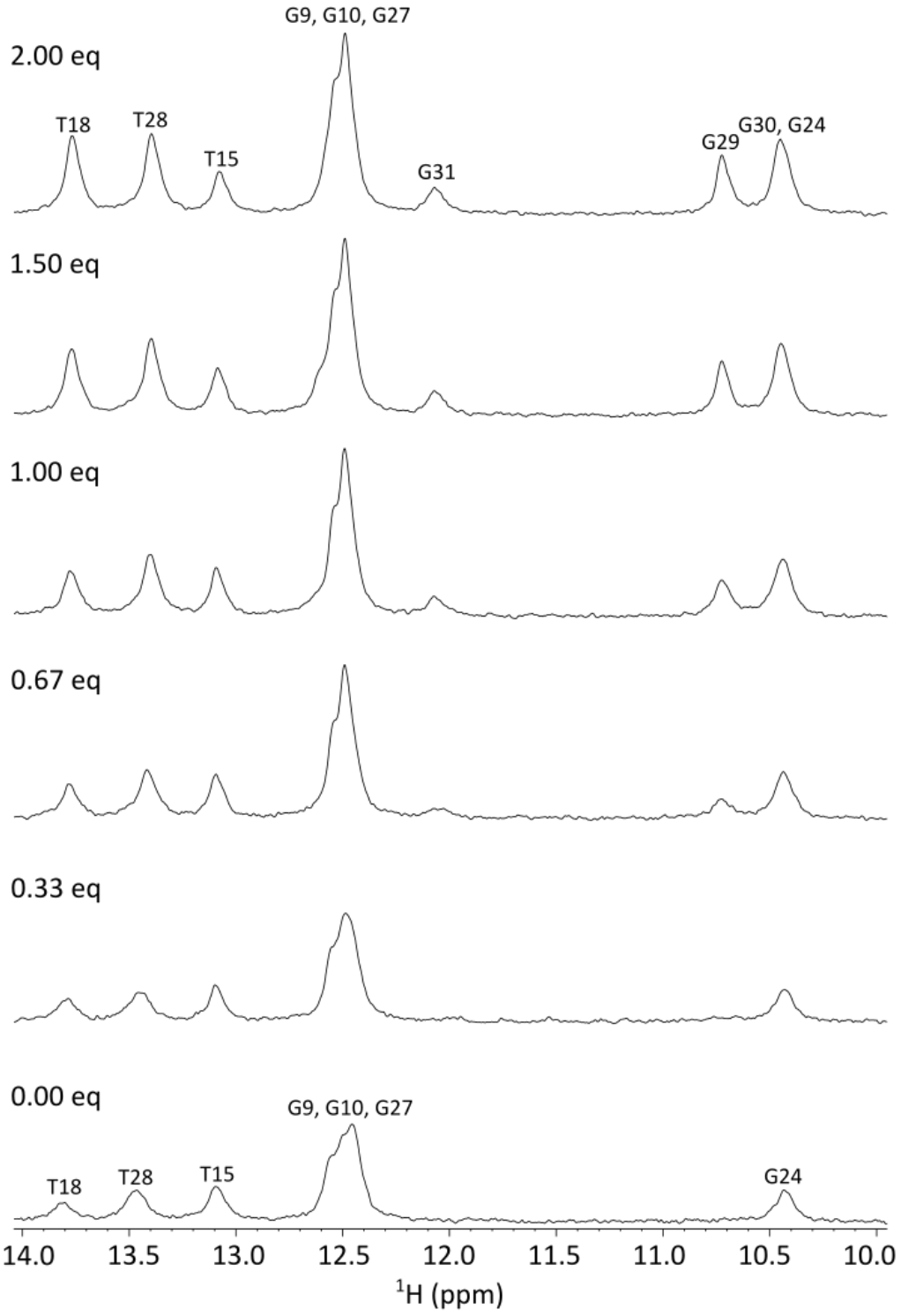

Figure 7.14. One-dimensional ^{1}H NMR spectra showing the titration of Dye-5 into the MN19 cocaine binding aptamer. Spectra show the imino proton resonances of the NMR spectra. Ratios on the spectrum denote the molar ratio of aptamer to Dye-5. Spectra were acquired with an MN4 concentration of 500 μM in 140 mM NaCl, 10 mM $Na_xH_yPO_4$, pH 6.8, 10% ^2H_2O–90% H_2O at 5 °C.

All three dyes were able to fold MN19 as seen by the emergence of new imino proton resonances. The identities of these resonances were found by comparing each MN19-dye titration with the corresponding MN4-dye titration. The MN19 imino proton resonances shifted to similar positions in the presence of each dye when compared to the MN4 imino proton resonaces. In all three titrations, the G29, G30, and G31 resonances appear as the dye is titrated into the sample, showing that the dye is stabilizing the base pairs around the three-way junction. For Dye-F and Dye-2Me the resonance of T32 also appeared indicated the structuring of stem 1. In these two cases, T32 was at a more downfield position in MN19 than in MN4. For the Dye-5-bound MN19 the T32 resonance does not form and the G31 resonance is less intense than both the Dye-F-bound and Dye-2Me-bound MN19. This could indicate that the T32-A5 base pair is more dynamic when Dye-5 is bound to MN19, meaning that stem 1 could be more dynamic. Dye-5 binds the weakest to MN4 out of the three dyes investigated. It would make sense that Dye-5 also binds the weakest the MN19. It is possible that the stabilization provided to the three-way junction by Dye-5 does not cause stem 1 to fold as anticipated when compared with the other dyes.

7.4 Concluding Remarks

In this chapter, the binding of Dye-F and two of its derivative dyes to the cocaine-binding aptamers MN4 and MN19 has been investigated and characterized. These dyes are three-way junction binders which are interesting as many other dyes focus on duplex DNA or quadruplex structures. The initial Dye-F is able to be displaced with quinine, while Dye-5 is able to be displaced by cocaine. This series of dyes appear to share a binding site with cocaine and quinine. If Dye-F is considered as the base dye, then by adding the two methyl groups to the benzothiazolium group the binding of the ligand and aptamer is weakened. This could potentially be due to steric clashes in the binding pocket or the change from a sulfur to a carbon distorts the

ring slightly make binding less favourable. On the other hand, by removing the fluorine group and adding in two methyl groups to the phenolic moiety, binding interaction is increased. This might add a little steric bulk to the opposite side of the phenol. Possibly the removal of the electronegative fluorine allows the phenol to more strongly hydrogen bond with the aptamer.

Chapter 8: Concluding Remarks

8.1 Summary

Aptamers are widely considered as a black box when it comes to how they function and how they interact with their ligand(s) of choice. The works shown in the previous chapters have helped deepen the understanding of the cocaine-binding aptamer and the ochratoxin A-binding aptamer, with the hope that the knowledge gained about these aptamers can be applied to other aptamer-ligand systems.

Chapter 3 investigated the imino proton exchange rate constants (k_{ex} values) of two cocaine-binding aptamer constructs. This was done for the free aptamers and two ligand-bound aptamers at a single temperature, allowing the dynamics of the aptamer at the base pair level to be investigated. Results showed that while binding of a ligand reduced k_{ex} values in the aptamer, this was occurred at and around the binding site as opposed to an aptamer wide phenomenon.

In Chapter 4 the k_{ex} values of the cocaine-binding aptamer were investigated again, but at a variety of temperatures and using multiple buffer conditions. Due to the extra variables measured it was possible to calculate the ΔH, ΔS, and ΔG of base pair opening for many base pairs within the aptamer. The ΔG values of the base pairs at the binding site increased with ligand binding for both ligands investigated, indicating that these base pair have become stronger. The ΔG value of base pairs away from the binding site either remained the same or decreased slightly with ligand binding, indicating those base pairs are not strengthened by the presence of a ligand.

Chapter 5 investigated the ochratoxin A-binding aptamer using ^{1}H NMR. The data presented shows a small helix that was previously unknown, and an aptamer structure that folds tightly with a relatively small amount of ligand present. ^{1}H NMR assignments of many of the nucleotide resonances were acquired, with the hopes that they can be used in the future to help

calculate a 3D structure. The k_{ex} values for the imino protons in the ochratoxin A-binding aptamer were also investigated, showing a much more rigid aptamer structure than the cocaine-binding aptamer investigated previously.

Chapter 6 characterized the binding of levamisole to the cocaine-binding aptamer. This interaction was found to be much weaker than of the aptamer for cocaine, but still at the same ligand binding site. This interaction was also found to be specific and when the structure of the binding site was disrupted so was the binding of levamisole.

Finally, chapter 7 investigated the binding of a set of three-way junction-binding dyes, with a conserved core structure. These dyes bound at the same ligand-binding site as cocaine and quinine, and the dyes were displaceable in the cases where the affinity of the aptamer for cocaine or quinine was greater than the affinity for the dye.

8.2 Future work

The primary objective of this thesis was to help continue to characterize the cocaine-binding aptamer using NMR spectroscopy. The base pair dynamics of the aptamer were investigated with two of its most well-known ligands, cocaine, and quinine. It would be interesting to continue these studies using a wider variety of ligands with different binding affinities such as levamisole and see how the trends in k_{ex} values change as a result.

Another research opportunity would be to determine the 3D structure of the cocaine-binding aptamer or the ochratoxin A-binding aptamer using either NMR or X-ray crystallography. With the cocaine-binding aptamer it would be interesting to see how the 3D structure of the aptamer varies as a function of what ligand is found at the binding site as it has a wide variety of ligands it has been shown to be able to interact with.

The cocaine-binding aptamer is used as a model system for the creation of various biosensor technique. These types of sensing techniques often involve conjugating molecules to the 5’ or 3’ ends of the aptamer to act as a reporter. Studying these aptamer-conjugate systems could be quite interesting and useful as it is possible these conjugated molecules are having some effect on the aptamer themselves. In addition, aptamers are often conjugated to a surface which could further change their structure and how they interact with the world around them. Gaining knowledge of how the cocaine-binding aptamer changes as a result of becoming conjugated to another small molecule or to a surface could provide useful information that could be applied to a wide array of different aptamer biosensor systems.

Bibliography

[1] C. Tuerk and L. Gold, "Systematic Evolution of Ligands by Exponential Enrichment: RNA Ligands to Bacteriophage T4 DNA Polymerase," *Science*, vol. 249, no. 4968, pp. 505–510, 1990.

[2] A. D. Ellington and J. W. Szostak, "In vitro selection of RNA molecules that bind specific ligands.," *Nature*, vol. 346, no. 6287, pp. 818–22, 1990.

[3] A. D. Ellington and J. W. Szostak, "Selection in vitro of single-stranded DNA molecules that fold into specific ligand-binding structures," *Nature*, vol. 355, no. 6363, pp. 850–852, 1992.

[4] P. Colas, B. Cohen, T. Jessen, I. Grishina, J. Mccoyt, and R. Brent, "Genetic selection of peptide aptamers that recognize and inhibit cyclin-dependent kinase 2," *Nature*, vol. 380, no. 11, pp. 548–550, 1996.

[5] Q. Zhu, G. Liu, M. Kai, and A. O. A. Miller, "DNA aptamers in the diagnosis and treatment of human diseases," *Molecules*, vol. 20, no. 12, pp. 20979–90997, 2015.

[6] S. Y. Toh, M. Citartan, S. C. B. Gopinath, and T. H. Tang, "Aptamers as a replacement for antibodies in enzyme-linked immunosorbent assay," *Biosens. Bioelectron.*, vol. 64, pp. 392–403, 2015.

[7] Z. Zhuo *et al.*, "Recent advances in SELEX technology and aptamer applications in biomedicine," *Int. J. Mol. Sci.*, vol. 18, no. 10, pp. 1–19, 2017.

[8] R. D. Jenison, S. C. Gill, A. Pardi, and B. Polisky, "High-resolution molecular discrimination by RNA.," *Science*, vol. 263, no. 5152, pp. 1425–1429, Mar. 1994.

[9] D. A. Daniels, H. Chen, B. J. Hicke, K. M. Swiderek, and L. Gold, "A tenascin-C aptamer identified by tumor cell SELEX: Systematic evolution of ligands by exponential

enrichment," *Proc. Natl. Acad. Sci. U. S. A.*, vol. 100, no. 26, pp. 15416–15421, 2003.

[10] J. Mi *et al.*, "In vivo selection of tumour-targeting RNA motifs," *Nat. Chem. Biol.*, vol. 6, no. 1, pp. 22–24, 2010.

[11] R. White *et al.*, "Generation of species cross-reactive aptamers using 'toggle' SELEX," *Mol. Ther.*, vol. 4, no. 6, pp. 567–573, 2001.

[12] S. D. Mendonsa and M. T. Bowser, "In vitro selection of high-affinity DNA ligands for human IgE using capillary electrophoresis," *Anal. Chem.*, vol. 76, no. 18, pp. 5387–5392, 2004.

[13] S. D. Mendonsa and M. T. Bowser, "In Vitro Evolution of Functional DNA Using Capillary Electrophoresis," *J. Am. Chem. Soc.*, vol. 126, no. 1, pp. 20–21, 2004.

[14] R. Stoltenburg, N. Nikolaus, and B. Strehlitz, "Capture-SELEX: Selection of DNA aptamers for aminoglycoside antibiotics," *J. Anal. Methods Chem.*, vol. 1, no. 1, pp. 1–14, 2012.

[15] G. Hybarger, J. Bynum, R. F. Williams, J. J. Valdes, and J. P. Chambers, "A microfluidic SELEX prototype," *Anal. Bioanal. Chem.*, vol. 384, no. 1, pp. 191–198, 2006.

[16] M. A. D. Neves *et al.*, "Defining the secondary structural requirements of the cocaine-binding aptamer by a thermodynamic and mutation study," *Biochemistry*, vol. 23, no. 48, pp. 2593–2597, 2010.

[17] M. A. D. Neves, O. Reinstein, and P. E. Johnson, "Defining a stem length-dependent binding mechanism for the cocaine-binding aptamer. A combined NMR and calorimetry study," *Biochemistry*, vol. 49, no. 39, pp. 8478–8487, 2010.

[18] D. E. Huizenga and J. W. Szostak, "A DNA aptamer that binds adenosine and ATP.," *Biochemistry*, vol. 34, no. 2, pp. 656–665, 1995.

[19] M. D. Frank-Kamenetskii and S. M. Mirkin, “TRIPLEX DNA STRUCTURES,” *Annu. Rev. Biochem.*, vol. 64, no. 1, pp. 65–95, 1995.

[20] T. Bing *et al.*, “Triplex-quadruplex structural scaffold: A new binding structure of aptamer,” *Sci. Rep.*, vol. 7, no. 1, pp. 1–10, 2017.

[21] M. Patel, A. Dutta, and H. Huang, “A selective adenosine sensor derived from a triplex DNA aptamer,” *Anal. Bioanal. Chem.*, vol. 400, no. 9, pp. 3035–3040, 2011.

[22] S. Neidle, “Human telomeric G-quadruplex: The current status of telomeric G-quadruplexes as therapeutic targets in human cancer,” *FEBS J.*, vol. 277, no. 5, pp. 1118–1125, 2010.

[23] M. L. Bochman, K. Paeschke, and V. A. Zakian, “DNA secondary structures: Stability and function of G-quadruplex structures,” *Nat. Rev. Genet.*, vol. 13, no. 11, pp. 770–780, 2012.

[24] K. Paeschke, T. Simonsson, J. Postberg, D. Rhodes, and H. J. Lipps, “Telomere end-binding proteins control the formation of G-quadruplex DNA structures in vivo,” *Nat. Struct. Mol. Biol.*, vol. 12, no. 10, pp. 847–854, 2005.

[25] P. A. Summers *et al.*, “Visualising G-quadruplex DNA dynamics in live cells by fluorescence lifetime imaging microscopy,” *Nat. Commun.*, vol. 12, no. 1, pp. 1–11, 2021.

[26] X. Yang *et al.*, “RNA G-quadruplex structures exist and function in vivo in plants,” *Genome Biol.*, vol. 21, no. 1, pp. 1–23, 2020.

[27] H. A. Day, P. Pavlou, and Z. A. E. Waller, “I-Motif DNA: Structure, stability and targeting with ligands,” *Bioorganic Med. Chem.*, vol. 22, no. 16, pp. 4407–4418, 2014.

[28] H. Kang, S. Kendrick, S. M. Hecht, and L. H. Hurley, “Is a Molecular Switch for Control of Gene Expression That Can Be,” *J. Am. Chem. Soc.*, vol. 135, pp. 4172-4185, 2014.

[29] S. Dzatko *et al.*, “Evaluation of the Stability of DNA i-Motifs in the Nuclei of Living Mammalian Cells,” *Angew. Chemie - Int. Ed.*, vol. 57, no. 8, pp. 2165–2169, 2018.

[30] M. Zeraati *et al.*, “I-motif DNA structures are formed in the nuclei of human cells,” *Nat. Chem.*, vol. 10, no. 6, pp. 631–637, 2018.

[31] H. Hasegawa, N. Savory, K. Abe, and K. Ikebukuro, “Methods for Improving Aptamer Binding Affinity,” *Molecules*, vol. 21, no. 421, 2016.

[32] Z. Y. Sun, X. N. Wang, S. Q. Cheng, X. X. Su, and T. M. Ou, “Developing novel G-quadruplex ligands: From interaction with nucleic acids to interfering with nucleic acid–protein interaction,” *Molecules*, vol. 24, no. 3, 2019.

[33] F. J. Grundy and T. M. Henkin, “tRNA as a positive regulator of transcription antitermination in B. subtilis,” *Cell*, vol. 74, no. 3, pp. 475–482, 1993.

[34] A. Nahvi, N. Sudarsan, M. S. Ebert, X. Zou, K. L. Brown, and R. R. Breaker, “Genetic control by a metabolite binding mRNA,” *Chem. Biol.*, vol. 9, no. 9, pp. 1043–1049, 2002.

[35] E. W. M. Ng, D. T. Shima, P. Calias, E. T. J. Cunningham, D. R. Guyer, and A. P. Adamis, “Pegaptanib, a targeted anti-VEGF aptamer for ocular vascular disease.,” *Nat. Rev. Drug Discov.*, vol. 5, no. 2, pp. 123–132, Feb. 2006.

[36] P. J. Bates, D. a Laber, D. M. Miller, S. D. Thomas, and J. O. Trent, “as a Novel Treatment for Cancer,” *Exp. Mol. Pathol.*, vol. 86, no. 3, pp. 151–164, 2009.

[37] S. Soundararajan *et al.*, “Plasma membrane nucleolin is a receptor for the anticancer aptamer AS1411 in MV4-11 leukemia cells,” *Mol. Pharmacol.*, vol. 76, no. 5, pp. 984–991, 2009.

[38] S. Soundararajan, W. Chen, E. K. Spicer, N. Courtenay-Luck, and D. J. Fernandes, “The nucleolin targeting aptamer AS1411 destabilizes Bcl-2 messenger RNA in human breast

cancer cells," *Cancer Res.*, vol. 68, no. 7, pp. 2358–2365, 2008.

[39] J. Rosenberg, R. A. Figlin, G. W. Smith, T. Choueiri, and F. Erlandsson, "A phase II trial of the nucleolin-targeted DNA aptamer AS1411 in metastatic refractory renal cell carcinoma," *Invest New Drugs*, vol. 32, no. 1, pp. 178–187, 2015.

[40] D. W. Hwang *et al.*, "A nucleolin-targeted multimodal nanoparticle imaging probe for tracking cancer cells using an aptamer," *J. Nucl. Med.*, vol. 51, no. 1, pp. 98–105, 2010.

[41] S. E. Lupold, B. J. Hicke, Y. Lin, and D. S. Coffey, "Identification and characterization of nuclease-stabilized RNA molecules that bind human prostate cancer cells via the prostate-specific membrane antigen," *Cancer Res.*, vol. 62, no. 14, pp. 4029–4033, 2002.

[42] T. C. Chu *et al.*, "Aptamer:toxin conjugates that specifically target prostate tumor cells," *Cancer Res.*, vol. 66, no. 12, pp. 5989–5992, 2006.

[43] J. P. Dassie *et al.*, "Targeted inhibition of prostate cancer metastases with an RNA aptamer to prostate-specific membrane antigen," *Mol. Ther.*, vol. 22, no. 11, pp. 1910–1922, 2014.

[44] M. Brayman, A. Thathiah, and D. D. Carson, "MUC1: A multifunctional cell surface component of reproductive tissue epithelia," *Reprod. Biol. Endocrinol.*, vol. 2, pp. 1–9, 2004.

[45] Y. F. Huang *et al.*, "Molecular Assembly of an Aptamer-Drug Conjugate for Targeted Drug Delivery to Tumour Cells," *ChemBioChem*, vol. 10, no. 5, pp. 862–868, 2009.

[46] Y. L. Luo, Y. S. Shiao, and Y. F. Huang, "Release of photoactivatable drugs from plasmonic nanoparticles for targeted cancer therapy," *ACS Nano*, vol. 5, no. 10, pp. 7796–7804, 2011.

[47] C. M. Dollins *et al.*, "Assembling OX40 Aptamers on a Molecular Scaffold to Create a

Receptor-Activating Aptamer," *Chem. Biol.*, vol. 15, no. 7, pp. 675–682, 2008.

[48] E. D. Pratico, B. A. Sullenger, and S. K. Nair, "Identification and characterization of an agonistic aptamer against the T cell costimulatory receptor, OX40," *Nucleic Acid Ther.*, vol. 23, no. 1, pp. 35–43, 2013.

[49] G. Zhang, Z. Liu, L. Fan, and Y. Guo, "Electrochemical prostate specific antigen aptasensor based on hemin functionalized graphene-conjugated palladium nanocomposites," *Microchim. Acta*, vol. 185, no. 3, 2018.

[50] E.-H. Lee, S. K. Lee, M. J. Kim, and S.-W. Lee, "Simple and rapid detection of bisphenol A using a gold nanoparticle-based colorimetric aptasensor," *Food Chem.*, vol. 287, pp. 205–213, 2019.

[51] T. Goda and Y. Miyahara, "Label-free monitoring of histone acetylation using aptamer-functionalized field-effect transistor and quartz crystal microbalance sensors," *Micromachines*, vol. 11, no. 9, 2020.

[52] M. N. Stojanovic, P. De Prada, and D. W. Landry, "Fluorescent sensors based on aptamer self-assembly [21]," *J. Am. Chem. Soc.*, vol. 122, no. 46, pp. 11547–11548, 2000.

[53] M. N. Stojanović, E. G. Green, S. Semova, D. B. Nikić, and D. W. Landry, "Cross-reactive arrays based on three-way junctions," *J. Am. Chem. Soc.*, vol. 125, no. 20, pp. 6085–6089, 2003.

[54] R. Pei, A. Shen, M. J. Olah, D. Stefanovic, T. Worgall, and M. N. Stojanovic, "High-resolution cross-reactive array for alkaloids," *Chem. Commun.*, no. 22, pp. 3193–3195, 2009.

[55] O. Reinstein *et al.*, "Engineering a Structure Switching Mechanism into a Steroid Binding Aptamer and Hydrodynamic Analysis of the Ligand Binding Mechanism," *Biochemistry*,

vol. 50, no. 43, pp. 9368–9376, 2011.

[56] S. Slavkovic, M. Altunisik, O. Reinstein, and P. E. Johnson, “Structure-affinity relationship of the cocaine-binding aptamer with quinine derivatives,” *Bioorganic Med. Chem.*, vol. 23, no. 10, pp. 2593–2597, 2015.

[57] S. Slavkovic, Z. R. Churcher, and P. E. Johnson, “Nanomolar binding affinity of quinine-based antimalarial compounds by the cocaine-binding aptamer,” *Bioorganic Med. Chem.*, vol. 26, no. 20, pp. 5427–5434, Nov. 2018.

[58] M. N. Stojanovic, P. De Prada, and D. W. Landry, “Aptamer-Based Folding Fluorescent Sensor for Cocaine,” *J. Am. Chem. Soc.*, vol. 4, no. 11, pp. 4928–4931, 2001.

[59] D. Roncancio *et al.*, “A label-free aptamer-fluorophore assembly for rapid and specific detection of cocaine in biofluids,” *Anal. Chem.*, vol. 86, no. 22, pp. 11100–11106, 2014.

[60] J. S. Swensen *et al.*, “Continuous, real-time monitoring of cocaine in undiluted blood serum via a microfluidic, electrochemical aptamer-based sensor,” *J. Am. Chem. Soc.*, vol. 131, no. 12, pp. 4262–4266, 2009.

[61] S. Slavkovic and P. E. Johnson, “Isothermal titration calorimetry studies of aptamer-small molecule interactions: practicalities and pitfalls,” *J. Aptamers*, vol. 2, pp. 45–51, 2018.

[62] R. W. Harkness, P. E. Johnson, and A. K. Mittermaier, “Measuring Biomolecular DSC Profiles with Thermolabile Ligands to Rapidly Characterize Folding and Binding Interactions,” *JoVE*, no. 129, p. 55959, 2017.

[63] D. Voet, W. B. Gratzer, R. A. Cox, and P. Doty, “Absorption spectra of nucleotides, polynucleotides, and nucleic acids in the far ultraviolet,” *Biopolymers*, vol. 1, no. 3, pp. 193–208, Jun. 1963.

[64] R. W. Harkness and A. K. Mittermaier, “G-quadruplex dynamics,” *Biochim. Biophys.*

Acta - Proteins Proteomics, vol. 1865, no. 11, pp. 1544–1554, 2017.

[65] R. E. Wang, Y. Zhang, J. Cai, W. Cai, and T. Gao, "Aptamer-Based Fluorescent Biosensors," *Curr. Med. Chem.*, vol. 18, no. 27, pp. 4175–4184, 2011.

[66] R. J. Trachman, L. Truong, and A. R. Ferré-D'Amaré, "Structural Principles of Fluorescent RNA Aptamers," *Trends Pharmacol. Sci.*, vol. 38, no. 10, pp. 928–939, 2017.

[67] S. Masiero *et al.*, "A non-empirical chromophoric interpretation of CD spectra of DNA G-quadruplex structures," *Org. Biomol. Chem.*, vol. 8, no. 12, pp. 2683–2692, 2010.

[68] V. J. B. Ruigrok, M. Levisson, J. Hekelaar, H. Smidt, B. W. Dijkstra, and J. van der Oost, "Characterization of Aptamer-Protein Complexes by X-ray Crystallography and Alternative Approaches," *Int. J. Mol. Sci.*, vol. 13, no. 12, pp. 10537–10552, 2012.

[69] G. W. Collie and G. N. Parkinson, "The application of DNA and RNA G-quadruplexes to therapeutic medicines," *Chem. Soc. Rev.*, vol. 40, no. 12, pp. 5867–5892, 2011.

[70] S. B. Long, M. B. Long, R. R. White, and B. A. Sullenger, "Crystal structure of an RNA aptamer bound to thrombin," *RNA*, vol. 14, no. 12, pp. 2504–2512, 2008.

[71] K. Wüthrich, *NMR of Proteins and Nucleic Acids*. Wiley, 1986.

[72] J. Lee, C. E. Vogt, M. McBrairty, and H. M. Al-Hashimi, "Influence of dimethylsulfoxide on RNA structure and ligand binding," *Anal. Chem.*, vol. 85, no. 20, pp. 9692–9698, 2013.

[73] O. Reinstein *et al.*, "Quinine binding by the cocaine-binding aptamer. thermodynamic and hydrodynamic analysis of high-affinity binding of an off-target ligand," *Biochemistry*, vol. 52, no. 48, pp. 8652–8662, 2013.

[74] J.-H. Lee and A. Pardi, "Thermodynamics and kinetics for base-pair opening in the P1 duplex of the Tetrahymena group I ribozyme.," *Nucleic Acids Res.*, vol. 35, no. 9, pp. 2965–74, 2007.

[75] J.-H. Lee, F. Jucker, and A. Pardi, “Imino proton exchange rates imply an induced-fit binding mechanism for the VEGF165-targeting aptamer, Macugen,” *FEBS Lett.*, vol. 582, pp. 1835–1839, 2008.

[76] Z. R. Churcher, M. A. D. Neves, H. N. Hunter, and P. E. Johnson, “Comparison of the free and ligand-bound imino hydrogen exchange rates for the cocaine-binding aptamer,” *J. Biomol. NMR*, vol. 68, no. 1, 2017.

[77] B. Klinkert, F. Narberhaus, and H. Schwalbe, “Direct observation of the temperature-induced melting process of the Salmonella fourU RNA thermometer at base-pair resolution,” *Nucleic Acids Res*, vol. 38, no. 11, pp. 3834–3847, 2010.

[78] H. S. Steinert, J. Rinnenthal, and H. Schwalbe, “Individual basepair stability of DNA and RNA studied by NMR-detected solvent exchange,” *Biophys. J.*, vol. 102, no. 11, pp. 2564–2574, 2012.

[79] Z. R. Churcher, and P. E. Johnson, “NMR for non-experts; a practical guide for applying NMR methods in studies of aptamer-ligand interactions,” *J. Aptamers*, vol. 4, pp. 3–9, 2020.

[80] P. E. Johnson, P. Tomme, M. D. Joshi, and L. P. McIntosh, “Interaction of soluble cellooligosaccharides with the N-terminal cellulose-binding domain of Cellulomonas fimi cenc. 2. NMR and ultraviolet absorption spectroscopy,” *Biochemistry*, vol. 35, no. 44, pp. 13895–13906, 1996.

[81] E. J. Cho, J.-W. Lee, and A. D. Ellington, “Applications of Aptamers as Sensors,” *Annu. Rev. Anal. Chem.*, vol. 2, no. 1, pp. 241–264, 2009.

[82] J. L. Vinkenborg, N. Karnowski, and M. Famulok, “Aptamers for allosteric regulation,” *Nat. Chem. Biol.*, vol. 7, no. 8, pp. 519–527, 2011.

[83] M. Mascini, I. Palchetti, and S. Tombelli, “Nucleic acid and peptide aptamers: Fundamentals and bioanalytical aspects,” *Angew. Chemie - Int. Ed.*, vol. 51, no. 6, pp. 1316–1332, 2012.

[84] Y. [Seok Kim], N. H. [Ahmad Raston], and M. [Bock Gu], “Aptamer-based nanobiosensors,” *Biosens. Bioelectron.*, vol. 76, pp. 2–19, 2016.

[85] M. Ilgu and M. Nilsen-Hamilton, “Aptamers in analytics,” *Analyst*, vol. 141, no. 5, pp. 1551–1558, 2016.

[86] M. Gueron and J.-L. Leroy, “Studies of Base Pair Kinetics by NMR Measurement of Proton Exchange,” *Methods Enzymol.*, vol. 261, no. 3, pp. 383–413, 1995.

[87] S. Nonin, F. Jiang, and D. J. Patel, “Imino Proton Exchange and Base-pair Kinetics in the AMP ± RNA Aptamer Complex,” *J. Mol. Biol.*, vol. 268, pp. 359-374, 1997.

[88] S. Nonin-Lecomte, C. H. Lin, and D. J. Patel, “Additional hydrogen bonds and base-pair kinetics in the symmetrical AMP-DNA aptamer complex,” *Biophys. J.*, vol. 81, no. 6, pp. 3422–3431, 2001.

[89] B. R. Baker, R. Y. Lai, M. S. Wood, E. H. Doctor, A. J. Heeger, and K. W. Plaxco, “An electronic, aptamer-based small-molecule sensor for the rapid, label-free detection of cocaine in adulterated samples and biological fluids,” *J. Am. Chem. Soc.*, vol. 128, no. 10, pp. 3138–3139, 2006.

[90] A. K. Sharma and J. M. Heemstra, “Small-Molecule-Dependent Split Aptamer Ligation,” *J. Am. Chem. Soc.*, vol. 133, pp. 12426–12429, 2011.

[91] M. A. D. Neves, C. Blaszykowski, S. Bokhari, and M. Thompson, “Ultra-high frequency piezoelectric aptasensor for the label-free detection of cocaine,” *Biosens. Bioelectron.*, vol. 72, pp. 383–392, 2015.

[92] A. Sachan, M. Ilgu, A. Kempema, G. A. Kraus, and M. Nilsen-Hamilton, “Specificity and Ligand Affinities of the Cocaine Aptamer: Impact of Structural Features and Physiological NaCl,” *Anal. Chem.*, vol. 88, no. 15, pp. 7715–7723, 2016.

[93] C. M. Grytz, A. Marko, P. Cekan, S. T. Sigurdsson, and T. F. Prisner, “Flexibility and conformation of the cocaine aptamer studied by PELDOR,” *Phys. Chem. Chem. Phys.*, vol. 18, no. 4, pp. 2993–3002, 2016.

[94] R. W. Harkness, S. Slavkovic, P. E. Johnson, and A. K. Mittermaier, “Rapid characterization of folding and binding interactions with thermolabile ligands by DSC,” *Chem. Commun.*, vol. 52, no. 92, pp. 13471–13474, 2016.

[95] M. A. D. Neves, S. Slavkovic, Z. R. Churcher, and P. E. Johnson, “Salt-mediated two-site ligand binding by the cocaine-binding aptamer,” *Nucleic Acids Res.*, vol. 45, no. 3, 2017.

[96] J. Zhang, C. P. Jones, and A. R. Ferré-D’Amaré, “Global analysis of riboswitches by small-angle X-ray scattering and calorimetry,” *Biochim. Biophys. Acta - Gene Regul. Mech.*, vol. 1839, no. 10, pp. 1020–1029, 2014.

[97] E. Green *et al.*, “A rational approach to minimal high-resolution cross-reactive arrays,” *J. Am. Chem. Soc.*, vol. 128, no. 47, pp. 15278–15282, 2006.

[98] Z. R. Churcher, D. Garaev, H. N. Hunter, and P. E. Johnson, “Reduction in Dynamics of Base pair Opening upon Ligand Binding by the Cocaine-Binding Aptamer,” *Biophys. J.*, vol. 119, no. 6, pp. 1147–1156, 2020.

[99] Y. Qiu, Y. Tang, B. Li, and M. He, “Rapid detection of cocaine using aptamer-based biosensor on an evanescent wave fibre platform,” *R. Soc. Open Sci.*, vol. 5, p. 180821, 2018.

[100] Y. Qiu, C. Gu, B. Li, and H. Shi, “Aptameric detection of quinine in reclaimed wastewater

using a personal glucose meter," *Anal. Methods*, vol. 10, no. 24, pp. 2931–2938, 2018.

[101] A. Celebanska *et al.*, "Label-free cocaine aptasensor based on a long-period fiber grating," *Opt. Lett.*, vol. 44, no. 10, p. 2482, 2019.

[102] M. A. D. Neves, A. A. Shoara, O. Reinstein, O. Abbasi Borhani, T. R. Martin, and P. E. Johnson, "Optimizing Stem Length to Improve Ligand Selectivity in a Structure-Switching Cocaine-Binding Aptamer," *ACS Sensors*, vol. 2, no. 10, pp. 1539–1545, 2017.

[103] M. N. Stojanovic and D. W. Landry, "Aptamer-Based Colorimetric Probe for Cocaine," *J. Am. Chem. Soc.*, vol. 124, no. 33, pp. 9678–9679, 2002.

[104] S. Slavkovic, M. Altunisik, O. Reinstein, and P. E. Johnson, "Structure-affinity relationship of the cocaine-binding aptamer with quinine derivatives," *Bioorganic Med. Chem.*, vol. 23, no. 10, pp. 2593–2597, 2015.

[105] J. Bao, S. M. Krylova, O. Reinstein, P. E. Johnson, and S. N. Krylov, "Label-free solution-based kinetic study of aptamer-small molecule interactions by kinetic capillary electrophoresis with UV detection revealing how kinetics control equilibrium," *Anal. Chem.*, vol. 83, no. 22, pp. 8387–8390, 2011.

[106] S. Slavkovic, S. R. Eisen, and P. E. Johnson, "Designed Alteration of Binding Affinity in Structure-Switching Aptamers through the Use of Dangling Nucleotides," *Biochemistry*, vol. 59, no. 5, pp. 663–670, 2020.

[107] H. Van Den Bedem and J. S. Fraser, "Integrative, dynamic structural biology at atomic resolution - It's about time," *Nat. Methods*, vol. 12, no. 4, pp. 307–318, 2015.

[108] G. P. Lisi and J. Patrick Loria, "Using NMR spectroscopy to elucidate the role of molecular motions in enzyme function," *Prog. Nucl. Magn. Reson. Spectrosc.*, vol. 92–93, pp. 1–17, 2016.

[109] M. Getz, X. Sun, A. Casiano-Negroni, Q. Zhang, and H. M. Al-Hashimi, “Biopolymers Volume 85 / Number 4 295,” *Biopolymers*, vol. 85, no. 4, pp. 392–406, 2007.

[110] B. Zhao and Q. Zhang, “Characterizing excited conformational states of RNA by NMR spectroscopy,” *Curr. Opin. Struct. Biol.*, vol. 30, pp. 134–146, 2015.

[111] A. Rangadurai, E. S. Szymaski, I. J. Kimsey, H. Shi, and H. M. Al-Hashimi, “Characterizing micro-to-millisecond chemical exchange in nucleic acids using off-resonance R1ρ relaxation dispersion,” *Prog. Nucl. Magn. Reson. Spectrosc.*, vol. 112–113, pp. 55–102, 2019.

[112] R. W. Harkness and A. K. Mittermaier, “G-quadruplex dynamics,” *Biochim. Biophys. Acta - Proteins Proteomics*, vol. 1865, no. 11, pp. 1544–1554, 2017.

[113] M. Marušič, J. Schlagnitweit, and K. Petzold, “RNA Dynamics by NMR Spectroscopy,” *ChemBioChem*, vol. 20, no. 21, pp. 2685–2710, 2019.

[114] S. R. Choi, N. H. Kim, H. S. Jin, Y. J. Seo, J. Lee, and J. H. Lee, “Base-pair Opening Dynamics of Nucleic Acids in Relation to Their Biological Function,” *Comput. Struct. Biotechnol. J.*, vol. 17, pp. 797–804, 2019.

[115] S. J. Cho, J. Bang, J.-H. Lee, and B.-S. Choi, “Base pair opening kinetics and dynamics in the DNA duplexes that specifically recognized by very short patch repair protein (Vsr),” *Arch. Biochem. Biophys.*, vol. 501, no. 2, pp. 201–206, 2010.

[116] F. Narberhaus, H. Schwalbe, and D. Wagner, “Mechanistic insights into temperature-dependent regulation of the simple cyanobacterial hsp17 RNA thermometer at base-pair resolution,” *Nucleic Acids Res*, vol. 43, no. 11, pp. 5572–5585, 2015.

[117] P. Cekan, E. Ö. Jonsson, and S. T. Sigurdsson, “Folding of the cocaine aptamer studied by EPR and fluorescence spectroscopies using the bifunctional spectroscopic probe Ç,”

Nucleic Acids Res., vol. 37, no. 12, pp. 3990–3995, 2009.

[118] B. Gülbakan, K. Barylyuk, P. Schneider, M. Pillong, G. Schneider, and R. Zenobi, "Native Electrospray Ionization Mass Spectrometry Reveals Multiple Facets of Aptamer-Ligand Interactions: From Mechanism to Binding Constants," *J. Am. Chem. Soc.*, vol. 140, no. 24, pp. 7486–7497, 2018.

[119] B. Malile and J. I. L. Chen, "Factors influencing polyelectrolyte-aptamer multilayered films with target-controlled permeability for sensing applications," *Analyst*, vol. 141, no. 12, pp. 3794–3802, 2016.

[120] N. G. Spiropulos and J. M. Heemstra, "Templating effect in DNA proximity ligation enables use of non-bioorthogonal chemistry in biological fluids," *Artif. DNA PNA XNA*, vol. 3, no. 3, pp. 123–128, 2012.

[121] A. A. Shoara *et al.*, "Development of a thermal-stable structure-switching cocaine-binding aptamer," *Biochimie*, vol. 145, 2018.

[122] T. Hermann and D. J. Patel, "Adaptive Recognition by Nucleic Acid Aptamers," *Science*, vol. 287, no. 5454, pp. 820–825, 2000.

[123] T. O. Larsen, A. Svendsen, and J. Smedsgaard, "Biochemical Characterization of Ochratoxin A-Producing Strains of the Genus Penicillium," *Appl. Environ. Microbiol.*, vol. 67, no. 8, pp. 3630–3635, 2001.

[124] H. A. Clark and S. M. Snedeker, "Ochratoxin A: Its cancer risk and potential for exposure," *J. Toxicol. Environ. Heal. - Part B Crit. Rev.*, vol. 9, no. 3, pp. 265–296, 2006.

[125] T. R. Bui-Klimke and F. Wu, "Ochratoxin A and Human Health Risk: A Review of the Evidence," *Crit. Rev. Food Sci. Nutr.*, vol. 55, no. 13, pp. 1860–1869, 2015.

[126] J. H. Hope and B. E. Hope, "A review of the diagnosis and treatment of ochratoxin a

inhalational exposure associated with human illness and kidney disease including focal segmental glomerulosclerosis," *J. Environ. Public Health*, vol. 2012, 2012.

[127] L.-E. Appelgren and R. G. Arora, "Distribution of 14C-labelled ochratoxin a in pregnant mice," *Food Chem. Toxicol.*, vol. 21, no. 5, pp. 563–568, 1983.

[128] J. D. Thrasher, M. R. Gray, K. H. Kilburn, D. P. Dennis, and A. Yu, "A water-damaged home and health of occupants: A case study," *J. Environ. Public Health*, vol. 2012, no. February 2008, 2012.

[129] I. P. Hallén, A. Breitholtz-Emanuelsson, K. Hult, M. Olsen, and A. Oskarsson, "Placental and lactational transfer of ochratoxin A in rats," *Nat. Toxins*, vol. 6, no. 1, pp. 43–49, Feb. 1998.

[130] Health Canada, "Ochratoxin A in Wheat Products , Oat Products , Rice Products and Other Grain Products - April." pp. 1–12, 2019.

[131] K. Jørgensen, "Occurrence of ochratoxin A in commodities and processed food - A review of EU occurrence data," *Food Addit. Contam.*, vol. 22, no. SUPPL. 1, pp. 26–30, 2005.

[132] J. A. Cruz-Aguado and G. Penner, "Determination of ochratoxin A with a DNA aptamer," *J. Agric. Food Chem.*, vol. 56, no. 22, pp. 10456–10461, 2008.

[133] A. De Girolamo, L. Le, G. Penner, R. Schena, and A. Visconti, "Analytical performances of a DNA-ligand system using time-resolved fluorescence for the determination of ochratoxin A in wheat," *Anal. Bioanal. Chem.*, vol. 403, no. 9, pp. 2627–2634, 2012.

[134] T. Zhao *et al.*, "Towards highly specific aptamer-affinity monolithic column by efficient UV light-initiated polymerization in 'one-pot,'" *Anal. Chim. Acta*, vol. 1165, 2021.

[135] Y. J. Yang *et al.*, "A Label-free aptasensor based on Aptamer/NH2 Janus particles for ultrasensitive electrochemical detection of Ochratoxin A," *Talanta*, vol. 199, no. February,

pp. 310–316, 2019.

[136] F. Tian *et al.*, “Multicolor colorimetric detection of ochratoxin A via structure-switching aptamer and enzyme-induced metallization of gold nanorods,” *Food Chem.*, vol. 320, no. November 2019, p. 126607, 2020.

[137] K. L. Fadock and R. A. Manderville, “DNA Aptamer–Target Binding Motif Revealed Using a Fluorescent Guanine Probe: Implications for Food Toxin Detection,” *ACS Omega*, vol. 2, no. 8, pp. 4955–4963, 2017.

[138] M. Adrian, B. Heddi, and A. T. Phan, “NMR spectroscopy of G-quadruplexes,” *Methods*, vol. 57, no. 1, pp. 11–24, 2012.

[139] A. A. Shoara, Z. R. Churcher, S. Slavkovic, and P. E. Johnson, “Weak Binding of Levamisole by the Cocaine-Binding Aptamer Does Not Interfere with an Aptamer-Based Detection Assay,” *ACS Omega*, vol. 6, no. 37, pp. 24209–24217, 2021.

[140] T. M. Brunt, J. van den Berg, E. Pennings, and B. Venhuis, “Adverse effects of levamisole in cocaine users: a review and risk assessment,” *Arch. Toxicol.*, vol. 91, no. 6, pp. 2303–2313, 2017.

[141] G. Hernando, I. Bergé, D. Rayes, and C. Bouzat, “Contribution of Subunits to Caenorhabditis elegans Levamisole-Sensitive Nicotinic Receptor Function,” *Mol. Pharmacol.*, vol. 82, no. 3, pp. 550–560, Sep. 2012.

[142] S. Spector, I. Munjal, and D. E. Schmidt, “Effects of the immunostimulant, levamisole, on opiate withdrawal and levels of endogenous opiate alkaloids and monoamine neurotransmitters in rat brain,” *Neuropsychopharmacology*, vol. 19, no. 5, pp. 417–427, 1998.

[143] C. G. Moertel *et al.*, “Levamisole and Fluorouracil for adjuvant therapy of resected colon

carcinoma," *New English J. Med.*, vol. 323, no. 6, pp. 352–358, 1990.

[144] K. M. Midthun, L. S. Nelson, and B. K. Logan, "Levamisole—a Toxic Adulterant in Illicit Drug Preparations: a Review," *Ther. Drug Monit.*, vol. 43, no. 2, 2021.

[145] W. K. P. Amery and J. P. J. M. Bruynseels, "Levamisole, the story and the lessons," *Int. J. Immunopharmacol.*, vol. 14, no. 3, pp. 481–486, 1992.

[146] N. Scheinfeld, J. D. Rosenberg, and J. M. Weinberg, "Levamisole in Dermatology," *Am. J. Clin. Dermatol.*, vol. 5, no. 2, pp. 97–104, 2004.

[147] S. Patnaik, P. Balderia, L. Vanchhawng, P. Markazi, J. Wykretowicz, and S. Perloff, "Is levamisole-induced vasculitis a relegated diagnostic possibility? A case report and review of literature," *Am. J. Case Rep.*, vol. 16, no. 215, pp. 658–662, 2015.

[148] J. Broséus, N. Gentile, F. Bonadio Pont, J. M. Garcia Gongora, L. Gasté, and P. Esseiva, "Qualitative, quantitative and temporal study of cutting agents for cocaine and heroin over 9 years," *Forensic Sci. Int.*, vol. 257, pp. 307–313, 2015.

[149] J. A. Buchanan *et al.*, "A Confirmed Case of Agranulocytosis after Use of Cocaine Contaminated with Levamisole," *J. Med. Toxicol.*, vol. 6, no. 2, pp. 160–164, 2010.

[150] J. Graf *et al.*, "Purpura, cutaneous necrosis, and antineutrophil cytoplasmic antibodies associated with levamisole-adulterated cocaine," *Arthritis Rheum.*, vol. 63, no. 12, pp. 3998–4001, 2011.

[151] N. Xu, W. Zhou, S. Li, G. Zhou, N. Zhang, and J. Liang, "Clinical and MRI Characteristics of Levamisole-Induced Leukoencephalopathy in 16 Patients," *J. Neuroimaging*, vol. 19, no. 4, pp. 326–331, Oct. 2009.

[152] L. Long, Y. Song, L. Xu, and B. Xiao, "Levamisole-induced leukoencephalopathy mimicking Baló disease," *Neurology*, vol. 84, no. 3, p. 328, 2015.

[153] E. Bertol, F. Mari, M. G. Di Milia, L. Politi, S. Furlanetto, and S. B. Karch, "Determination of aminorex in human urine samples by GC–MS after use of levamisole," *J. Pharm. Biomed. Anal.*, vol. 55, no. 5, pp. 1186–1189, 2011.

[154] F. Rongioletti *et al.*, "Purpura of the ears: a distinctive vasculopathy with circulating autoantibodies complicating long-term treatment with levamisole in children," *Br. J. Dermatol.*, vol. 140, no. 5, pp. 948–951, May 1999.

[155] M. De Jong *et al.*, "Levamisole: A Common Adulterant in Cocaine Street Samples Hindering Electrochemical Detection of Cocaine," *Anal. Chem.*, vol. 90, no. 8, pp. 5290–5297, 2018.

[156] J. M. Carothers, S. C. Oestreich, and J. W. Szostak, "Aptamers selected for higher-affinity binding are not more specific for the target ligand," *J. Am. Chem. Soc.*, vol. 128, no. 24, pp. 7929–7937, 2006.

[157] S. Nonin, F. Jiang, and D. J. Patel, "Imino proton exchange and base-pair kinetics in the AMP-RNA aptamer complex11Edited by I. Tinoco," *J. Mol. Biol.*, vol. 268, no. 2, pp. 359–374, 1997.

[158] F. Bottari *et al.*, "Do Aptamers Always Bind? The Need for a Multifaceted Analytical Approach When Demonstrating Binding Affinity between Aptamer and Low Molecular Weight Compounds," *J. Am. Chem. Soc.*, vol. 142, no. 46, pp. 19622–19630, 2020.

[159] C. Zong and J. Liu, "The arsenic-binding aptamer cannot bind arsenic: critical evaluation of aptamer selection and binding," *Anal. Chem.*, vol. 91, no. 16, pp. 10887–10893, 2019.

[160] X. Tao *et al.*, "Detection of chloramphenicol with an aptamer-based colorimetric assay: critical evaluation of specific and unspecific binding of analyte molecules," *Microchim. Acta*, vol. 187, no. 12, 2020.

[161] L. Zara *et al.*, “Anti-pesticide DNA aptamers fail to recognize their targets with asserted micromolar dissociation constants,” *Anal. Chim. Acta*, vol. 1159, p. 338382, 2021.

[162] E. Daems, G. Moro, R. Campos, and K. De Wael, “Mapping the gaps in chemical analysis for the characterisation of aptamer-target interactions,” *TrAC Trends Anal. Chem.*, vol. 142, p. 116311, 2021.

[163] A. A. Shoara, S. Slavkovic, L. W. Donaldson, and P. E. Johnson, “Analysis of the interaction between the cocaine-binding aptamer and its ligands using fluorescence spectroscopy,” *Can. J. Chem.*, vol. 95, no. 12, pp. 1253–1260, Aug. 2017.

[164] A. J. Van Riesen *et al.*, “Visible Fluorescent Light-up Probe for DNA Three-Way Junctions Provides Host–Guest Biosensing Applications,” *ACS Appl. Bio Mater.*, vol. 4, pp. 6732–6741, 2021.

[165] K. C. Woods, S. S. Martin, V. C. Chu, and E. P. Baldwin, “Quasi-equivalence in site-specific recombinase structure and function: crystal structure and activity of trimeric cre recombinase bound to a three-way lox DNA junction,” *J. Mol. Biol.*, vol. 313, no. 1, pp. 49–69, 2001.

[166] K. Duskova *et al.*, “Identification of Three-Way DNA Junction Ligands through Screening of Chemical Libraries and Validation by Complementary in Vitro Assays,” *J. Med. Chem.*, vol. 62, no. 9, pp. 4456–4466, 2019.

[167] Y. Dong, C. Yao, Y. Zhu, L. Yang, D. Luo, and D. Yang, “DNA functional materials assembled from branched DNA: Design, synthesis, and applications,” *Chem. Rev.*, vol. 120, no. 17, pp. 9420–9481, 2020.

[168] H. Seo *et al.*, “A DNA-Based MRI Contrast Agent for Quantitative pH Measurement,” *ACS Sensors*, vol. 6, no. 3, pp. 727–732, 2021.

[169] Y. Du and S. Dong, “Nucleic acid biosensors: Recent advances and perspectives,” *Anal. Chem.*, vol. 89, no. 1, pp. 189–215, 2017.

[170] I. Lubitz, D. Zikich, and A. Kotlyar, “Specific high-affinity binding of thiazole orange to triplex and g-quadruplex DNA,” *Biochemistry*, vol. 49, no. 17, pp. 3567–3574, 2010.

[171] J. Mohanty, N. Barooah, V. Dhamodharan, S. Harikrishna, P. I. Pradeepkumar, and A. C. Bhasikuttan, “Thioflavin T as an efficient inducer and selective fluorescent sensor for the human telomeric G-quadruplex DNA,” *J. Am. Chem. Soc.*, vol. 135, no. 1, pp. 367–376, 2013.

[172] H. Zipper, H. Brunner, J. Bernhagen, and F. Vitzthum, “Investigations on DNA intercalation and surface binding by SYBR Green I, its structure determination and methodological implications,” *Nucleic Acids Res.*, vol. 32, no. 12, p. e103, 2004.

[173] A. Fürstenberg, M. D. Julliard, T. G. Deligeorgiev, N. I. Gadjev, A. A. Vasilev, and E. Vauthey, “Ultrafast excited-state dynamics of DNA fluorescent intercalators: New insight into the fluorescence enhancement mechanism,” *J. Am. Chem. Soc.*, vol. 128, no. 23, pp. 7661–7669, 2006.

[174] Z. Yang *et al.*, “Supramolecular Recognition of Three Way Junction DNA by a Cationic Calix [3]carbazole,” *Chem. – A Eur. J.*, vol. 24, no. 23, pp. 6087–6093, Apr. 2018.

[175] P. S. Deore, M. D. Gray, A. J. Chung, and R. A. Manderville, “Ligand-Induced G-Quadruplex Polymorphism: A DNA Nanodevice for Label-Free Aptasensor Platforms,” *J. Am. Chem. Soc.*, vol. 141, no. 36, pp. 14288–14297, 2019.

[176] Q. Wan, S. Chen, W. Shi, L. Li, and H. Ma, “Lysosomal pH Rise during Heat Shock Monitored by a Lysosome-Targeting Near-Infrared Ratiometric Fluorescent Probe,” *Angew. Chemie Int. Ed.*, vol. 53, no. 41, pp. 10916–10920, Oct. 2014.

[177] M. A. D. Neves *et al.*, “Defining the secondary structural requirements of a cocaine-binding aptamer by a thermodynamic and mutation study,” *Biophys. Chem.*, vol. 153, no. 1, pp. 9–16, 2010.